Université de Montréal

The role of Organic Cation Transporters in the pharmacokinetics of clinically relevant DNA damaging agents: *in vivo* and *in silico* studies

Par Arturo Papaluca

Département de Médecine
Faculté de Médecine

Thèse présentée à la Faculté des études supérieures et postdoctorales
en vue de l'obtention du grade de *Philosophiae Doctor (Ph.D.)*
en Sciences Biomédicales
Spécialisation Médecine Expérimentale

Mars 2018

Université de Montréal
Faculté de Médecine
Faculté des études supérieures et postdoctorales

Cette thèse intitulée:

The role of Organic Cation Transporters in the pharmacokinetics of clinically relevant DNA damaging agents: *in vivo* and *in silico* studies

Présentée par:
Arturo Papaluca

A été évaluée par un jury composé des personnes suivantes:

Dr. Stephen Michnick	Président-rapporteur
Dr. Uri Saragovi	Directeur de recherche
Dr. Alex Parker	Membre du jury
Dr. Mohan Malleshaiah	Examinateur externe
Dr. Hugo Wurtele	Représentant du doyen de la FES

Résumé

Dans les systèmes cellulaires, l'homéostasie des nutriments, définie comme la capacité d'un système à maintenir l'équilibre des concentrations de nutriments dans des gradients fluctuants par rapport à l'environnement interne et externe, est essentielle pour survivre dans des conditions difficiles. Entre l'espace intracellulaire et extracellulaire de la membrane, une pléthore de signaux de signalisation moléculaires et cellulaires interagissent pour coordonner le maintien de l'homéostasie cellulaire. L'un des principaux mécanismes contrôlant cette interaction est orchestré par les protéines de la membrane plasmique. Selon leurs structures et fonctions, ces protéines membranaires existent en plusieurs classes, et sont spécialisées dans le contrôle du trafic de molécules, dont des nutriments, à travers la membrane.

L'une des plus importantes familles de protéines membranaires est celle des transporteurs de cations organiques (OCTs). Le but de ce projet de recherche était d'étudier la relation structure-fonction des OCTs. Les OCTs sont impliqués dans l'absorption physiologique de divers nutriments, et des preuves récentes ont démontré que ces transporteurs peuvent aussi jouer un rôle important dans la régulation du transport des xénobiotiques et des médicaments thérapeutiques dans les cellules.

Le nématode du sol, *Caenorhabditis elegans*, a permis de clarifier les rôles des OCTs. Ce nématode utilise le transporteur membranaire OCT-1 comme transporteur d'absorption, qui a été classé comme un transporteur de cations organiques basé sur le transport du substrat prototypique, le cation ammonium tétraéthylammonium (TEA) (Wu *et al*., 1999). Près d'une décennie et demie plus tard, il a été démontré que OCT-1 transporte l'antioxydant ergothionéine (Cheah *et al*., 2013). L'analyse des séquences a révélé l'existence de transporteurs supplémentaires et apparentés tels que OCT-2 chez *C. elegans*; cependant, les rôles d'OCT-2 n'ont pas été décrits jusqu'à présent. Dans cet esprit, nous avons cherché à savoir si OCT-1 et OCT-2 pourraient coordonner et se partager les responsabilités de l'absorption de composés cationiques chez *C. elegans*.

Dans cette thèse, nous dévoilons pour la première fois le rôle de l'OCT-2 chez *C. elegans*. Nous avons montré que, de manière inattendue, OCT-1 a un petit rôle direct dans

l'absorption de composés cationiques; néanmoins, il exerce des fonctions de régulation sur l'expression d'OCT-2. En l'absence d'*oct-1*, l'expression d'*oct-2* est régulée positivement et, par conséquent, OCT-2 serait le principal transporteur d'absorption pour les médicaments chimiothérapeutiques cliniquement pertinents tels que la doxorubicine, le cisplatine et le méthotrexate utilisés pour plusieurs traitements contre le cancer. Notre recherche réfute donc l'hypothèse initiale selon laquelle OCT-1 agit comme un transporteur d'absorption cationique? directe chez *C. elegans*. Dans ce travail, nous avons établi une méthode de criblage de composé *in vivo* pour découvrir l'efficacité d'absorption des médicaments cationiques par OCT-1 et OCT-2 en surveillant l'apoptose des cellules germinales induite par les dommages à l'ADN par ces composé. Nous avons observé que la suppression du gène *oct-1* et / ou de la régulation négative d'OCT-1 par un ARNi entraîne une régulation positive d'*oct-2*, stimulant ainsi l'absorption de médicaments chimiothérapeutiques et de métabolites toxiques potentiels qui provoquent des effets délétères sur l'animal. De plus, les vers ayant des voies de réparation de l'ADN défectueuses étaient extrêmement sensibles aux agents chimiothérapeutiques lorsque *oct-2* était régulée positivement. Il est important de noter que l'épuisement d'*oct-2* a complètement entravé l'absorption de ces médicaments, empêchant ainsi leurs effets génotoxiques et conduisant ainsi à des phénotypes de résistance aux médicaments.

De plus, nous avons effectué un criblage comparatif basé sur la modélisation *in silico* de OCT-1 et OCT-2 et avons démontré que cette approche discriminait sélectivement parmi les ligands qui se lient de manière robuste à OCT-2 et non OCT-1. Nous avons validé cette approche *in vivo* et démontré que le transport dépendant d'OCT-2 de composés endommageant l'ADN sensibilisait les vers avec des voies de réparation de l'ADN défectueuses, et que cet effet était inversé une fois qué *oct-2* était régulée à la baisse.

Collectivement, ces méthodes expérimentales servent de preuves de concept dans l'étude des caractéristiques clés des transporteurs cationiques pertinents. L'application de méthodes *in silico* pour la présélection des molécules cibles et la validation subséquente avec notre modèle *in vivo* basé sur les OCTs augmenteront sans aucun doute le succès dans l'identification de nouvelles molécules chimiothérapeutiques tout en réduisant le cout de recherche et développement. Notre travail a des implications cruciales, car il indique que (i) les transporteurs d'absorption hyperactive sont susceptibles d'importer des concentrations anormalement élevées de composés génotoxiques et de métabolites pendant de nombreuses années, causant l'instabilité génomique et finalement des cancers, et (ii) ces transporteurs d'absorption sont responsables de la résistance aux médicaments observée pour de nombreux types de cancers.

En bref, ces résultats soulignent l'importance des transporteurs pour réguler l'entrée des médicaments chimiothérapeutiques dans les cellules et soulèvent la possibilité que la résistance aux médicaments et les réponses sensibles aux médicaments observées chez les patients cancéreux puissent être régies au niveau de l'absorption des médicaments. Cette étude utilisant *C. elegans* est donc de la plus haute importance car elle exploite les transporteurs d'absorption comme une nouvelle approche pour expliquer des effets indésirables, développer de nouvelles molecules et aussi pour développer plusieurs programmes de dépistage de drogues. Ainsi, notre travail a des applications immédiates à un large éventail de disciplines.

Pour terminer, dans un thème connexe, nous présentons la découverte d'un nouveau mécanisme de réparation de l'ADN par lequel les lésions créées par le nucléoside 5-hydroxymethyuracil (5-hmU) sont éliminés par la voie de réparation de l'excision de base (BER) impliquant APN-1 et UNG-1 chez *C. elegans*. Dans ce travail, nous avons examiné *in vivo* les rôles de quatre enzymes de réparation de l'ADN, les deux ADN glycosylases UNG-1 et NTH-1 et les deux AP endonucléases APN-1 et EXO-3, dans le traitement de produit modifié par oxydation de la thymine, 5-hmU. UNG-1 a déjà été caractérisé *in vitro*; capable d'éliminer l'uracile, tandis que NTH-1 a été prouvé capable d'éliminer la thymine glycol, 5-formyl cytosine et 5-hmU. De même, les deux endonucléases AP ont été caractérisées et les deux peuvent inciser des sites abasiques et éliminer les lésions 3'-bloquantes lors des cassures d'ADN a simple brin. Cependant, APN-1 est distinct d'EXO-3, car il possède deux activités supplémentaires, une activité exonucléase 3'-5 'et une activité de réparation d'incision de nucléotide qui agit directement sur certaines bases modifiées par oxydation (i.e. 5-hmU). Pour prouver l'implication d'UNG-1, nous avons utilisé des mutants de *C. elegans* et observé que les mutants *ung-1* présentaient une diminution de la taille et de la durée de vie

des couvées, et un niveau élevé d'apoptose des cellules germinales lorsqu'ils sont stimulés par 5-hmU.

Des phénotypes similaires ont été observés avec le mutant *apn-1*, qui ont été exacerbés par la régulation négative de l'ARNi de l'*apn-1* dans le mutant *ung-1*. D'autre part, les mutants *nth-1* ou *exo-3* ont présenté des phénotypes de type sauvage vers 5-hmU. Nous proposons un modèle suggérant que UNG-1 est impliqué dans l'élimination de 5-hmU incorporé dans le génome et le site abasique résultant est clivé par APN-1 ou EXO-3. En l'absence d'UNG-1, 5-hmU est éliminée par NTH-1, ce qui crée une lésion génotoxique 3'-bloquante qui nécessite l'action de l'activité 3'-diesterase ou 3'- à 5'-exonucléase de l'APN -1. Nos données fournissent la première preuve que UNG-1 possède la capacité d'éliminer 5-hmU *in vivo* chez *C. elegans*, et qui pourrait avoir été remplacé par l'activité de type SMUG1 dans les cellules de mammifères.

Mots-clés : Absorption et résistance des médicaments, transporteurs de cations organiques, *C. elegans*, apoptose, dommages et voies de réparation de l'ADN, modélisation *in silico*, expression génique, inhibiteur de la voie de réparation de l'ADN, 5-hydroxyméthyluracil, ADN glycosylases, AP endonucléases.

Abstract

In cellular systems, nutrient homeostasis - defined as the ability of a system to maintain *in equilibrium* nutrient concentrations within fluctuating gradients relative to the internal and external environment - is essential to thrive in harsh conditions. Between the intracellular and extracellular space of the cell membrane, a plethora of molecular and cellular signalling cues interact to coordinate the maintenance of cellular homeostasis. One of the main mechanisms that controls this interaction is orchestrated by membrane proteins. These membrane proteins exist in several classes, structures and functions and are specialized in controlling the traffic of all sorts of nutrients and molecules across the membrane.

The aim of this study was to investigate the structure-function relationship of Organic Cation Transporters (OCTs), one of the most important family of membrane proteins. OCTs are involved in the physiological uptake of various nutrients and recent evidences show that these transporters may be far more important in regulating the entry of xenobiotics and therapeutic drugs into cells.

The soil nematode *Caenorhabditis elegans* has provided powerful insights into the roles of OCTs. This nematode uses the membrane-bound transporter OCT-1 as an uptake transporter, which has been classified as an organic cation transporter based on the transport of the prototypical substrate, the ammonium cation tetraethylammonium (TEA) (Wu *et al*. 1999). Nearly a decade and a half later, it was shown that OCT-1 transports the antioxidant ergothioneine (Cheah *et al*., 2013). DNA sequence analysis revealed the existence of additional and related transporters such as OCT-2 in *C. elegans*; however, the roles of OCT-2 have not been described so far. With this in mind, we set out to investigate whether OCT-1 and OCT-2 might coordinate and share the responsibilities in the uptake of cationic compounds in *C. elegans*.

In this thesis, we unveil for the first time the role of OCT-2 in *C. elegans*. We showed that, unexpectadly, OCT-1 has little role in the uptake of cationic compounds; nonetheless it exerts regulatory functions on *oct-2* expression. In the absence of *oct-1*, *oct-2* expression is significantly upregulated and, thus, it is OCT-2 that serves as the major uptake transporter for clinically relevant chemotherapeutic drugs such as doxorubicin, cisplatin and

methotrexate used for several cancer treatments. Our research therefore refutes the initial hypothesis that OCT-1 is/acts as a direct uptake transporter in *C. elegans*.

In this work, we established an *in vivo* screening method to uncover the uptake efficiency of cationic drugs by OCT-1 and OCT-2 by monitoring DNA damage-induced germ cell apoptosis. We observed that deletion of *oct-1* gene and/or RNAi-driven downregulation of *oct-1* causes upregulation of *oct-2*, therefore stimulating the uptake of chemotherapeutic drugs and potential toxic metabolites which cause deleterious effects on the animal. Moreover, worms with defective DNA repair pathways were particularly sensitive to the chemotherapeutic agents when *oct-2* was upregulated. Importantly, depletion of *oct-2* completely impeded the uptake of these drugs thus preventing their genotoxic effects, and hence leading to drug resistance phenotypes. Additionally, we performed an *in silico* modeling-based comparative screening of OCT-1 and OCT-2, and showed that this approach selectively discriminated amongst ligands that bind robustly to OCT-2 and not OCT-1. We validated this approach *in vivo*, and demonstrated that OCT-2-dependent transport of DNA-damaging compounds successfully sensitized worms with defective DNA repair pathways, and this effect was reversed once *oct-2* was downregulated.

Collectively, these experimental methods serve as a proof of concept in studying key characteristics of relevant cationic transporters. Applying *in silico* methods for the preselection of target molecules and subsequent validation with our OCTs-based *in vivo* model will undoubtedly increase the success of chemotherapeutics and screening of newly synthesized molecules with a cost-efficient model system. Our work has pivotal implications, as it indicates that (i) hyperactive uptake transporters are likely to import abnormally high concentrations of genotoxic compounds and metabolites over many years causing genomic instability and eventually cancers and (ii) these uptake transporters may hold the key to the mechanisms of drug resistance observed in many types of cancers.

In short, these results underscore the importance of uptake transporters in regulating the entry of chemotherapeutic drugs into cells and raises the possibility that drug-resistance and drug-sensitive responses observed in cancer patients could be governed at the level of drug uptake. This study is therefore pivotal as it exploits uptake transporters as a novel

approach to expand on several drug screening programs using *C. elegans*. Thus, our work has immediate applications to a broad range of disciplines.

Finally, in a related theme, we present the discovery of a new DNA repair mechanism whereby lesions created by the nucleoside 5-hydroxymethyuracil (5-hmU) are removed by the base excision repair pathway. In this work, we examined the *in vivo* roles of four base-excision DNA repair enzymes in *C. elegans* - the two DNA glycosylases UNG-1 and NTH-1 and the two AP endonucleases APN-1 and EXO-3 - in processing the oxidatively modified product of thymine, 5-hmU. *C. elegans* UNG-1 has been previously characterized *in vitro* to remove uracil, while NTH-1 was shown to remove thymine glycol, 5-formyl cytosine and 5-hmU. Likewise, the two AP endonucleases have been characterized and both can incise abasic sites and remove 3′-blocking lesions at DNA single strand breaks. However, APN-1 is distinct from EXO-3, as it possesses two additional activities, a 3′- to 5′-exonulease activity and a nucleotide incision repair activity that acts directly on certain oxidatively modified bases. Herein, we used *C. elegans* mutants and observe that *ung-1* mutants exhibited a decrease in brood size and lifespan, and an elevated level of germ cell apoptosis when challenged with 5-hmU.

Similar phenotypes were seen with *apn-1* mutant, which were exacerbated by RNAi downregulation of *apn-1* in the *ung-1* mutant. The *nth-1* or *exo-3* mutants displayed wild type phenotypes towards 5-hmU. We propose a model suggesting that UNG-1 is involved in removing 5-hmU incorporated into the genome and the resulting abasic site is cleaved by APN-1 or EXO-3. In the absence of UNG-1, the 5-hmU is removed by NTH-1, which creates a genotoxic 3′-blocking lesion that requires the action of the 3′-diesterase or 3′- to 5′-exonuclease activity of APN-1. Our data provide the first evidence that *C. elegans* UNG-1 possesses the ability to remove 5-hmU *in vivo*, which may have been replaced with SMUG1-like activity in mammalian cells.

Keywords : Drug uptake and resistance, Organic Cation Transporters, *C. elegans*, apoptosis, DNA damage and repair pathways, *in silico* modeling, gene expression, DNA repair pathway inhibitor, 5-hydroxymethyluracil, DNA glycosylases, AP endonucleases.

Table of contents

List of tables

Chapter 2:

Supplementary tables:

List of figures

Chapter 1:

Chapter 2:

Supplementary figures:

Chapter 3:

Supplementary figures:

Chapter 4:

List of abbreviations

17-DMAG	17-(dimethylaminoethylamino)-17-demethoxy-geldanamycin (Alvespimycin)
ABC	ATPbinding cassette
ACT-1 (*act-1*)	Actin 1
APN-1 (*apn-1*)	APurinic/apyrimidinic endonuclease 1
α-helices	Alpha helices
ASP^+	4-[4-(dimethylamino)-styryl]-N-methylpyridinium
AT13387	(2,4-dihydroxy-5-isopropylphenyl)-(5-(4-methylpiperazin-1-ylmethyl)-1,3-dihydroisoindol-2-yl)methanone
ATP	Adenosine triphosphate
BER	Base Excision Repair
BCRP	Breast Cancer Resistance Protein (ABCG2)
BSEP	Bile-Salt Export Pump (SPGP; ABCB11)
C. elegans	*Caenorhabditis elegans*
Cd^{++}	Cadmium cation
CaM	Calmodulin
CDDP	Cisplatin
CED-1 (*ced-1*)	CEll Death abnormality 1
CED-3 (*ced-3*)	CEll Death abnormality 3
CED-4 (*ced-4*)	CEll Death abnormality 4
CED-9 (*ced-9*)	CEll Death abnormality 9
CEP-1 (*cep-1*)	*C. elegans* P-53-like protein 1
Cis-Pt	Cisplatin
CLL	Chronic lymphocytic leukemia
CML	Chronic myeloid leukemia
CNS	Central nervous system
CKU-70	*Caenorhabditis* KU 70
CKU-80	*Caenorhabditis* KU 80
CPD	Cyclobutane pyrimidine dimer

Cs^+	Cesium cation
DNA	Deoxyribonucleic acid
DNMT1	DNA (cytosine-5)-methyltransferase 1
DNMT3	DNA (cytosine-5)-methyltransferase 3
E3330	(2E)-2-[(4,5-dimethoxy-2-methyl-3,6-dioxocyclohexa-1,4-dien-1-yl)methylidene]undecanoic acid
ECF	Extracellular fluid
EGL-1 (*egl-1*)	EGg Laying defective 1
EJ	End-joining
EMT	Extraneuronal monoamine transporter
ET	Ergothioneine
ET-743	Trabectedin
E. coli	*Escherichia coli*
EXO-1	Exonuclease 1
EXO-3 (*exo-3*)	Exonuclease 3
5-FU	5-fluorouracil
F11782	Tafluposide
FDA	Food and Drug Administration
FdCyd	5-fluoro-2-deoxycytidine
5-hmU	5-hydroxymethyluracil
5-hmU:A	5-hmU paired with adenine
5-hmU:G	5-hmU paired with guanine
5-hmC	5-hydroxymethylcytosine
5-mC	5-methylcytosine
H_2O_2	Hydrogen peroxide
HCC	Hepatocellular carcinoma
HNPCC	Hereditary nonpolyposis colorectal cancer
HR	Homologous recombination repair
HSP90	Heat shock protein 90
HTS	High-throughput screening

IC50	Half maximal inhibitory concentration
ICF	Intracellular fluid
ASBT	Apical Sodium/Bile acid co-Transporter (SLC10A2)
in silico	Performed via computer simulation
in vivo	Performed on living organisms
IPI-504	17-(allylamino)-17-demethoxy-geldanamycin (retaspimycin)
IR	Infrared radiation
KW-2478	2-(2-ethyl-3,5dihydroxy-6-(3-methoxy-4-(2-morpholin-4-ylethoxy)benzoyl)phenyl)-N,N-bis(2-methoxyethyl)acetamide monohydrochloride
LAPTM4α	Lysosomal associated protein transmembrane 4 alpha
LIG-4	DNA ligase IV
^{131}I-MIBG	[^{131}I]metaiodobenzylguanidine
MATE1	Multidrug and Toxin Extrusion Protein 1 (SLC47A1)
MATE2 (k)	Multidrug and Toxin Extrusion Protein 2 (SLC47A2) (kidney)
MBD4	Methyl-CpG-binding domain 4
MCI13E	Isoborneol haloacetate derivate
Mirin	6-(4-hydroxyphenyl)-2-thioxo-2,3-dihydro-4(1H)-pyrimidinone
µL	Microliter
mL	Milliliter
µg	Microgram
mg	Milligram
MLH1	MutL homolog 1
µM	Micromolar
mM	Millimolar
MMC	Mitomycin C
MMR	Mismatch Repair
MCT1	Monocarboxylic Acid Transporter 1 (SLC16A1)
MPP^{+}	1-methyl-4-phenylpyridinium
MRP2	Multidrug Resistance Protein 2 (ABCC2)

MRP3	Multidrug Resistance Protein 3 (ABCC3)
MRP4	Multidrug Resistance Protein 4 (ABCC4)
MRP5	Multidrug Resistance Protein 5 (ABCC5)
MRP6	Multidrug Resistance Protein 6 (ABCC6)
MSH-2 (*msh-2*)	MutS Homolog 2
MSH-6	MutS Homolog 6
MutLα	Heterodimer complex MLH1-PMS2
MutSα	Heterodimer complex MSH2-MSH6
MX	Methoxyamine
NER	Nucleotide Excision Repair
NHEJ	Non-homologous end joining repair
nM	Nanomolar
NMN	N-methylnicotinamide
NTCP	Sodium/Taurocholate Co-Transporting Peptide (SLC10A1)
NTH-1 (*nth-1*)	NTH (eNdonuclease THree like) homolog) 1
NVP-AUY922	5-(2,4-dihydroxy-5-isopropylphenyl)-4-(4-morpholin-4-ylmethylphenyl)isoxazole-3-carboxylic acid ethylamide
$O_2^{\bullet-}$	Superoxide anion
OAT1	Organic Anion Transporter 1 (SLC22A6)
OAT2	Organic Anion Transporter 2 (SLC22A7)
OAT3	Organic Anion Transporter 3 (SLC22A8)
OAT4	Organic Anion Transporter 4 (SLC22A11)
OAT7	Organic Anion Transporter 7 (SLC22A9)
OATP	Organic Anion Transporter Polypeptide
OATP1B1	Organic Anion Transporter Polypeptide 1B1 (SLCO1B1)
OATP1B3	Organic Anion Transporter Polypeptide 1B3 (SLCO1B3)
OATP2B1	Organic Anion Transporter Polypeptide 2B1 (SLCO2B1)
OATP4C1	Organic Anion Transporter Polypeptide 4C1 (SLCO4C1)
OCT(s)	Organic Cation Transporter(s)
OCT-1 (*oct-1*)	Organic Cation Transporter 1 (SLC22A1)

OCT-2 (*oct-2*)	Organic Cation Transporter 2 (SLC22A2)
OCTN1	Organic Cation/Ergothioneine Transporter 1 (SLC22A4)
OCTN2	Organic Cation/Carnitine Transporter 2 (SLC22A5)
OH	Hydroxyl radical
OSTα – OSTβ	Heteromeric Organic Solute Transporter α – β
(6–4)PP	(6–4) Photoproduct
P-gp	P-glycoprotein (MDR1, ABCB1)
PKA	Protein kinase A
PKC	Protein kinase C
PI3K	Phosphatidylinositol-3-kinase
PCNA	Proliferating cell nuclear antigen
PEPT1	Peptide Transporter 1 (SLC15A1)
PEPT2	Peptide Transporter 2 (SLC15A2)
PES-23 (*pes-23*)	Patterned Expression Site 23
PMP-3 (*pmp-3*)	Peroxisomal Membrane Protein related 3
Pol β	Polymerase Beta
Pol γ	Polymerase Gamma
PolH	Polymerase Eta
PolQ	Polymerase Theta
PolQ-1 (*polq-1*)	Polymerase Theta 1
qRT-PCR	Quantitative real-time polymerase chain reaction
RAD-51 (*rad-51*)	RADiation sensitivity abnormal/yeast RAD-related
RI-1	3-chloro-1-(3,4-dichlorophenyl)-4-(4-morpholinyl)-1H-pyrrole-2,5-dione
RNA	Ribonucleic acid
RNAi	RNA interference
ROS	Reactive oxigen species
RPA-1	Replication protein A homolog 1
S-1	Fluoropyrimidine containing 5-fluorouracil (5-FU)
S-1/CDDP	S-1 plus cisplatin

S. cerevisiae	*Saccharomyces cerevisiae*
SLC(s)	Solute Carrier Transporter(s)
SLC22A1	Solute Carrier Transporter 22 A1 gene encoding OCT1
SLC22A2	Solute Carrier Transporter 22 A2 gene encoding OCT2
SMUG1	Single-strand selective monofunctional uracil DNA glycosylase
SNP(s)	Single nucleotide polymorphism(s)
TDG	Thymine-DNA glycosylase
TEA	Tetraethylammonium (ammonium cation)
TET	Ten-eleven translocation
TMD(s)	Transmembrane domain(s)
TPA	Tetrapropylammonium
UCN-01	7-hydroxystaurosporine
UNG-1 (*ung-1*)	Uracil DNA N-Glycosylase 1
URAT1	Urate Transporter 1 (SCL22A12)
USF	Upstream stimulating factor
XPA-1 (*xpa-1*)	Human XPA (*Xeroderma pigmentosum* component group A) related 1

Amino Acid Codes

Amino acid	Three letter code	One letter code
Alanine	ala	A
Asparagine	asn	R
Aspartic acid	asp	D
Cysteine	cys	C
Glutamic acid	glu	E
Glutamine	gln	Q
Glycine	gly	G
Histidine	his	H
Isoleucine	ile	I
Leucine	leu	L
Lysine	lys	K
Methionine	met	M
Phenylalanine	phe	F
Proline	pro	P
Serine	ser	S
Threonine	thr	T
Tryptophan	try	W
Tyrosine	tyr	Y
Valine	val	V

Dedication

To my beautiful and beloved wife Lia

A Mamá, Papá y a mis
queridos hermanos quienes amo
sin dependencia

To all the people with dreams, desires and positive ambitions.
Don't let anyone take them away, stay strong!

Acknowledgements

"Gratitude is heaven itself; there could be no heaven without gratitude" – William Blake.

A lot can change during the years, a plethora of events and a variation of all of it. Then there are things that stand still like love, friendship and madness. This work represents the end of a long journey that reached its destination, and which has been as much endured and influenced by myself, as by the nature surrounding me.

The family: My precious Lia –sua alma, amor infinito e apoio, é a minha eterna fonte de felicidade! Obrigado por tudo! – you are my home and inspiration, shine on you crazy diamond… forever more! To my beloved family, without your support, nothing would be possible. I am indebted in every possible way. I pay eternal gratitude to Mamá y Papá, who provided me every possible opportunity, within their reach, to educate me. To my brothers Oscar and Ulyses, my doggies and my babies! Thank you all for making my life so special.

The faculty: I would like to express my sincere gratitude and appreciation to my supervisor Dr. Uri Saragovi, whose ethics and mentorship has been very instrumental in my success. Thank you for believing in me and giving me the opportunity to spend such valuable time in your laboratory. I am sincerely thankful to Dr. Stephen Michnick for his encouragement and guidance since my early beginnings as a researcher. Among many, I am particularly indebted to them for inculcating a sense of direction and encouragement to conduct independent research. Apart from science and the construction of my thesis, I am also thankful to them for providing me with a learning opportunity over the years. My learnings will never be forgotten or surpassed. Also, I would like to extend my sincere gratitude to the jury of my Ph.D. thesis for accepting to review my work, Dr. Mohan Malleshaiah, Dr. Alex Parker and Dr. Hugo Wurtele.

The colleagues: I thank my colleagues from McGill University and University of Montreal for sharing the similar ups and downs of research, for discussions and for the good moments we had together; Sean Jmaeff, Iulia Pirvulescu, Dr. Alba Galán, Dr. Fouad Brahimi, Dr. Serge Moffett, Dr. Hinyu Nedev, Reilly Pidgeon, Dr. Raj Roychoudhury.

The funding: I am grateful for the Ph.D. fellowship awarded by the Fonds de Recherche du Québec – Santé and recognition awards from the University of Montréal which made this work possible.

The sources of inspiration: The Father of Creation – The Mother of Nature, my guides when I can't see. The number of musicians whose determination and persistence to follow what they believe to create the greatest pieces in music history, inspired me to never give up. And the long list of metal bands –which I listen continuously– helped me channel out negative feelings and frustrations encountered during this long journey.

A todos los que con palabras, anécdotas, sueños o silencios, lograron convencerme de que hay cosas en este mundo que no se pueden dejar pasar, que no se repiten, que tienen vida propia, que reclaman un destino y que vale la pena el aguante. Toda insistencia tiene su recompensa, eso no se puede negar – Gracias!

All in all, let love land where it lands…

Introduction

Chapter 1 : Membrane Proteins

1.1. Preamble

The presence of interconnections between vital organs, the bloodstream and across the blood brain barrier is achieved thanks to the function of membrane proteins, one of the most important classes of proteins expressed ubiquitiously in humans and across most kingdoms of life[1]. Membrane proteins are responsible for the import and export of most chemical substances that are crucial for development - including water, ions, gases, nutrients, vitamins, substrates, cofactors and drugs – between organs and the bloodstream[2,3]. Thus, the regulation of small molecule transport across cellular membranes is pivotal to maintain homeostasis and is the gatekeeper to its interaction with the environment[4]. In these regards, keeping the integrity of cellular membranes is key to control the traffic of molecules, preserve the transmission of genetic information and prevent the intrusion of toxic elements[5].

Membrane transporters consist of solute carriers, water channels, ion channels, and ATPbinding cassette transporters. Among these, the largest family is composed by the Solute Carrier Transporters (SLCs), which comprise 456 proteins grouped phylogenetically in 52 subfamilies[2,3]. Solute Carrier Transporters are expressed on the plasma membrane and in organellar membranes[2]. Despite being one of the most understudied group of membrane proteins in humans, many small molecules including FDA-approved drugs, have been shown to have preferential uptake into the organs specifically through SLCs[2]. Notably, defects in the functionality of SLCs are linked to the development of many disorders including mendelian diseases, neurological conditions and resistance to chemotherapeutic drugs[2]. Consequently, a tremendous potential exists in exploring the mechanisms of Solute Carrier Transporters in the context of controlling the disposition of drugs into tissues for the treatment of cancer and the discovery of new drugs.

1.2. Solute Carrier Transporters

Transporters represent a group of membrane-bound proteins that control the entry and exit of compounds, and a number of biological processes. These transporters mediate the translocation of a myriad of endogenous and exogenous substrates across cellular membranes. These include the transport of major nutrient metabolites such as sugars, amino acids, nucleosides, peptides, hormones, neurotransmitters, saccharides and xenobiotics. Membrane transporters are expressed in an organ-specific manner throughout the epithelia of major organs of the human body, for instance, the liver, kidney and intestine, as well as in organs with barrier properties such as the brain and placenta[2] (Figure 1).

Different transporters are expressed and localized to the plasma membrane and act as entry and exit gates between the extracellular fluid (ECF) and intracellular fluid (ICF). As well, these transporters can also be localized to membranes that build intracellular organelles (e.g. the nucleus), therefore controlling the delivery and elimination of both required and unnecessary substrates thereby promoting cellular homeostasis. These transporters have specific physiological roles in the uptake, allocation and elimination of nutrients, drugs and various substances[2]. Moreover, detoxification of environmental contaminants and metabolic byproducts is attributed to transporters.

Two main superfamilies encode these transporters: the ATPbinding cassette (ABC) superfamily and the Solute Carrier (SLC) uptake transporter superfamily, accounting for approximately 4% of the genes in the human genome. The ABC superfamily encodes transporters that utilize energy from ATP hydrolysis to perform efflux functions[6], whereas the SLC superfamily encodes transporters involved in the physiological uptake of small molecules[2]. It has been demonstrated that several clinically approved drugs often have similar physiochemical characteristics with certain endogenous compounds, substrates of SLC and ABC membrane transporters[6]. In drug development, such characteristics are of high interest as a variety of membrane transporters have been characterized and designated as drug transporters[2,6]. These transporters are pivotal in determining the uptake, efflux, pharmacokinetics, efficacy and adverse effects of prevalent and experimental drugs to treat human diseases. The pharmacological roles of the SLC transporters is of utmost importance, particularly those with broad substrate specificities such as the subfamily of Organic Cation Transporters (OCTs) and its equivalents that serve in the uptake and allocation of structurally and pharmacologically diverse drugs.

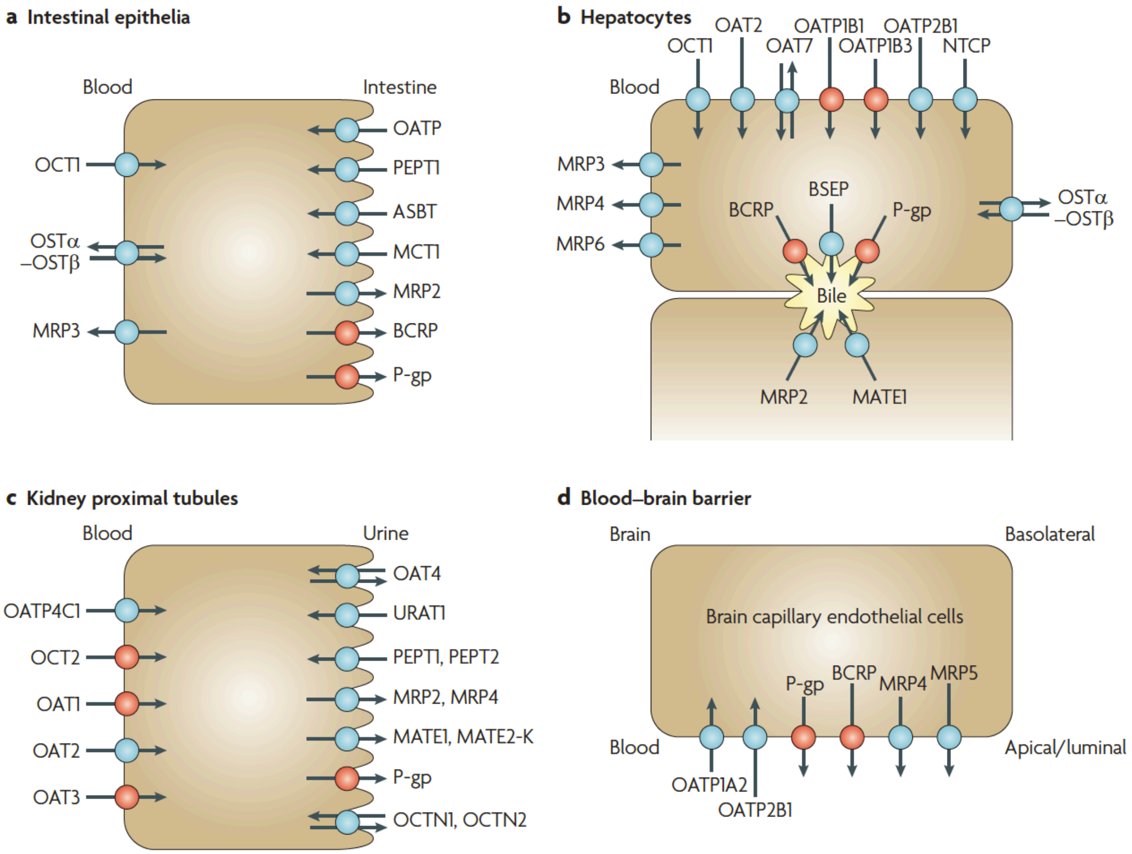

Figure 1. Human membrane proteins for the transport and excretion of drugs and endogenous molecules. Cellular membrane transporter domains of intestinal epithelia, hepatocytes, kidney proximal tubules and brain capillary endothelial cells are indicated. **A**, Uptake transporters localized at the intestinal epithelia includes members of the organic anion transporters polypeptide (OATP) family; peptide transporter 1 (PEPT1; SLC15A1); ileal apical sodium/bile acid co-transporter (ASBT; SLC10A2); and monocarboxylic acid transporter 1 (MCT1; SLC16A1). The apical ATP-dependent efflux pumps include multidrug resistance protein 2 (MRP2; ABCC2); breast cancer resistance protein (BCRP;

ABCG2); and P-glycoprotein (P-gp; MDR1, ABCB1). The basolateral membrane of intestinal epithelia contains organic cation transporter 1 (OCT1; SLC22A1); heteromeric organic solute transporter (OSTα–OSTβ); and MRP3 (ABCC3). **B**, Uptake transporters in the basolateral membrane of hepatocytes includes the sodium/taurocholate co-transporting peptide (NTCP; SLC10A1); three members of the OATP family (OATP1B1 (SLCO1B1), OATP1B3 (SLCO1B3) and OATP2B1 (SLCO2B1)); organic anion transporter 2 (OAT2; SLC22A7) and OAT7 (SLC22A9); and OCT1. Efflux pumps in the hepatocyte basolateral membrane include MRP3, MRP4 (ABCC4) and MRP6 (ABCC6). Apical (canalicular) efflux pumps of the hepatocyte comprise P-gp; bile-salt export pump (BSEP or SPGP; ABCB11); BCRP (ABCG2); and MRP2. As well, the multidrug and toxin extrusion protein 1 (MATE1; SLC47A1) is localized in the apical membrane of hepatocytes. **C**, Uptake transporters expressed in kidney includes OAT4 (SLC22A11); urate transporter 1 (URAT1; SCL22A12); PEPT1 and PEPT2 (SLC15A2); MRP2 and MRP4; MATE1 and MATE2-K (SLC47A2); P-gp; organic cation/ergothioneine transporter (OCTN1; SLC22A4); and organic cation/carnitine transporter (OCTN2; SLC22A5). Basolateral uptake transporters in proximal tubule epithelia include OATP4C1 (SLCO4C1); OCT2; and OAT1, OAT2 and OAT3 (SLC22A8). **D**, Uptake transporters contributing to the blood–brain barrier features the OATP1A2 and OATP2B1; and the efflux pumps P-gp, BCRP, MRP4 and MRP5 (ABCC5). (Adapted from / For further details on the transporters coloured in red and in blue indicate, please refer to The International Transporter Consortium, 2010[7]).

1.2.1. Organic Cation Transporters

One of the main routes of clearance (efflux) for many drugs and drug metabolites is through renal elimination via passive glomerular filtration and active tubular secretion. In mammals, the kidney in the renal proximal tubule excretes drugs actively. In this particular zone of the tissue, drug transporters facilitate actively and passively the flux of a variety of molecules from the blood to the tubular lumen. As such, transport systems were recognized to exist helping the elimination of a wide range of structurally different organic cations, including drugs and toxic metabolites[8]. Moreover, it has been demonstrated that the uptake (influx) of organic cations into the renal proximal tubule is expedited by a polyspecific membrane transport system as the first step in active secretion of organic cations[8]. Clearance of organic cations occurs through an H^+ - or cation-exchange system into the tubular lumen. As well, the uptake of organic cations into other tissues such as the liver and kidney, or movement across the blood–brain barrier, is known to exhibit functional properties of protein-mediated transport across the plasma membrane, such as saturability, and sensitivity upon exposure to temperature changes, membrane potential fluctuations and small-molecule inhibitors[2,8].

The different attributes of uptake transporters have been dissected into individual OCTs identified primarily in rat tissues[9]. Many uptake transporters have been cloned to date[10], and three have become the focus of many studies due to their potential membrane–driven functions and polyspecificity: OCT1 (SLC22A1), OCT2 (SLC22A2) and OCT3 (SLC22A3) - members of the SLC22A family of SLC transporters. The clarification of the molecular mechanisms of OCTs has supported the development of more detailed research related to uptake and transport mechanisms, as well as substrate specificity, protein structure, tissue distribution and has led to deep understanding of their functions in the allocation and elimination of organic cations.

1.2.2. Protein structure and substrate specificity

Solute Carrier Transporters usually consist of 10 – 14 transmembrane α-helices which arrange their largest domain[11]. Structurally, OCTs share four pivotal features: (1) similar transmembrane topology, (2) a common group of preferred substrates, (3) a shared transport mechanism, and (4) a putative secondary structure of 12 transmembrane α-helices[8]. Furthermore, structural genomics studies indicated that OCTs share a common sequence of 11 coding exons[8]. The genes encoding OCTs are confined specifically on the human chromosome 6q26 and they are thought to descend from a diversion of a single ancient OCT gene via duplication.

Structurally, OCTs are composed of 12 putative transmembrane α-helices featuring cytoplasmic amino and carboxy termini and they share large extracellular domains between transmembrane domains (TMDs) 1 and 2 that contain N-glycosylation sites, as well as large intracellular domains between TMDs 6 and 7, which contain phosphorylation sites[8] (See Figure 2B and Figure 3B for details on the typical transmembrane topology of human OCT1 and OCT2 respectively). The N-glycosylation and phosphorylation sites are believed to modulate OCTs' activity[12]. For instance, in mice, OCT2 activity has been found to be modulated by a phosphotyrosine switch mechanism[13]. These observations are of utmost importance since modulating the uptake activity of OCTs could bring a powerful tool to assess the efficacy of pharmacological agents and could thus become a strategy for drug discovery. In this sense, TMDs are pivotal for substrate recognition by the OCTs in order to be transported. Recently, evidence indicates that TMDs 4 and 10 are critically involved in the recognition of many substrates needed for cellular development[14]. As well, differences in these critical regions may impact substrate recognition by distinct OCTs isoforms[14].

It is noteworthy that given the wide substrate selectivity of OCTs, distinct key residues are involved in recognizing different substrates even within the same protein. As such, mutational sequence analysis of rat OCT1 in the TMD 4 showed that the mutations Trp218Tyr and Tyr222Leu have an increased affinity for the quaternary ammonium cation tetraethylammonium (TEA) and the neurotoxin 1-methyl-4-phenylpyridinium (MPP^+)[14]. Consequently, a third point mutation, Thr226Ala, has increased affinity for MPP^+ but not towards TEA. This sequence analysis suggests that OCT1 – and possibly the majority of SLCs - possesses a series of overlapping and nonidentical recognition motifs to recognize structurally different substrates[14]. TEA, MPP^+ and the endogenous molecule N-methylnicotinamide (NMN) have been characterized as common substrates for OCT1, OCT2 and OCT3[8,15]. As well, clinically important drugs such as the antidiabetic metformin, have been identified as common substrates for OCT1, OCT2 and OCT3, which demonstrates the potential of OCTs on drug uptake[15]. Endogenous compounds such as the amine neurotransmitters dopamine, epinephrine, norepinephrine, histamine and serotonin have all been shown to interact with OCTs[16], again proving their efficacy in the uptake and transport of a wide range of molecules, either endogenous or exogenous.

In this regard, OCT3 is of special interest as it has been characterized as the extraneuronal monoamine transporter (EMT) and it acts through an '$uptake_2$' mechanism of catecholamine transport, responsible for clearance of catecholamines in brain tissues[17]. Nevertheless, it is suggested that OCT1, OCT2 and OCT3 uptake transporters synchronize to contribute for the clearance of amine neurotransmitters from brain tissues. These observations lead to the conclusion that OCTs indeed possess a broad distinction in substrate specificity as observed by the existence of relatively isoform-specific substrates and inhibitors. For instance, corticosterone has 40-fold higher affinity for rat OCT2 than OCT1; inversely, mepiperphenidol and O-methylisoprenaline show 70-fold higher affinity for rat OCT1 than for OCT2. Importantly, among the OCTs, OCT3 emerges as the transporter with the narrowest substrate selectivity, with a preference for endogenous monoamines such as dopamine and norepinephrine.

Even though most OCT substrates are cations, there are exeptions to this rule as there is evidence of a small proportion of OCT substrates being either anionic or neutral molecules at physiological pH (e.g. prostaglandin E2 and prostaglandin F2α, substrates for OCT1 and OCT2)[18]. As well, OCT3 interacts with high affinitiy with the neutral steroid β-estradiol[17]. Therefore, a net positive charge does not appear to be an absolute requirement for interaction with OCTs. Moreover, OCT orthologs from different species exhibit distinct behaviours towards substrate selectivity. For instance, human, rabbit, mouse and rat OCTs are able to uptake TEA and the low-molecular-weight tetraalkylammonium compound tetramethylammonium (TMA). On the other hand, rat and mouse OCT1 do not transport the large tetrapropylammonium (TPA) or tetrabutylammonium (TBA) whereas both human and rabbit OCT1 do[19]. These observations suggest that dissimilarities in recognition of substrates by OCTs across species might be due to differences in molecular mass, hydrophobicity and other chemical and physical features.

Overall, the subgroup of OCT1, OCT2 and OCT3 displays high similarity regarding structure and transport mechanisms, and these transporters function to translocate a number of distinct cationic molecules across the plasma membrane. However, despite the vast research done with OCTs, most SLC transporters have not been crystallized so far, and this might be the last piece of the puzzle for a better understanding of membrane protein dynamics. Importantly, this becomes a limiting factor for computer-aided drug discovery programs towards ameliorating, for instance, chemotherapies and screening methods to seek for newly synthesized molecules.

1.2.3. OCT1 (SLC22A1)

The gene SLC22A1 was cloned from rat for the first time in 1994[9]. Years later, this gene was cloned from human and other mammals, and the importance of its product - the uptake transporter OCT1 – has gradually been recognized[20]. In mammals, OCT1 is characterized as liver-specific and is mainly expressed in the basolateral membrane of hepatocytes although lower levels of OCT1 expression are also observed in other tissues like the kidney, spleen and lymph nodes[10,20]. As mentioned previously, mammalian OCT1 shares structural and topological similarities to other SLCs, consisting of 12 transmembrane domains of which TMD4 and TMD10 contribute to substrate recognition and transport (Figure 2).

Early studies in rat showed that OCT1 could be regulated by different means[9,12]. For instance, it has been shown that stimulation of PKA results in an important increase of OCT1 levels, as measured by a significant uptake of the fluorescent cation 4-[4-(dimethylamino)-styryl]-N-methylpyridinium (ASP+) in HEK-293 cell lines expressing OCT1[12]. Moreover, stimulation of PKC also results in significantly increased uptake of tetrapropylammonium (TPA), TEA and the anti-malarial drug quinine[8]. The effect of PKC activity on OCT1 is believed to occur by phosphorylation of the OCT1 protein, inducing conformational changes that promote enhanced substrate affinity. This effect was significantly reduced after treatment with the tyrosine kinase inhibitor aminogenistein p56lck. These observations, coupled with the fact that other tyrosine kinase inhibitors do not affect OCT1 function, suggest that aminogenistein p56lck is a specific OCT1 endogenous inhibitor[21]. Opposite to rat OCT1, the activity of human OCT1 decreases upon stimulation of PKA and shows no changes in activity upon PKC activation. Nevertheless, similar to rat OCT1, human OCT1 is positively modulated after treatment with the tyrosine kinase inhibitor aminogenistein p56lck[12]. Overall, these results indicate that protein kinases can cause conformational changes of the OCT1 protein due to phosphorylation, resulting in either increased or decreased uptake activity of specific substrates.

Overall, OCT1 is a dynamic membrane protein as it is capable of transporting a number of endogenous compounds – for instance - neuromodulators like salsolinol and histidyl-proline diketopiperazine (cyclo(His-Pro)), the L-arginine metabolite agmatine and polyamines like putrescine[10]. Moreover, OCT1 is not limited to endogenous compounds as it is also able to transport clinically relevant drugs such as the widely used antidiabetic drug metformin, the antiviral drugs acyclovir, ganciclovir and lamuvidine, antineoplastic drugs like oxaliplatin, picoplatin, cis-diammine(pyridine)chloroplatin(II), irinotecan and paclitacel[10]. And the latest addition of the anthracyclines doxorubicin and daunorubicin, chemotherapeutics used to treat leukemia[22].

1.2.4. Therapeutic implications of OCT1

The uptake and pharmacokinetics of drugs is dependent on the expression and transport activity of OCTs. In this regard, OCT1 is a major modulator of the dose–response – and consequently the toxicity - of cationic drugs. Logically, OCT1 expression and proper activity in specific cells (e.g. adipocytes) targeted by drugs such as metformin is pivotal to allow the entry of these compounds and achieve therapeutic effects[23]. As such, inhibitors of OCT1 could reduce the therapeutic effects of drugs by modulating their entry into the cell. For instance, diabetes and cancer are prevalent conditions and their co-diagnosis is common in the general population[24]. The initial pharmacological treatment for type 2 diabetes is metformin, and, on the other hand, several tyrosine kinase inhibitors such as imatinib, desatinib, nilotinib, gefitinib and sunitinib are commonly used for cancer treatments[24]. As tyrosine kinase inhibitors are known to inhibit OCT1 activity, the concomitant use of these two classes of drugs results in a decreased uptake of metformin into the cells, inhibiting its therapeutic effects[24].

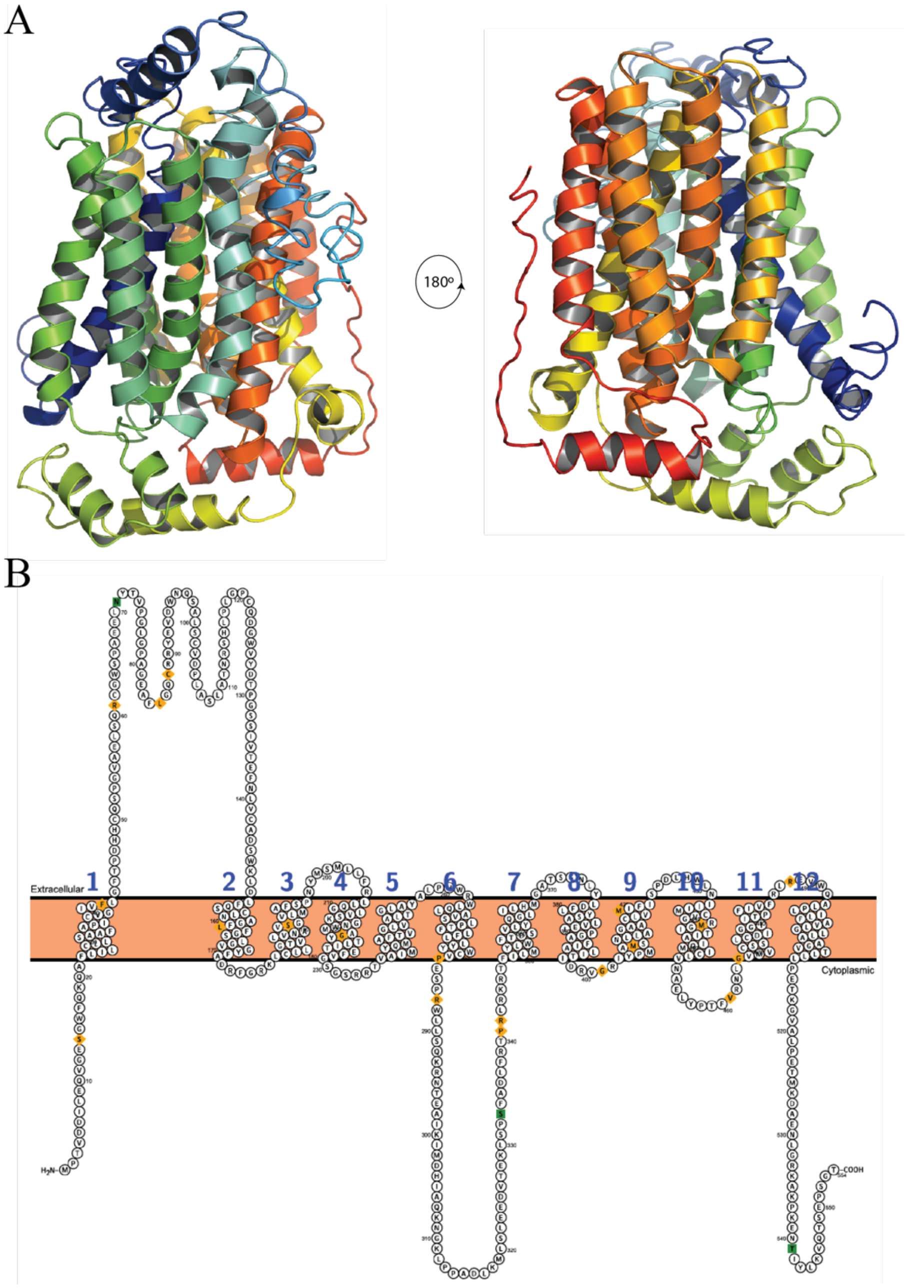

Figure 2. Homology-based model of human OCT1. **A,** Tertiary structure and **B,** Secondary structure predicted for OCT1. Representative figures were rendered as published by[25]. TMD4 and TMD10 have been shown to contribute to substrate recognition by OCT1.

During drug therapy, vast interindividual differences in OCT1 gene expression have been documented[2,15]. These differences in gene expression are correlated with hepatic excretion and tissue distribution of drugs like metformin, oxaliplatin and picoplatin observed in patients treated with these drugs[8]. Such variations in gene expression are directly linked to genetic and epigenetic factors that are defective during diseases. For instance, the promoter of SLC22A1 is hypermethylated in human hepatocellular carcinoma leading to downregulation of OCT1 suggesting that defective OCT1 activity might have a role during tumorigenesis[26]. As well, certain single nucleotide polymorphisms (SNPs) have been identified in OCT1 as many of these mutations affect expression, transport activity and substrate selectivity[27,28].

Moreover, several lines of evidence have demonstrated that OCT1 is highly expressed in colon cancer and polyps as OCT1 mRNA level was augmented in human colon cancer cells[29]. Drugs from the platinum family, including cisplatin and oxaliplatin are highly efficient in forming DNA adducts inducing DNA damage and subsequently triggering apoptosis specially in colon cancer cells. Cisplatin displays high substrate affinity for OCT1 with an IC50 dose within 7-8 μM[6]. However, it has been reported that human OCT1 has a more pronounced affinity towards oxaliplatin than cisplatin as accumulation and toxicity of oxaliplatin in stable cell lines expressing OCT1 was observed[6]. Aditionally, the toxicity produced by oxaliplatin was also significantly higher than that of cisplatin in colon cancer cell lines[6,30]. The efficacy of oxaliplatin as a cancer treatment was further linked to the activity of OCTs by the observation that colon cancer cell lines exposed to cimetidine – a potent OCT inhibitor – reduced the cytotoxic effects of oxaliplatin, indicating that the effects observed as a result of oxaplatin exposure are dependent on the uptake activity of OCTs[30]. Another platinum agent, picoplatin, is effective in lung cancer treatments, highlighting its importance in platinum-based treatments[2], as reports show that the tumor size of OCT1-expressing xenografts in mice was substantially reduced upon picoplatin treatment, indicating that OCT1 could increase the antitumor efficacy of picoplatin as well[31]. Additionally, significant expression of OCT1 has been detected in chronic myeloid leukemia (CML)[32]. As such, it has been demonstrated that OCT1 mediates the transport of the antineoplastic agent imatinib whose powerful tyrosine kinase inhibitor function is applied to treat CML[32]. These observations indicate that OCT1 activity is a key determinant in the molecular outcome of imatinib, as OCT1 expression levels in leukemic cells is associated with the therapeutic outcome in CML[32].

Competition assays have demonstrated that antineoplastic agents such as irinotecan, mitoxantrone and paclitaxel, inhibit the uptake of the organic cation ^{3}H-1-methyl-4-pyridinium iodide into chinese hamster ovary cells expressing human OCT1[33]. Also, these OCT1-expressing cells exhibited significant susceptibility to the toxicity of irinotecan and paclitaxel when compared with control cells, indicating that OCT1 may contribute to the uptake of selected antineoplastic drugs in these cells[33]. The evidence presented highlights the need for further studies regarding the expression patterns of OCTs during cancer development, which could potentially serve as a cellular marker designed to select more effective drugs and ultimately improve cancer therapy.

1.2.5. OCT2 (SLC22A2)

In 1996, the gene SLC22A2 which encodes the uptake transporter OCT2 was cloned from rat[34], and has subsequently been cloned from other mammals[20]. Mammalian OCT2 is considered kidney-specific, as human OCT2 is expressed mainly in the basolateral membrane of renal proximal tubules. Nevertheless, expression of human OCT2 was also identified in the brain, the choroid plexus, the luminal membrane of endothelial cells in microvessels, small intestine, lung, placenta and thymus[20,35,36]. Importantly, OCT2 shares common protein structure and transmembrane topology with other OCT members, featuring 12 transmembrane domains of which TMD4 and TMD10 provide the site for substrate recognition and transport (Figure 3).

The cations TEA, MPP$^+$, ASP$^+$, N1-methylnicotinamide and aminoguanidine as well as several neurotransmitters such as epinephrine, norepinephrine, serotonin, acetylcholine, dopamine and histamine; neuroregulators like cyclo(His-Pro) and salsolinol, the L-arginine metabolite agmatine[37], the polyamine putrescine, and choline[10] are known substrates for human OCT2. Importantly, human OCT2 mediates the transport of clinically relevant drugs, including memantine and amantadine, used for treatment of Parkinson’s disease, and antineoplastic drugs from the platinum family oxaliplatin, picoplatin, cisplatin[38] and ifosfamide[39]. It also mediates the transport of histamine H2 receptor antagonists like cimetidine, famotidine and ranitidine, the antiviral drugs zalcitabine and lamuvidine, the diuretic amiloride, and the antidiabetic drug metformin[20]. Also transports the mycotoxin aflatoxin B1, the viologen paraquat and the DNA intercalating agent ethidiumbromide[38].

Evidence in other mammals also indicates that OCT2 has high binding specificity towards cationic molecules[40-42]. Research with rats and rabbits have documented that rat OCT2 is responsible for the transport of the cation cesium (Cs^+)[40] and rabbit OCT2 mediates the transport of the cation cadmium (Cd^{++})[41]. Moreover, rat OCT2 also mediates the transport of inorganic cations along with organic cation substrates when membrane potential is reduced[42]. Genetic imprinting modulates the expression of human OCT2 in an organ-specific manner. For instance, human OCT2 shows high levels of expression in the kidney as compared to the liver, where DNA methylation blocks binding of the upstream stimulating factor (USF) to its promoter reducing OCT2 expression[43]. Moreover, diverse signalling pathways such as PKA, PKC, calmodulin and phosphatidylinositol-3-kinase (PI3K) take part in the posttranscriptional regulation of human OCT2[12]. This posttranscriptional regulation results in endocytosis mediated by (i) the lysosomal associated protein transmembrane 4 alpha (LAPTM4α) as overexpression of LAPTM4α significantly decreased the uptake of ASP+ in HEK293 cells expressing human OCT2[44], and (ii) control of substrate selectivity and affinity[12]. These are clear modes of regulation of OCT2 activity, but it still remains elusive whether or not these OCTs detach or not from the membrane in order to transport and deliver the compounds inside the cell.

1.2.6. Therapeutic implications of OCT2

It is established that human OCT2 mediates the translocation and renal excretion of many compounds, like the antihistamine cimetidine, oxaliplatin, used for colorectal cancer treatments, and the antiretroviral agent lamivudine. OCT2 also mediates the reabsorption of the vitamin-like essential nutrient choline and organic cation substrates or in the proximal tubule like the catecholamine dopamine[45].

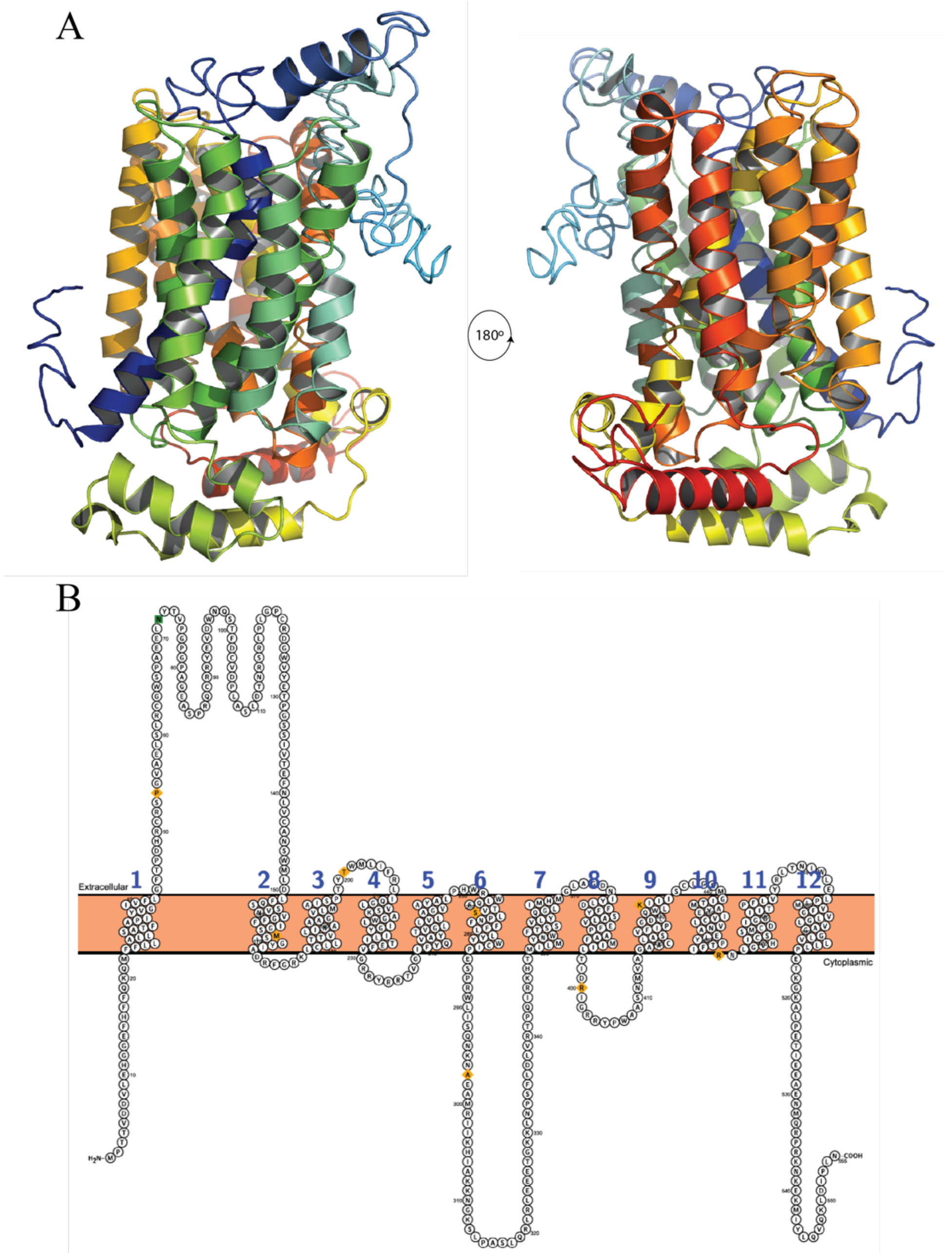

Figure 3. Homology-based model of human OCT2. **A,** Tertiary structure and **B,** Secondary structure predicted for OCT2. Representative figures were rendered as published by[25]. Similar to OCT1, TMD4 and TMD10 have been shown to contribute to substrate recognition by OCT2.

In the central nervous system (CNS), OCT2 also plays an important role in mediating the uptake of drugs used for the treatment of Parkinson's disease like amantadine and memantine across the blood–brain barrier. As such, this transporter takes part in modulating interstitial and intracellular concentrations of neurotransmitters, neuromodulators and cationic compounds by allocating these compounds into neurons[10].

In therapeutic interventions, the use of cationic drugs is common as they are highly efficient and these drugs only achieve their efficacy by being successfully transported into the cells. Importantly, a number of these compounds are substrates for OCT2, which are improved by comedication and mainly excreted by the kidney[38]. Several clinical studies reported that nephrotoxicity and ototoxicity of the anticancer agent cisplatin is correlated with the over activity and high expression of OCT2 in the kidney and the inner ear respectively, leading to high uptake of cisplatin in such organs[35]. These effects have been shown to decrease by coadministration of cimetidine, which inhibits OCT2 activity[35].

In short, the data compiled from numerous works indicates that changes in pharmacokinetics and nephrotoxicity of compounds that are substrates for OCT2 is due to downregulation of this cation transporter leading to – for instance - acute and chronic renal failure[6,35]. Altered gene expression also has pathological implications, for instance, in the SLC22A2 gene, 8 infrequent nonsynonymous SNPs and one frequent nonsynonymous SNP were reported[38] to be related to poor renal excretion of cationic compounds and poor translocation of drugs across the blood–brain barrier; e.g. poor clearance of free serotonin and norepinephrine in the brain, having as a consequence mood disorders[36].

Although the role of OCT2 in cancer needs more investigation, it has been shown that the anticancer drug cisplatin is a substrate of OCT2, as significant uptake of cisplatin has been observed in cells expressing OCT2[35]. Several lines of evidence have reported that human OCT2 mediates the translocation of cisplatin across the membrane of proximal tubules from the blood stream, playing a critical role in the nephrotoxicity produced by cisplatin[46]. Moreover, single point mutations in the OCT2 gene have been correlated with decreased nephrotoxicity of cisplatin in patients under treatment[46]. Also, mice devoid of Oct2 activity have reduced urinary excretion of cisplatin thus less cisplatin-induced nephrotocixity[46] which correlated with the reduced uptake of cisplatin. These data indicate that modulation of OCT2 expression at the basolateral membrane in the proximal tubules might act to protect the kidney from cisplatin-induced nephrotoxicity by increasing the uptake activity of this transporter.

In addition, other members of the platinum family have been documented to be substrates of OCT2, such as oxaliplatin[6]. However, as opposed to cisplatin, oxaliplatin does not seem to induce severe nephrotoxicity and this might be due to the action of another cationic uptake transporter expressed in the kidney: MATE2 (MATE2K)[47]. This transporter is localized to the apical membrane of proximal tubules and is able to eliminate oxaliplatin, but not cisplatin, suggesting a differential contribution of both uptake transporters[47]. As well, it has been demonstrated that OCT2 expression significantly enhances the uptake of picoplatin increasing DNA adduct formation and cellular toxicity[31]. These studies underscore the importance of OCT2 function in the uptake and renal disposition of platinum compounds pivotal for platinum-based chemotherapy.

1.2.7. Clinical importance of Organic Cation Transporters

The pharmacological and clinical importance of OCT1 and OCT2 have been explored *in vivo* utilizing deletion genotypes for OCT1 and OCT2 generated in mice[16]. Oct1$^{(-/-)}$, Oct2$^{(-/-)}$ and double Oct1/2$^{(-/-)}$ mice are viable, fertile and do not present any abnormal phenotype, however they displayed altered pharmacokinetics in the uptake of organic cations[16]. Oct1$^{(-/-)}$ deletion mutant mice displayed a significant lower accumulation of TEA in liver as compared to wild type mice, when subjected to intravenous administration of TEA[48]. Moreover, direct intestinal excretion of TEA was two-fold reduced[48]. Similarly, decreased accumulation in liver and normal intestinal secretion was found in Oct1$^{(-/-)}$ mice for the neurotoxin MPP$^+$ and the anticancer drug [^{131}I]metaiodobenzylguanidine (^{131}I-MIBG), used in the clinics for identification and treatment of tumors derived from neuroadrenergic sources like neuroblastoma and pheochromocytoma[49].

The modulation of drug uptake in the liver could have a positive impact by limiting the hepatotoxicity of a number of agents. On the other hand, this may produce a decrease in efficacy for drugs that have to undergo metabolic activation in the liver[50]. In fact, it has been demonstrated that Oct1 expression affects the distribution of the antidiabetic biguanide drug metformin, and regulates the lactic acidosis produced by metformin, a dangerous adverse effect of biguanides derivate[50]. Following intravenous administration of metformin in Oct1$^{(-/-)}$ mice, a significant decreased distribution of metformin was observed in liver and small intestine accompanied with low lactate concentration in blood as compared to wild type mice[50].

Undoubtedly, these results support the notion that OCT1 function plays an important role in the distribution of substrate cationic drugs in the liver. Extrapolating these observations to humans, regulation of OCT1 gene expression and protein function might impact the results in drug therapy. Moreover, no clear difference was observed in the renal distribution and elimination of the OCT1 substrate drugs assayed in the course of these experiments possibly due to a change from hepatobiliary to renal elimination and to the functional overlap of OCT1 with OCT2 in mice[48,50].

Therefore, by generating Oct2 single- and Oct1/Oct2 double-deletion mice, the activity of OCTs in the kidney and the distribution of cationic substrates was elucidated[51]. By using this *in vivo* model, the authors reported that despite the absence of Oct2, little effect on the renal distribution of compounds like TEA was observed, and the related deficiency of Oct1 and Oct2 in mice resulted in complete abrogation of TEA secretion in the kidney[51]. As such, by extrapolating these observations from mice to humans (where OCT2 is solely expressed in the kidney)[51], it is expected that the deficit of OCT2 in humans may impact the renal elimination of drugs as a consequence of increased exposure to certain drugs.

OCTs have become central towards understanding cancer development and treatment. Antineoplastic agents attack at nuclear and cytoplasmic targets in tumor cells, and their cellular uptake is pivotal for their efficacy. Lymphoma cell lines and primary samples from chronic lymphocytic leukemia (CLL) patients displayed significant expression of OCT1[33], highlighting the role of OCTs in tumorigenesis. Furthermore, OCT-1-expressing lymphoma cell lines showed significant susceptibility to treatment with the antineoplastic agents irinotecan and paclitaxel as compared to OCT1-negative controls[33]. As irinotecan and paclitaxel are antineoplastic agents used to treat several forms of cancer such as colon cancer and small cell lung cancer, ovarian cancer, breast cancer, lung cancer, Kaposi sarcoma, cervical cancer and pancreatic cancer, respectively, both are administered intravenously[52]. This underscores the role of OCT1 as a key player in the uptake of irinotecan and paclitaxel from the blood stream and distribute them to the target tumors.

Following these observations, the clinical relevance of OCTs in chemotherapeutics became evident as their role in the intracellular uptake of drugs that targets several forms of cancer[2] was identified. Notably, the functional expression of OCT1 in patients affected by chronic myeloid leukemia (CML) correlated significantly with the response to imatinib treatment[32,53]. Therefore, these results indicate that OCT1-dependent uptake of imatinib is a pivotal factor that could increase the efficacy of CML chemotherapy. In a similar fashion, it has been reported that human OCT1 and OCT2 tumor expression might be a determinant of the antineoplastic function of oxaliplatin to prevent tumor growth[30]. As oxaliplatin is the main antineoplastic currently approved for patients with metastatic colorectal cancer, its uptake and resulting cytotoxicity is influenced by the expression of OCT2[54]. Moreover, samples from metastatic colorectal cancer patients showed high levels of OCT2 expression associated with severe tumor invasion[54]. These results, however, suggested better prognosis in patients treated with oxaliplatin, possibly due to the role of OCT2 in the uptake and mechanism of action of oxaliplatin[54].

Besides the uptake function of OCT2, this transporter has also been attributed as a 'protective transporter' in cisplatin-based chemotherapy[35]. The mechanism of action of cisplatin is quite effective and to a certain degree curative for colon cancer[55], however, it has been reported that administration of cisplatin causes nephrotoxicity therefore limiting its therapeutic use[56]. In these regards, a study presented an *in vivo* model demonstrating that OCT2 plays an important role during the development of cisplatin-induced nephrotoxicity and ototoxicity[35], in which expression of OCT2 is directly linked to the uptake of cisplatin in renal cells and hair cells of the cochlea[35]. These observations serve as lead to the development of therapeutic methods – utilizing OCT2 - aimed to reduce the risk of cisplatin-associated toxicities[35].

Furthermore, some studies have shown an additional role of OCT2 in neoadjuvant chemotherapy in gastric cancer[57]. Results suggested that OCT2 expression may represent a potential predictor of response to neoadjuvant chemotherapy using S-1/cisplatin to treat gastric cancer[57]. As such, OCTs can contribute to the susceptibility of cancer cells to clinically relevant antineoplastic drugs and prevent their adverse effects. The analysis of OCTs and their transport of specific antineoplastic drugs could help to tailor chemotherapy and their application could be expanded to transporters of different natures.

1.3. *Caenorhabditis elegans* as a model system

The multicellular organism *Caenorhabditis elegans* has been instrumental in a number of groundbreaking discoveries both in fundamental biology as well as in medicine involving DNA repair mechanisms and apoptosis signalling pathways[58,59]. These studies revealed a compelling conservation in molecular and cellular pathways between mammals and *C. elegans* and further detailed comparison of the human and *C. elegans* genomes corroborated that a number of genes and signalling pathways linked to human diseases also exist in *C. elegans*[60]. Therefore, these features make the nematode *C. elegans* a prototypical model for the study of signalling response outputs.

Some of the features that make this nematode one of a kind model system to study *in vivo* processes are its easy manipulation, fast development and unique biological features[44]. In response to drugs, *C. elegans* has a number of attributes that make it a powerful tool for pharmaceutical research[61]. For instance, the culture system is simple, *C. elegans* reproduce rapidly, it is cost efficient since its small size allows the development of assays with large samples, *in vivo* fluorescent markers are easily visualized since this animal is transparent and it is a complex multicellular organism with different organs and tissues. Also, a *C. elegans* model can be developed to study the serotonergic signalling pathway, which could be one of the underlying causes of depression. In a pharmacological point of view, this model could be enhanced to validate newly synthesized drugs targeting the serotonergic pathway.

Despite that *C. elegans* has shed light into the underlying mechanisms of human diseases[61], many still question whether this nematode can really be used as a pharmaceutical tool and, if so, how relevant such a tool can be to elicit the exact drug response. In many cases, there is no immediate correlation between human pathology and *C. elegans* phenotypes. Given that even mammalian models are often not well stablished tools to predict drug response in humans, it is — from a preclinical point of view - unfeasible to expect an invertebrate organism to provide sufficient confidence to foresee safe drug response in humans. Nevertheless, the advantage that *C. elegans* possesses over *in vitro* models is that, as an alternative of studying solely the drug–receptor interaction of a given target, a functional serotonergic synapse can be investigated in the context of a whole multicellular organism. This includes actual behavioural responses of the nematode that can be easily monitored as an alternative of quantifying fluctuations in an unicellular fluorescence assays[61].

Certainly, the simplicity of *C. elegans* should not be taken for granted as high developmental complexity underlies at the cellular and physiological levels (Figure 4). Thus, if we consider investigating the positive and adverse effects of a drug with its receptor in a *C. elegans* assay, we first need to understand how the drug is ingested in order to trigger a response. It is believed that molecules are absorbed through the skin of the nematode, but this assumption is controversial. For example, if in a given assay analogous drugs are absorbed equally through the skin, this aspect will make difficult to dissect the exact role of each drug, e.g. DNA damage-induced apoptosis of germ cells or somatic cells[62], as well in neurodegenerative diseases like amyotrophic lateral sclerosis (ALS)[63,64] and Huntington's disease in which both proteinopathies affect motor neuronal processes[65]. Moreover, the use of the whole animal approach could increase the chances of recognizing synergistic and/or adverse effects, as the drug can simultaneously trigger multiple targets. Therefore, these important features of *C. elegans* in combination with the activity of uptake transporters could provide a powerful tool to overcome the limitations of pharmacological assays in mammals.

1.3.1. Organic Cation Transporters in *C. elegans*

To date, information about the role of OCTs in *C. elegans* is quite scarce. In 1999, the gene product of *F52F12.1* was identified as OCT-1: the first uptake transporter in *C. elegans*[66].

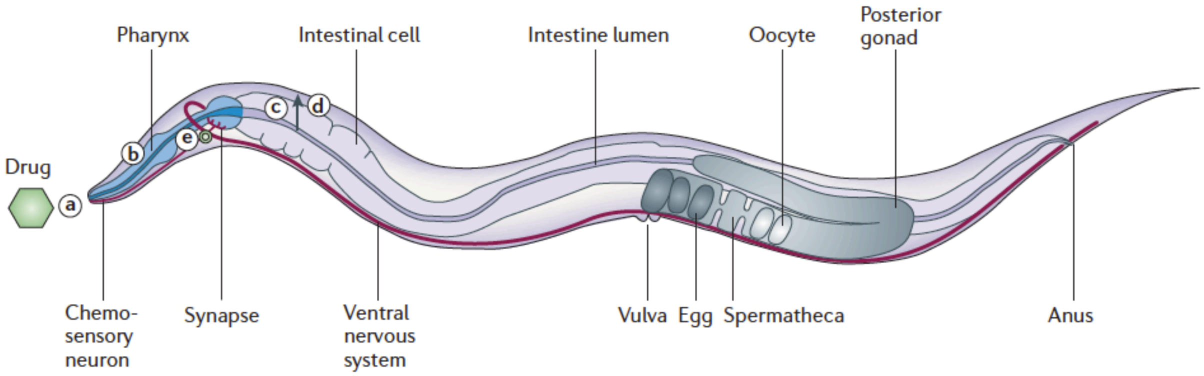

Figure 4. Anatomy of a *C. elegans* adult hermaphrodite showing drug entry route. Uptake by ingestion occurs in minutes and involves several distinct steps. **A,** Chemosensory neurons act in the selection of nutrient sources. Compounds emanating disagreeable taste or smell might be evaded or not taken up efficiently. **B,** Drugs are ingested through the pharynx. The feeding function of the pharynx depends on satiety or food availability and is modulated by several neurotransmitter networks. **C,** Once the drug has entered the intestinal lumen, intestinal cells absorb it. The apical face of the lumen is composed of microvilli, augmenting the absorption surface. Indeed, intestinal cells express many transport membrane proteins like P-glycoproteins and peptide transporters. **D,** From the body cavity the drug is dispersed throughout the body. **E,** The drug reaches its target binding to receptors at a synapse in the central nervous system, eliciting a behavioural response like reduced feeding and/or motility. (Adapted from Kaletta *et al.* 2006[61]).

The functionality of the *oct-1* gene was elucidated upon expression in mammalian cell lines and demonstrated to mediate the transport of the amonium cation tetraethylammonium (TEA), a prototypical substrate that is utilized to investigate OCTs. This indicated that OCT-1 has the ability to perform as an uptake transporter[66].

However, no further research was pursued to detail the substrate specificity of OCT-1 following its expression in mammalian cells. It took 14 years when in 2013 further studies surfaced demonstrating that upon depletion of the *oct-1* gene, nematodes exhibited a shortened lifespan and increased susceptibility to oxidative stress[67]. These important observations led to the hypothesis that OCT-1 facilitates the uptake of antioxidants into *C. elegans*, which is pivotal to protect *oct-1* mutant animals from oxidative stress[67]. On the other hand, the levels of ergothioneine, a substrate of OCT-1, was not altered in *oct-1* deletion mutant animals as compared to the wild type. Therefore, it seems plausible to think that an alternative mechanism could be considered to explain the *oct-1* mutant animal phenotypes.

In an effort to discover more substrates for OCT-1, the use of cross-complementation assays and further expression of the *C. elegans oct-1* gene in the heterologous model organism budding yeast *Saccharomyces cerevisiae*[68], made a suitable scenario to list a number of substrates. As characterized that human OCT1 can transport chemotherapeutic drug anthracyclines, *C. elegans* OCT-1 can also elicit the uptake of doxorubicin into *S. cerevisiae* cells[68] indicating that uptake of diverse cations by OCT-1 is not limited in *C. elegans*. By targeting a yeast strain devoid of the plasma membrane amino acid transporter Agp2, which also possess regulatory functions[69], deletion of the *AGP2* gene, impeded the expression of the polyamine transporters Dur3 and Sam3[68]. However, either Dur3 or Sam3 can uptake doxorubicin when overexpressed in yeast cells[68]. Thus, more investigation is needed to dissect whether the expression of *C. elegans* OCT-1 in budding yeast replaced the regulatory function of Agp2 or the transport roles of Dur3 and Sam3. As such, it became necessary to continue further investigation on OCTs in *C. elegans* that led the development of this thesis. Thus far, DNA sequence analyses extracted from the Wormbase – a *C. elegans* developmental database - revealed that presently 21 SLC transporters exist in *C. elegans* (Figure 5). However, further details about the existence of another related organic cation transporter in *C. elegans*, named OCT-2, are given in the following chapter.

In short, it is logical to propose that any molecule that competes – for instance - for doxorubicin uptake into *C. elegans* via OCT-1, is likely a putative path to pursue SLC research and to be employed as a screening strategy to test the contribution of each transporter towards the uptake of clinically relevant drugs and newly synthesized drugs in order to improve therapeutics.

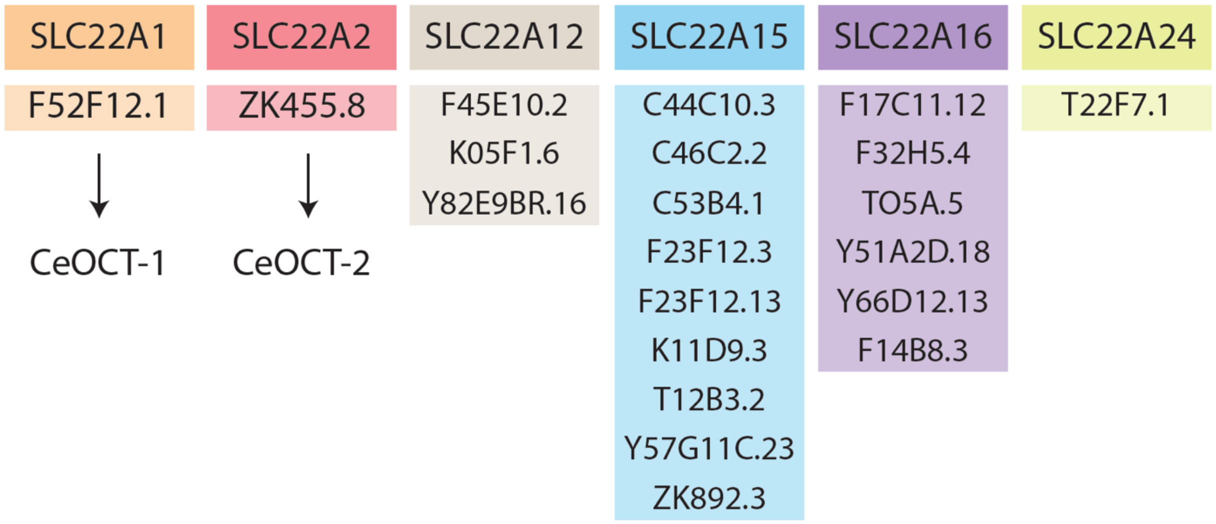

Figure 5. Solute Carrier Transporters in *C. elegans*. DNA sequence analyses revealed the existence of 21 SLC transporters in the nematode. To date, only the human homologs OCT-1 and OCT-2 have been characterized in the uptake of a number of compounds. This figure was created based on information available and extracted from the online source: www.wormbase.org / version WS261.

1.4. DNA repair pathways

DNA damage generated by endogenous or exogenous genotoxic agents can prevail in multiple forms, and if not repaired, they can induce genomic instability leading to a variety of human diseases, such as cancer, neurological disorders, immunodeficiency, inborn illnesses and ageing. To prevent the harmful effects of these agents, cells have evolved DNA repair pathways dedicated to sense and repair DNA damages[70]. Four different DNA repair mechanisms exist, named base excision repair (BER), nucleotide excision repair (NER), mismatch repair (MMR) and DNA double strand break repair (DSBR), each dedicated to repair different type of lesions (Figure 6)[71]. In addition, gene homology analysis, protein-protein interaction mapping studies, and genetic screening have revealed that the major DNA repair pathways found in mammalian systems are conserved to the molecular level in *C.*

elegans[72] validating this nematode as a suitable model organism to study the fundamentals of the DNA repair response.

The BER is mostly, but not solely, in charge of repairing lesions of endogenous origin such as single DNA base alterations. These single alterations, known as point mutations, may or may not hinder transcription and replication[73]. Thus, the BER is pivotal for preventing mutagenesis. As opposed to the BER, the NER handle most of helix-distorting lesions, like DNA adducts, that obstruct base pairing and generally impede transcription and replication. Moreover, most NER lesions originate from exogenous sources with the exception of few lesions derived from oxidative processes[71]. The MMR is in charge of recognizing and repairing incorrect insertions, deletions and also miss-incorporated bases that mostly emerge during DNA replication and recombination. This pathway is also capable of repairing certain types of DNA lesions as it is strand specific[70]. On the other hand, the DSBR presents a more complex repair mechanism, as both strands are affected and the cell has to identify the corresponding ends. As such, two sub-pathways evolved specialized to repair DSBs: the homologous recombination (HR) and homologous end joining (HEJ)[71] repair pathways.

Defective DNA repair pathways enable the accumulation of specific mutations across the genome that have the potential to induce cell transformation and cancer phenotypes[71]. In contrast, most cancer cells use residual DNA repair functions to bypass the damage produced by genotoxic environments. With this in mind, strategies that could simultaneously increase the uptake of DNA damaging agents (e.g. chemotherapeutics) and bypass DNA repair responses could enhance the chances of killing tumorous cells and consequently improve therapeutic success in a pre-clinical point of view.

1.4.1. Base Excision Repair

Among the major DNA repair pathways, the BER is the main protective mechanism against damage created as a result of metabolic reactions, e.g. as a result of reactive oxygen species (ROS), hydroxylation, methylation and deamination[74]. A minor modification to a base threatening DNA integrity is sufficient to initiate the process of base excision repair[73]. Like many other signalling pathways, minimal perturbations in this repair pathway could end in catastrophic events — like cancer and neurological disorders[75]. The activity of the BER relies on only four functional enzymes as the basic steps must be completed to remove the single damaged DNA base and replace it with the correct base[75].

Parallel with the human BER model[75], the current *C. elegans* BER model reveals the following enzymatic steps: (i) recognition and excision of the damaged base by DNA glycosylases UNG-1[76] or NTH-1[77] resulting in an abasic (AP) site; (ii) incision of the DNA adjacent to the resulting AP site by AP endonucleases APN-1 or EXO-3[78]; (iii) end cleaning of the DNA terminus resulting in a 3′-hydroxyl group (3′-OH) and a 5′-phosphate group (5′-P); (iv) DNA synthesis by DNA polymerase by POLQ-1[79], and (vi) DNA ligation by DNA ligase to seal the nick. Therefore, *C. elegans* has a minimally complex BER mechanism whose fundamental understanding could be extrapolated to humans and it is well suited to rapidly reveal small-molecule inhibitors targeting components of the BER pathway hence cancer cells.

Recent studies have demonstrated that alkylating agents, cytotoxic antibiotics and taxanes create single DNA lesions that the BER pathway have efficiently evolved to repair[80]. Therefore, hindering BER components that are unique to this pathway open avenues for potentiating the effects of those treatments and are candidates for inhibition. Some inhibitors initially attributed as specific for human APE1 have further been regarded as BER inhibitors instead, as they bind to the aldehyde of the AP site on the DNA[80]. For instance, methoxyamine (MX), studied as a small-molecule inhibitor used in combination treatment for a variety of cancers, has progressed through clinical trial phases[80]. Moreover, E3330 and newer synthesized analogs show potential for specifically inhibiting human APE1 functions[80]. Also, advanced clinical research indicates that E3330 will be utilized as combination treatment in adults and children with acute lymphoblastic leukemia and other forms of cancer in near future[80].

1.4.2. Nucleotide Excision Repair

The NER senses and repairs bulky adducts and helix-distorting DNA lesions originated by UV irradiation and chemical mutagens that crosslink adjacent purine bases and form inter-strand crosslinks[81]. Defective NER functions render cells sensitive to platinum-derived agents that cause G2-cell cycle arrest[82]. The efficiency of platinum-derived drugs is shown most impressively in the 95% cure rate of testicular cancer patients treated with cisplatin[83]. Nonetheless, intact NER function confers chemoresistance as it can efficiently repair DNA damage induced by cisplatin, carboplatin and oxaliplatin[82] –drugs known to interact with OCTs[30,46].

In mammalian systems, as well as in *Saccharomyces cerevisiae* and in *C. elegans,* the NER is executed in four conserved steps: (i) DNA damage recognition by XPC-1, (ii) DNA unwinding and damage verification by XPA-1 and RPA-1, (iii) incision of the DNA surrounding the lesion by endonucleases XPG-1 and ERCC-1, and finally (iv) DNA synthesis by POLH-1 and ligation to fill the resulting gap[81]. Extensive line of evidence indicates that NER in *C. elegans* is fully operational and represents the solely DNA repair mechanism which removes UV-induced and platinum-induced DNA damage[81].

Inhibitors for NER have been under constant investigation as they appear to possess poor specificity[80]. Clinical trials have been concluded for inhibitors like UCN-01 to be utilized as a monotherapy or combination therapy for a variety of recurrent or relapsed blood-based and solid tumors[80]. Also, the topoisomerase I and II inhibitor F11782 (tafluposide), possess the capacity to inhibit the helicase and incision step in NER[84]. Many other NER inhibitors are considered important for combination therapy. The small-molecule ET-743 (trabectedin) showed inhibition activity against the NER and HR repair pathways[80]. However, cells deficient in NER components and colorectal cancer cells show resistance to ET-743[85] indicating that ET-743 mechanism of action needs careful investigation. Furthermore, the novel small-molecule inhibitor MCI13E appears to be RPA-specific in cell culture and acts as a sensitizer to cisplatin, being suitable for combination therapy targeting a number of cancers, however its precise mechanism of action still needs further characterization[82].

The study of small-molecule inhibitors has highlighted the importance of another venue on drug discovery programs: the use of *in silico* modeling. More specifically, the identification of the small-molecule inhibitor NERI01 has been brought about thanks to an *in silico* modeling approach showing that NERI01 targets ERCC activity[86]. As such, a correlation between ERCC overexpression and cisplatin resistance in testis tumour cells[87], has been demonstrated indicating the importance of using NERI01 to inhibit ERCC activity[86]. These studies are pivotal since ERCC expression surfaced as a predictive biomarker of resistance to platinum-based chemotherapy, and the discovery of ERCC inhibitors will bring substantial benefits to platinum-based chemotherapeutics.

1.4.3. Mismatch Repair

The MMR pathway contributes to genome integrity by correcting base–base mismatches and repairing insertion and/or deletion loops developed in the course of DNA replication[88]. Also, the MMR is capable of inducing apoptosis in response to DNA damage[88]. It has been shown that dysfunction of MMR in humans increases the risk of kidney, liver and hereditary nonpolyposis colorectal cancer (HNPCC)[89]. Moreover, MMR-deficient colorectal cells quickly accumulate mutations due to their high turnover, which in turn induces tumorigenesis[88].

Post-replicative MMR damage control is capable to sense and remove the defective DNA strand before the damage can become permanent or duplicated in future cell cycles[88]. Specialized enzymes replace the damaged strand with a new DNA segment synthesized from the daughter strand as a template[88]. A conserved mechanism across eukaryotes begins with detection of DNA damage by the heterodimer complex MSH2-MSH6 (MutSα) which repairs base substitutions and small mismatched loops, followed by recruitment of the heterodimer complex MLH1-PMS2 (MutLα), proliferating cell nuclear antigen (PCNA), and EXO1. This complex excises the newly synthesized strand by the exonuclease function of EXO1 and notably, the repair finalize specifically on the new DNA strand[88]. Mutations in MMR components predispose cells to hereditary nonpolyposis colon cancer and up to 20% to sporadic cancers[90].

Defective MMR activity promotes damage tolerance that contributes to increased mutagenicity, tumorigenesis and resistance to antineoplastic drugs[88]. It has been reported that an alternative to exploit the deficiency of MMR is to induce a synthetic lethality which will ensure an unrepairable damage[90]. As such, the antineoplastic methotrexate has shown high efficiency on MSH2-deficient colorectal cancer cells by inducing high levels of oxidative stress creating such synthetic lethality[80,90]. Similarly, it has been demonstrated that Pol β and Pol γ inhibitors can induce synthetic lethality by creating significant amounts of 8-oxoG lesions in MSH2-deficient cells[90,91]. Normally, in such scenario, the BER pathway would recognize and repair the 8-oxoG lesions, however, because those polymerase inhibitors would also impede BER repair activity, a synthetic lethality is created[91].

MMR competence increases cellular susceptibility to alkylating agents and fluoropyrimidine derivative promoting G2-cell cycle arrest and later trigger apoptosis[92]. Because hypermethylation of the MLH1 gene promoter decreases its activity in sporadic cancers, hypomethylation could fully restore MMR functions, thus sensitizing cells to alkylating agents and fluoropyrimidine derivative[80,92]. Notably, investigations regarding 5-fluoro-2-deoxycytidine (FdCyd) mechanism of action –a fluoropyrimidine derivative-, have shown this potential function[93].

1.4.4. DNA Double Strand Break Repair

DSBs occur mainly when topoisomerases uncoil the DNA strand or by the action of IR or chemotherapeutics[94]. Commonly, it is originated when replication forks stall and break at the site of unrepaired DNA lesions[94]. Unrepaired DSBs are highly toxic and result in aneuploidy that could be inherited in future cell cycles leading to cancer, or cell death[94]. To avoid this threat, cells evolved with an elaborate and highly conserved network of DSB repair mechanisms. *C. elegans* has become instrumental to investigate DSB repair leading to important discoveries in this mechanism during development[94]. DSBs are repaired via two main mechanisms identified as non-homologous end joining repair (NHEJ) and homologous recombination repair (HR)[94].

NHEJ features a specific complex of proteins that coordinates to join the two-fragmented strand ends without the need of a homologous template. However, it may result in errors such as nucleotide addition or deletion, depending on the complexity of the damage[94]. This process is quite important in a pre-replication scenario where no template is available and breaks must be rapidly repaired[94]. In eukaryotes, NHEJ is triggered upon sensing the damage by a complex assembly of Ku70, Ku80, and DNA ligase IV (XRCC4)[95]. The *C. elegans* orthologs CKU-70, CKU-80, and LIG-4, have been characterized as subunits forming the Ku heterodimer performing NHEJ repair[95].

Oppositely, HR requires a homologous template from the sister chromatid which allows the strand to be restored[94]. The HR process is a highly efficient mechanism that preserves the integrity of the DNA sequence[94]. In the HR pathway, the RPA/RPA-1 complex and Rad51/RAD-51 are crucial to initiate the repair process[94]. RPA-1 starts the repair process by stimulating unwinding of the damaged DNA, then shields and stabilizes the resected single strand[94]. The next crucial step follows the recruitment of RAD-51 which initiates DNA strand exchange by interacting with other repair proteins[94]. RAD-51 acts downstream of CHK-2 and SPO-11 and localize to DNA breaks foci[94]. In short, as RPA-1 possess a common cleft for binding a number of proteins, and RAD-51 is pivotal for chromosomal morphology[94], efforts are underway to create small-molecule inhibitors targeting RPA-1[96] and RAD-51[80]. Importantly, in humans, Rad51 overexpression is a biomarker of several forms of cancer such as leukemia, breast and pancreatic cancers and lung cancer[80].

A number of small-molecule inhibitors targeting HR lack specificity. For instance, the MRN complex (HR's damage sensor) inhibitor mirin impedes ATM function and downregulates NHEJ simultaneously[97]. Only RI-1 has been demonstrated to possess specificity against HR[97]. It is likely that RI-1 inhibits Rad51 by blocking its recombinase activity inhibiting the polymerization process onto ssDNA, thus impeding monofilament formation[97]. Furthermore, it has been shown that inhibition of the molecular chaperone HSP90 decreases Rad51 activity and hampers the activity of multiple checkpoint proteins promoting cell cycle arrest which, upon accumulation, can trigger apoptosis[98]. As such, HSP90 inhibition can simultaneously disrupt metastasis, resistance to apoptosis and neo-angiogenesis[99]. Distinct classes of HSP90 inhibitors are currently undergoing clinical trials for a variety of cancers[100]. This includes Geldanamycin-derived analogs like 17-DMAG, restapimycin (IPI-504), and tanespimycin[100]. As well, resorcinol-derived analogs such as ganetespib, NVP-AUY922, KW-2478 and AT13387[98].

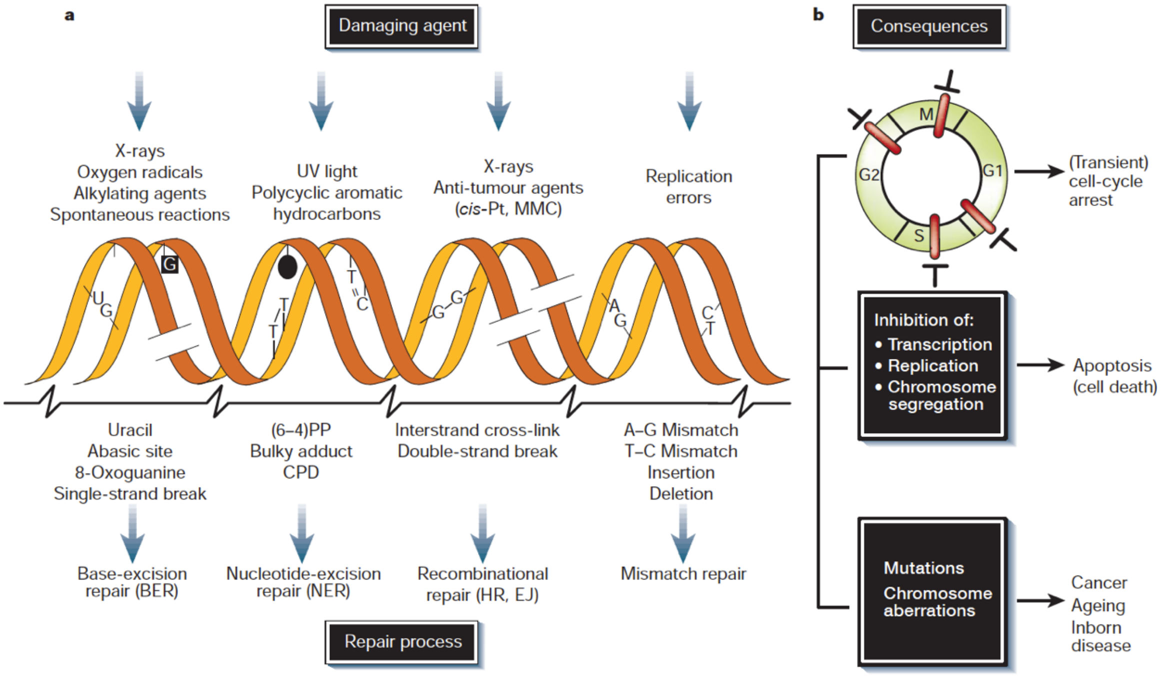

Figure 6. DNA damage and repair mechanisms. **A**, Common DNA damaging agents (top); examples of DNA lesions induced by DNA damaging agents (middle); and principal DNA repair mechanisms responsible for the removal of DNA lesions (bottom). **B,** Acute effects of DNA damage on the cell-cycle, leading to transient arrest in the G1, S, G2 and M phases (top), and on DNA metabolism (middle). Long-term consequences of DNA injury (bottom) includes point DNA mutations affecting single genes or chromosome aberrations which may involve multiple genes. (Adapted from Jan Hoeijmakers, 2001)[71].

1.5. *C. elegans* in drug discovery

C. elegans has been extensively used as a model organism for diverse molecular and cellular aspects of complex human diseases such as Alzheimer's disease[101], Parkinson's disease[102], amyotrophic lateral sclerosis[63,64], diabetes[103], Duchenne muscular dystrophy[104] and cancer[105,106]. This is facilitated by the fact that *C. elegans* shares homology for around 80% of human genes and presents counterparts for many genes associated with human diseases[106,107]. More recently, this model organism has been explored as a tool for high-throughput drug discovery due to advances in imaging platforms and data analysis software.

The same genetic and phenotypical properties mentioned previously (Section 1.3) also provide leverage for whole organism-based high throughput screening (HTS)[61,106]. Major benefits for the use of *C. elegans* in HTS are: (i) the whole organism-based *C. elegans* approach allows for more accurate modeling of complex human diseases with a large range of observable phenotypes that could not be easily mimicked *in vitro* or with unicellular models; (ii) with this model, it is easy to evaluate several aspects of therapeutic agents, i.e. drug absorption and efficacy, distribution, metabolism, excretion and toxicity, which are the critical steps in drug discovery; and (iii) the complex responses observed in multicellular and multi-organ systems increases the chances of identifying agents that could ultimately be translated into therapeutic approaches in more complex multicellular organisms such as humans[61,106].

Several HTS advances have been described in *C. elegans*; for instance, automation of animal transfer and automated image acquisition and data analysis, which have proven to be highly efficient in handling large numbers of animals[106]. On the other hand, a number of approaches targeting drug absorption and distribution with a large number of animals presented significant variations from one method to another[108-110] and only a few HTS methods achieved optimal drug absorption efficiency in *C. elegans*, however, using significantly high concentrations of drugs with a yield of drug's bioactivity of less than 1%[108,111]. These features could possibly be avoided if there is greater uptake of molecules leading to an increase in recovery rate.

1.6. Aims of this work

Based on the above mentioned evidence, we propose that the modulation of the uptake activity of membrane transporters in *C. elegans* could be a far-reaching strategy not only to identify novel bioactive molecules, but also to overcome the limitations of previous *C. elegans*-based HTS. In these regards, small-molecule inhibitors of DNA repair pathways hold significant promise for killing tumor cells. Collectively, as the above information indicates, the application of small-molecule inhibitors of DNA repair pathways combined with enhanced entry of these agents into the cells through functional OCTs might serve as novel strategies to ameliorate chemotherapies.

The aim of this work is to evaluate the extent to which OCT-mediated uptake may modulate the pharmacokinetics and efficacy of chemotherapeutics, by affecting their distribution and subsequent elimination. *C. elegans* is particularly well suited to tackle this problem because it features a less complex DNA repair system, which enables us to bypass limitations presented by the considerable redundancy of DNA repair components in mammalian systems.

Therefore, in this thesis, we introduce a screening strategy that: **(i)** combines DNA repair pathway inhibitors whose transport across cellular membranes could be facilitated by OCTs, and in parallel being used in combination with chemotherapeutics to efficiently induce tumor cell death; **(ii)** targets specialized drugs that create specific DNA lesions which could be transported in high quantities to overburden the damage response in order to kill tumor cells and rapidly abolish metastasis; **(iii)** identifies newly synthesized molecules, their cellular entry, absorption and subsequent mechanism of action and potential adverse effects.

Results

Chapter 2 : A novel approach using *C. elegans* DNA damage-induced apoptosis to characterize the dynamics of uptake transporters for therapeutic drug discoveries

Arturo Papaluca [1] and Dindial Ramotar [1*]

[1]Maisonneuve-Rosemont Hospital, Research Center, Université de Montréal, Department of Medicine, 5415 Boul. de l' Assomption, Montréal, Québec, Canada, H1T 2M4

Running title: OCT-2 mediates drug transport into *C. elegans*

[*]To whom correspondence should be addressed: Prof. Dindial Ramotar, Maisonneuve-Rosemont Hospital, Research Center, Université de Montréal, Department of Medicine, 5415 Boul. de l'Assomption, Montréal, Québec, Canada, H1T 2M4. Telephone: (514) 252-3400 ext. 4684; Fax: (514) 252-3430; email: dindial.ramotar@umontreal.ca

Keywords: drug uptake and resistance, organic cation transporters, *C. elegans*, germ cells apoptosis, brood size, DNA damage and repair pathways, *in silico* modeling and validation, high resolution microscopy, gene expression, DNA repair pathway inhibitor

Citation: Papaluca, A. and Ramotar, D. A novel approach using *C. elegans* DNA damage-induced apoptosis to characterize the dynamics of uptake transporters for therapeutic drug discoveries. *Sci. Rep.* 6, 36026; doi: 10.1038/srep36026 (2016).

Background: OCTs orchestrate the uptake of cationic compounds into cells. In humans, OCTs are localized in vital organs and believed to be linked to the development of chemoresistance.

Results: *C. elegans* devoid of OCT-1 stimulates the expression of OCT-2, which is the main uptake transporter for a number of compounds including chemotherapeutic agents. Downregulation of OCT-2 rescues the shortened lifespan of *oct-1* mutants by preventing the entry of toxic compounds into the animals.

Conclusion: *C. elegans* OCT-2 is a novel uptake transporter and a target for therapeutic drug discoveries.

Significance: The approach of exploiting *C. elegans* uptake transporters in combination with defective DNA repair pathway will have broad applications in medicinal chemistry.

ABSTRACT

Organic cation transporter (OCT) function is critical for cellular homeostasis. *C. elegans* lacking OCT-1 displays a shortened lifespan and increased susceptibility to oxidative stress. We show that these phenotypes can be rescued by downregulating the OCT-1 paralogue, OCT-2. Herein, we delineate a biochemical pathway in *C. elegans* where uptake of genotoxic chemotherapeutics such as doxorubicin and cisplatin, and subsequent DNA damage-induced apoptosis of germ cells, are dependent exclusively upon OCT-2. We characterized OCT-2 as the main uptake transporter for doxorubicin, as well as a number of other therapeutic agents and chemical compounds, some identified through ligand-protein docking analyses. We provide insight into conserved features of the structure and function and gene regulation of *oct-1* and *oct-2* in distinct tissues of *C. elegans*. Importantly, our innovative approach of exploiting *C. elegans* uptake transporters in combination with defective DNA repair pathways will have broad applications in medicinal chemistry.

2.1. Introduction

The nematode *Caenorhabditis elegans* has a plethora of advantages for use as an *in vivo* model system [1]. Indeed, this organism exhibits a broad array of phenotypes that can be easily monitored for changes in various genetic/physiological pathways. For example, it can be utilized to understand the roles of Organic Cation Transporters (OCTs) in the uptake of therapeutic substrates[2]. In fact, evidence from mammalian systems dictates that OCTs mediate the uptake of chemotherapeutic drugs such as oxaliplatin and daunorubicin[3,4]. Hence, elucidating the molecular underpinnings of OCTs and consequent development of tools to modulate their transport activity *in vivo* are expected to improve chemotherapeutic outcome.

In *C. elegans*, little is known about the roles of OCTs and their affinity towards distinct substrates. OCT-1 was the first uptake transporter characterized from *C. elegans* and when expressed in mammalian cells was shown to mediate the transport of the organic cation tetraethylammonium, a prototypical substrate used for classifying OCTs[5]. *C. elegans* deleted for *oct-1* exhibits a shortened lifespan and increased susceptibility to oxidative stress, which led to the proposition that OCT-1 facilitates the import of antioxidants required to protect *oct-1* mutant animals from oxidative stress[2]. However, uptake of ergothioneine, the purported antioxidant substrate of OCT-1, was not reduced in *oct-1* mutant animals as compared to the parent[2]. Therefore, it seems plausible that an alternative explanation could account for the *oct-1* mutant animal phenotypes.

Recently, we documented that the expression of OCT-1 can restore uptake of the chemotherapeutic drug doxorubicin into *Saccharomyces cerevisiae* cells lacking the amino acid transporter Agp2, which when deleted blocked the expression of several target genes including the polyamine transporters Dur3 and Sam3[6]. No further studies were done to determine whether OCT-1 substituted for the regulatory function of Agp2 or directly for the roles of Dur3 and Sam3, as both of these transporters also mediate the transport of doxorubicin[6]. Furthermore, it remained unknown whether OCT-1 might mediate the transport of doxorubicin into *C. elegans*. Besides OCT-1, *C. elegans* possesses another related member of the SLC22 organic cation transporter family, i.e., OCT-2. OCT-2 shares

22.56% identity with OCT-1 but differs in having an extended N-terminal of 172 amino acid residues that is unrelated to OCT-1. To date, no studies have assigned a structural and functional role to the putative OCT-2 transporter.

During the last decade, *C. elegans* has become instrumental in several drug discovery programs[1,7]. However, in many high-throughput screens performed so far to identify novel small molecules that, e.g., act as antimicrobials, extend lifespan, inhibit oxidative stress or prevent multidrug resistance, the yield of bioactive compounds is typically in the range of 0.03% to less than 1%[1,8]. It is possible that the recovery rate could be higher if there is greater influx of the molecules. High-throughput screens at higher initial concentrations may alleviate this issue, but could be cost prohibitive. As such, we propose characterization of the function and substrate specificities of uptake transporters in *C. elegans* will be advantageous towards improving the strategies employed to identify novel bioactive molecules.

In this study, we report a number of novel findings regarding the OCT-1 and OCT-2 transporters of *C. elegans*. We show for the first time that (i) unlike downregulation of *oct-1*, depletion of *oct-2* did not affect the lifespan of the animals and, instead, rescues the shortened lifespan of *oct-1* deletion animals, (ii) *oct-1* downregulation leads to *oct*-2 upregulation, which in turn mediates uptake of toxic environmental compounds and chemotherapeutic drugs, (iii) upregulation of OCT-2 increases uptake of prooxidants, as judged by the activation of the oxidative stress response reporter GST-4::GFP, leading to germ cell death, as well as to damages to other tissues that could account for the shortened lifespan of *oct-1* deletion animals, (iv) *oct-2* upregulation mediates the accumulation of clinically relevant genotoxic anticancer drugs that sensitizes DNA repair deficient animals to germ cell death and diminishes their survival, and (v) ligand-protein docking analysis can be exploited to define substrates such as DNA damaging agents that tightly bind to OCT-2 and which can be validated by suitable readouts. Our findings represent a robust OCT-based strategy to screen a plethora of new therapeutic drugs useful for treating human illnesses, and provide crucial information for rapid recognition of their pharmaceutical benefits and adverse effects.

2.2. Results

2.2.1. *oct-2* deficiency rescues the shortened lifespan of *oct-1* deletion mutants

It has been postulated that *C. elegans* mutants deleted for *oct-1* are defective in uptake of antioxidants and, as a consequence, exhibit shortened lifespan and increased susceptibility to oxidative stress[2]. However, the fact that *oct-1* mutants show no defect in the uptake of the key antioxidant ergothioneine is inconsistent with this hypothesis. As such, we postulate that *oct-1* gene deletion could instead lead to increased uptake of prooxidants from the environment if the loss of OCT-1 activates expression of a related transporter. This notion is based on the fact that *OCT1* knockout mice manifest upregulation of two related transporter genes, *OCT2* and *OCT3*[9]. We therefore performed a homology search using *C. elegans* OCT-1 as a query for protein sequences in the *C. elegans* Wormbase. This analysis revealed a second *C. elegans* member of the organic cation transporter family SLC22, i.e., OCT-2, which shares 22.56% identity with OCT-1 (Figure S1). The predicted protein sequence of OCT-2 indicated that it possesses an extended N-terminal of 172 amino acid residues (Figure S1), suggesting that it is structurally distinct from OCT-1. To date, there is no previous report assigning a functional role to the putative transporter OCT-2. We set out to characterize the molecular function of OCT-2 by first evaluating whether its RNA-interference (RNAi)-driven depletion might influence lifespan of *C. elegans*. In this experiment, L1-staged wild type animals were systematically fed bacteria harbouring the HT115 RNAi vector targeting *oct-2* to measure adult lifespan, using *oct-1* downregulation or the *oct-1* gene deletion mutant *oct-1(ok1051)* for comparison (Figure 1A)[10]. As expected, *oct-1(RNAi)* or *oct-1* deletion mutants exhibited a shortened lifespan compared to wild type (Figure 1B)[2]. In contrast, *oct-2(RNAi)* animals displayed a normal lifespan (Figure 1B). Quantitative real-time PCR (qRT-PCR) was used to ensure that *oct-1* and *oct-2* expression were indeed downregulated by the RNAi-driven approach (Figure S2A), and that this did not interfere with the expression of another transporter gene, namely *pes-23* (Figure S2B), indicating that RNAi did not have off-target effects. Surprisingly, when *oct-2* was downregulated in the *oct-1* deletion mutant *oct-1(ok1051)*, the resulting *oct-1(ok1051); oct-2(RNAi)* animals exhibited prolonged lifespan as compared to the *oct-1(ok1051)* mutants alone and approaching that of wild type worms (Figure 1B). Thus, it would appear that the *oct-1* mutant phenotype is dependent on OCT-2 function. A simple interpretation is that depletion of OCT-1 may cause the upregulation of *oct-2* expression, such that OCT-2 mediates the uptake of toxic compounds that affect survival.

A gene expression analysis dataset available from the Wormbase for both *oct-1* and *oct-2*[11], revealed that *oct-2* expression is normally higher than *oct-1* across *C. elegans* developmental stages (i.e. from the first larval stage (L1) to the fourth larval stage (L4)), as well as in the hermaphrodite gonads (Figure S3). We examined whether downregulation of *oct-1* would alter *oct-2* expression levels by comparing the *oct-1* and *oct-2* gene expression in the wild type to that of the *oct-1(ok1051)* mutant. We found in the latter that *oct-2* gene expression was significantly augmented, while the *act-1* mRNA levels, used as a control, were unchanged (Figure 1C). This finding further supports the notion that the effects of *oct-1* depletion on the lifespan of the worms are attributable to *oct-2* upregulation.

2.2.2. The SKN-1 target GST-4::GFP is upregulated by *oct-1(RNAi),* and blocked by *oct-2(RNAi)*

We examined whether the elevated levels of oxidative damage reported for the *oct-1* deletion mutant is dependent on OCT-2 function[2]. To test this, we used a reporter strain *dvls19* (GST-4::GFP) in which the promoter of the *gst-4* gene (encoding glutathione *S*-transferase 4) is fused to GFP. GST-4 is a target for the conserved SKN-1/Nrf2 transcriptional activator that plays a role in the defense against oxidative stress[12,13]. The *dvls19* strain showed a basal level of GST-4::GFP expression in the intestine of a representative animal (Figure 1D), which was upregulated following RNAi downregulation of *oct-1* (Figure 1D). In contrast, this *dvls19* strain showed lower than basal levels of GST-4::GFP expression when *oct-2* was downregulated by RNAi (Figure 1D) and quantified by plate assay (Figure 1E). These findings are consistent with a model whereby *oct-2* upregulation, *via oct-1* deletion, allows entry of toxic compounds such as prooxidants into *C. elegans*, in turn causing oxidative stress leading to a shortened lifespan.

2.2.3. OCT-2, and not OCT-1, mediates the genotoxic effects of the anticancer drug doxorubicin

To determine whether OCT-1 regulation of OCT-2 would be involved in the differential uptake of toxic compounds, we treated worms with the chemotherapeutic drug doxorubicin at concentrations that did not lead to developmental arrest[14], and monitored the survival of the animals by scoring brood size. Doxorubicin uptake depends upon cationic transporters in *Saccharomyces cerevisiae*[6] and mammalian cells[4], and has been shown to trigger germ cell apoptosis in *C. elegans*[14]. L1stage wild type animals treated with doxorubicin showed ~ 55 % decrease in brood size as compared to the untreated animals (Figure 1F). In contrast, the *oct-1(ok1051)* mutants displayed a significant level of unhatched or dead embryos, and when treated with doxorubicin showed a sharp decrease (nearly 80 %) in brood size (Figure 1F). While these observations were unexpected as the loss of the uptake transporter should cause drug resistance, we reasoned that the enhanced doxorubicin sensitivity of the *oct-1(ok1051)* mutant animals can be explained by an increase uptake of the drug due to the upregulation of *oct-2*. We therefore examined the sensitivity of worms depleted for *oct-2* following exposure to doxorubicin. *oct-2(RNAi)* caused wild type animals to become less sensitive to doxorubicin with only 27% decrease in brood size, as compared to 55% for the control RNAi (Figure 1F). Importantly, RNAi-driven depletion of *oct-2* in the *oct-1(ok1051)* mutant partially suppressed embryonic arrest and abolished the hypersensitivity of these animals towards doxorubicin showing less than a 20% reduction in brood size compared to 80 % in *oct-1(ok1051)* mutant RNAi control (Figure 1F). *oct-2(RNAi)* did not completely block doxorubicin toxicity on brood size of the *oct-1(ok1051)* mutant, perhaps reflecting residual *oct-2* expression. Also since this mutant was deleted for the *oct-1* gene, a direct role for OCT-1 in doxorubicin uptake is excluded (Figure 1F). Collectively, these observations strongly support the notion that OCT-2 has a predominant role over OCT-1 in uptake of doxorubicin.

2.2.4. OCT-2 allows the accumulation of doxorubicin in *C. elegans* tissues

Based on the above findings, we examined whether OCT-2 might allow the accumulation of doxorubicin in *C. elegans* tissues. As target we chose the pharynx, a relatively large muscular organ that allow food consumption (Figure 2A). We found that OCT-1 was localized at the anterior and posterior sides of the terminal bulb of the pharynx by imaging the *dpy-5(e907); sEx12154* strain featuring an *oct-1::GFP* transcriptional fusion (Figure 2B), thereby validating this organ for uptake studies. Since no similar *oct-2::GFP* transcriptional fusion has yet been constructed, we assessed the pharynx for *oct-2* expression by measuring RNA levels in the heads, severed just posterior to the pharynx, of 300 each of wild type and *oct-1(ok1051)* animals. The results reveal that *oct-2* is expressed at higher levels than *oct-1* in the pharynx of the wild type animals and that its expression was stimulated nearly 2-fold in *oct-1(ok1051)* animals as compared to the wild type (Figure 2C), suggesting that *oct-2* is inducible in the pharynx.

We took advantage of the physical property of doxorubicin, which emits fluorescence at wavelengths of λ^{ex}470 nm - λ^{em}585 nm, as a convenient means to monitor its uptake through OCT-1 and OCT-2 *in situ* by imaging the pharynx. Of note, *C. elegans* tissues have low levels of autofluorescence particularly at the posterior terminal bulb of the pharynx (Figure 2D [i]) where most substances accumulate prior to consumption[15]. However, following exposure of wild type animals to doxorubicin, the emitted fluorescence was greater than background autofluorescence confirming consumption of the drug by the animals (Figure 2D [iv]). Strikingly, the *oct-1(ok1051)* mutant did not reduce the fluorescence intensity of doxorubicin in the pharynx, instead depicting a markedly stimulated intensity (Figure 2D [v]). To test whether the stimulated uptake of doxorubicin in the *oct-1(ok1051)* mutant could result from upregulation of *oct-2*, we downregulated *oct-2* expression in this mutant. Under this condition, extremely low levels of doxorubicin accumulated in the *oct-1(ok1051); oct-2(RNAi)* animals (Figure 2D [vi]). It is noteworthy that the deletion mutant *eat-2(ad453)*, i.e., with a slow pumping pharynx[16], also showed OCT-2-dependent uptake of doxorubicin, excluding the possibility that this transporter functions only when there is a surplus of nutrients (Figure S4).

Doxorubicin uptake in the pharynx of the *oct-1(ok1051)* strains were independently confirmed using another assay employing the Fluoroskan instrument, which measures the fluorescence intensity of the drug (Figure 2E). Using this approach, *oct-1(ok1051)* animals showed a concentration-dependent uptake over a range (10 -100 μM) of doxorubicin into the pharynx, which was blocked by RNAi-driven depletion of *oct-2* (Figure 2F). We tested whether uptake of another fluorescence compound, fluorescein, is similarly dependent upon OCT-2. While fluorescein showed a concentration dependent uptake, ranging from 1 to 100 μM, into the pharynx of the *oct-1(ok1051)* mutant, it was not affected by *oct-2* downregulation in *oct-1(ok1051); oct-2(RNAi)* animals (Figure 2F). These findings suggest that OCT-2 may display specificity in the uptake of substrates into *C. elegans* tissues.

2.2.5. OCT-2-mediated uptake of doxorubicin is blocked by choline in the pharynx

Human OCT1 and OCT2 were shown to transport other cationic molecules such as choline[17]. Thus if choline is also a substrate of *C. elegans* OCT-2 we would expect it to compete for doxorubicin uptake into the pharynx. Choline has the physical property of emitting fluorescence, but at lower wavelengths of λ^{ex}290 nm - λ^{em}345 nm and is undetectable at the wavelength index used for monitoring doxorubicin uptake. Treatment of the *oct-1(ok1051)* animal with doxorubicin in the presence of equimolar amounts of choline (50 and 100 μM), impeded uptake of doxorubicin into the pharynx (Figure 2G), clearly indicating that OCT-2 has the ability to recognize and compete for other cationic compounds. Therefore, we predict that the competition for doxorubicin uptake can be readily exploited as an assay to determine whether a putative ligand can serve as a substrate for OCT-2.

2.2.6. The *oct-1(ok1051)* mutant animals display increased spontaneous and drug-induced germ cell death that is suppressed by *oct-2* downregulation

Analogous to many stem cell systems, *C. elegans* has a self-renewing germ cell population derived from a cellular niche located at the distal tip (see Figure 2A)[18]. These germ cells progress through distinct stages of differentiation and must faithfully maintain the genome. They are very sensitive to genotoxic compounds and respond by using conserved DNA repair mechanisms to maintain genomic stability[19]. Germ cells with excessive DNA damage undergo apoptosis and are unable to form viable embryos[18,20]. We chose to monitor germ cell apoptosis as an experimental system to determine whether OCT-2 would be involved in the uptake of genotoxic anticancer drugs. This approach has the advantage of allowing assessment of the uptake of genotoxic anticancer drugs that do not emit fluorescence or are unavailable in radioactively labeled form. To monitor apoptotic germ cells, we first quantified *in vivo* germ cell corpses in the proximal zone of the gonad arm (see Figure 2A) by utilizing differential interference contrast (DIC) microscopy and staining with the DNA dye acridine orange[21]. In wild type animals, one to four apoptotic cells were detected (Figure 3A [i]), as previously reported[22]. In contrast, the *oct-1(RNAi)* or the *oct-1(ok1051)* mutants depicted an average of five to eight apoptotic cells (Figure 3A [ii and iv]). Analysis of gene expression in the gonads from 100 each of dissected wild type and *oct-1(ok1051)* animals revealed that *oct-1* gene deletion greatly stimulated the expression of *oct-2* mRNA (Figure 3B). Thus, the two-fold increase of apoptotic cells in the gonads of the *oct-1(ok1051)* animals may result from import of prooxidants, as assessed by activation of GST-4::GFP, that can damage the genome of the germ cells leading to embryos with hatching defects (Figure 1F). Unlike the *oct-1(RNAi)*, the *oct-2(RNAi)* animals displayed nearly the same average number of apoptotic cells as the wild type (Figure 3A [iii vs. i]). Interestingly, RNAi-driven depletion of *oct-2* in the *oct-1(ok1051)* mutant sharply reduced germ cell death, which was undetectable in some animals (Figure 3A [v]).

To confirm that the acridine orange-stained germ cells are undergoing apoptosis, as well as to avoid uptake differences of this dye, we evaluated a downstream step of the apoptotic pathway, i.e., engulfment of apoptotic cells by the CED-1 protein to signal phagocytic degradation[23,24]. We employed an imaging strategy that utilizes the *bcls39* strain which carries CED-1::GFP as a reporter of engulfed apoptotic cells[25]. The *bcls39* strain with control RNAi showed engulfment of 1 to 3 physiological apoptotic cells (Figure 3C [i]), whereas downregulation of *oct-1* engendered increased engulfment recapitulating the enhanced germ cell apoptosis observed in the *oct-1(ok1051)* mutant (Figure 3C [ii]) vs. Figure 3A [iv]). As expected, downregulation of *oct-2* in the *bcls39; oct-2(RNAi)* background displayed control levels of engulfment (Figure 3C [iii]). Taken together, we propose that OCT-2 possesses the ability to transport toxic compounds such as prooxidants that cause germ cell death. These prooxidants are likely to cause damages to various tissues and may therefore account for reduced lifespan observed in the *oct-1(RNAi)* or *oct-1(ok1051)* animals (Figure 1B).

We examined whether the OCT-2 dependent accumulation of doxorubicin would lead to the stimulation of germ cell death. Treatment of wild type worms with doxorubicin elevated the levels of apoptotic cell corpses as visualized by both acridine orange staining (Figure 3A [vi]) and engulfment of the cells (Figure 3C [iv]) (and quantified as in Figure 3D and 3E, respectively). *oct-1(RNAi)* or the *oct-1* deletion mutants treated with doxorubicin showed substantially higher levels of acridine orange-stained apoptotic cells (Figure 3A [vii and ix] and quantified as in Figure 3D), which paralleled increased CED-1::GFP engulfment of the cells as compared to the wild type (Figure 3C [v vs. iv] and quantified as in Figure 3E). In contrast, far fewer engulfed apoptotic corpses appeared in doxorubicin exposed animals downregulated for *oct-2* (Figure 3C [vi] and 3E). As expected based on acridine orange staining and engulfment of apoptotic cells, mutants deleted for *cep-1*, *egl-1*, *ced-9*, *ced-4* or *ced-3*, which manifest defects in the apoptotic pathway did not show enhanced apoptotic corpses (Figure S5 [ii to vi], respectively), i.e., unlike wild type animals upregulated for OCT-2 and treated with doxorubicin (Figure S5 [i]). Several conclusions can be derived from these observations: (i) OCT-2 has a predominant role over OCT-1 in the uptake of doxorubicin, (ii) doxorubicin uptake leads to induced germ cell death that correlates with decrease survival, and (iii) both the drug uptake and the induced-germ cell death are OCT-2 dependent.

2.2.7. Cisplatin-induced germ cell death requires OCT-2 function

We assessed whether germ cell death in our experimental model can be used to monitor the uptake of genotoxic drugs that are not readily available as either fluorescently- or radioactively-labeled form. Since human OCT1 has been shown to transport members of the platinum family of anticancer drugs that act by creating intra- and inter-strand DNA cross-links[26], we tested the role of *C. elegans* OCT-1 and OCT-2 in the uptake of cisplatin using germ cell death as a reporter. We monitored germ cell apoptosis in the absence and presence of cisplatin in the following four genotypes: wild type, *oct-1(ok1051), oct-2(RNAi)* and *oct-1(ok1051); oct-2(RNAi)*. Cisplatin induced an increased level of germ cell death in the wild type, which was further greatly stimulated in the *oct-1(ok1051)* mutants (Figure 3F). Downregulation of *oct-2* in the *oct-1(ok1051)* mutants prevented cisplatin-induced germ cell death (Figure 3F). These observations strongly indicate that germ cell death induced by cisplatin primarily depends upon its uptake via OCT-2. We noted that the DNA damaging agent methyl methanesulfonate (MMS), which alkylates DNA bases resulting in both DNA-single and -double strand breaks, induced germ cell death, but independently of OCT-1 and OCT-2 function (Figure S6A). Likewise, γ-rays that create multiple DNA lesions also induced germ cell death (Figure S6B) independently of these transporters (Figure S6C). Thus, the transporter function of OCT-2 is not directly involved in the process whereby DNA damaging agents induce germ cell death.

2.2.8. OCT-2-dependent transport of doxorubicin or cisplatin stimulates germ cell death in *C. elegans* mutants defective in DNA repair

We next systematically examined whether mutants defective in major DNA repair pathways would show OCT-2 dependent sensitization of DNA damage-induced germ cell death. As shown in Figure S7B, the *rad-51* deletion mutant, *rad-51(ok2218)*, lacking the RAD-51 protein needed for DNA strand invasion during homologous recombination (HR)-dependent double strand break repair, exhibited higher endogenous levels of apoptotic cell death due to spontaneous unrepaired meiotic breaks [27] as compared to wild type (Figure S7A). Treatment of the *rad-51(ok2218)* mutant with doxorubicin greatly stimulated apoptosis, which was further induced upon downregulation of *oct-1* in the *rad-51(ok2218); oct-1(RNAi)* genotype (Figure S7C). Consistent with this data, *oct-2* gene expression was indeed upregulated in the *rad-51(ok2218); oct-1(RNAi)* genetic background (Figure S7J). In contrast, depletion of *oct-2* by RNAi in *rad-51(ok2218)* animals suppressed the high level of apoptotic cells observed in this mutant upon exposure to doxorubicin (Figure S7C). These data indicate that upregulated of *oct-2* burdens the *rad-51(ok2218)* animals with doxorubicin-induced DNA lesions leading to enhanced germ cell death.

We also found that *apn-1(tm6691)* animals lacking the key enzyme APN-1, required for removing a variety of DNA lesions including oxidized bases via the base-excision DNA repair (BER) pathway [28], showed enhance germ cell death by doxorubicin when *oct-2* expression was stimulated (Figure S7E and K). This induced apoptosis was strongly attenuated following depletion of *oct-2* by RNAi (Figure S7E). These data suggest that BER in *C. elegans* is also involved in processing doxorubicin-induced oxidative DNA lesions [29] but, more importantly, OCT-2 controls the toxicity of the drug in *apn-1(tm6691)* mutant animals.

Unlike doxorubicin, cisplatin damages the DNA by creating DNA cross-links most of which are processed by the nucleotide excision repair (NER) and DNA mismatch repair (MMR) pathways [30]. We set out to investigate whether *oct-2* expression levels modulate cisplatin-induced germ cell death in mutants defective in either NER or MMR. Remarkably, cisplatin induced substantial levels of apoptotic cells in the *xpa-1(ok698); oct-1(RNAi)* (Figure S7G) and *msh-2(ok2410); oct-1(RNAi)* (Figure S7I) mutants, when *oct-2* was upregulated (Figure S7L and M, respectively). These two DNA repair defective mutants were effectively protected from the onslaught of cisplatin-induced DNA lesions upon RNAi-driven depletion of *oct-2* (Figure S7G and S7I, respectively), consistent with the involvement of OCT-2 in the transport of cisplatin.

It is noteworthy that amongst the DNA repair deficient animals, only in the case of the *apn-1(tm6691); oct-1(RNAi)* genotype was there a significant increase in spontaneous germ cell death (Figure S7D). One possible explanation for this observation is that OCT-2 mediated uptake of prooxidants may lead to oxidative lesions that must be repaired by BER[28]. Collectively, the above data suggest that by combining defects in DNA repair pathways with functional organic cation transporters such as OCT-2, it is possible to determine whether an unknown compound has genotoxic effects and the type of lesions it may create.

2.2.9. Ligand-protein docking analysis predicts the substrate specificity of OCT-2

To gather insights into the substrates that can be recognized by OCT-2, we first made predictions of its protein structure relative to OCT-1 by inputting the respective primary protein sequences into the I-TASSER protein structure prediction server for *in silico* analyses[31]. The I-TASSER server employed known Protein Data Bank (PDB) structures as threading templates to predict the OCT-1 and OCT-2 structures (Table S1A, B). OCT-1 and OCT-2 were both modeled based on the X-ray diffraction structure of the glucose transporter GLUT3/SLC2A3 from *Homo sapiens* (PDB ID: 5c65) and validated with the glucose transporters GLUT1-4 structures (PDB ID: 4gc0) (Table S2A and S2B)[32]. The analysis revealed that OCT-1 and OCT-2 have predicted structures similar to each other (Figure 4A, B). The comparative models of OCT-1 and OCT-2 were computed by utilizing several criteria as described in the materials and methods (Table S3). The final predicted 3D structure of OCT-1 and OCT-2 featured the entire 12 transmembrane domain helices (Figure S8A, B). Overall, the analysis predicted structures for both OCT-1 and OCT-2 that belong to solute carrier transporter family (Figure 4A, B).

We next determined whether the anticancer drugs, doxorubicin and cisplatin, would dock onto the predicted structures of OCT-1 and OCT-2. We utilized the BSP-SLIM and COACH algorithms[33,34] to predict the amino acid residues of the transporters constituting the ligand–protein docking sites (Figure 4C and Table S4). Since the BSP-SLIM server did not recognize the cisplatin chemical structure, a related member of the platinum drug family, carboplatin, was used. The OCT-1 and OCT-2 models interacting with doxorubicin computed a C-score of 0.38 and 0.75, respectively (Figure 4C) (see materials and methods, Table S4). The predicted key residues mediating interaction between the drugs and the transporters suggest that the binding pockets of OCT-1 and OCT-2 are structurally different (Figure 4C), making the ligand-protein binding highly selective depending upon the chemical structure of the ligand.

The OCT-1 and OCT-2 models were also evaluated for their ability to discriminate between the interacting ligands and probable non-binder compounds. As non-binder compounds, we targeted the nonsteroidal anti-inflammatory drug diclofenac, which is classified as an organic anion. The predicted models showed that no residues of OCT-1 or

OCT-2 interact with diclofenac (Figure 4D, Table S5). Thus, it is possible to perform protein-ligand modeling studies in order to predict and uncover novel substrates for uptake by these transporters, which could be further corroborated by the above *in vivo* assays.

2.2.10. Predicted ligands of OCT-1 and OCT-2 and experimental validation

So far, the roles of transporters in the uptake of a vast majority of genotoxic cationic drugs have not been tested in *C. elegans*. We sought to identify which of the known cationic drugs would be taken up by OCT-1 and/or OCT-2. A number of drugs were selected based on two criteria (i) mechanism of action and (ii) biological response. We assessed the docking ability of each compound with OCT-1 and OCT-2. From 19 tested ligands, four resulted with a docking score of zero, whereas the remaining 15 revealed a docking score > 3.5 favouring avid binding with OCT-2 (Table 1 dataset, docking score columns). Amongst these 15 ligands, some possess distinct pharmacological attributes such as creating different types of DNA lesions (Table S6). We next experimentally validated the *in silico* analyses using our drug-induced apoptosis assay as readout. We found that a number of the compounds that docked onto OCT-2 were capable of triggering high level of apoptotic cell death when *oct-2* was upregulated by *oct-1(RNAi)*, as compared to the control RNAi (Table 1 dataset; numbers in the bracket are from control RNAi). There were also ligands that act by damaging the DNA such as melphalan and methoxyamine, which did not dock onto OCT-2, but induced apoptotic corpses (Table 1 dataset). We postulate that these non-binders might use alternative transporters to enter the animal.

As a final validation, we focused on the ligand B02, which robustly docked only onto OCT-2 resulting with a docking score of 5.4 (Table 1 dataset, Figure 5B vs. A). B02 was shown to interfere with human RAD51 in DNA strand exchange and nuclear focus formation in response to DNA damage [35-37]. However, to our knowledge the pharmacological effect of B02 has not been tested in *C. elegans*. To confirm that B02 enters via the OCT-2 transporter, we tested the effect of the compound on wild type, *oct-1(ok1051)* and the *oct-1(ok1051); oct-2(RNAi)* backgrounds at concentrations ranging from 1 to 75 μM. Notably, extreme toxicity was observed with 75 μM B02 for all the genotypes. Therefore, we reduced the concentrations to 5 μM and observed that *oct-2* upregulation caused sterility (Figure 5C) resulting in a decrease in viable animals (Figure 5E) and phenocopying the *rad-51* homozygotes as previously reported [38]. As predicted from our model, the B02 ligand did not cause reduction in viable animals in the *oct-1(ok1051); oct-2(RNAi)* genetic background (Figure 5D) and restored the number of broods to nearly untreated levels (Figure 5E). These compelling data revealed for the first time that the B02 inhibitor of RAD51 is functionally active in *C. elegans* and requires exclusive uptake by OCT-2. We conclude that the docking scores of ligands and quantifiable endpoints provide valuable tools to monitor transporter-mediated drug uptake into *C. elegans.* This approach is particularly suitable for newly developed drugs that cannot be readily labeled or lack fluorescent properties.

2.3. Discussion

In this study, we established for the first time the function of OCT-2 in *C. elegans*, as well as the specific roles for OCT-1 and OCT-2 in mediating tissue transport of distinct compounds, such as the chemotherapeutic drugs anthracyclines and cisplatin. We show that OCT-1 has no direct role in the transport of these compounds, however, it exerts control on *oct-2* expression, and it is OCT-2 that is primarily involved in the uptake of these agents. This conclusion is derived from three key findings. First, the *oct-1* deletion mutant *oct-1(ok1051)* or RNAi-driven knockdown of *oct-1* triggered the upregulation of *oct-2* in the whole body, the head and gonads of the animal, causing hypersensitivity to chemotherapeutic drugs. This phenotype is observed only when OCT-2 is present. Second, RNAi-driven knockdown of *oct-2* blocked uptake of chemotherapeutic drugs thus preventing their genotoxic effects. Since no additional drug resistance was observed in *oct-1(ok1051)*; *oct-2(RNAi)* double mutant animals as compared to ones depleted for *oct-2* alone, a role for OCT-1 in the uptake of these chemotherapeutic drugs can be excluded; nonetheless OCT-1 could act as a transporter for selective ligands. And third, our *in silico* modeling-based screening of OCT-1 and OCT-2 selectively discriminated amongst DNA damaging agents those that are potential ligands for OCT-2. By validating this approach *in vivo*, we show that OCT2-dependent transport of the DNA damaging agents can sensitize mutant animals that are defective in DNA repair pathways. Collectively, these results underscore the importance of uptake transporters in regulating the entry of chemotherapeutic drugs into cells and raise the possibility that the drug-resistance and drug-sensitive responses observed by cancer patients could be governed at the level of drug uptake.

The downregulation of *oct-1* leading to upregulation of *oct-2* was an unexpected finding, and provides a compelling argument that the animal has evolved tight regulation of OCT-2. So how might OCT-1 depletion lead to the activation of OCT-2? One possibility is that both transporters have the ability to transport common essential nutrients and thus deletion of *oct-1* would stimulate OCT-2 to compensate for the deprivation of pivotal nutrients. However, we argue against this possibility, as depletion of both *oct-1* and *oct-2* expression did not result in animals with any dramatic phenotypes under normal growth conditions. A more likely possibility is that OCT-1 might belong to the recent characterized class of surface sensors that act as non-transporting transceptors by sensing the availability of nutrients and signal the regulation of downstream plasma membrane transporters [39,40]. In this model, when nutrients become scarce, OCT-1 might serve as a sensor to promote the upregulation of OCT-2 to scavenge limiting resources. Conversely, when nutrients are plentiful OCT-1 might function to sustain the basal expression of OCT-2. Precedence for this mode of regulation exists in *S. cerevisiae*, *Drosophila melanogaster* and *Homo sapiens* [41]. For instance, in *S. cerevisiae* the Ssy1 sensor, a plasma membrane protein belonging to the amino acid permease family, is endowed with no, or only limited, transport function [42]. Ssy1 senses amino acid availability by direct interaction with extracellular amino acids and transmitting the signal to zinc-finger transcription factors that trigger the expression of several downstream target genes encoding amino acid permeases [42-44]. Similar sensors exist in mammalian cells, e.g., the SGLT3 glucose sensor that binds, but does not transport, sugar molecules [45]. Thus, in view of the increasing number of sensors that are currently being identified, it is plausible that OCT-1 may indeed act either as a non-transporting or transporting sensor leading to regulation of OCT-2 expression. The exact role by which OCT-1 exerts control on OCT-2 will need further investigation, but it is noteworthy that a similar regulation appears to occur in mice where deletion of *OCT1* causes significant upregulation of mRNA transcripts of its homologues *OCT2* and *OCT3* [9].

Remarkably, *oct-2* downregulation rescued shortened lifespan and sharply decreased spontaneous apoptosis observed in the *oct-1(ok1051)* deletion mutant (Figure 1B and 3B). The most direct interpretation is that OCT-2 indiscriminately transports toxic compounds such as prooxidants. Although the source of these compound(s) is unknown, i.e., whether they originate from the feeding bacteria or re-adsorption of metabolites secreted by *C. elegans*, they are capable of inducing DNA lesions that must be removed by BER. This is supported by the observation that only the BER defective *apn-1* deletion mutant exhibited higher levels of spontaneous apoptosis when *oct-2* expression is upregulated. Thus, the previous report showing that *oct-1* deletion animal exhibit a decline in lifespan due to reduced uptake of the antioxidant ergothioneine can alternatively be explained if the sulphur atom on the imidazole ring of ergothioneine serves to detoxify the OCT-2-dependent uptake of prooxidants [2]. Nonetheless, our findings raise a very important concern regarding genetic variations leading to hyperactivation of uptake transporters as previously reported [46]. This hyperactivation likely to cause accumulation of abnormally high concentrations of genotoxic compounds and metabolites. Consequently, such toxic agents could induce substantial DNA damage over the lifetime of an individual causing genomic instability and eventually cancer.

Our study is the first to demonstrate that *C. elegans* OCT-2 plays a role in ligand uptake. We tested doxorubicin and cisplatin as the initial cationic ligands because they are first-line chemotherapeutics believed to be transported by OCTs in human cells [4,47]. Besides these anticancer drugs, we postulate that OCT-2 may recognize a vast array of other cationic compounds. *Per se*, we implemented the OCT-based ligand-protein docking approach and explore a short list of selected cationic compounds to deduce that OCT-2 was promiscuous compared to OCT-1 and that it interacts robustly with several cationic ligands. Importantly, the analysis produced a refined list of genotoxic compounds that display high protein-ligand docking scores all of which show an OCT-2 dependent *in vivo* effect of triggering germ cells apoptosis. We believe that exploiting OCT-2 in *C. elegans* could have far reaching applications and supersede other whole model systems in drug discovery programs with respect to cost and time. Thus, maintaining the OCT-2 transporter at optimal levels by deleting *oct-1* should represent a useful step for incorporation into any high-throughput screens to more efficiently identify bioactive molecules from chemical libraries. A key aspect of this strategy is that overexpressed OCT-2 is expected to operate with significantly lower chemical concentrations as observed with cisplatin where a fixed lower concentration of the drug had no effect on the wild type, but significantly induced apoptosis in the *oct-1(ok1051)* mutant (Figure S9). Thus, the previous barriers posed by *C. elegans* to find bioactive molecules could be explained by the lack of an activated mechanism to efficiently take up the compounds at lower concentrations. In short, we now provide a comprehensive readout of the OCT-2 functional selectivity towards cationic molecules that have a deleterious effect on *C. elegans,* and therefore provide a foundation to understand the regulatory control of drug uptake to circumvent genotoxicities. In addition, we hypothesize that OCT-2 could be exploited either through the *oct-1* gene deletion mutant or *oct-2* over-expression transgenic animals to generate a hypersensitive `screening´ *C. elegans* to facilitate high-throughput drug screening.

2.4. Acknowledgements

We acknowledge Dr. John Pascal (Département de Biochimie et Médecine Moléculaire, Université de Montréal) for guidance with the protein structure modeling analysis. We thank Drs. Marie-Eve Lalonde and Florence Coteau (Centre de Recherche Hôpital Maisonneuve-Rosemont) for technical assistance with the gene expression and *C. elegans* genetic analyses, respectively. We thank Drs. Ivan Topisirovic (Lady Davis Institute Jewish General Hospital, McGill University), Nigel O'Neil (Michael Smith Laboratories, Vancouver, BC) and Elliot Drobetsky (Université de Montréal) for critically reading the manuscript. We also thank the CGC and Shohei Mitani for strains. This work was funded by the research grant (RGPIN/202432–2012) to D.R. from the Natural Science and Engineering Research Council of Canada. A.P. was awarded with a Ph.D. bourse d'excellence du Programme en Médecine Expérimentale, Université de Montréal.

Conflict of interest: The authors declare that they have no conflicts of interest with the contents of this article.

Competing financial interests: The authors declare that there are no competing financial interests associated with this work.

Author contributions: A.P. and D.R. designed the experiments. A.P. performed 100% of the experiments. A.P. and D.R. analyzed the data. A.P. wrote the manuscript. A.P. and D.R. corrected the final version of the manuscript.

2.5. Materials and methods

Nematode strains and culture conditions—The Bristol N2 (wild type), RB1084 [*oct-1(ok1051)* I], VC1973 [*rad-51(ok2218)* IV/nT1 [qIs51] (IV;V)]*, RB864 [*xpa-1(ok698)* I], RB1864 [*msh-2(ok2410)* I], MD701 [*bcIs39* [lim-7p::ced-1::GFP + lin-15(+)] and DA453 [*eat-2(ad453)* II], TJ1 [*cep-1(gk138)* I], MT1082 [*egl-1(n487)* V], MT4770 [*ced-9(n1950)* III], MT5287 [*ced-4(n1894)* III], MT3002 [*ced-3(n1286)* IV] and CL2166 [*dvIs19* [(pAF15) gst-4p::GFP::NLS] III] *Caenorhabditis elegans* strains were obtained from the CGC Stock center (*Caenorhabditis* Genetics Centre, University of Minnesota, Minneapolis, USA). The [*apn-1(tm6691)* II] were obtained from Shohei Mitani (Tokyo Women's Medical University School of Medicine, Japan and the National Bioresource Project for the nematode *C. elegans*). The alleles used in this study were all previously validated to be null. All *C. elegans* strains were maintained at 20°C on nematode growth medium (NGM) agar (2.5 g/L peptone, 51.3 mM NaCl, 17 g/L agar, 1 mM $CaCl_2$, 1 mM $MgSO_4$, 25 mM KPO_4, and 12.9 µM cholesterol) enriched with a lawn of streptomycin-resistant *Escherichia coli* OP50 bacterial strain as a source of food. For all *in vivo* experiments, developmental staged-synchronized nematodes were obtained by hypochlorite treatment of gravid adult hermaphrodites. Eggs were allowed to hatch on M9 buffer (6g Na_2HPO_4, 3g KH_2PO_4, 5g NaCl, 0.25g $MgSO_4 \cdot 7H_2O$ per liter filter sterilized). In all experiments, animals were monitored from day 1 post-L1 larvae stage and from L4 to avoid experimental bias. *Homozygous *rad-51/rad-51* nematodes [27] show almost complete inviability due to high embryonic lethality in their progeny, thus we analyzed heterozygote nematodes due to the ease of RNAi-feeding for further analyses. *C. elegans* strains were backcrossed at least three times.

Lifespan assay— Lifespan assays were performed at 20°C in standard conditions and assessed blindly as previously described [10].

Drug treatment— The anthracycline doxorubicin, water-soluble platinum complex cisplatin and alkylating agent methyl methanesulfonate (Sigma Cat. N° 129925) were added to the NGM agar medium before solidification (~55°C) to obtain a final concentration of 100 µM for doxorubicin and cisplatin and 0.25 μM for methyl methanesulfonate, respectively. For all experiments, L1-staged from F1 synchronized nematodes were transferred to NGM control agar plates and containing doxorubicin, cisplatin and methyl methanesulfonate. Doxorubicin and cisplatin working concentrations were chosen based on previously reported assays [14]. All drug-containing plates were freshly made prior to each experiment. Our oncology pharmacy department (Maisonneuve-Rosemont Hospital (HMR) provided doxorubicin and cisplatin.

Microscopy and imaging— All microscopy was performed utilizing a DeltaVision Elite Image Restoration System (Applied Precision) with either 40x/0.65-1.35 or 63x/1.42 oil objective. The worms were anesthetized with levamisole (5 μM, Sigma Cat. N° L0380000) and mounted on 2% agarose pads for their respective imaging and quantification. Images were processed utilizing ImageJ imaging software [48].

DNA damage response assay and germ cells imaging—The methods previously described were used [21]. Briefly, to quantify the number of apoptotic corpses in nematodes, L1-staged synchronized N2 wild type, *oct-1(ok1051)* and DNA repair deficient mutants were exposed to different doses of drugs followed by germ cells apoptosis assay. Between 18 to 24 hours past L4-staged nematodes, adult moult staged nematodes were assayed with differential interference contrast (DIC) microscopy (Nomarski) optics and the vital DNA dye acridine orange (Sigma Cat. N° A6024). Nematodes were incubated in the dark for 2 hours at 20°C on NGM plates containing 1 ml of 50 μg/μl of acridine orange DNA dye dissolved in M9 buffer. Stained nematodes were transferred to fresh OP50-seeded NGM plates to incubate for 2 hours in order to clear off the stained bacteria. The acridine orange-stained and DIC-visible apoptotic corpses were counted with an exposure time of 1 second and 0.8 seconds, respectively. The engulfment of apoptotic corpses was scored utilizing the CED-1::GFP reporter and imaged similarly with an exposure time of 1 second utilizing the GFP channel. Images were collected as a series of 25/0.5 μm optical sections covering the complete thickness of the gonad arm.

Imaging the oxidative stress-inducible GFP reporter GST-4::GFP—The uptake of prooxidants was detected by imaging the oxidative stress-inducible GFP reporter GST-

4::GFP. L4-staged synchronized nematodes were maintained in NGM plates at 20^{o}C overnight and imaged the next day at the adult moult stage. The image analysis was performed by measuring the GFP fluorescence intensity of the whole animal utilizing the GFP channel exposed for 0.8 seconds and DIC exposed for 0.05 seconds.

Imaging the pharynx to measure the uptake of doxorubicin— To measure the uptake of doxorubicin, an approach focusing on the pharynx of *C. elegans* was developed. L4-staged synchronized nematodes were treated with doxorubicin 100 μM in NGM plates, incubated at 20^{o}C overnight and imaged the next day at the adult moult stage. The image analysis was performed by measuring the doxorubicin fluorescence intensity (λ^{ex}470 nm - λ^{em}585 nm) localized at the pharynx by utilizing the GFP channel and observed under a 40x/0.65-1.35 oil objective exposed for a period of time of 0.5 seconds. ImageJ [48] imaging software was utilized to determine the level of fluorescence in the pharynx region. The data of measured fluorescence intensity for doxorubicin uptake was depicted by implementing the custom built-in interactive 3D Surface Plot featured in ImageJ, which display the intensities of pixels from a region of interest of a given image. The uptake was corroborated by two means: (i) The area, the integrated density and the mean gray value were considered to calculate the corrected total pharynx fluorescence [CTPF = Integrated Density – (Area of selected pharynx X Mean fluorescence of background readings)] [49], and (ii) Fluoroskan analysis (see below). To measure doxorubicin uptake in a dose-dependent manner, the nematodes were treated with 1 ml of varying concentrations (10 to 100 μM) of the drug in M9 buffer. Uptake of Fluorescein (Sigma Cat. N^{o} F2456), at concentrations ranging from 1 to 100 μM, was used as a control.

Relative RNA quantification to monitor gene expression—Total RNA (RNeasy mini kit Qiagen Cat. N^{o} 74104) was prepared from ~1000 L4 synchronized nematodes and used for cDNA synthesis (Invitrogen Cat. N^{o} 28025-013) followed by quantitative real-time PCR (qRT-PCR). qRT-PCR was performed with the Supergreen Mastermix (Wisent Bioproducts Cat. N^{o} 800-431-UL) starting at 95^{o}C for 2 min, followed by 40 cycles at 95 ^{o}C for 5 sec, 63 ^{o}C for 30 sec and 72 ^{o}C for 30 sec. Transcript levels were normalized to the internal controls *act-1* and *pmp-3* encoding actin and the peroxisomal membrane protein, respectively.

Because there is a putative third organic cationic transporter PES-23, which shares 21.31% and 17.18 % identity with OCT-1 and OCT-2, respectively, we monitored *pes-23* gene expression for off targets. The forward and reverse primer sequences utilized in this study were: *oct-1*: 5'-TTTGGAGCAGCTATGGCTTT-3' and 5'-CTTAGCGTCAGCCCATTTTC-3'; *oct-2*: 5'-TTGGAGTCGTGCTCACGTTC-3' and 5'-GAGTATGTGAGAAGAAAGCC-3'; *act-1*: 5'-TGCTGATCGTATGCAGAAGG-3' and 5'-TAGATCCTCCGATCCAGACG-3'; *pmp-3*: 5'-GTTCCCGTGTTCATCACTCAT-3' and 5'-ACACCGTCGAGAAGCTGTAGA-3'; *pes-23*: 5'-TTCTTGCCGGAGTACCTGCC-3' and 5'-GCACACATGGAGATTCCGTT-3'.

Dissection of C. elegans heads and gonads for relative RNA quantification—Nematodes were first transferred to a dried 2% agarose pad in 10 μl of M9 buffer. Exactly 300 N2 wild type and 300 *oct-1(ok1051)* L4 ~ young adult moult staged nematodes were decapitated just posterior to the pharynx by utilizing a $26^{1/2}$ gauge syringe. Severed heads were washed and collected with M9 buffer in a micro-centrifuge tube and rapidly stored at -80^{o}C in Trizol (Ambion Life Technologies Cat. N^{o} 15596-018). The same procedure was followed to dissect 100 gonads from L4 ~ young adult staged nematodes. In order to preserve optimum tissue integrity, the collection was made every 15 severed heads and every 10 gonads respectively. RNA extraction was performed from the pool of all collected severed heads and dissected gonads and stored at -80^{o}C for further qRT-PCR analysis.

RNA interference analysis—*Escherichia coli* HT115^{DE3} strain harboring specific RNAi constructs against *oct-1* and *oct-2* was grown on lysogeny broth (LB) agar plates containing ampicillin and tetracycline. Overnight cultures were grown in LB media containing ampicillin. For *oct-1* and *oct-2* RNAi-driven knockdown experiments, nematodes were maintained until first generation (F1) on NGM agar plates containing 1 mM IPTG (isopropyl-β-D-1-thiogalactopyranoside) enriched with a lawn of *E. coli* HT115^{DE3} expressing RNAi constructs in the pL4440-feeding vector at standard temperature 20 ^{o}C. For *oct-1* and *oct-2* RNAi-driven knockdown efficiency, mRNA expression levels were measured in synchronized L4-staged collected from the F1 generation of nematodes fed with *E. coli* expressing RNAi targeted to the indicated genes. The RNAi clones were obtained from the Ahringer laboratory library [112] and verified by sequencing. The depletion efficiency of *oct-1* and *oct-2* genes was validated by qRT-PCR. In all experiments synchronized L4 animals were fed RNAi expressing bacteria and the resulting F1 animals were analyzed for phenotypes.

Choline-based competition assay—L4-staged F1 nematodes were treated overnight with 50 μM and 100 μM concentrations of choline and doxorubicin as separate conditions and together in equimolar amounts in NGM agar plates. The differences in wavelength indexes between doxorubicin (λ^{ex}470 nm - λ^{em}585 nm) and choline (λ^{ex}290 nm - λ^{em}345 nm), allowed us to measure the competitive uptake in the pharynx utilizing the GFP wavelength index where only doxorubicin is detectable and not choline.

Statistical analyses—Lifespan analyses were performed utilizing the Kaplan-Meier estimator calculating the Log-rank test for statistical significance utilizing OASIS software (Online Application for the Survival Analysis of Lifespan Assays Performed in Aging Research) [51]. Germ cell death statistical significance was assessed with the Mann-Whitney U-test calculator Mean values ± s.e.m were calculated for each condition. $^{*}P<0.05$; $^{**}P<0.01$; $^{***}P<0.001$; $^{****}P<0.0001$ were considered to be statistically significant. For the Brood size analysis, statistical differences were calculated by the unpaired two-tail t-test ($^{*}P<0.03$; $^{**}P<0.01$; $^{***}P< 0.0005$) and represented as ± S.D. The Fluoroskan data and the Mean Fluorescence Intensity measurements extracted from the competition assay, Student T-test was calculated and represented as ± S.D ($^{***}P<0.001$ significant). N.S. = Non Significant. Statistical differences were calculated by using the GraphPad Prism Statistical Software Mac Version 6.

Comparative structure and model construction—*C. elegans* OCT-1 (F52F12.1) and OCT-2 (ZK455.8) putative protein sequences were first obtained from the Wormbase. OCT-1 and OCT-2 were modeled using I-TASSER (Iterative Threading ASSEmbly Refinement) [31] which utilized the best 10 threading template structures from distinct species from the PDB database (Table S1a, b). We relied on the top 5 threading templates ranked by their identity and Z-score, where a Z-score higher than 1 signified a correct alignment. The final models of

OCT-1 and OCT-2 were assessed based on the X-ray diffraction structural analogs of the glucose transporter GLUT3 (PDB ID: 5c65) from *Homo sapiens* (Table S2a, b). The models took into account the following (i) the C-score criteria, a confidence score for estimating the quality of predicted models and TM-score criteria, a metric measurement of the structural similarity between two protein models from I-TASSER [52], (ii) the TM-score from ModRefiner [53] and (iii) the Z-DOPE from Modeller, an atomic distance-dependent statistical calculation from samples of native protein structures that does not depend on any adjustable criteria [54]. These final predicted structures were also assessed based on primary sequence alignment and evolutionary conservation profiles using the PROMALS3D multiple sequence and structure alignment server [55]. Finally, for the predictions of the transmembrane domains, the ResQ B-factor profile provided a consensus prediction where the secondary structure helices (SS) are depicted as red tubes [56] (Figure S8A, B), and corroborated with the Orientation of Protein in Membranes (OPM) server [57], the Dense Alignment Surface (DAS) method [58] and the Open-source tool for visualization of proteoforms (PROTTER) [59].

Ligand-protein docking—The ligand chemical structures for doxorubicin (ID: 31703) and diclofenac (ID: 3033) were obtained from the PubChem database[60]. Ligand-protein docking were performed through the BSP-SLIM (Binding Site Prediction with Shape-based Ligand Matching with binding pocket) and COACH algorithms [33,34], featured in the I-TASSER unified platform, to predict the residues constituting the ligand–protein docking sites and conformations of OCT-1 and OCT-2 with doxorubicin and diclofenac.

Structure visualization—OCT-1 and OCT-2 three-dimensional structures and protein-ligand interacting structures were visualized using the OpenGL PyMOL Molecular Graphics System, Mac Version 1.7.4 Schrödinger, LLC.

In vivo validation of the predicted ligand-protein docking models—The ligand-protein docking was performed utilizing the BSP-SLIM server and validated following the same strategy as described in the drug treatment and DNA damage response assay and germ cells imaging sections. Synchronized L1-staged worms were exposed to the following compounds dissolved in DMSO; the RAD-51 inhibitor B02 (5 μM) (ID: 5738263) (EMD Millipore Cat.

Nº553525), Camptothecin (75 µM) (ID: 24360) (Sigma Cat. Nº C9911), Cycloheximide (50 µM) (ID: 6197) (Sigma Cat. Nº C7698), Ketamine (ID: 3821) (predicted virtually), Melphalan (ID: 460612) (predicted virtually), and these additional compounds dissolved in water; Metformin (75 µM) (ID: 4091), Methotrexate (50 µM) (ID: 126941), Methoxyamine (10 µM) (ID: 4113) (Santa Cruz Biotechnology Cat. Nº SC257710), Methyl methane sulfonate (0.25 µM) (ID: 5156) (Sigma Cat, Nº 129925), Nicotinamide (100 µM) (ID: 936) (Sigma Cat. Nº N3376), 4-Nitroquinoline N-oxide (75 µM) (ID: 5955) (ICN Biomedicals Cat. Nº 15596), Olaparib (ID: 23725625) (predicted virtually), Paraquat (100 µM) (ID: 15939) (Sigma Cat. Nº 856177), Phenformin (75 µM) (Sigma Cat. Nº P7045), Puromycin (100 µM) (ID: 439530) (Sigma Cat. Nº P9620), Zeocin (25 µM) (ID: 71668282) (Santa Cruz Biotechnology Cat. Nº SC496345), and analyzed at the young adult stage. Methotrexate and Metformin were obtained from our oncology pharmacy department (Maisonneuve-Rosemont Hospital (HMR). A concentration of 0.2 % DMSO was used for control plates. All drug-treated plates were made fresh and seeded with bacteria 12 hours prior to each experiment.

Brood size quantification to validate the effects of the RAD-51 inhibitor, B02—Single L1-staged worm from wild type and mutant genotypes were transferred to seeded NGM plates without and with B02 and maintained at 20 °C. Animals were transferred to fresh plates each day until they stopped laying eggs. The hatched larvae on each plate were counted and total number of viable larvae that developed to the L1 stage descended from a single hermaphrodite was counted. The average number of viable larvae from 10 to 25 animals of a strain was plotted as brood size where the progeny is allowed to reach adulthood and scored as being fertile or sterile. The brood size of doxorubicin-treated animals was performed similarly where unhatched and hatched progeny was plotted as the total brood size. Statistical differences were calculated by unpaired two-tail t-test (*P<0.03; **P<0.01; ***P< 0.0005; N.S. = Non Significant) and represented as ± S.D using GraphPad Prism Statistical Software.

Fluoroskan analysis—Synchronized L1-staged nematodes were exposed to doxorubicin (100 µM) as described above. L4 ~ young adult-staged nematodes were washed at least two times with M9 buffer prior to quantification. A total of 50 worms were placed into each well in duplicate in a 96 format black-well plate with optical bottom (Fisher Scientific). Doxorubicin uptake was measured with a microplate fluorometer (Fluoroskan Ascent, Thermo Scientific, USA) utilizing λ^{ex}544 nm - λ^{em}590 nm filters. Fluorescein 1 μM was used as an internal control for all genotypes. Student T-test was calculated and represented as ± S.D $***P<0.001$ statistical significance and N.S. = Non Significant.

2.6. Figure legends

Figure 1. Upregulation of *oct-2* gene expression shortens the lifespan and increases the sensitivity of *C. elegans* towards doxorubicin. **A**, Scheme of the experimental design and the readouts analyses under different conditions. **B**, Lifespan analysis of the indicated genotypes. L1-staged animals (*n* = 100) were fed the control and the indicated RNAi under normal growth conditions and lifespan was blindly assessed starting from young adult animals. The mean lifespan of two independent experiments is depicted. **C**, The relative gene expression of the *oct-1* and *oct-2* transcripts in the wild type and the *oct-1(ok1051)* deletion mutant animals was measured and corrected on actin as an internal control. Synchronized young adult animals were collected and mRNA levels were assessed by qRT-PCR. Data shown represent the average ± s.d. and student T-test $*P<0.05$ from a 60 x 15 mm petri dish of animals (*n* ~ 1000) pooled from two independent experiments. **D**, Representative images of the oxidative stress-inducible GST-4::GFP reporter and DIC (higher right) of the indicated genotypes. All images were maximum projections of the whole *dvsI19* strain, but cropped from the pharynx to the primary section of the intestine for representation. **E**, Increased GFP intensity depicting uptake of prooxidants. The GST-4::GFP activation was measured with Fluoroskan Ascent Microplate reader set at λ^{ex}544 nm - λ^{em}590 nm. The mean fluorescence intensity (MFI) is represented as percentage corrected on wild type. **F**, Brood size analysis of the indicated animals under standard conditions (no treatment) and upon exposure to 100 μM doxorubicin. The data are mean±S.D. No treatment: Wild type = 369.5±27 (*n* = 17), *oct-1(ok1051)* = 280±29 (*n* = 23), *oct-2(RNAi)* = 335.5±20.5 (*n* = 20), *oct-1(ok1051); oct-2(RNAi)* = 360.5±14.8 (*n* = 21). Doxorubicin treatment (100 μM): Wild type = 170±29.1 (*n* = 24), *oct-1(ok1051)* = 58±29.2 (*n* = 19), *oct-2(RNAi)* = 220.5±47 (*n* = 21), *oct-1(ok1051); oct-2(RNAi)* = 283±23.1 (*n* = 27). Error bars represent the S.D. Unpaired two-tail t-test $*P<0.03$;

**P<0.01; ***P< 0.0005 were considered to be statistically significant. N.S. = Non Significant.

Figure 2. Doxorubicin transport into the pharynx is stimulated by *oct-2* upregulation and efficiently competed by choline. **A**, Model suggesting OCT-2 localization at the terminal bulb of the pharynx, the fluorescence (red dots) where the drug is detected, i.e., the posterior side of the pharynx and the initial part of the intestine (as imaged in **F**), and **t**he region of germ cells analysed for apoptotic corpses in the gonad (see below). **B**, DIC (upper left) and fluorescence image of *dpy-5(e907); sEx12154* [OCT-1::GFP] genotype depicting OCT-1 localization in the pharynx (arrows in **B**). Enlargement of the pharynx is represented by a scale bar = 7 µm. **C**, Relative gene expression of *oct-1* and *oct-2* transcripts measured in severed heads (*n* = 300) collected from wild type and *oct-1(ok1051)* animals and corrected to actin and *pmp-3*. **D**, Representative 'fire' look-up images of the pharynx from untreated (control) and doxorubicin treated animals. The respective DIC images are shown in the upper left corner of each panel. Images to the right of each pharynx depict a 3D representation of the doxorubicin (100 µM) treatment signal intensity for the indicated genotypes. Data is representative of experiments performed in duplicates (*n* = 20). Enlargement of the pharynx is represented by a scale bar = 10 µm. Fluorescence posterior to the pharynx is autofluorescence detected from the intestine. **E**, Quantification of doxorubicin uptake using a Fluoroskan plate reader. The mean fluorescence intensity (MFI) is represented as percentage corrected to wild type. White bars denote untreated animals where similar autofluorescence was detected in all genotypes. **F**, *oct-2(RNAi)* diminishes the concentration-dependent uptake of doxorubicin (DOX) and not fluorescein (Fl) into the pharynx of *oct-1(ok1051)* mutant animals. **G**, Comparison of doxorubicin uptake in the absence and presence of equimolar amounts of choline. Box and whisker plots represent duplicates (*n* = 10) of signal intensity measured from both compounds in the pharynx. Data is represented as ± S.D Student T-test ± S.D Student T-test *P<0.05; **P<0.01; ***P<0.001; ****P<0.0001 and N.S. = Non Significant.

Figure 3. OCT-2-mediated transport of genotoxic compounds induce apoptotic cell death of meiotic germ cells in *C. elegans*. **A**, Representative images of acridine orange-

stained and DIC (lower left) of control and doxorubicin-induced apoptotic cell corpses from the indicated genotypes. Apoptotic cell corpses were identified as bright spots correlating with raised-bottom-like refractive corpses shown on DIC images. Posterior is right and dorsal is top. Scale bar = 15 µm. **B**, Relative gene expression of *oct-1* and *oct-2* transcripts measured in dissected gonads (*n* = 100) collected from wild type and *oct-2(ok1051)* animals and corrected to actin and *pmp-3* (see experimental procedures). **C**, Representative images of control and doxorubicin-induced *bcls39* [CED-1::GFP] clusters around apoptotic cell corpses indicated by white arrows. Data showing that OCT-2 mediated transport of compounds signal the apoptotic pathway in germ cells. Scale bar = 10 µm. **D**, Box and whisker plots depicting quantification of apoptotic cell corpses from untreated and doxorubicin treated worms and showing maximum, minimum, upper & lower quartiles, and sample median. Statistical significance bars represent results of Mann-Whitney U-test of mean difference (*P<0.05; **P<0.01; ***P<0.001 and ****P<0.0001) computed from three independent experiments (*n* = 30). L1-stage animals were treated with doxorubicin (100 µM), and apoptotic cell corpses were analysed in young adult staged animals. Control is depicted as white and doxorubicin as red boxes. **E**, Quantification of *bcls39* engulfment of apoptotic cell corpses in the indicated genotypes without and with doxorubicin treatment. The results are presented as shown in (D). **F**, Box and whisker plots depicting quantification of apoptotic cell corpses from untreated and cisplatin treated worms and quantified as in (D).

Figure 4. Structural modelling and protein-ligand docking of *C. elegans* OCT-1 and OCT-2. **A and B**, Structural models of OCT-1 and OCT-2 were generated on the basis of GLUT3 (PDB ID: 5c65) structure and sequence conservation. N-terminal and C-terminal are coloured blue and red, respectively. **C and D**, Predicted binding models of OCT-1 and OCT-2 with cationic and anionic ligands doxorubicin (pink) and diclofenac (purple), respectively. Residues making polar contacts with the ligands are depicted with sticks and represented with dotted red lines; oxygen atoms are coloured in red, nitrogen atoms in blue and carbon atoms in white. All representative figures were rendered with PyMol.

Figure 5. The B02 inhibitor of RAD-51 mimics the *rad-51/rad-51* homozygotes phenotypes when *oct-2* is upregulated. **A and B**, Depiction of the ligand-protein docking of OCT-1 and OCT-2 modelled with B02 and showing exclusive binding of the drug to OCT-2. **C**, DIC image showing that B02 causes embryonic lethality (diminishing number of germ cells) in the *oct-1(ok1051)* mutant. **D**, DIC image showing that *oct-2* downregulation in the *oct-1(ok1051)* mutant animals restores fertility. In C and D, Scale bar = 35 µm. **E**, B02 diminishes the number of viable animals when *oct-2* is expressed. Brood size analysis of wild type, *oct-1(ok1051)* and *oct-1(ok1051); oct-2(RNAi)* and *rad-51(ok2218)/nT1* animals under standard conditions (no treatment) and upon exposure to 5 µM B02. Data are mean±S.D. No treatment: Wild type = 366±26.7 (*n* = 20), *oct-1(ok1051)* = 296±7.1 (*n* = 29), *oct-2(RNAi)* = 307±11.3 (*n* = 23), *oct-1(ok1051); oct-2(RNAi)* = 321±19.7 (*n* = 25), *rad-51(ok2218)/nT1* = 35±5.6 (*n* = 9). B02 treatment (5 µM): Wild type = 158±29.7 (*n* = 21), *oct-1(ok1051)* = 32±7.0 (*n* = 17), *oct-2(RNAi)* = 196±26.8 (*n* = 25), *oct-1(ok1051); oct-2(RNAi)* = 272±7.1 (*n* = 25), *rad-51(ok2218)/nT1* = 30±4.2 (*n* = 10). Error bars represent the S.D. Unpaired two-tail t-test *P<0.03; **P<0.01; ***P< 0.0005 were considered to be statistically significant. N.S. = Non Significant. **F,** The RAD-51 inhibitor, B02, mode of action in *C. elegans* germline.

2.7. References

1. O'Reilly, L.P., Luke, C.J., Perlmutter, D.H., Silverman, G.A. & Pak, S.C. C. elegans in high-throughput drug discovery. *Adv Drug Deliv Rev* **69-70**, 247-53 (2014).
2. Cheah, I.K. *et al.* Knockout of a putative ergothioneine transporter in Caenorhabditis elegans decreases lifespan and increases susceptibility to oxidative damage. *Free Radic Res* **47**, 1036-45 (2013).
3. Koepsell, H. The SLC22 family with transporters of organic cations, anions and zwitterions. *Mol Aspects Med* **34**, 413-35 (2013).
4. Andreev, E., Brosseau, N., Carmona, E., Mes-Masson, A.M. & Ramotar, D. The human organic cation transporter OCT1 mediates high affinity uptake of the anticancer drug daunorubicin. *Sci Rep* **6**, 20508 (2016).
5. Wu, X. *et al.* Identity of the F52F12.1 gene product in Caenorhabditis elegans as an organic cation transporter. *Biochim Biophys Acta* **1418**, 239-44 (1999).
6. Brosseau, N., Andreev, E. & Ramotar, D. Complementation of the Yeast Model System Reveals that Caenorhabditis elegans OCT-1 Is a Functional Transporter of Anthracyclines. *PLoS One* **10**, e0133182 (2015).
7. Kaletta, T. & Hengartner, M.O. Finding function in novel targets: C. elegans as a model organism. *Nat Rev Drug Discov* **5**, 387-98 (2006).
8. Burns, A.R. *et al.* A predictive model for drug bioaccumulation and bioactivity in Caenorhabditis elegans. *Nat Chem Biol* **6**, 549-57 (2010).
9. Chen, L. *et al.* OCT1 is a high-capacity thiamine transporter that regulates hepatic steatosis and is a target of metformin. *Proc Natl Acad Sci U S A* **111**, 9983-8 (2014).
10. Lionaki, E. & Tavernarakis, N. Assessing aging and senescent decline in Caenorhabditis elegans: cohort survival analysis. *Methods Mol Biol* **965**, 473-84 (2013).
11. McKay, S.J. *et al.* Gene expression profiling of cells, tissues, and developmental stages of the nematode C. elegans. *Cold Spring Harb Symp Quant Biol* **68**, 159-69 (2003).
12. Fishel, M.L. *et al.* Apurinic/apyrimidinic endonuclease/redox factor-1 (APE1/Ref-1) redox function negatively regulates NRF2. *J Biol Chem* **290**, 3057-68 (2015).
13. Cabreiro, F. *et al.* Metformin retards aging in C. elegans by altering microbial folate and methionine metabolism. *Cell* **153**, 228-39 (2013).

14. Sendoel, A. *et al.* DEPDC1/LET-99 participates in an evolutionarily conserved pathway for anti-tubulin drug-induced apoptosis. *Nat Cell Biol* **16**, 812-20 (2014).
15. Hall, D. & Altun, Z. *C. elegans Atlas*, (Cold Spring Harbor Laboratory Press, 2008).
16. McKay, J.P., Raizen, D.M., Gottschalk, A., Schafer, W.R. & Avery, L. eat-2 and eat-18 are required for nicotinic neurotransmission in the Caenorhabditis elegans pharynx. *Genetics* **166**, 161-9 (2004).
17. Hoffmann, K., Grafe, F., Wohlrab, W., Neubert, R.H. & Brandsch, M. Functional characterization of a high-affinity choline transport system in human keratinocytes. *J Invest Dermatol* **119**, 118-21 (2002).
18. Gartner, A., Boag, P.R. & Blackwell, T.K. Germline survival and apoptosis. *WormBook*, 1-20 (2008).
19. Lans, H. & Vermeulen, W. Tissue specific response to DNA damage: C. elegans as role model. *DNA Repair (Amst)* **32**, 141-8 (2015).
20. Horvitz, H.R. Genetic control of programmed cell death in the nematode Caenorhabditis elegans. *Cancer Res* **59**, 1701s-1706s (1999).
21. Craig, A.L., Moser, S.C., Bailly, A.P. & Gartner, A. Methods for studying the DNA damage response in the Caenorhabdatis elegans germ line. *Methods Cell Biol* **107**, 321-52 (2012).
22. Gumienny, T.L., Lambie, E., Hartwieg, E., Horvitz, H.R. & Hengartner, M.O. Genetic control of programmed cell death in the Caenorhabditis elegans hermaphrodite germline. *Development* **126**, 1011-22 (1999).
23. Savill, J. & Fadok, V. Corpse clearance defines the meaning of cell death. *Nature* **407**, 784-8 (2000).
24. Zhou, Z., Hartwieg, E. & Horvitz, H.R. CED-1 is a transmembrane receptor that mediates cell corpse engulfment in C. elegans. *Cell* **104**, 43-56 (2001).
25. Li, Z., Lu, N., He, X. & Zhou, Z. Monitoring the clearance of apoptotic and necrotic cells in the nematode Caenorhabditis elegans. *Methods Mol Biol* **1004**, 183-202 (2013).
26. Lin, L., Yee, S.W., Kim, R.B. & Giacomini, K.M. SLC transporters as therapeutic targets: emerging opportunities. *Nat Rev Drug Discov* **14**, 543-60 (2015).
27. Rinaldo, C., Bazzicalupo, P., Ederle, S., Hilliard, M. & La Volpe, A. Roles for Caenorhabditis elegans rad-51 in meiosis and in resistance to ionizing radiation during

development. *Genetics* **160**, 471-9 (2002).

28. Yang, X. *et al.* Functional characterization of the Caenorhabditis elegans DNA repair enzyme APN-1. *DNA Repair (Amst)* **11**, 811-22 (2012).
29. Minotti, G., Menna, P., Salvatorelli, E., Cairo, G. & Gianni, L. Anthracyclines: molecular advances and pharmacologic developments in antitumor activity and cardiotoxicity. *Pharmacol Rev* **56**, 185-229 (2004).
30. Wang, D. & Lippard, S.J. Cellular processing of platinum anticancer drugs. *Nat Rev Drug Discov* **4**, 307-20 (2005).
31. Roy, A., Kucukural, A. & Zhang, Y. I-TASSER: a unified platform for automated protein structure and function prediction. *Nat Protoc* **5**, 725-38 (2010).
32. Sun, L. *et al.* Crystal structure of a bacterial homologue of glucose transporters GLUT1-4. *Nature* **490**, 361-6 (2012).
33. Lee, H.S. & Zhang, Y. BSP-SLIM: a blind low-resolution ligand-protein docking approach using predicted protein structures. *Proteins* **80**, 93-110 (2012).
34. Yang, J., Roy, A. & Zhang, Y. Protein-ligand binding site recognition using complementary binding-specific substructure comparison and sequence profile alignment. *Bioinformatics* **29**, 2588-95 (2013).
35. Huang, F. & Mazin, A.V. A small molecule inhibitor of human RAD51 potentiates breast cancer cell killing by therapeutic agents in mouse xenografts. *PLoS One* **9**, e100993 (2014).
36. Huang, F. & Mazin, A.V. Targeting the homologous recombination pathway by small molecule modulators. *Bioorg Med Chem Lett* **24**, 3006-13 (2014).
37. Alagpulinsa, D.A., Ayyadevara, S. & Shmookler Reis, R.J. A Small-Molecule Inhibitor of RAD51 Reduces Homologous Recombination and Sensitizes Multiple Myeloma Cells to Doxorubicin. *Front Oncol* **4**, 289 (2014).
38. Alpi, A., Pasierbek, P., Gartner, A. & Loidl, J. Genetic and cytological characterization of the recombination protein RAD-51 in Caenorhabditis elegans. *Chromosoma* **112**, 6-16 (2003).
39. Aouida, M., Rubio-Texeira, M., Thevelein, J.M., Poulin, R. & Ramotar, D. Agp2, a member of the yeast amino acid permease family, positively regulates polyamine transport at the transcriptional level. *PLoS One* **8**, e65717 (2013).

40. Popova, Y., Thayumanavan, P., Lonati, E., Agrochao, M. & Thevelein, J.M. Transport and signaling through the phosphate-binding site of the yeast Pho84 phosphate transceptor. *Proc Natl Acad Sci U S A* **107**, 2890-5 (2010).
41. Schothorst, J. *et al.* Yeast nutrient transceptors provide novel insight in the functionality of membrane transporters. *Curr Genet* **59**, 197-206 (2013).
42. Gaber, R.F., Ottow, K., Andersen, H.A. & Kielland-Brandt, M.C. Constitutive and hyperresponsive signaling by mutant forms of Saccharomyces cerevisiae amino acid sensor Ssy1. *Eukaryot Cell* **2**, 922-9 (2003).
43. Didion, T., Regenberg, B., Jorgensen, M.U., Kielland-Brandt, M.C. & Andersen, H.A. The permease homologue Ssy1p controls the expression of amino acid and peptide transporter genes in Saccharomyces cerevisiae. *Mol Microbiol* **27**, 643-50 (1998).
44. Ljungdahl, P.O. Amino-acid-induced signalling via the SPS-sensing pathway in yeast. *Biochem Soc Trans* **37**, 242-7 (2009).
45. Bianchi, L. & Diez-Sampedro, A. A single amino acid change converts the sugar sensor SGLT3 into a sugar transporter. *PLoS One* **5**, e10241 (2010).
46. Shu, Y. *et al.* Evolutionary conservation predicts function of variants of the human organic cation transporter, OCT1. *Proc Natl Acad Sci U S A* **100**, 5902-7 (2003).
47. Zhang, S. *et al.* Organic cation transporters are determinants of oxaliplatin cytotoxicity. *Cancer Res* **66**, 8847-57 (2006).
48. Schneider, C.A., Rasband, W.S. & Eliceiri, K.W. NIH Image to ImageJ: 25 years of image analysis. *Nat Methods* **9**, 671-5 (2012).
49. McCloy, R.A. *et al.* Partial inhibition of Cdk1 in G 2 phase overrides the SAC and decouples mitotic events. *Cell Cycle* **13**, 1400-12 (2014).
50. Kamath, R.S. & Ahringer, J. Genome-wide RNAi screening in Caenorhabditis elegans. *Methods* **30**, 313-21 (2003).
51. Yang, J.S. *et al.* OASIS: online application for the survival analysis of lifespan assays performed in aging research. *PLoS One* **6**, e23525 (2011).
52. Zhang, Y. & Skolnick, J. Scoring function for automated assessment of protein structure template quality. *Proteins* **57**, 702-10 (2004).
53. Xu, D. & Zhang, Y. Improving the physical realism and structural accuracy of protein models by a two-step atomic-level energy minimization. *Biophys J* **101**, 2525-34 (2011).

54. Colubri, A. *et al.* Minimalist representations and the importance of nearest neighbor effects in protein folding simulations. *J Mol Biol* **363**, 835-57 (2006).
55. Pei, J. & Grishin, N.V. PROMALS3D: multiple protein sequence alignment enhanced with evolutionary and three-dimensional structural information. *Methods Mol Biol* **1079**, 263-71 (2014).
56. Yang, J., Wang, Y. & Zhang, Y. ResQ: An Approach to Unified Estimation of B-Factor and Residue-Specific Error in Protein Structure Prediction. *J Mol Biol* (2015).
57. Lomize, M.A., Pogozheva, I.D., Joo, H., Mosberg, H.I. & Lomize, A.L. OPM database and PPM web server: resources for positioning of proteins in membranes. *Nucleic Acids Res* **40**, D370-6 (2012).
58. von Heijne, G. Membrane protein structure prediction. Hydrophobicity analysis and the positive-inside rule. *J Mol Biol* **225**, 487-94 (1992).
59. Omasits, U., Ahrens, C.H., Muller, S. & Wollscheid, B. Protter: interactive protein feature visualization and integration with experimental proteomic data. *Bioinformatics* **30**, 884-6 (2014).
60. Kim, S. *et al.* PubChem Substance and Compound databases. *Nucleic Acids Res* (2015).

2.8. Figures

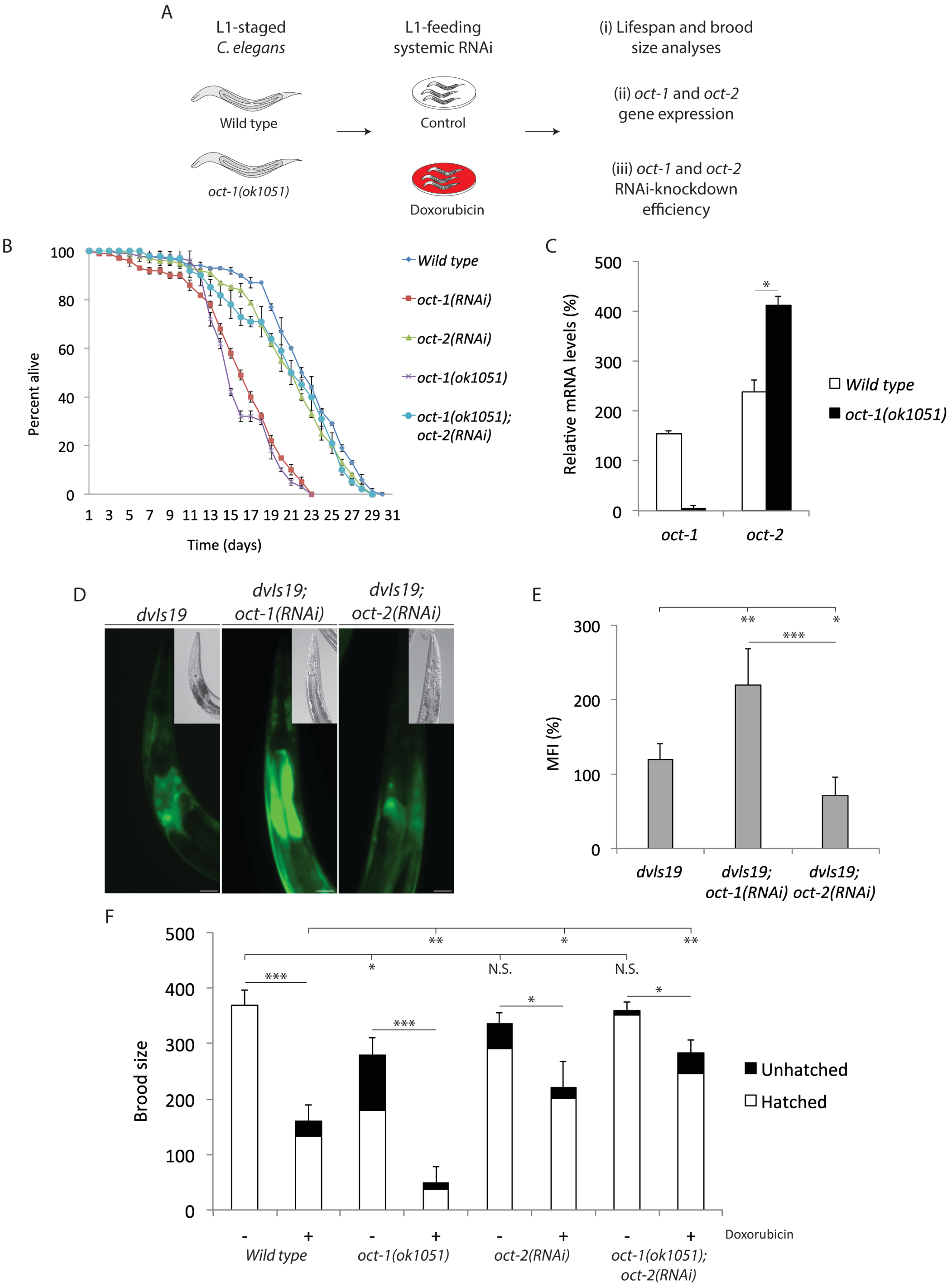

Figure 1. Upregulation of *oct-2* gene expression shortens the lifespan and increases the sensitivity of *C. elegans* towards doxorubicin.

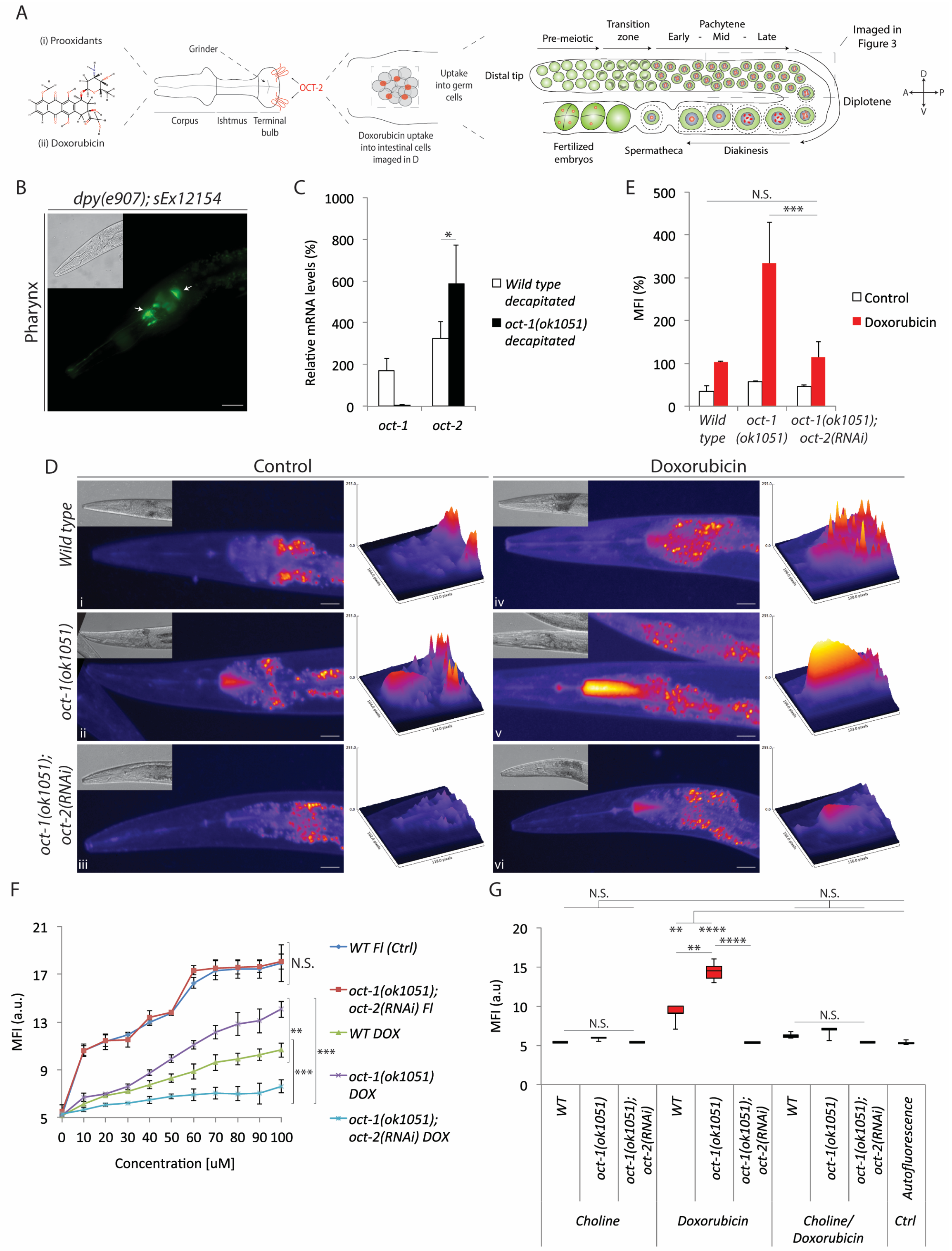

Figure 2. Doxorubicin transport into the pharynx is stimulated by *oct-2* upregulation and efficiently competed by choline.

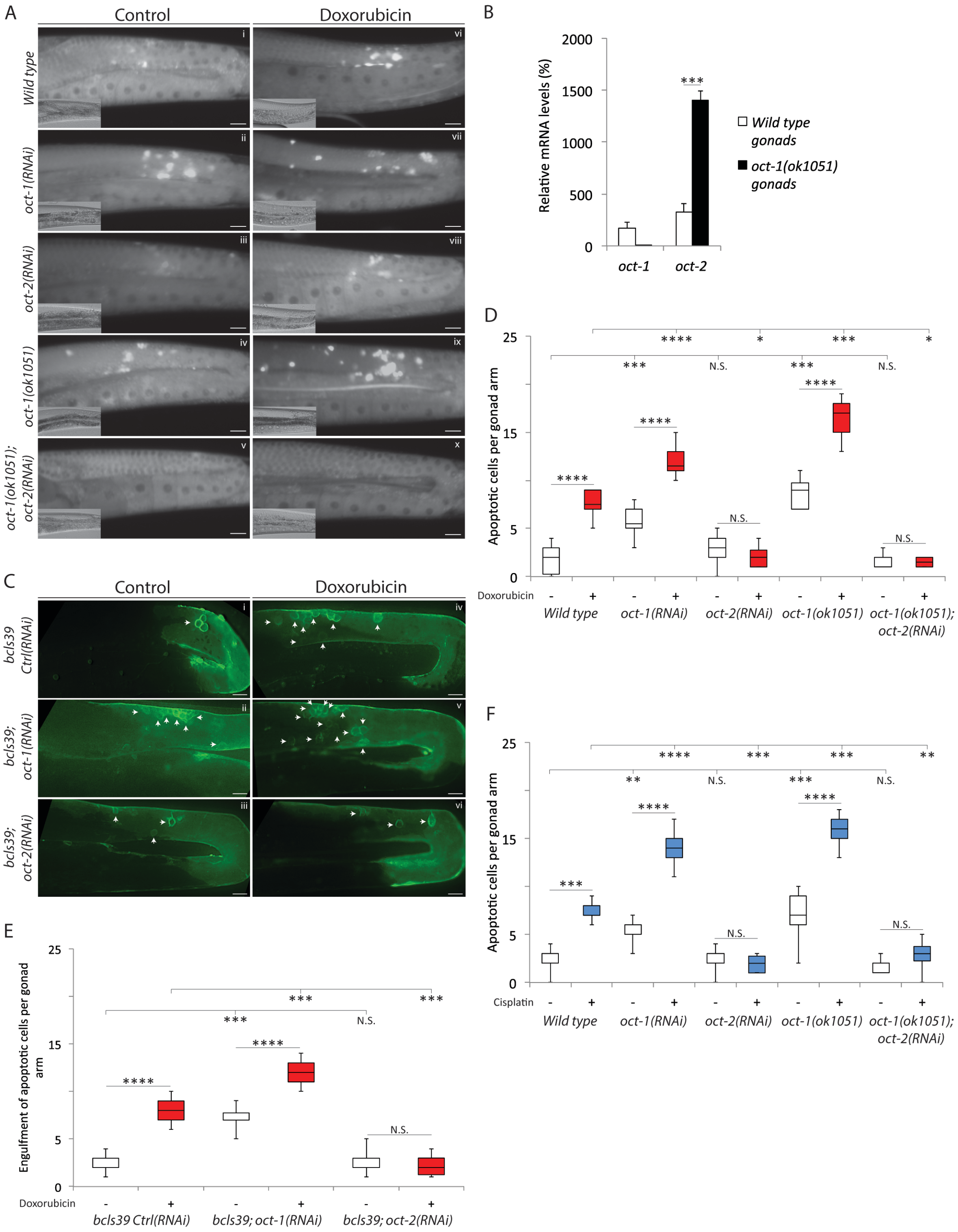

Figure 3. OCT-2-mediated transport of genotoxic compounds induce apoptotic cell death of meiotic germ cells in *C. elegans*.

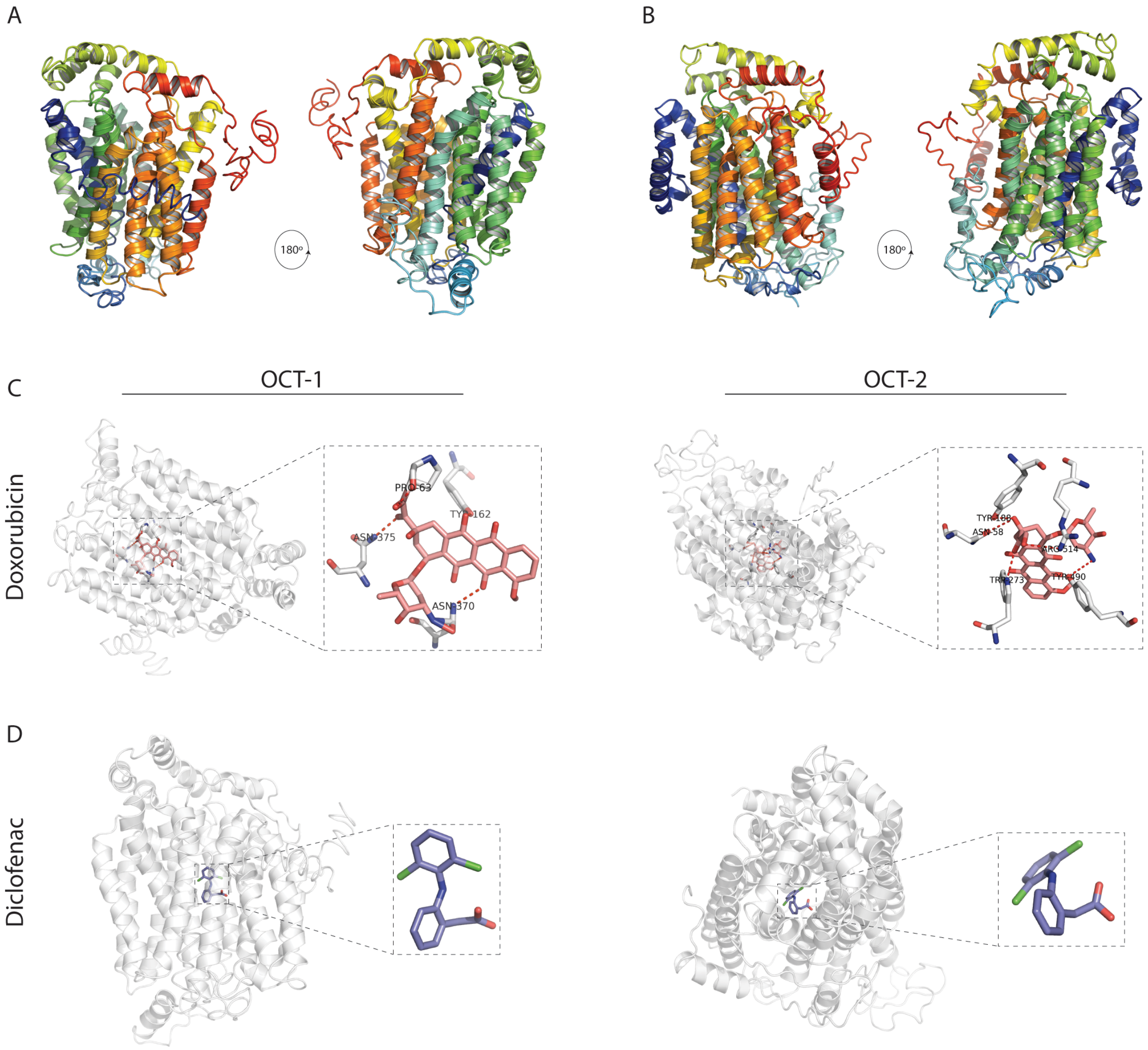

Figure 4. Structural modelling and protein-ligand docking of *C. elegans* OCT-1 and OCT-2.

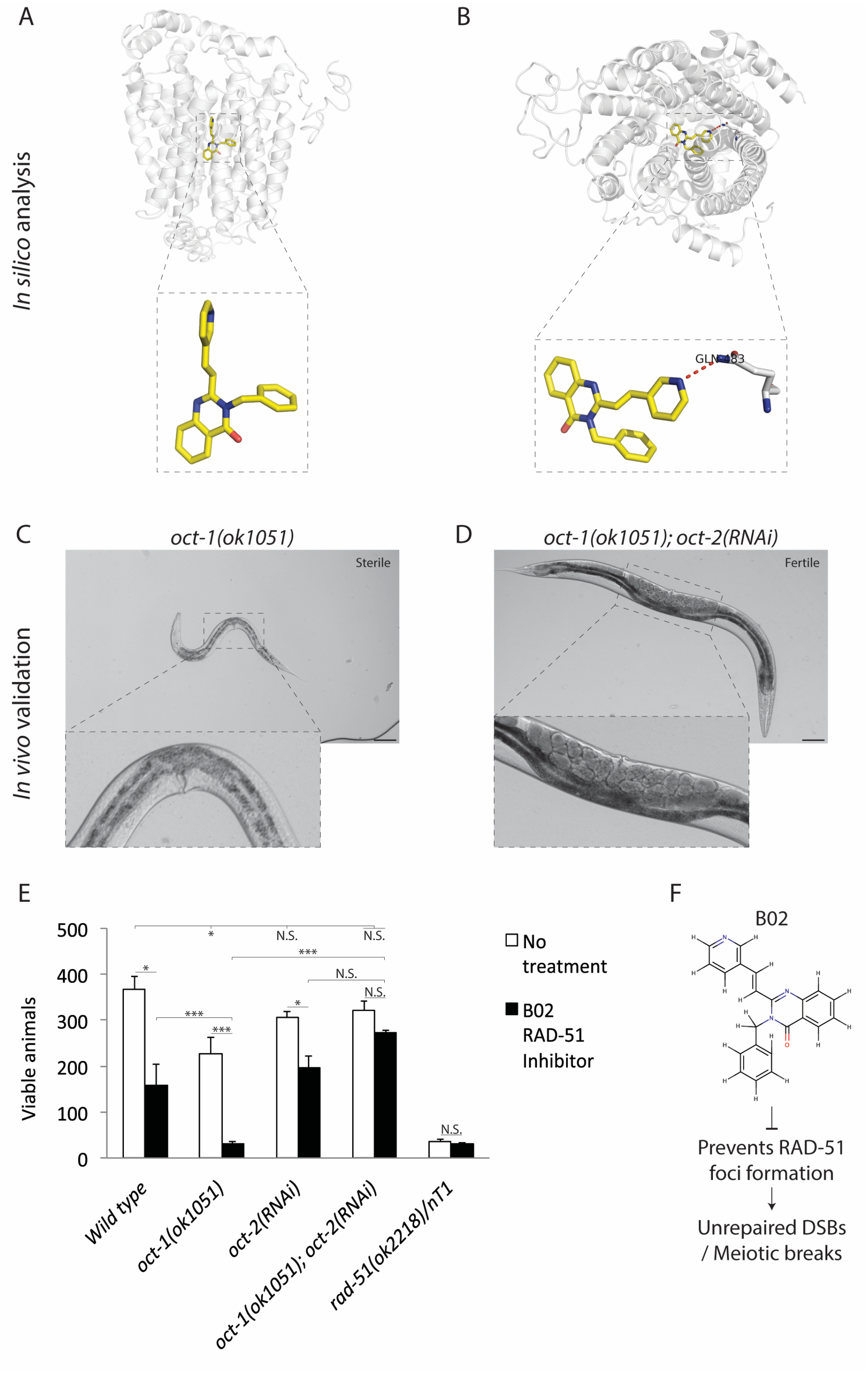

Figure 5. The B02 inhibitor of RAD-51 mimics the *rad-51/rad-51* homozygotes phenotypes when *oct-2* is upregulated.

Table 1. *In vivo* validation of ligand-protein docking analysis.

Ligand		Docking Score		DNA Repair Pathways / Apoptotic cells counts			
		OCT-1	OCT-2	HR - *rad-51(ok2218); oct-1(RNAi)*	BER - *apn-1(tm6691); oct-1(RNAi)*	NER - *xpa-1(ok698); oct-1(RNAi)*	MMR - *msh-2(ok2410); oct-1(RNAi)*
B02 ‘α’	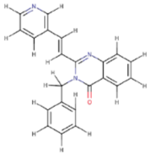	0.0	4.5	>20	>20	15-20	15-20
Camptothecin	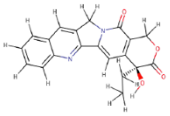	3.2	3.4	15-20	15-20	<5	<5
Cisplatin	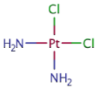 $H_2N-\overset{Cl}{\underset{NH_2}{Pt}}-Cl$	3.4	4.5	5-10	5-10	15-20	15-20
Cycloheximide	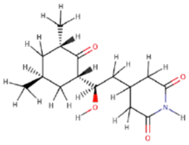	6.5	7.7	15-20	<5	<5	<5
Diclofenac ‘Φ’	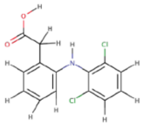	0.0	0.0	N.D	N.D	N.D	N.D
Doxorubicin	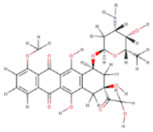	3.8	4.0	>20	15-20	<5	<5
Ketamine ‘Φ’	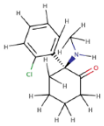	4.6	7.6	N.D	N.D	N.D	N.D
Melphalan ‘Ω’	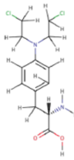	0.0	0.0	<5	15-20	<5	<5
Metformin	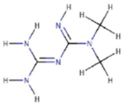	0.0	3.6	N.D	N.D	N.D	N.D
Methotrexate	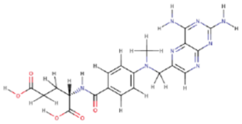	5.1	7.3	<5	15-20	<5	15-20

Methoxyamine ‘Ω’	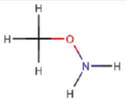	0.0	0.0	<5	>20	<5	<5
Methyl metanesulfonate ‘Ω’	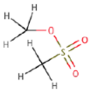	0.0	0.0	>20	15-20	5-10	<5
Nicotinamide	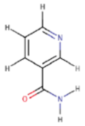	0.0	5.5	<5	>20	15-20	5-10
4-Nitroquinoline N-oxide	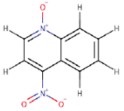	2.3	4.2	<5	<5	15-20	<5
Olaparib ‘Φ’	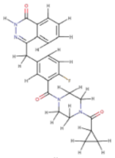	5.4	6.1	N.D	N.D	N.D	N.D
Paraquat	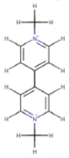	3.1	3.4	<5	>20	<5	<5
Phenformin	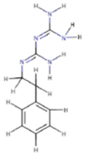	7.7	7.2	<5	<5	<5	<5
Puromycin	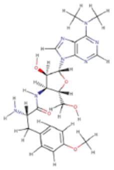	5.3	7.0	<5	15-20	<5	<5
Zeocin	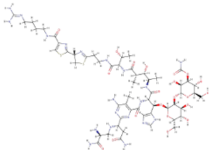	8.5	6.1	>20	<5	<5	<5

See Table S6 for detailed mechanism of action of each drug used in this assay.
Ligand-protein docking scores: > 3; binder | 0; non-binder
An average of 2 – 5 apoptotic cells were counted in not treated wild type and *“mutant”; oct-2(RNAi)* animals. After exposure to the drugs, wild type animals depicted an average of 7 – 12 apoptotic cells, whereas *“mutant”; oct-2(RNAi)* animals were comparable to the not treated animals.
‘α’ Wild type animals treated with 5 µM B02 RAD51 inhibitor, signal similar apoptosis-induced response as the drug-induced *rad-51(ok1051)* deletion mutant. B02 caused the animals to become sterile and/or animals that lay eggs that do not hatch as the *rad-51* homozygous sterile deletion (Rinaldo *et al.* 2002) (Figure 5c)
‘Φ’ Predicted virtually
‘Ω’ Uptake by a different transporter
‘N.D’ Not Determined
Chemical structures were rendered utilizing MarvinView 16.1.18 (ChemAxon)

2.9. Supplementary information

Legends for Supplemental Figures

Figure S1. Sequence alignment of members belonging to the family of organic cation transporters from *C. elegans* (CeOCT-1 and CeOCT-2), *Homo sapiens* (hOCT1 and hOCT2) and *Mus musculus* (mOCT1 and mOCT2). Numbers indicate amino acid positions. Identical or similar amino acid residues amongst the members are shaded in black or gray, respectively. Dashes indicate gaps. The stretch of amino acid residues, PESPRW (consensus in red), is the longest identical region in all six transporters. CeOCT-2 contains the four conserved cysteine residues Cys203, 250, 280 and 302 present in the N-terminus of each member. The OCT2 from the different species lack the conserved cysteine Cys49, Cys27, and Cys27 present in the OCT1 members CeOCT-1, hOCT1 and mOCT1, respectively.

Figure S2. Relative gene expression. (A) *oct-1* and *oct-2* gene expression are downregulated by the *oct-1(RNAi)* and *oct-2(RNAi)*, respectively. (B) *pes-23* gene expression is not affected by either *oct-1(RNAi)* and *oct-2(RNAi).* The RNA expression was measured as described in the experimental procedures.

Figure S3. *oct-1* and *oct-2* gene expression data measured (A) across all developmental stages and (B) hermaphrodite soma and hermaphrodite gonads. The *oct-1* (WBGene00003842) and *oct-2* (WBGene00003843) RNA expression data was extracted from the Wormbase/SPELL database.

Figure S4. OCT-2-dependent doxorubicin uptake into the pharynx of *C. elegans* is not affected by the eating defective *eat-2(ad453)* mutant animals. Experiment is represented by ‘fire’ look-up images of the pharynx from eating defective *eat-2(ad453)* untreated and doxorubicin treated animals. The respective DIC images are shown in the upper left corner of each panel. Images to the right of each pharynx depict a 3D representation of the doxorubicin (100 μM) treatment signal intensity for the indicated genotypes. Data are representative of experiments performed in duplicates (n = 15). Enlargement of the pharynx is represented by a scale bar = 10 µm. Fluorescence posterior to the pharynx is auto-fluorescence detected from the intestine.

Figure S5. Genetic analysis of doxorubicin- and cisplatin-induced apoptotic cell death. (A) Representative images of wild type*, *cep-1*, *egl-1*, *ced-9*, *ced-4* and *ced-3* mutant animals untreated and RNAi-driven depletion of oct-1 exposed to 100 µM doxorubicin. Apoptotic cells were observed and quantified as described in the experimental procedures. (B) Apoptotic pathway in *C. elegans* (C) Data shown represent the average quantification of three independent experiments (n =30). *Images from Figure 2 were used for comparison purposes.

Figure S6. Methyl methanesulfonate and Gamma rays (γ-rays)-induced germ cell apoptosis are independent of OCT-1 and OCT-2 function. (A and C) Box and whisker plots depict quantification of apoptotic cell corpses upon MMS (0.25 µM) and γ-rays (75 grays) treatment, respectively. (B) Representative images of right gonad arms after exposure to γ-rays. Posterior is right. The results are the averages from three independent experiments (n = 30) Mann-Whitney U-test (*P<0.05; **P<0.01; ***P<0.001; ****P<0.0001 and N.S. = Non Significant).

Figure S7. RNAi-driven downregulation of *oct-1* upregulates *oct-2* expression and sensitizes *C. elegans* DNA repair deficient mutants to drug-induced apoptotic cell death.

(A) Wild type. (B and C) The homologous recombination mutant *rad-51(ok2218)* downregulated for oct-1 shows stimulated doxorubicin-induced apoptotic cell death. (D and E) The base excision repair mutant *apn-1(tm6691)* downregulated for *oct-1* displays enhanced spontaneous, as well as doxorubicin-induced apoptotic cell death. (F and G and H and I) The nucleotide excision and mismatch repair defective mutants, *xpa-1(ok698)* and *msh-2(ok2410)*, respectively, downregulated for *oct-1* exhibit enhanced cisplatin-induced apoptotic cell death. Treatment with doxorubicin (100 µM, red boxes) and cisplatin (100 µM, blue boxes) started with L1-staged animals. Apoptotic cell corpses were analysed in young adult staged animals. Untreated animals are depicted as white boxes. The results are the averages from three independent experiments (n = 30 each). Mann-Whitney U-test of mean difference (*P<0.05; **P<0.01; ***P<0.001 and ****P<0.0001) was calculated. (J - M) RNAi-driven downregulation of *oct-1* upregulates *oct-2* in the wild type and the DNA repair defective mutants. The Y-axis represents the same scale for *oct-1* and *oct-2* gene expression in all genotypes.

Figure S8. Structural modeling prediction of (A) OCT-1 and (B) OCT-2 computed with ResQ. The predicted Normalized B-factor and estimated residues accuracy in Ångstrom were computed based on the I-TASSER models. The twelve transmembrane domains are represented as red bars at the bottom of each panel.

Figure S9. Apoptotic cell corpses as a function of cisplatin concentrations. At 25 µM of cisplatin, apoptotic cell corpses were induced in the *oct-1(ok1051)* mutant, but not in the wild type.

2.9. Supplementary figures

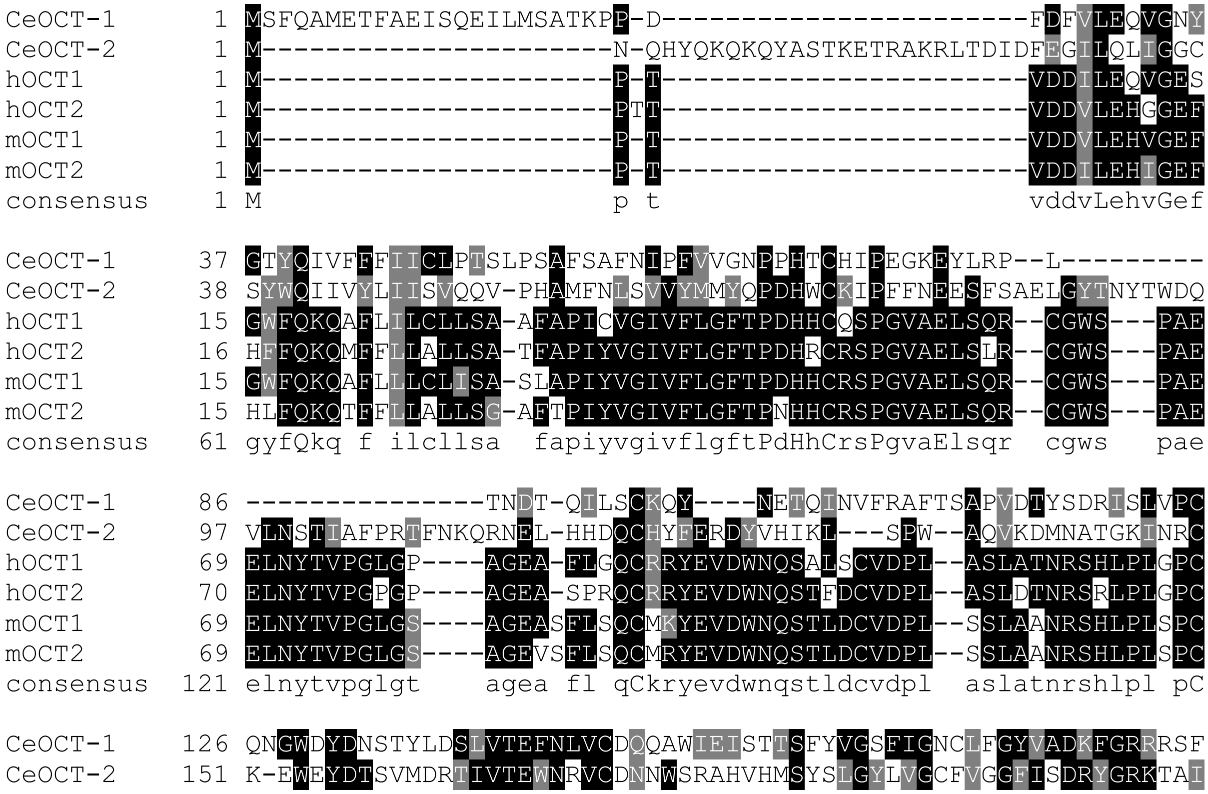

```
CeOCT-1      1 MSFQAMETFAEISQEILMSATKPP-D-----------------------FDFVLEQVGNY
CeOCT-2      1 M----------------------N-QHYQKQKQYASTKETRAKRLTDIDFEGILQLIGGC
hOCT1        1 M----------------------P-T-----------------------VDDILEQVGES
hOCT2        1 M----------------------PTT-----------------------VDDVLEHGGEF
mOCT1        1 M----------------------P-T-----------------------VDDVLEHVGEF
mOCT2        1 M----------------------P-T-----------------------VDDILEHIGEF
consensus    1 M                      p t                       vddvLehvGef

CeOCT-1     37 GTYQIVFFFIICLPTSLPSAFSAFNIPFVVGNPPHTCHIPEGKEYLRP--L---------
CeOCT-2     38 SYWQIIVYLIISVQQV-PHAMFNLSVVYMMYQPDHWCKIPFFNEESFSAELGYTNYTWDQ
hOCT1       15 GWFQKQAFLILCLLSA-AFAPICVGIVFLGFTPDHHCQSPGVAELSQR--CGWS---PAE
hOCT2       16 HFFQKQMFFLLALLSA-TFAPIYVGIVFLGFTPDHRCRSPGVAELSLR--CGWS---PAE
mOCT1       15 GWFQKQAFLLLCLISA-SLAPIYVGIVFLGFTPDHHCRSPGVAELSQR--CGWS---PAE
mOCT2       15 HLFQKQTFFLLALLSG-AFTPIYVGIVFLGFTPNHHCRSPGVAELSQR--CGWS---PAE
consensus   61 gyfQkq f ilcllsa  fapiyvgivflgftPdHhCrsPgvaElsqr  cgws   pae

CeOCT-1     86 ---------------TNDT-QILSCKQY----NETQINVFRAFTSAPVDTYSDRISLVPC
CeOCT-2     97 VLNSTIAFPRTFNKQRNEL-HHDQCHYFERDYVHIKL---SPW--AQVKDMNATGKINRC
hOCT1       69 ELNYTVPGLGP----AGEA-FLGQCRRYEVDWNQSALSCVDPL--ASLATNRSHLPLGPC
hOCT2       70 ELNYTVPGPGP----AGEA-SPRQCRRYEVDWNQSTFDCVDPL--ASLDTNRSRLPLGPC
mOCT1       69 ELNYTVPGLGS----AGEASFLSQCMKYEVDWNQSTLDCVDPL--SSLAANRSHLPLSPC
mOCT2       69 ELNYTVPGLGS----AGEVSFLSQCMRYEVDWNQSTLDCVDPL--SSLAANRSHLPLSPC
consensus  121 elnytvpglgt    agea fl qCkryevdwnqstldcvdpl  aslatnrshlpl pC

CeOCT-1    126 QNGWDYDNSTYLDSLVTEFNLVCDQQAWIEISTTSFYVGSFIGNCLFGYVADKFGRRRSF
CeOCT-2    151 K-EWEYDTSVMDRTIVTEWNRVCDNNWSRAHVHMSYSLGYLVGCFVGGFISDRYGRKTAI
```

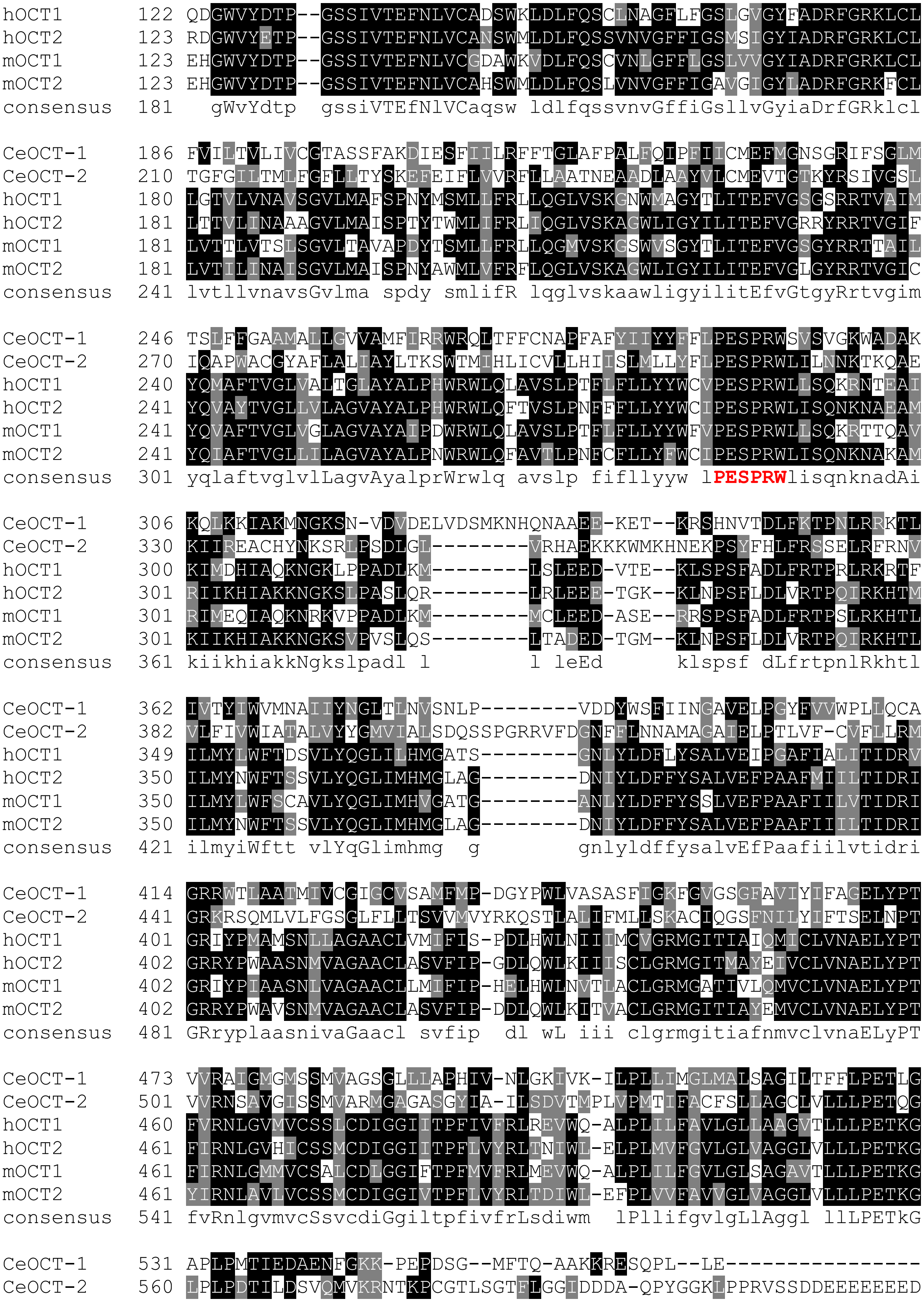

```
hOCT1      122 QDGWVYDTP--GSSIVTEFNLVCADSWKLDLFQSCLNAGFLFGSLGVGYFADRFGRKLCL
hOCT2      123 RDGWVYETP--GSSIVTEFNLVCANSWMLDLFQSSVNVGFFIGSMSIGYIADRFGRKLCL
mOCT1      123 EHGWVYDTP--GSSIVTEFNLVCGDAWKVDLFQSCVNLGFFLGSLVVGYIADRFGRKLCL
mOCT2      123 EHGWVYDTP--GSSIVTEFNLVCAHSWMLDLFQSLVNVGFFIGAVGIGYLADRFGRKFCL
consensus  181   gWvYdtp  gssiVTEfNlVCaqsw ldlfqssvnvGffiGsllvGyiaDrfGRklcl

CeOCT-1    186 FVILTVLIVCGTASSFAKDIESFIILRFFTGLAFPALFQIPFIICMEFMGNSGRIFSGLM
CeOCT-2    210 TGFGILTMLFGFLLTYSKEFEIFLVVRFLLAATNEAADLAAYVLCMEVTGTKYRSIVGSL
hOCT1      180 LGTVLVNAVSGVLMAFSPNYMSMLLFRLLQGLVSKGNWMAGYTLITEFVGSGSRRTVAIM
hOCT2      181 LTTVLINAAAGVLMAISPTYTWMLIFRLIQGLVSKAGWLIGYILITEFVGRRYRRTVGIF
mOCT1      181 LVTTLVTSLSGVLTAVAPDYTSMLLFRLLQGMVSKGSWVSGYTLITEFVGSGYRRTTAIL
mOCT2      181 LVTILINAISGVLMAISPNYAWMLVFRFLQGLVSKAGWLIGYILITEFVGLGYRRTVGIC
consensus  241 lvtllvnavsGvlma spdy smlifR lqglvskaawligyilitEfvGtgyRrtvgim

CeOCT-1    246 TSLFFGAAMALLGVVAMFIRRWRQLTFFCNAPFAFYIIYYFFLPESPRWSVSVGKWADAK
CeOCT-2    270 IQAPWACGYAFLALIAYLTKSWTMIHLICVLLHIISLMLLYFLPESPRWLILNNKTKQAE
hOCT1      240 YQMAFTVGLVALTGLAYALPHWRWLQLAVSLPTFLFLLYYWCVPESPRWLLSQKRNTEAI
hOCT2      241 YQVAYTVGLLVLAGVAYALPHWRWLQFTVSLPNFFFLLYYWCIPESPRWLISQNKNAEAM
mOCT1      241 YQVAFTVGLVGLAGVAYAIPDWRWLQLAVSLPTFLFLLYYWFVPESPRWLLSQKRTTQAV
mOCT2      241 YQIAFTVGLLILAGVAYALPNWRWLQFAVTLPNFCFLLYFWCIPESPRWLISQNKNAKAM
consensus  301 yqlaftvglvlLagvAyalprWrwlq avslp fifllyyw lPESPRWlisqnknadAi

CeOCT-1    306 KQLKKIAKMNGKSN-VDVDELVDSMKNHQNAAEE-KET--KRSHNVTDLFKTPNLRRKTL
CeOCT-2    330 KIIREACHYNKSRLPSDLGL--------VRHAEKKKWMKHNEKPSYFHLFRSSELRFRNV
hOCT1      300 KIMDHIAQKNGKLPPADLKM--------LSLEED-VTE--KLSPSFADLFRTPRLRKRTF
hOCT2      301 RIIKHIAKKNGKSLPASLQR--------LRLEEE-TGK--KLNPSFLDLVRTPQIRKHTM
mOCT1      301 RIMEQIAQKNRKVPPADLKM--------MCLEED-ASE--RRSPSFADLFRTPSLRKHTL
mOCT2      301 KIIKHIAKKNGKSVPVSLQS--------LTADED-TGM--KLNPSFLDLVRTPQIRKHTL
consensus  361 kiikhiakkNgkslpadl l        l leEd      klspsf dLfrtpnlRkhtl

CeOCT-1    362 IVTYIWVMNAIIYNGLTLNVSNLP--------VDDYWSFIINGAVELPGYFVVWPLLQCA
CeOCT-2    382 VLFIVWIATALVYYGMVIALSDQSSPGRRVFDGNFFLNNAMAGAIELPTLVF-CVFLLRM
hOCT1      349 ILMYLWFTDSVLYQGLILHMGATS--------GNLYLDFLYSALVEIPGAFIALITIDRV
hOCT2      350 ILMYNWFTSSVLYQGLIMHMGLAG--------DNIYLDFFYSALVEFPAAFMIILTIDRI
mOCT1      350 ILMYLWFSCAVLYQGLIMHVGATG--------ANLYLDFFYSSLVEFPAAFIILVTIDRI
mOCT2      350 ILMYNWFTSSVLYQGLIMHMGLAG--------DNIYLDFFYSALVEFPAAFIIILTIDRI
consensus  421 ilmyiWftt vlYqGlimhmg  g        gnlyldffysalvEfPaafiilvtidri

CeOCT-1    414 GRRWTLAATMIVCGIGCVSAMFMP-DGYPWLVASASFIGKFGVGSGFAVIYIFAGELYPT
CeOCT-2    441 GRKRSQMLVLFGSGLFLLTSVVMVYRKQSTLALIFMLLSKACIQGSFNILYIFTSELNPT
hOCT1      401 GRIYPMAMSNLLAGAACLVMIFIS-PDLHWLNIIIMCVGRMGITIAIQMICLVNAELYPT
hOCT2      402 GRRYPWAASNMVAGAACLASVFIP-GDLQWLKIIISCLGRMGITMAYEIVCLVNAELYPT
mOCT1      402 GRIYPIAASNLVAGAACLLMIFIP-HELHWLNVTLACLGRMGATIVLQMVCLVNAELYPT
mOCT2      402 GRRYPWAVSNMVAGAACLASVFIP-DDLQWLKITVACLGRMGITIAYEMVCLVNAELYPT
consensus  481 GRryplaasnivaGaacl svfip  dl wL iii clgrmgitiafnmvclvnaELyPT

CeOCT-1    473 VVRAIGMGMSSMVAGSGLLLAPHIV-NLGKIVK-ILPLLIMGLMALSAGILTFFLPETLG
CeOCT-2    501 VVRNSAVGISSMVARMGAGASGYIA-ILSDVTMPLVPMTIFACFSLLAGCLVLLLPETQG
hOCT1      460 FVRNLGVMVCSSLCDIGGIITPFIVFRLREVWQ-ALPLILFAVLGLLAAGVTLLLPETKG
hOCT2      461 FIRNLGVHICSSMCDIGGIITPFLVYRLTNIWL-ELPLMVFGVLGLVAGGLVLLLPETKG
mOCT1      461 FIRNLGMMVCSALCDLGGIFTPFMVFRLMEVWQ-ALPLILFGVLGLSAGAVTLLLPETKG
mOCT2      461 YIRNLAVLVCSSMCDIGGIVTPFLVYRLTDIWL-EFPLVVFAVVGLVAGGLVLLLPETKG
consensus  541 fvRnlgvmvcSsvcdiGgiltpfivfrLsdiwm  lPllifgvlgLlAggl llLPETkG

CeOCT-1    531 APLPMTIEDAENFGKK-PEPDSG--MFTQ-AAKKRESQPL--LE----------------
CeOCT-2    560 LPLPDTILDSVQMVKRNTKPCGTLSGTFLGGIDDDA-QPYGGKLPPRVSSDDEEEEEEED
```

```
hOCT1       519 VALPETMKDAENLGRK-AKPKEN--TIYL-KVQTSE-------P----------------
hOCT2       520 KALPETIEEAENMQRP-RKNKEK--MIYL-QVQKLD-------I----------------
mOCT1       520 VALPETIEEAENLGRRKSKAKEN--TIYL-QVQTGK-------S----------------
mOCT2       520 KALPETIEDAEKMQRP-RKKKEK--RIYL-QVKKAE-------L----------------
consensus   601 laLPeTiedaenmgrk  kpke     iyl qvqk e       l

CeOCT-1     569 -----PHTPMDRRRRSSRLMNI
CeOCT-2     619 SEESIPEKTA------------
hOCT1       552 -----SGT--------------
hOCT2       553 -----PLN--------------
mOCT1       554 -----PHT--------------
mOCT2       553 -------S--------------
consensus   661      p t
```

Figure S1. Sequence alignment of members belonging to the family of organic cation transporters from C. elegans (CeOCT-1 and CeOCT-2), Homo sapiens (hOCT1 and hOCT2) and Mus musculus (mOCT1 and mOCT2).

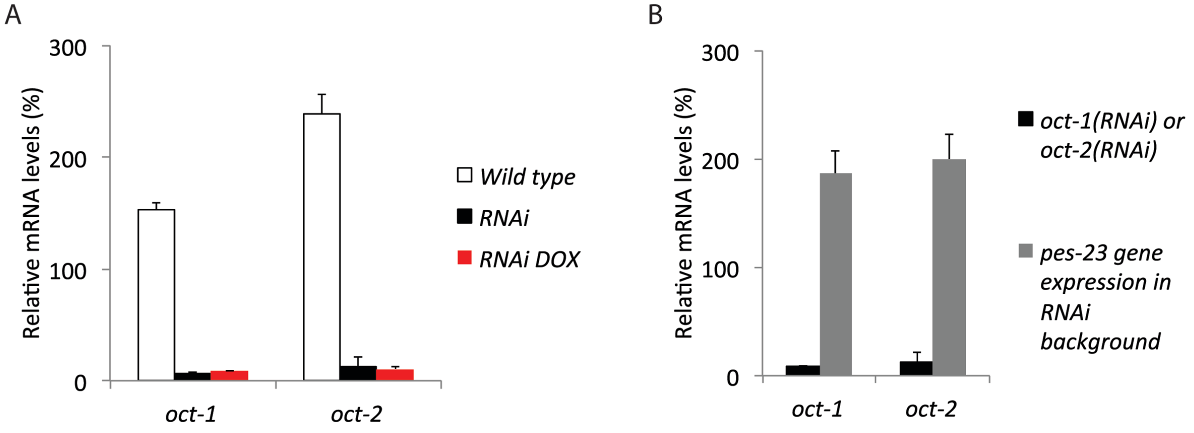

Figure S2. Relative gene expression.

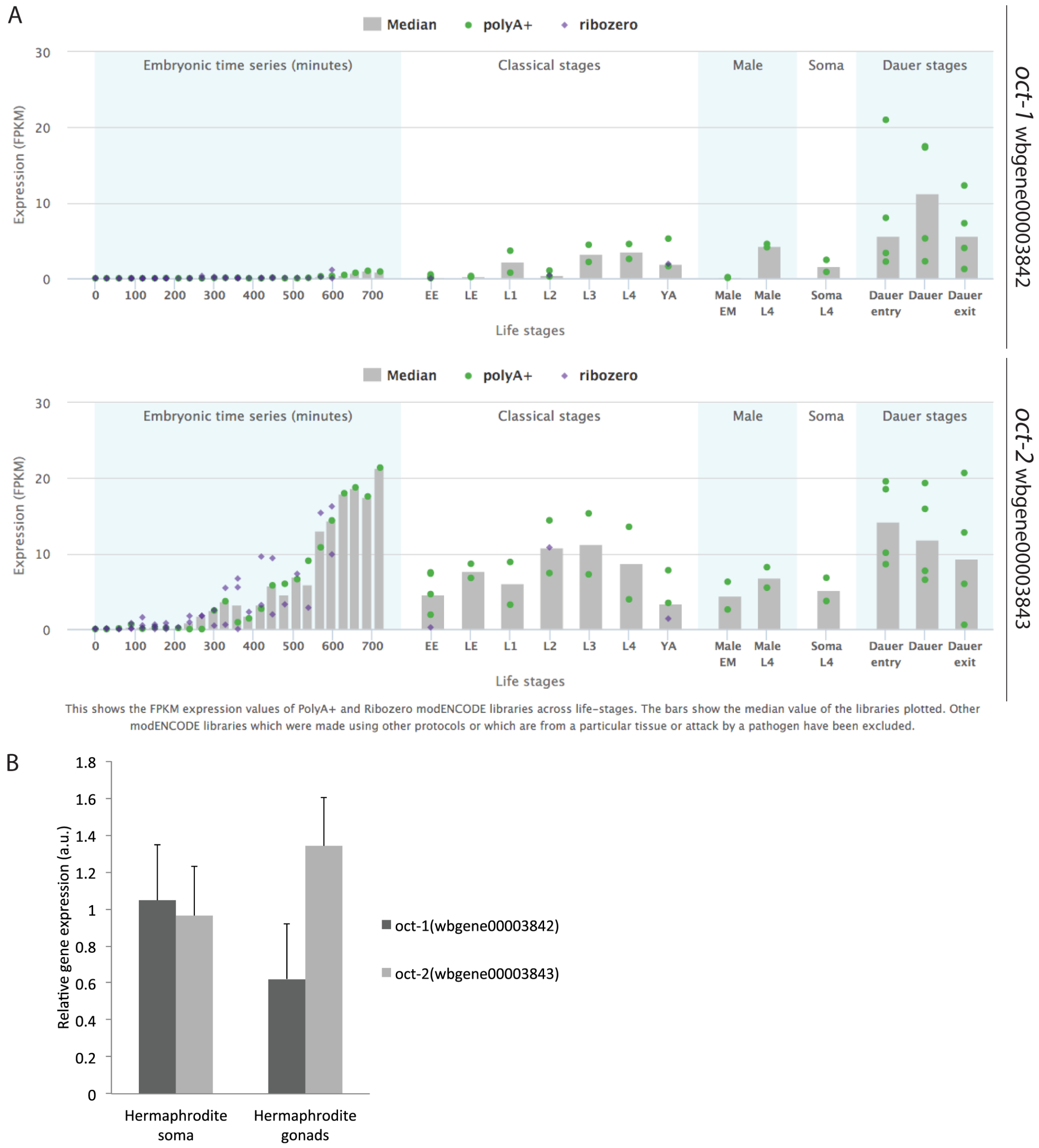

This shows the FPKM expression values of PolyA+ and Ribozero modENCODE libraries across life-stages. The bars show the median value of the libraries plotted. Other modENCODE libraries which were made using other protocols or which are from a particular tissue or attack by a pathogen have been excluded.

Figure S3. *oct-1* and *oct-2* gene expression data measured.

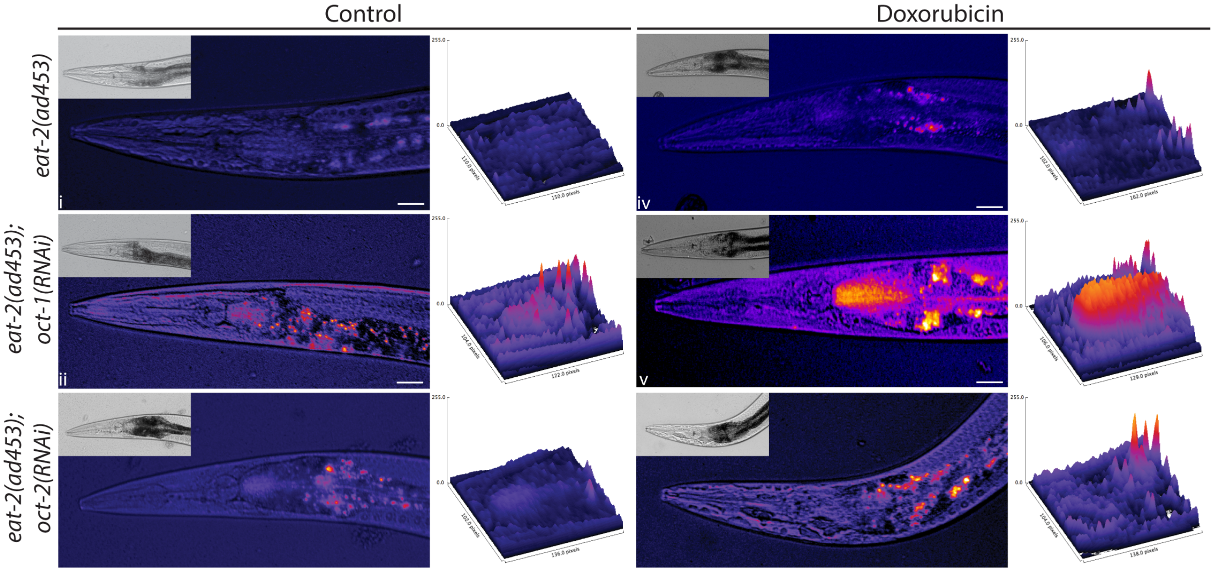

Figure S4. OCT-2-dependent doxorubicin uptake into the pharynx of *C. elegans* is not affected by the eating defective *eat-2(ad453)* mutant animals.

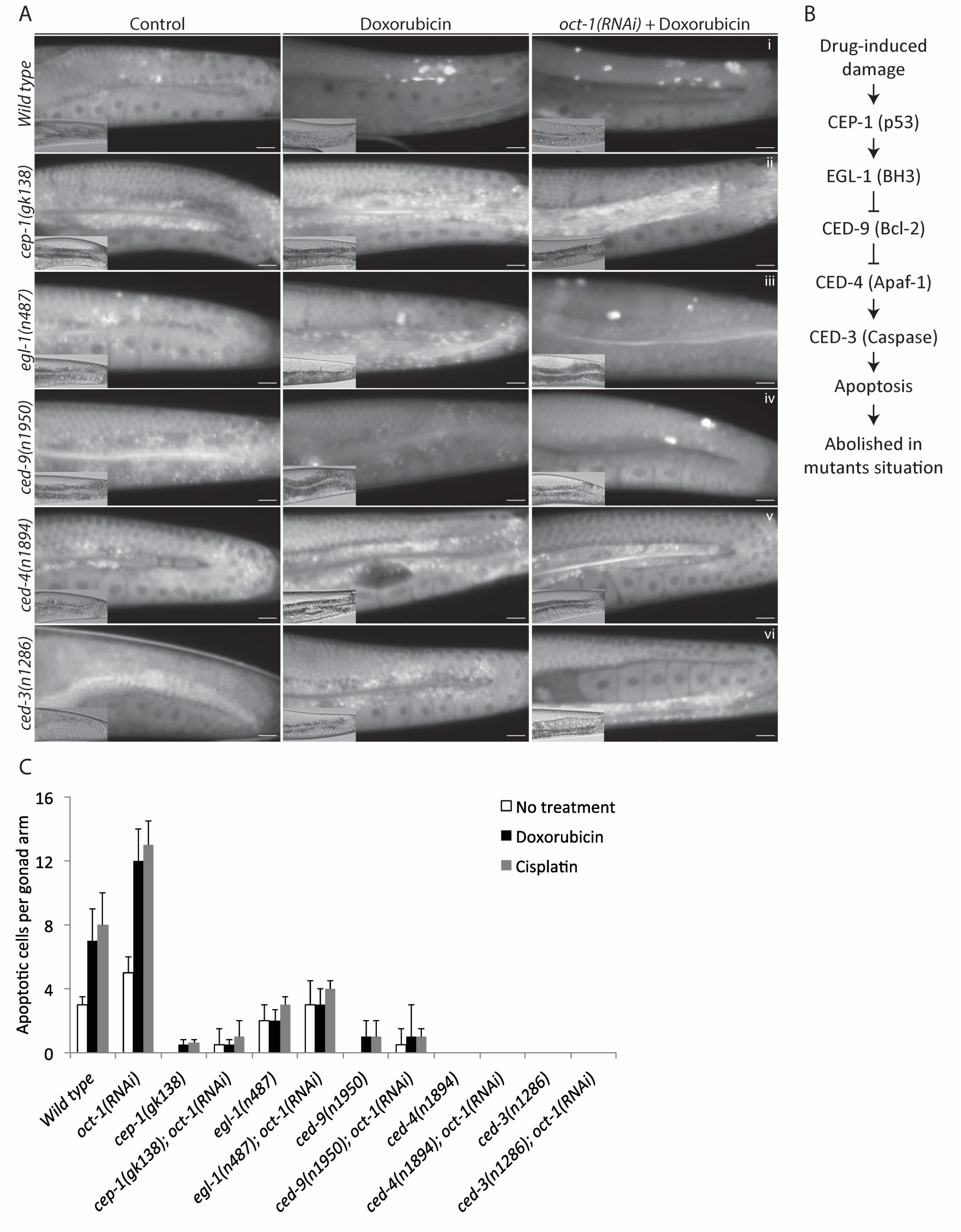

Figure S5. Genetic analysis of doxorubicin- and cisplatin-induced apoptotic cell death.

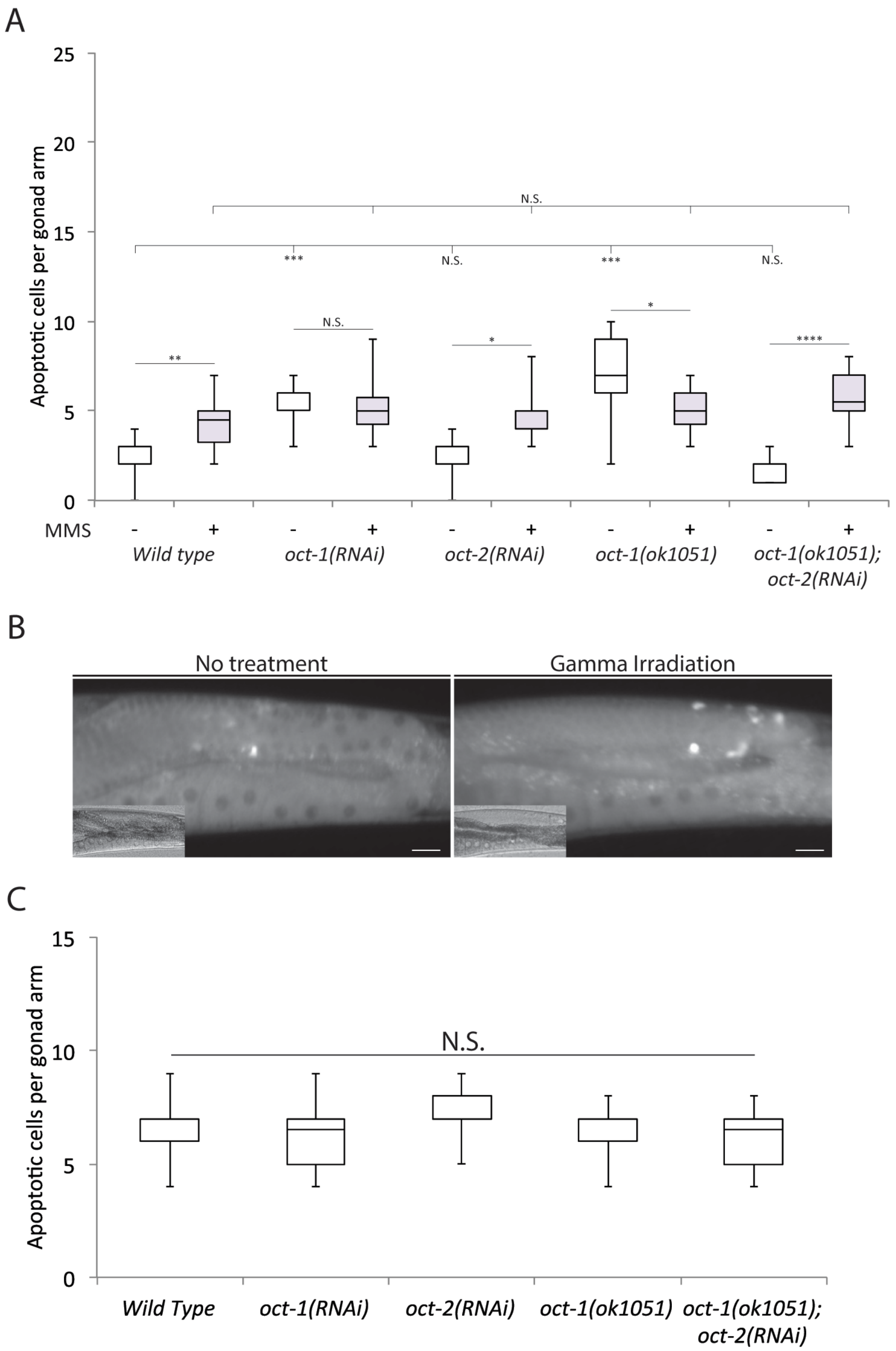

Figure S6. Methyl methanesulfonate and Gamma rays (γ-rays)-induced germ cell apoptosis are independent of OCT-1 and OCT-2 function.

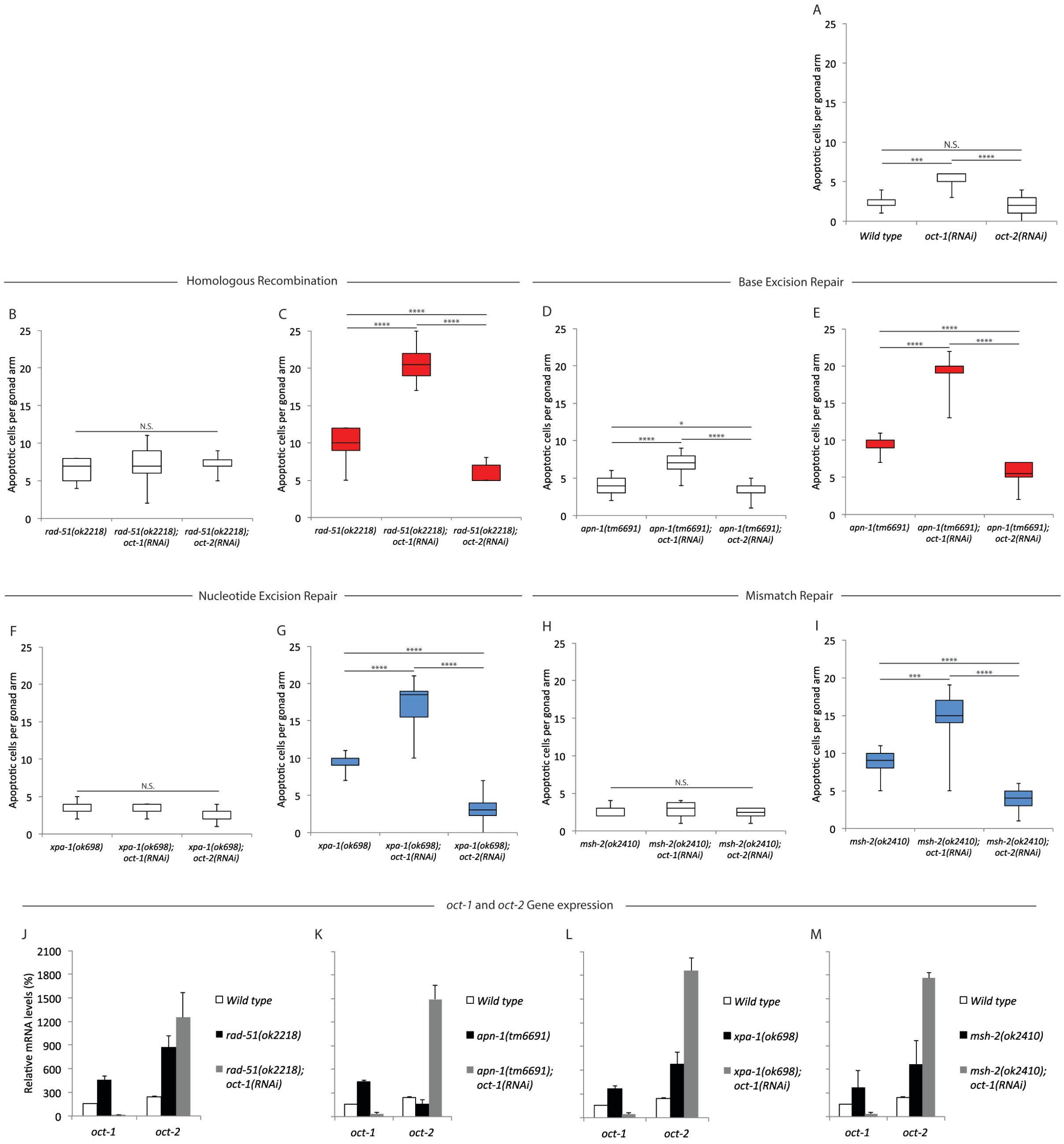

Figure S7. RNAi-driven downregulation of *oct-1* upregulates *oct-2* expression and sensitizes *C. elegans* DNA repair deficient mutants to drug-induced apoptotic cell death.

A: OCT-1

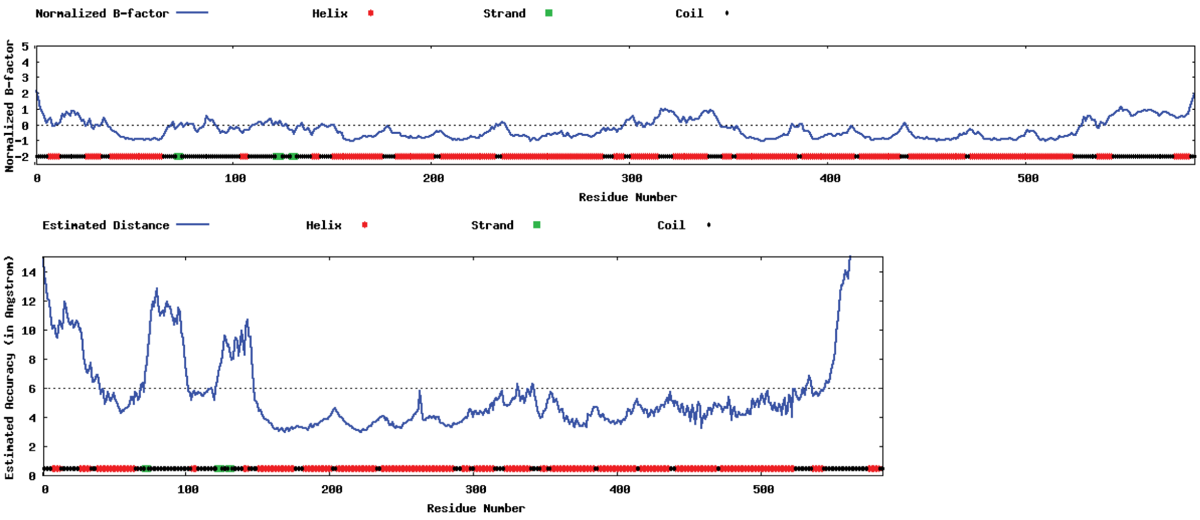

B: OCT-2

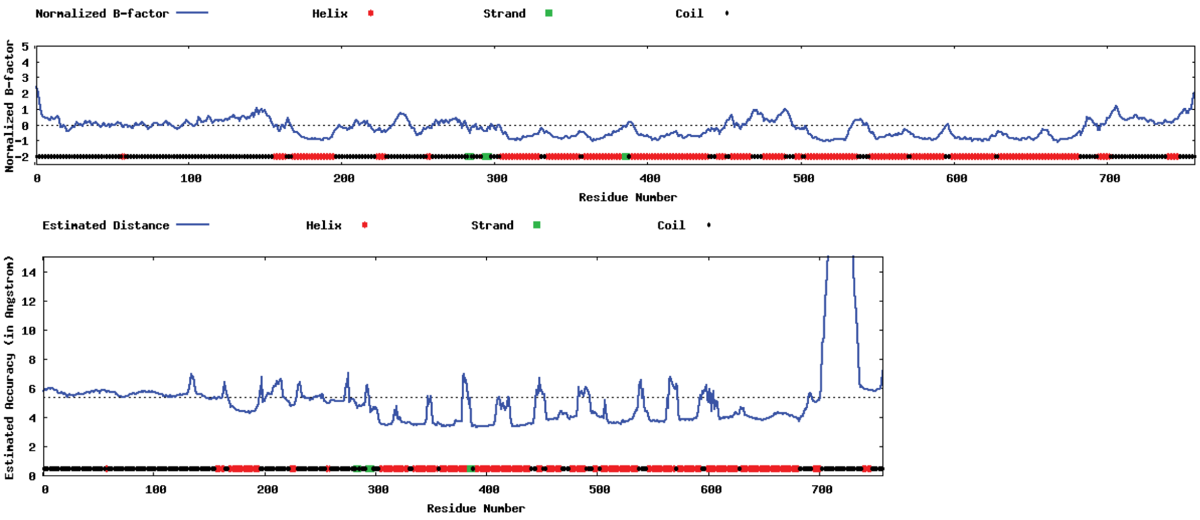

Figure S8. Structural modeling prediction of (A) OCT-1 and (B) OCT-2 computed with ResQ.

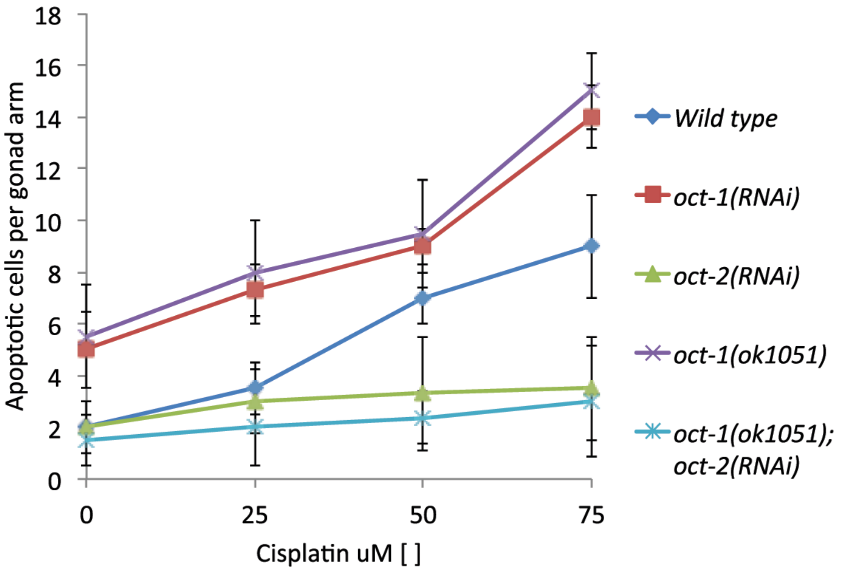

Figure S9. Apoptotic cell corpses as a function of cisplatin concentrations.

Supplemental tables:

Table S1a: Threading template structures used for predicting *C. elegans* OCT-1.

Rank[a]	PDB Hit[b]	Protein name[c]	Specie[d]	Identity 1[e]	Identity 2[e]	Normalized Z-Score[f]	Method[g]
1	5c65A	GLUT3 / SLC2A3	*Homo sapiens*	0.18	0.20	1.48	X-Ray diffraction
2	4gbyA	MFS (major facilitator superfamily) proton:xylose symporter XylE	*Escherichia coli*	0.20	0.17	3.09	X-Ray diffraction
3	5c65A	GLUT3 / SLC2A3	*Homo sapiens*	0.18	0.20	2.38	X-Ray diffraction
4	4pypA	GLUT1	*Homo sapiens*	0.18	0.19	3.51	X-Ray diffraction
5	4pypA	GLUT1	*Homo sapiens*	0.18	0.19	2.86	X-Ray diffraction
6	5c65A	GLUT3 / SLC2A3	*Homo sapiens*	0.17	0.20	2.16	X-Ray diffraction
7	4gc0A	MFS (major facilitator superfamily) proton:xylose symporter XylE	*Escherichia coli*	0.18	0.17	4.17	X-Ray diffraction
8	4gc0A	MFS (major facilitator superfamily) proton:xylose symporter XylE	*Escherichia coli*	0.18	0.17	3.40	X-Ray diffraction
9	4ldsA	Inward-facing structure of glucose transporter	*Staphylococcus epidermidis*	0.21	0.18	1.44	X-Ray diffraction
10	4ldsA	Inward-facing structure of glucose transporter	*Staphylococcus epidermidis*	0.21	0.18	1.31	X-Ray diffraction

Table S1b: Threading template structures used for predicting *C. elegans* OCT-2.

Rank[a]	PDB Hit[b]	Protein name[c]	Specie[d]	Identity 1[e]	Identity 2[e]	Normalized Z-Score[f]	Method[g]
1	5c65A	GLUT3 / SLC2A3	*Homo sapiens*	0.18	0.16	1.53	X-Ray diffraction
2	4gbyA	MFS (major facilitator superfamily) proton:xylose symporter XylE	*Homo sapiens*	0.18	0.18	2.92	X-Ray diffraction
3	5c65A	GLUT3 / SLC2A3	*Escherichia coli*	0.17	0.16	2.38	X-Ray diffraction
4	4pypA	GLUT1	*Homo sapiens*	0.18	0.16	3.46	X-Ray diffraction
5	4gc0A	MFS (major facilitator superfamily) proton:xylose symporter XylE	*Escherichia coli*	0.18	0.18	2.86	X-Ray diffraction
6	5c65A	GLUT3 / SLC2A3	*Escherichia coli*	0.16	0.16	2.18	X-Ray diffraction
7	4gc0A	MFS (major facilitator superfamily) proton:xylose symporter XylE	*Escherichia coli*	0.17	0.18	4.21	X-Ray diffraction
8	4gc0A	MFS (major facilitator superfamily) proton:xylose symporter XylE	*Escherichia coli*	0.19	0.18	4.28	X-Ray diffraction
9	5c65A	GLUT3 / SLC2A3	*Escherichia coli*	0.18	0.16	1.51	X-Ray diffraction
10	4ldsA	Glucose transporter	*Staphylococcus epidermidis*	0.22	0.16	2.55	X-Ray diffraction

[a] Rank of templates represents the top ten threading templates used by I-TASSER.

[b] PDB Hit IDs from reported protein structures used as threading templates.

[e] Identity 1 and 2 are the percentage sequence identity of the templates in the threading aligned region with the query sequence.

[f] Normalized Z-score is the normalized Z-score of the threading alignments. Alignment with a Z-score >1 signifies a correct alignment.

[g] Method used to resolved the crystal structure.

*The top 10 alignments reported above (in order of their ranking) are from the following threading programs: 1: MUSTER 2: FFAS-3D 3: SPARKS-X 4: HHSEARCH2 5: HHSEARCH I 6: Neff-PPAS 7: HHSEARCH 8: pGenTHREADER 9: wdPPAS 10: cdPPAS.

Table S2a: Top 10 identified structural analogs in PDB database for OCT-1.

Rank[a]	PDB Hit[b]	TM-score[c]	RMSD[d]	Identity[e]	Coverage[f]
1	5c65A	0.713	2.15	0.172	0.756
2	4pypA	0.689	2.00	0.184	0.723
3	4gbyA	0.675	2.58	0.147	0.732
4	4ldsA	0.628	2.70	0.190	0.685
5	4j05A	0.583	3.18	0.194	0.644
6	3wdoA	0.573	3.79	0.106	0.665
7	4zowA	0.560	3.35	0.131	0.632
8	1pw4A	0.553	4.17	0.102	0.663
9	4w6vA	0.552	4.23	0.076	0.658
10	4ikvA	0.546	4.23	0.072	0.655

Table S2b: Top 10 identified structural analogs in PDB database for OCT-2.

Rank[a]	PDB Hit[b]	TM-score[c]	RMSD[d]	Identity[e]	Coverage[f]
1	4gc0A	0.675	1.63	0.182	0.694
2	5c65A	0.670	2.19	0.165	0.707
3	4ybqA	0.643	2.54	0.181	0.686
4	4pypA	0.593	3.54	0.151	0.675
5	4ldsA	0.564	3.62	0.175	0.646
6	3wdoA	0.556	3.43	0.122	0.624
7	4j05A	0.551	3.47	0.163	0.616
8	3o7qA	0.533	3.28	0.115	0.597
9	4zowA	0.518	3.90	0.108	0.603
10	4m64A	0.511	4.46	0.120	0.617

[a] Rank of templates represents the top ten threading templates used by I-TASSER.

[b] PDB Hit IDs from reported protein structures used as threading templates.

[c] TM-score is a metric for measuring the structural similarity of two protein models. It is designed to solve two major problems in the traditional metrics such as root-mean-square deviation (RMSD): (1) TM-score measures the global fold similarity and is less sensitive to the local structural variations; (2) magnitude of TM-score for random structure pairs is length-independent. TM-score has the value in [0,1], where 1 indicates a perfect match between two structures. Following strict statistics of structures in the PDB, scores below 0.17 corresponds to randomly chosen unrelated proteins whereas with a score higher than 0.5 assume generally the same fold in SCOP/CATH.

[d] RMSD is the root-mean-square deviation between residues that are structurally aligned by TM-align.

[e] Identity is the percentage sequence identity in the structurally aligned region.

[f] Coverage represents the coverage of the alignment by TM-align and is equal to the number of structurally aligned residues divided by length of the query protein.

Table S3: Confidence measurement of *C. elegans* OCT-1 and OCT-2 structures computed with I-TASSER, and after structural refinement with ModRefiner and Modeller.

	I-TASSER			**ModRefiner**		**Modeller**
Protein	C-score[a]	RMSD[b]	TM-score[c]	RMSD[b]	TM-score[d]	Z-DOPE[e]
OCT-1 (F52F12.1)	-2.35	13.4±4.0Å	0.44±0.14	25.78	0.24	-1.765
OCT-2 (ZK455.8)	-2.52	14.1±3.8Å	0.42±0.14	18.03	0.35	-0.472

[a]C-score is a confidence score for estimating the quality of predicted models by I-TASSER. C-score range between [-5 and 2], where a C-score of higher value signifies a model with a high confidence.
[b]RMSD is the root-mean-square deviation between residues that are structurally aligned[1].
TM-score is the metric for measuring the structural similarity of two protein models. [c]TM-score is based on their correlation with I-Tasser's C-score, and ModRefiner [d]TM-score indicates a model of correct topology whose value range between [>0.5 and <0.17].
[e]Z-DOPE is the atomic distance-dependent statistical calculation from samples of native protein structures. Protein structures computed lower than -1, score as native-like structures.

Table S4: Predicted amino acid positions for ligand-protein interaction.

Protein	Residues	C-score[a]
OCT-1	63, 64, 67, 72, 73, 75, 155, 162, 219, 223, 367, 370, 374, 375, 379, 382, 389, 392, 459, 490, 494	0.38
OCT-2	58, 188, 273, 490, 514, 278, 282, 296, 299, 302, 303, 314, 365, 392, 403, 435, 462, 463, 516, 519	0.75

[a]C-score is the confidence score of predicted binding site. Scores falls in between 0-1; where a score close or equal to 1 signifies a reliable prediction. Amino acids in blue are the ones forming polar contacts with doxorubicin (Fig. 4c).

Table S5: Computed ligand-protein docking scores with BSP-SLIM.

	OCT-1		**OCT-2**	
Drug	Docking score[a]	Predicted amino acids	Docking score[a]	Predicted amino acids
Doxorubicin	3.805	Pro63, Tyr162, Asn370, Asn375	3.993	Asn58, Tyr188, Trp273, Tyr490, Arg514
Carboplatin	3.359	Asn370	4.506	
Methyl methanesulfonate	0	0	0	0
Diclofenac	0	0	0	0

[a]Docking score is the confidence score of predicted ligand-protein docking. Scores higher than 1 are considered being a reliable docking.

Table S6: Mechanism of action of the drugs used in this study.

Ligand	Mechanism of action	PubChem CID
1. B02	RAD51 inhibitor resulting in unrepaired double strand breaks.	5738263
2. Camptothecin	Inhibits the nuclear enzyme DNA Topoisomerase I.	24360
3. Cisplatin	Produce intra and interstrand DNA crosslinks.	441203
4. Cycloheximide	Inhibits elongation during protein synthesis.	6197
5. Diclofenac	Non-steroidal anti-inflammatory agent	3033
6. Doxorubicin	Intercalates between base pairs in the DNA helix, thereby preventing DNA replication and inhibiting protein synthesis. Inhibits Topoisomerase II.	31703
7. Ketamine	Induction of anesthesia	3821
8. Melphalan	Alkylates DNA at the N7 position of guanine and induces DNA interstrand crosslinkages, resulting in the inhibition of DNA and RNA synthesis and cytotoxicity against both dividing and non-dividing tumor cells.	460612
9. Metformin	Decrease hepatic glucose production, mostly through a mild and transient inhibition of the mitochondrial respiratory-chain complex 1.	4091
10. Methotrexate	Binds to and inhibits the enzyme dihydrofolate reductase, resulting in inhibition of purine nucleotide and thymidylate synthesis and, subsequently, inhibition of DNA and RNA syntheses. Induce oxidative DNA damage.	126941
11. Methoxyamine	Binds to apurinic/apyrimidinic (AP) DNA damage sites and inhibits base excision repair (BER), which may result in an increase in DNA strand breaks.	4113
12. Methyl methanesulfonate	Acts as a mutagen by altering and damaging DNA producing distinct types of lesions.	4156
13. Nicotinamide	Acts as a chemo- and radio-sensitizing agent by enhancing tumor blood flow, thereby reducing tumor hypoxia. This agent also inhibits poly(ADP-ribose) polymerases, enzymes involved in the rejoining of DNA strand breaks induced by radiation or chemotherapy.	936
14. 4-Nitroquinoline N-oxide	4-NQO and its metabolite 4-Hydroxyaminoquinolone-1-oxide bind to nucleic acids.	5955
15. Olaparib	Inhibits PARP-mediated repair of single strand DNA breaks; also enhance the cytotoxicity of DNA-damaging agents.	23725625
16. Paraquat	Catalyze the formation of reactive oxygen species (ROS), more specifically, the superoxide free radical. Paraquat will undergo redox cycling in vivo, being reduced by an electron donor such as NADPH, before being oxidized by an electron receptor such as dioxygen to produce superoxide, a major ROS.	15939
17. Phenformin	Hypoglycemic agent closely related to metformin.	8249
18. Puromycin	Acting as an analog of the 3' terminal end of aminoacyl-tRNA, puromycin incorporates itself into a growing polypeptide chain and causes its premature termination, thereby inhibiting protein synthesis and producing oxidative damages.	439530
19. Zeocin	Acts by intercalating into DNA and induces DNA double strand breaks.	71668282

Chapter 3 : UNG-1 and APN-1 are the major enzymes to efficiently repair 5-hydroxymethyluracil DNA lesions in *C. elegans*

Arturo Papaluca[1,3], J. Richard Wagner[2], H. Uri Saragovi[3] and Dindial Ramotar[1*]

[1]Maisonneuve-Rosemont Hospital, Research Center, Université de Montréal, Department of Medicine, 5415 Boul. de l'Assomption, Montréal, Québec, Canada, H1T2M4.
[2]Département de Médecine Nucléaire et Radiobiologie, Faculté de Médecine et des Sciences de la Santé, Université de Sherbrooke, 3001 12^{e} Avenue Nord, Sherbrooke, Québec, Canada, J1H5N4.
[3]Lady Davis Institute for Medical Research, Jewish General Hospital, McGill University, Department of Pharmacology and Therapeutics, 3755 Chemin de la Côte Sainte-Catherine, Montréal, Québec, Canada, H3T1E2.

Running title: UNG-1 and APN-1 process 5-hmU lesions in *C. elegans*

[*]To whom correspondence should be addressed: Prof. Dindial Ramotar, Maisonneuve-Rosemont Hospital, Research Center, Université de Montréal, Department of Medicine, 5415 Boul. de l'Assomption, Montréal, Québec, Canada, H1T 2M4. Telephone: (514) 252-3400 ext. 4684; Fax: (514) 252-3430; email: dindial.ramotar@umontreal.ca

Keywords: 5-hydroxymethyluracil, DNA glycosylases, AP endonucleases, DNA repair pathways, *C. elegans*

ABSTRACT

Oxidatively modified DNA bases are primarily removed and replaced by the base-excision repair (BER) pathway. In *Caenorhabditis elegans* at least four enzymes, two DNA glycosylases UNG-1 and NTH-1 and two AP endonucleases APN-1 and EXO-3, have been characterized that belong to the BER pathway. UNG-1 removes uracil, while NTH-1 can remove 5-hydroxymethyluracil (5-hmU), an oxidation product of thymine, as well as other lesions. Both APN-1 and EXO-3 can incise AP sites and remove 3′-blocking lesions at DNA single strand breaks. APN-1, but not EXO-3, also possesses a 3′- to 5′-exonulease activity and a nucleotide incision repair activity. We used *C. elegans* mutants to study the role of the BER pathway in processing 5-hmU. We observe that *ung-1* mutants exhibited a decrease in brood size and lifespan, and an elevated level of germ cell apoptosis when challenged with 5-hmU. These phenotypes were exacerbated by RNAi downregulation of *apn-1* in the *ung-1* mutant. The *nth-1* or *exo-3* mutants displayed wild type phenotypes towards 5-hmU. We show that partially purified UNG-1 can act on 5-hmU lesion *in vitro*. We propose that UNG-1 removes 5-hmU incorporated into the genome and the resulting AP site is cleaved by APN-1 or EXO-3. In the absence of UNG-1, the 5-hmU is removed by NTH-1 creating a genotoxic 3′-blocking lesion that requires the action of APN-1.

3.1. Introduction

Endogenous and exogenous reactive oxygen species (ROS), such as superoxide radical anions and hydrogen peroxide generate hydroxyl radicals that react with DNA to induce a variety of DNA damage [1]. Hydroxymethyluracil (5-hmU) is a common oxidative DNA lesion induced by ROS and due to active DNA repair, it is usually present at relatively low levels in mammalian cells [1,2]. This modified base and its glucosylated derivative (base J) is also formed by enzymatic reactions in bacteriophage and protozoa [3]. In *Caenorhabditis elegans*, the main source of 5-hmU is likely ROS induced oxidation of thymine, which displays normal base pairing with adenine (5-hmUA). Another potential source of 5-hmU involves the enzymatic oxidation of 5-methylcytosine (5-mC), which generates 5-hydroxymethylcytosine (5-hmC), followed by deamination by an activation-induced deaminase creating a mismatch with guanine (5-hmUG) [2]. Efficient removal of 5-hmU would restore normal DNA base pairing, otherwise in the case of 5-hmUG leads to a transition mutation from 5-methylcytosine to thymine [2,4,5]. However, this latter pathway is unlikely to occur in *C. elegans* because they lack 5-methycytosine, ten eleven translocation (TET) family enzymes, and other BER enzymes associated with DNA methylation (see below).

At least, four DNA glycosylases belonging to the base-excision DNA repair (BER) pathway have been identified that remove 5-hmU from the genome and these include (i) the single-strand specific monofunctional uracil DNA glycosylase 1, SMUG1 [6], (ii) the bifunctional DNA glycosylase/AP lyase NTH1 that also removes a variety of oxidatively modified bases [7], (iii) the thymine DNA glycosylase TDG [8], and (iv) the methyl-CpG binding domain protein 4, MBD4 DNA glycosylase [9]. These DNA glycosylases cleave the *N*-glycosidic bond between the oxidatively modified base and the sugar moiety to produce a C1′ hydrolyzed abasic sugar. The abasic site created by these DNA glycosylases, except for NTH1 with an associated β-lyase activity (see below), is incised by an apurinic/apyrimidinic (AP) endonuclease creating a 3′-hydroxyl group and 5′-deoxyribose phosphate. The latter is removed by the lyase activity of DNA polymerase β, which simultaneously with its DNA polymerase activity inserts the correct nucleotide leaving a nick that is sealed by a DNA ligase in a set of reactions that constitutes the BER pathway [10-12].

Of the multiple DNA glycosylases involved in removing 5-hmU in various organisms, only NTH-1 that shares 67.4 % similarity with human NTH1 (see Figure S1A) has been conserved in *Caenorhabditis elegans* [13]. Besides NTH-1, *C. elegans* has retained one other DNA glycosylases, namely uracil DNA glycosylase UNG-1 that shares 58.2 % similarity with human UNG1 (see Figure S1B) [14,15]. It seems enigmatic that this multicellular organism would conserved only two DNA glycosylases, NTH-1 and UNG-1, while the unicellular organisms *Escherichia coli* and the budding yeast *Saccharomyces cerevisiae* conserved eight and five, respectively, and humans retained even more, eleven [12]. There might be a rationale for the evolutionary conservation of only NTH-1 and UNG-1 in *C. elegans*. This organism does not harbor homologs of the enzymes that program the methylation of cytosine, i.e., the DNA (cytosine-5-)-methyltransferases DNMT1 or DNMT3 to form 5-mC, as an epigenetic mark [16,17]. Furthermore, a search of the *C. elegans* genome database revealed that it lacks the <u>T</u>en <u>E</u>leven <u>T</u>ranslocation proteins TET1, 2 and 3 that are required to hydroxylate 5-mC to form 5-hmC and further oxidation products 5-formylcytosine and 5-carboxylcytosine in a pathway to regenerate the nonmethylated cytosine [16,17]. The lack of the TET1, 2 and 3 proteins would also prevent the conversion of thymine to 5-hmU to create the base pair 5-hmUA in this organism. Moreover, *C. elegans* does not appear to harbor an AID/APOBEC deaminase to convert 5-hmC to 5-hmU. Since the MBD4 DNA glycosylase co-localizes to heterochromatin sites in a DNA methylation-dependent manner [9], it would seem less important for *C. elegans* to conserve a homolog of MBD4 because its genome has no or undetectable 5-mC.

Likewise, it would seem unnecessary for *C. elegans* to also conserve the thymine DNA glycosylase TDG, which would be required to remove TG mispair formed by deamination of 5-mC in the 5-mCG base pair. Indeed, *C. elegans* lacks both MBD4 and TDG, raising the possibility that 5-hmU lesions generated as a consequence of thymine oxidation would be processed by either a SMUG1-like and or the NTH-1 activity in *C. elegans*. However, *C. elegans* also lacks in its genome a gene encoding a SMUG1-like DNA glycosylase. Altogether, *C. elegans* appears to lack a system to methylate, hydroxylate and demethylate cytosine in a process that would lead to 5-hmU formation, as well as lacking three DNA glycosylases, SMUG1, TDG and MBD4, that would ordinarily remove 5-hmU. Therefore, we anticipate that the task of removing 5-hmU lesions from the genome of *C. elegans* would be a function devoted strictly to the NTH-1 DNA glycosylase.

The *C. elegans* NTH-1 has been expressed and purified from an *E. coli* expression system and shown to efficiently remove oxidatively modified bases such as thymine glycol, 5-formyluracil and 5-hmU from oligonucleotide substrates [13]. NTH-1 acts as a bifunctional DNA glycosylase/AP-lyase, and following the removal of the modified base, the resulting AP site is cleaved by its AP-lyase activity via a β-elimination reaction to produce a single strand break terminated with a bulky 3′-α, β unsaturated aldehyde [7]. This 3′-blocking lesion must be removed by one of the two conserved AP endonucleases/3′-diesterases, APN-1 and EXO-3, to produce a 3′-hydroxyl group for DNA repair synthesis [18-20]. If the 3′-blocking lesions are not efficiently removed, they can also generate DNA and protein crosslinks that become more deleterious than simple abasic sites [21].

In this study, we set out to investigate whether *C. elegans* mutants lacking enzymes of the BER pathway would be sensitive to exposure of the nucleoside form of 5-hmU. We report the surprising finding that *ung-1*, and not *nth-1*, mutants showed a number of phenotypes that are associated with a defect in DNA damage response when the animals were challenged with 5-hmU, suggesting that UNG-1 is the major DNA glycosylase involved in processing 5-hmU lesions. Consistent with this observation, partially purified UNG-1 was capable of removing 5-hmU from a deoxyoligonucleotide stem-loop substrate. We further show that APN-1-, but not EXO-3, -deficient mutant animals were sensitive to 5-hmU exposure and the effects were more dramatic in *ung-1*; *apn-1(RNAi)* knockdown mutants. We propose that UNG-1 has the ability to remove 5-hmU and channel the resulting AP site to be cleaved by APN-1 or EXO-3. In the absence of UNG-1, the 5-hmU lesion is processed by NTH-1, which creates the toxic 3′-bocking group that must be repaired by APN-1.

Keywords: 5-hydroxymethyluracil, DNA glycosylases, AP endonucleases, DNA repair pathways, *C. elegans*

3.2. Results

3.2.1. *C. elegans* mutants deficient in both APN-1 and EXO-3 are hypersensitive to DOX-, MMS- and CDDP-induced DNA lesions

It has been shown that *C. elegans* mutants deleted for the *apn-1* gene are defective in the repair of damaged DNA that contains oxidative base lesions and AP sites [22]. These mutants exhibit elevated frequency of spontaneous mutations, as well as a short lifespan [22]. Since AP endonucleases serve as key components of the BER pathway, animals deleted for the *exo-3* gene also exhibit short lifespan [23]. These observations indicate that both enzymes bear the responsibility of repairing damaged DNA lesions to maintain *C. elegans* longevity. To date, no previous evidence exists indicating that the simultaneous deletion of the *apn-1* and *exo-3* genes would render the animals to even greater sensitivity to genotoxic agents due to the accumulation of unrepaired lesions in the genome in comparison to the single deletion mutants. We set out to investigate this idea by monitoring the viability of the animals by scoring the brood size and the lifespan following exposure to different DNA damaging agents (Figure 1A). In this experiment, L1-staged wild type and mutant animals were systematically fed the HT115 bacteria harbouring the RNAi plasmid targeting *apn-1* and *exo-3* to score the brood size and using the *apn-1* and *exo-3* gene deletion mutants *apn-1(tm6691)* and *exo-3(tm4374)* for comparison, respectively. As expected, the deletion mutants *apn-1(tm6691)* and *exo-3(tm4374)* exhibited a significant decrease in brood size in comparison to the wild type control animals (Figure 1B-D, white bars) consistent with previous observations [22,23]. RNA-interference (RNAi)-driven depletion of *apn-1* in the *exo-3* deletion mutant *exo-3(tm4374)* caused the resulting *exo-3(tm4374); apn-1(RNAi)* knockdown mutant animals to exhibit nearly 65 % decrease in brood size as compared to the single mutants *apn-1(tm6691)* and *exo-3(tm4374)* showing ~ 40 % and 30 % decreased in brood size, respectively (Figure 1B-D, white bars). The effectiveness of the *apn-1(RNAi)* and *RNAi* against other genes (see below) was tested against the wild type (Figure S2A).

We investigated whether there would be a different requirement for APN-1 and EXO-3 molecular activities for processing DNA lesions produced by distinct DNA damaging agents. For this purpose, we exposed the animals to the DNA damaging agents doxorubicin (DOX), methyl methanesulfonate (MMS), and cisplatin (CDDP) that are known to create a range of DNA lesions that include oxidatively damaged bases, alkylated bases that are unstable, single and double strand breaks and interstrand crosslinks [24,25]. We used drug concentrations that allowed the animals to develop and found that DOX, MMS and CDDP induced nearly 50 % decrease in brood size as scored for either the single deletion mutant *apn-1(tm6691)* or *exo-3(tm4374)* (Figure 1B-D). The brood size decreased to 80 % when the mutant *exo-3(tm4374)* knockdown for *apn-1(RNAi)* was exposed to the drugs (Figure 1B-D). These results indicated that the repair of the lesions induced by the distinct DNA damaging agents were dependent upon the single and/or combined activity of APN-1 and EXO-3 as depletion of both enzymes resulted in an additive effect on the brood size. Thus, it would appear that these genotoxic agents are likely generating at least a common DNA lesion, such as indirect formation of AP sites from damaged base, which APN-1 and EXO-3 can compete to repair. In fact, it is known that oxidatively damaged bases are produced by doxorubicin and that the cytosine adjacent to CDDP-induced interstrand crosslinks can preferentially endure oxidative deamination to create uracil [24,25].

3.2.2. *C. elegans apn-1*, but not *exo-3*, mutants are sensitive to the nucleoside 5-hmU

We have previously shown that APN-1, but not EXO-3, has the ability to process oxidized base DNA lesions, as well as exert a 3′ to 5′-exonuclease activity presumably to act on strand breaks with blocked 3′-ends [20,22]. Oxidation and deamination of 5-methylcytosine lead to 5-hydroxymethyluracil (5-hmU) as a mispair opposite guanine (5-hmUG) [2]. Likewise, oxidation of thymine can also lead to 5-hmU, but as a mispair opposite adenine (5-hmUA) [2]. We assume that feeding *C. elegans* 5-hmU would lead to its conversion into the triphosphate form and subsequent incorporation into the genome as observed for mammalian cells [1]. Since the purified *C. elegans* NTH-1 enzyme has been shown to remove 5-hmU from oligonucleotide substrate followed by a β-elimination reaction to produce the product 3′-α,β unsaturated aldehyde, instead of an AP site [13]. We predict that this latter lesion would require the function of the 3′-diesterase of either APN-1 or EXO-3 or both for its removal. Following treatment with 5-hmU, we observed that the *apn-1(tm6691)* mutants exhibited nearly 50 % decrease in brood size as oppose to *exo-3(tm4374)* that showed only 5 % decrease in brood size (Figure 2A).

However, when the *exo-3(tm4374); apn-1(RNAi)* knockdown mutant was exposed to 5-hmU, we observed the same deleterious effect caused by the *apn-1(tm6691)* mutation alone: close to 50 % decrease in brood size (Figure 2A), again suggesting that EXO-3 has no major role in processing the 5-hmU lesions. To further test this possibility, we examined whether the expression level of the *apn-1* and the *exo-3* genes would be affected by 5-hmU treatment. Interestingly, we observed a nearly 3-fold induction in the expression of the *apn-1* gene when the animals were exposed to 5-hmU, while the *exo-3* gene was unaffected (Figure S2B), consistent with the notion that APN-1, and not EXO-3, is the major AP endonuclease involved in processing the 5-hmU lesion.

We next checked whether exposure to 5-hmU would affect the longevity of the animals by measuring the lifespan of the wild type and the mutant worms in the absence and presence of the nucleoside. We noticed that the lifespan of the *apn-1(tm6691)* mutants was further decreased, but not that of the *exo-3(tm4374)* mutants, when exposed to 5-hmU as compared to the untreated (Figure 2B-C vs. Figure S3A). Downregulation of *apn-1* by RNAi in the *exo-3(tm4374)* mutants yielded the *exo-3(tm4374); apn-1(RNAi)* knockdown mutants showing a shortened lifespan towards 5-hmU that was similar to the decreased lifespan observed for the *apn-1(tm6691)* single mutant (Figure 2B-C). We interpret this observation to suggest that APN-1, and not EXO-3, is the predominant endonuclease that is recruited to process the damaged base 5-hmU when it is incorporated into the genome of *C. elegans*. Therefore, the diminished brood size and lifespan caused by 5-hmU in the *apn-1(tm6691)* mutants are attributed to unrepaired lesions in the mitotic and post-mitotic tissues, respectively.

3.2.3. The *apn-1(tm6691)* mutant animals display increase spontaneous and 5-hmU-induced germ cell apoptosis

Like many other stem cell systems, *C. elegans* features a self-renewing germ cell population originated from a cellular lineage located at the distal tip (Figure 3A) [26]. In these germ cells, differentiation occurs throughout distinct stages and they must maintain the integrity of the genome. When exposed to environmental insults, germ cells respond by using conserved DNA damage repair pathways that act to maintain genomic stability. Germ cells that are unable to repair damaged DNA undergo apoptosis and subsequent embryonic death [26-29]. We used this sensitive germ cell apoptosis assay to investigate whether 5-hmU would induce germ cell death in the animals and whether this effect would be enhanced in the absence of APN-1 and EXO-3. To do this, we utilized differential interference contrast (DIC) microscopy and DNA staining with acridine orange [30] to quantify the levels of apoptosis in the proximal zone of the gonad arm *in vivo* (Figure 3A). Consistent with previous reports [31], we observed an average of 2.0±1 apoptotic corpses per wild type animal (Figure 3B [i]). In contrast, the *apn-1(tm6691)* and the *exo-3(tm4374)* mutants showed an average of 6.0±1.3 and 5.5±0.9 apoptotic corpses per animal, respectively (Figure 3B [ii and iii] and Figure 3C). Unlike the single mutants, the *exo-3(tm4374); apn-1(RNAi)* knockdown mutant depicted an average of 8.0±1.5 apoptotic corpses per animal significantly higher than the wild type and the single mutants (Figure 3B [iv] and Figure 3C). The observation that the deficiency of both APN-1 and EXO-3 resulted in an additive effect on germ cells apoptosis, indicates that both of these enzymes function independently to promote base excision repair of spontaneous DNA damage in these germ cells.

On the basis of the above results, we challenged the wild type and mutant animals with 5-hmU, as well as the DNA damaging agents DOX and MMS that are known to induce germ cell apoptosis [22,28]. When the wild type animals were exposed to either 5-hmU, DOX and MMS they displayed an average 3.0±1.0, 4.0±2.0 and 5.0±1.0 apoptotic cells per animal, respectively (Figure 3B [v, ix and xiii] and Figure 3D-F), suggesting that these doses are effective at causing slight genotoxicity to the germ cells of the wild type animals. In contrast, when the *apn-1(tm6691)* mutant animals were exposed to either 5-hmU, DOX and MMS they showed significantly higher levels of apoptotic cells as compared to both untreated and treated wild type animals (5-hmU: 14.3±1.7; DOX: 10.4±1.3; MMS: 8.5±1.4) (Figure 3B [vi, x and xiv vs. ii and i] and Figure 3D-F). The high levels of apoptotic cells observed in the *apn-1(tm6691)* mutant exposed to 5-hmU is in agreement with previous studies showing that 5-hmU incorporates into the genome and triggers apoptosis in mammalian cells [32,33]. Thus, it would also appear that 5-hmU is incorporated into the genome of the germ cells and requires at least the DNA repair functions of APN-1.

Unlike the *apn-1(tm6691)* mutant, the *exo-3(tm4374)* mutants treated with either 5-hmU or DOX, respectively, showed an average of 2.7±1.1 or 5.1±1.2 apoptotic cells per animal, which was comparable to the wild type (Figure 3B [vii and xi vs. v and ix] and Figure 3D and E), suggesting that EXO-3 has minimal role compared to APN-1 in processing 5-hmU and DOX-induced DNA lesions. However, *exo-3(tm4374)* mutants exposed to MMS, depicted an average of 8.3±1.8 apoptotic cells per animal similar to the *apn-1(tm6691)* mutants (8.5±1.4) (Figure 3B [xv vs. xiv] and Figure 3F). In addition, the level of apoptotic cells was augmented when the *exo-3(tm4374); apn-1(RNAi)* knockdown mutant was exposed to MMS (10.5±1.7) (Figure 3B [xvi] and Figure 3F). This observation indicates that EXO-3 can compete with APN-1 to repair MMS-induced DNA lesions, but not for the 5-hmU or the DOX-induced DNA lesions (see also for lifespan Figure S3). Collectively, our results suggest that (i) 5-hmU is incorporated into the genome of the germ cells and causes genotoxicity and (ii) APN-1 plays a key role in repairing 5-hmU lesions and not EXO-3.

3.2.4. 5-hmU induces CED-1 engulfment of apoptotic germ cells

To ensure that the quantification of the germ cell death caused by 5-hmU is not a contribution from potential artifacts induced by the acridine orange staining method and or endogenous autofluorescence, we assessed the presence of apoptotic cells using a downstream component of the apoptotic pathway, CED-1. This protein engulfs apoptotic cells to signal phagocytic degradation[34]. As previously reported, we utilized an imaging method in which the *bcls39* strain carries the CED-1::GFP as a reporter of engulfed apoptotic cells [28,35]. This *bcls39* strain with control RNAi showed an average engulfment of 2.0±1.0 apoptotic cells per animal (Figure 4A [i]), whereas depletion of *apn-1* via RNAi in the *bcls39* reporter caused an increase average engulfment of 6.7±0.9 apoptotic cells due to spontaneous DNA damage (Figure 4A [ii]) and consistent with the acridine orange staining observed by the *apn-1(tm6691)* mutant (Figure 3B [ii]). Furthermore, exposure of the *bcls39* reporter strain and the *bcls39; apn-1(RNAi)* to 5-hmU elevated the appearance of apoptotic cells (4.0±0.8 and 16.0±1.5 respectively) (Figure 4A [iii and iv] and Figure 4B), supporting the notion that indeed 5-hmU creates genotoxic lesions in the germ cells that must be processed by APN-1. To confirm that 5-hmU can promote apoptotic signaling, we tested several mutants deleted for key components of the apoptotic pathway including *cep-1*, *egl-1*, *ced-9*, *ced-4* and *ced-3*[26]. As expected, none of these mutants showed significant increase in apoptotic cells following exposure to 5-hmU (Figure S4A).

3.2.5. UNG-1, but not NTH-1, mediates the genotoxic effects of 5-hmU

So far only two DNA glycosylases UNG-1 and NTH-1 have been identified and partially characterized in *C. elegans* [13,15]. Both UNG-1 and NTH-1 function upstream of the APN-1 and EXO-3 AP endonucleases and catalyze the first step of the BER pathway. While purified UNG-1 removes uracil, purified NTH-1 acts on thymine glycol, 5-formyl uracil and 5-hmU [13,15]. We found that both *ung-1* and *nth-1* gene expression were elevated when wild type worms were treated with 5-hmU (2B). However, based on the biochemical activities, we anticipate that *nth-1* mutant would display sensitivity to 5-hmU. Survival analysis, scoring for brood size, revealed that the *nth-1(ok724)* mutant was not sensitive to 5-hmU exposure (Figure 5A) or showed increase in germ cell apoptosis under normal growth conditions or when treated with 5-hmU (2.0±1.0 and 2.0±1.0 respectively) (Figure 5D and E). In fact, these findings are consistent with a previous report showing that the *nth-1(ok724)* mutant do not show lifespan defects or sensitivities to oxidants such as hydrogen peroxide and paraquat [13], raising the possibility that the burden of 5-hmU lesions could be processed by another DNA glycosylase. As such, we next examined the *ung-1* mutant for responses towards 5-hmU. Unexpectedly, we found that the *ung-1(tm2862)* deletion mutants exhibited decrease viability (nearly 45 %), as well as elevated levels of germ cell death upon exposure to 5-hmU (Figure 5B and F), suggesting that UNG-1 might recognize and remove 5-hmU lesions from the genome. RNAi downregulation of *apn-1* in the *ung-1(tm2862)* mutant further decreased the viability of the animals and enhanced the number of apoptotic germ cells (nearly 80 %) upon 5-hmU exposure (Figure 5B and F), suggesting that both

UNG-1 and APN-1 contribute independently to process the 5-hmU lesion. Interestingly, the diminished viability and enhanced germ cell death observed by RNAi downregulation of *apn-1* in the *ung-1(tm2862)* mutant was not seen when similar experiment was conducted in the *nth-1(ok724)* mutant (Figure 5A and E). We interpret this finding to suggest that NTH-1 might act *in vivo* to remove some of the 5-hmU lesions and at the same time produce toxic 3′-α,β unsaturated aldehyde that requires the 3′-diesterase function of APN-1. As such, in the absence of NTH-1 these toxic 3′-α,β unsaturated aldehyde lesions are not generated.

Since *exo-3(tm4374)* mutants were not sensitive to 5-hmU, we tested whether RNAi downregulation of *ung-1* would alter its sensitivity. Interestingly, the knockdown of *ung-1* in the *exo-3(tm4374)* mutant did not sensitize the *exo-3(tm4374)* mutant to 5-hmU (Figure S5A). This unexpected finding prompted us to check whether *apn-1* gene expression level would be induced in the *exo-3(tm4374)* mutant, and as such, compensates to repair 5-hmU lesions in the absence of UNG-1. Indeed, the *apn-1* expression level was at least 2-fold higher in the *exo-3(tm4374)* mutant as compared to the wild type, and which was stimulated to 3-fold upon treatment of the animals with 5-hmU (Figure S5B). We believe that the lack of sensitivity of the *exo-3(tm4374)* mutant to 5-hmU might be explained by the induction of *apn-1* gene expression.

3.2.6. Recombinant UNG-1 exhibits 5-hmU activity

We next checked whether UNG-1 has the ability to remove 5-hmU from an oligonucleotide substrate. To do this, we created stem-loop deoxyoligonucleotide substrates bearing either uracil, 5-hmU or the AP site tetrahydrofuran (THF) opposite adenine (U:A, 5-hmU:A and THF:A) at the six position from the 5′-end bearing 6-Carboxyfluorescein [36]. We incubated the substrates for 30 mins at 25 °C without and with GST-UNG-1 purified from an *E. coli* expression system (Figure S6) [14] followed by the addition of *C. elegans* APN-1 purified from a *S. cerevisiae* expression system [20] and then a further incubation for 30 mins at 37 °C. The enzymatic incision of the substrate released a fluorescently labeled 5-mer product that can be detected by a fluorometer. The purified GST-UNG-1 removed uracil from the U:A substrate to create an AP site that was cleaved by the purified GST-APN-1

(Figure 6). Interestingly, the purified GST-UNG-1 also processed the 5-hmU substrate, which was subsequently cleaved by GST-APN-1 (Figure 6). In control experiments, GST-UNG-1 alone did not produce the cleaved product from either the U:A or the 5-hmU:A substrate, unless GST-APN-1 was added (Figure 6), suggesting that the GST-UNG-1 preparation has no contaminating AP endonuclease or AP lyase activity. In additional controls, GST-APN-1 alone did not incise the U:A or 5-hmU:A substrate, unless the substrates were pre-incubated with GST-UNG-1 (Figure 6). However, GST-APN-1 alone incised the THF substrate (Figure 6) and not the GST-UNG-1 as determined in other control experiments. These data strongly suggest that UNG-1 possesses the ability to remove 5-hmU, albeit less effectively as compared to uracil (Figure 6).

3.2.7. POLQ-1 is required for DNA synthesis after removal of 5-hmU lesions

Upon removal of the 5-hmU lesion and incision of the AP site by the BER pathway, a DNA polymerase would be required to fill the single nucleotide gap with a correct nucleotide [37]. A previous study identified POLQ-1 as the DNA polymerase required for the insertion of single nucleotide in the BER pathway in *C. elegans* [38]. In addition, another study showed that POLQ-1 is involved in the repair of DNA interstrand cross-link (ICL) [39]. *C. elegans* disrupted for the *polq-1* gene show hyper-activation of the DNA damage checkpoint-dependent cell-cycle arrest, as well as enhanced apoptosis in germ cells following treatment with ICL agents [39]. As such, we reasoned that POLQ-1 could be involved in processing 5-hmU and that its downregulation would leave a single nucleotide gap in the damaged strand, which in turn will trigger germ cell apoptosis. Indeed, we found that the *polq-1(tm2572)* mutants exposed to 5-hmU showed a significant increase in the average number of apoptotic cells (9.0±1.0) as compared to the no treatment condition (5.0±1.0) (Figure S7). Depletion of *apn-1* in the *polq-1(tm2572)* mutant resulting in the *polq-1(tm2572); apn-1(RNAi)* knockdown mutant that showed an increase in the average number of 12.0±2.0 of apoptotic germ cells when treated with 5-hmU, as compared to 8.0±1.0 in the untreated (Figure S7). The data suggest that POLQ-1 performs additional roles besides serving as the DNA polymerase required to fill the single nucleotide gap created following removal of 5-hmU from the genome. In fact, *C. elegans* POLQ-1 is related to the human DNA polymerase *theta* that is responsible for repairing double strand breaks in the alternative NHEJ pathway[40].

3.2.8. Mutants defective in either the MMR, NER or HR pathway do not show significant increase in germ cell death upon 5-hmU exposure

We next examined whether processing of the 5-hmU lesions would be specific to the BER pathway or the lesion could be channeled to other DNA repair pathways. To do this, we selected representative mutants of the three additional DNA repair pathways, namely *msh-2* of the mismatch repair (MMR), *xpa-1* of the nucleotide excision repair (NER) and *rad-51* of the homologous recombination (HR) repair pathways and checked for the extent of germ cells apoptosis following exposure to 5-hmU.

We first assessed the levels of germ cell apoptosis in the MMR deficient mutant *msh-2(ok2410)*. These *msh-2(ok2410)* mutants did not display significant numbers of apoptotic cells either under standard growth conditions or when treated with 5-hmU (4.0±1.0 and 4.0±1.0, respectively) (Figure 7A [i] and 6B). Downregulation of the *apn-1* gene *via* RNAi in the *msh-2(ok2410)* mutant did not increase the average number of apoptotic cells in the *msh-2(ok2410); apn-1(RNAi)* mutant following 5-hmU exposure (4.0±1.0 and 6.0±2.0, respectively) (Figure 7B), as compared to level (14.3±1.7) in the treated *apn-1(tm6691)* mutant (Figure 3B [vi vs. ii] and Figure 3D). Since it was previously reported that defects in the MMR pathway reduce DNA damage-induced germ cell apoptosis following exposure to genotoxic stress [41], we interpret our finding to suggest that MSH-2 could act to recognize the 5-hmU lesion and recruit NTH-1. Thus, in the absence of MSH-2, NTH-1 would be blocked from generating the toxic 3′-α,β unsaturated aldehyde lesions in DNA and therefore protect the *apn-1* mutant.

We next examined whether the NER pathway mutant *xpa-1(ok698)* would undergo germ cell apoptosis when challenged with 5-hmU. These *xpa-1(ok698)* mutant animals devoid of the XPA-1 protein showed an increase in the average number of germ cell apoptosis under standard growth conditions and which was slightly elevated after exposure to 5-hmU (6.0±2.0 and 8.0±1.0, respectively) (Figure 7A [ii] and 7C). Upon downregulation of apn-1 by RNAi, the resulting *xpa-1(ok698); apn-1 (RNAi)* knockdown mutant displayed higher levels of apoptotic cells upon exposure to 5-hmU, and depicting the same average number (14.0±1.0) of apoptotic cells per animal (Figure 7C), as the treated *apn-1(tm6691)* mutant (Figure 3B [vi vs. ii] and Figure 2D), excluding a major role for the NER pathway in processing the 5-hmU lesion.

We finally examined the involvement of the HR pathway in processing the 5-hmU lesion using the *rad-51(ok2218)/nT1* mutant. This rad-51 mutant already showed high endogenous levels of germ cell apoptosis due to spontaneous unrepaired meiotic breaks as evidenced by an average number of apoptotic cells of 8.0±1.0 under standard growth conditions (Figure 7D). However, the number of germ cell corpse did not increase upon exposure to 5-hmU (8.0±1.0) (Figure 7A [iii] and 7D), suggesting that the 5-hmU lesion is this mutant is processed by other dominant DNA repair pathway. We therefore depleted *apn-1* expression via RNAi in the *rad-51*(*ok2218*)/*nT1* mutant and the resulting *rad-51(ok2218)/nT1*; *apn-1(RNAi)* knockdown mutant showed a substantial increase in the average number of apoptotic cells after treatment with 5-hmU (18.0±1.0) (Figure 7D). Thus, it would appear that the high level of germ cell death in the *rad-51(ok2218)/nT1*; *apn-1(RNAi)* mutant can be explained by an additive effect from the spontaneous germ cell death from the *rad-51* mutant and that caused by the lack of APN-1 to process the 5-hmU lesions. Taken together, we conclude that BER is the predominant pathway involved in processing the 5-hmU lesions, while the NER pathway may have a minor role and not that of the MMR and HR pathways.

3.3. Discussion

In this study, we present several novel findings regarding the base-excision repair pathway in *C. elegans* that is equipped with two DNA glycosylases, UNG-1 and NTH-1, as well as two AP endonucleases/3′-diesterases, APN-1 and EXO-3, to remove damaged bases and process the resulting AP sites [4,13,15]. *C. elegans* UNG-1 has been shown to remove uracil, while NTH-1 has a broader substrate specificity and removes thymine glycol, 5-formyluracil and 5-hmU from lesion containing DNA substrates using purified enzymes [13-15]. In the case of the two AP endonuclease/3′-diesterases, we have previously shown that APN-1 has additional enzymatic activities and can act on many types of DNA lesions *in vitro*, while this ability is restricted for EXO-3 [4]. Based on the *in vitro* specificities of these enzymes one might expect that *C. elegans* devoid of both NTH-1 and APN-1 would have the most severe phenotypes when challenged with DNA damaging agents. Herein, we challenged *C. elegans* BER-deficient mutants with the nucleoside form of 5-hmU, and unexpectedly observed very striking phenotypes that prompted a reconsideration of the *in vivo* roles of UNG-1 and NTG-1 in this organism. In our approach, we exposed the animals to 5-hmU and monitored several readouts including brood size, lifespan and germ cell apoptosis. The latter analysis is a very sensitive reporter especially for agents that induce genotoxic stress and mutants defective in DNA repair exhibit elevated levels of germ cell death. The observations that 5-hmU caused a decrease in the brood size and lifespan, as well as an increase in germ cell apoptosis, prompted the conclusion that 5-hmU must be incorporated into the genome of the animals to trigger a DNA damage respond. In fact, mass spectrometry analysis revealed that if mammalian cells were exposed to 5-hmU this oxidized nucleoside became incorporated into the genome [32,33]. We attempted to monitor the levels of 5-hmU lesion in *C. elegans* genome, but we were unable to see an increase over background using the wild type and the BER deficient mutants such as *ung-1(tm2862)* and *apn-1(tm6691)*, which we ascribed to several technical problems that will be resolved. Nonetheless, we have partially purified recombinant UNG-1 as a GST fusion protein and demonstrated that it has the ability to act on 5-hmU lesion installed on a stem-loop deoxynucleotide substrate. This finding is consistent with the *ung-1* mutants being very sensitive to 5-hmU exposure. In fact, we were surprised that the *nth-1* mutants showed very little or no sensitivity towards 5-hmU, although

NTH-1 was previously shown to possess the ability to remove 5-hmU from lesion containing DNA substrates *in vitro* [13-15]. We propose that *C. elegans* UNG-1 may have evolved to acquire a broader substrate specificity and thus could act as the dominant DNA glycosylase *in vivo* to remove various modified forms of uracil such as the 5-hmU lesion. It is noteworthy that *C. elegans* lacks the related human SMUG1 DNA glycosylase, which has been shown to remove 5-hmU [6], and the *C. elegans* UNG-1 shares a modest 12.6 % identity with SMUG1 [33]. A closer examination of the identity revealed that *C. elegans* UNG-1 shares five amino acid residues Ser58, Pro218, Gly226, Glu233 and Leu234 that are unique to human SMUG1 residues Ser48, Pro166, Gly174, Glu181 and Leu182 and the mouse SMUG1, but which are absent in human UNG1 (Figure S?). Whether these five residues are involved in conferring upon *C. elegans* UNG-1 the human SMUG1 ability to recognize and process 5-hmU will need to be investigated.

UNG-1 action on 5-hmU would leave an AP site that can be processed by either APN-1 or EXO-3 (see model in Figure 8). If the AP endonuclease function of APN-1 and EXO-3 is redundant in *C. elegans*, then the absence of either enzyme would not cause sensitivity to 5-hmU. Since our data revealed that (i) *C. elegans* mutants devoid of APN-1 were sensitive to 5-hmU, but not EXO-3 deficient animals, (ii) *apn-1*, and not *exo-3*, gene expression was inducible upon treatment of the animals with 5-hmU, and (iii) *apn-1* gene expression is constitutively higher in the *exo-3* mutant, we strongly suggest that APN-1 has a vital role in processing the 5-hmU lesions. In fact, we have previously reported that APN-1 has distinct function(s) from EXO-3, and more recently SenGupta et al., 2013 showed that accumulation of the early DNA damage response foci, RPA-1, following treatment with the anticancer agent 5-fluorouracil, depends primarily on EXO-3 role to incise the DNA in order to initiate the mismatch repair pathway [18,42]. We propose a model whereby UNG-1 removes 5-hmU creating an AP site that is either processed by APN-1 or EXO-3 [23,43] (Figure 8). In the absence of UNG-1, the 5-hmU lesion is processed by the second pathway whereby NTH-1 removes the lesion, but simultaneously creates a genotoxic single strand break with a blocked 3′-end, α,β unsaturated aldehyde that blocks DNA repair synthesis [7]. It is possible that the resulting blocked 3′-end is not rapidly removed by APN-1, in particular, if EXO-3 stimulates NTH-1, as seen for the DNA glycosylases OGG1 and TDG by APE1 in human cells [44,45], to create an abundance of blocked 3′-ends that overwhelms the 3′-diesterase and or 3′- to 5′-exonuclease repair capacity of APN-1. Therefore, animals devoid of both UNG-1 and APN-1 would be extremely sensitive to 5-hmU due to excessive accumulation of single strand breaks with blocked 3′-ends. If indeed the *apn-1* mutant sensitivity to 5-hmU is a result of NTH-1 β-lyase activity generating the production of single strand breaks with blocked 3′-ends, then the removal of NTH-1 should rescue the lethality of the *apn-1* mutant. In fact, we showed herein that RNAi downregulation of *nth-1* can suppress the genotoxic effects of 5-hmU in the *apn-1* mutants. A similar suppressive effect was also observed in the *msh-2*; *apn-1(RNAi)* knockdown mutant, which may implicate MSH-2 in the same pathway as NTH-1. Thus, in the absence of NTH-1 and APN-1, as in the *nth-1(ok724)* mutant downregulated for *apn-1* by RNAi, the 5-hmU lesion would be removed by UNG-1 leaving an AP site that will be processed by the AP endonuclease activity of EXO-3 [23,43]. We exclude the possibility that EXO-3 acts to remove the 3′- α,β unsaturated aldehyde generated by NTH-1, as the *exo-3(tm4374); apn-1(RNAi)* knockdown mutant is no more sensitive to 5-hmU than the *apn-1(tm6691)* single mutant. Consistent with this notion, we have previously shown that EXO-3, unlike APN-1, lacks a 3′- to 5′-exonuclease activity, which might be the activity needed to remove such bulky and toxic 3′-blocked end [18-21]. In fact, it has been reported that diminishing UNG-1 activity to prevent production of AP sites recues the lifespan defect of the *exo-3* mutants [23]. This phenomenon was not observed in *exo-3* mutants devoid of NTH-1, suggesting that this DNA glycosylase is not producing intermediate lesions to be processed by EXO-3 [23].

In short, we have established that the oxidized product of thymine, 5-hmU, is genotoxic in *C. elegans* and that this lesion is predominantly processed by the BER pathway. The most striking observation from our study is the requirement of UNG-1 for the removal of 5-hmU. We believe that *C. elegans* may have conserved only UNG-1 and NTH-1, which have evolved to recognize a broad spectrum of modified bases.

3.4. Acknowledgements

We thank Taramatti Harihar and Rana Rizk for the preparation of the recombinant GST-UNG-1 and repeating the data in Figure 6. We thank Dr. Alex Parker (Département de Neurosciences Université de Montréal and Centre de Recherche du CHUM) for providing the RNAi strains. We are grateful to the CGC and Shohei Mitani for providing the *C. elegans* strains. This work was supported by a grant from the Natural Science and Engineering Research Council of Canada to D.R. (RGPIN/202432–2012). A.P. holds a Fonds de Recherche du Québec – Santé (FRQS) Research Doctoral Award.

Conflict of interest: The authors declare that they have no conflicts of interest with the contents of this article.

Competing financial interests: The authors declare that there are no competing financial interests associated with this work.

Author contributions: A.P., J.R.W., and D.R. designed the experiments. A.P. performed most of the experiments. A.P., J.R.W., H.U.S., and D.R. analyzed the data. A.P. and D.R. wrote the manuscript. A.P., D.R., J.R.W., and H.U.S corrected the final version of the manuscript..

3.5. Materials and methods

Nematode strains and culture conditions—The [*apn-1(tm6691)* II], [*exo-3(tm4374)* I], [*ung-1(tm2862)* III] and [*polq-1(tm2572)* III] were obtained from Shohei Mitani (Tokyo Women′s Medical University School of Medicine, Japan and the National Bioresource Project for the nematode *C. elegans*). The Bristol N2 (wild type), MD701 [*bcIs39* [lim-7p::ced-1::GFP + lin-15(+)], RB877 [*nth-1(ok724)* III], RB1864 [*msh-2(ok2410)* I], RB864 [*xpa-1(ok698)* I], VC1973 [*rad-51(ok2218) IV/nT1* [qIs51] (IV;V)] *, TJ1 [*cep-1(gk138)* I], MT1082 [*egl-1(n487)* V], MT4770 [*ced-9(n1950)* III], MT5287 [*ced-4(n1894)* III], MT3002 [*ced-3(n1286)* IV] *Caenorhabditis elegans* strains were obtained from the CGC Stock center (*Caenorhabditis* Genetics Centre, University of Minnesota, Minneapolis, USA). The alleles utilized in this work were all previously validated to be null. All *C. elegans* strains were maintained at 20°C on nematode growth medium (NGM) agar (2.5 g/L peptone, 51.3 mM NaCl, 17 g/L agar, 1 mM $CaCl_2$, 1 mM $MgSO_4$, 25 mM KPO_4, and 12.9 μM cholesterol) enriched with a lawn of streptomycin-resistant *Escherichia coli* OP50 bacterial strain as a source of food. For all *in vivo* experiments, developmental staged-synchronized nematodes were obtained by hypochlorite treatment of gravid adult hermaphrodites. Eggs were allowed to hatch on M9 buffer (6g Na_2HPO_4, 3g KH_2PO_4, 5g NaCl, 0.25g $MgSO_47H_2O$ per liter filter sterilized). In all experiments, animals were monitored from day 1 post-L1 larvae stage and from L4 to avoid experimental bias. *Homozygous *rad-51/rad-51*[46] animals show almost complete inviability due to high embryonic lethality in their progeny, therefore we monitored heterozygote animals due to the easy RNAi-feeding for further analyses. *C. elegans* strains were backcrossed at least three times.

Drug treatment—For drug treatment we followed the same protocol as recently reported[28]. The anthracycline doxorubicin, alkylating agent methyl methanesulfonate (Sigma Cat. No 129925), the oxidative agent 5-hydroxymethyluracil and the water-soluble platinum compound cisplatin were added to the NGM agar medium (55°C) before solidification to obtain a final concentration of 100 μM for doxorubicin and cisplatin, 0.25 μM for methyl methanesulfonate and 1 μM for 5-hydroxymethyluracil (molecular weight 258 g/mole), respectively. For all experiments, L1-staged from F1 synchronized nematodes were transferred to NGM control agar plates and containing doxorubicin, cisplatin and methyl methanesulfonate. Doxorubicin and cisplatin working concentrations were chosen based on previously reported assays[47]. All drug-containing plates were freshly made prior to each experiment. 5-hydroxymethyluracil was prepared by Dr. Richard Wagner (Département de Médecine Nucléaire et Radiobiologie, Faculté de Médecine et des Sciences de la Santé, Université de Sherbrooke). The oncology pharmacy department of the Maisonneuve-Rosemont Hospital (HMR), provided doxorubicin and cisplatin.

Brood size analyses—Single L1-staged worm from wild type and mutant genotypes were transferred to seeded NGM plates without and with the drugs and maintained at 20 °C. Worms were transferred to fresh plates each day until they ceased laying eggs. The hatched larvae on each plate were counted and total number of viable larvae that developed to the L1 stage descended from a single hermaphrodite was counted. The average number of viable larvae from 10 to 25 animals of a strain was plotted as brood size where the progeny is allowed to reach adulthood and scored as being fertile or sterile. The brood size quantification in this analysis follows the same method as previously reported[28].

Lifespan assay—Lifespan analyses were performed at 20°C in standard conditions and assessed blindly as previously reported[48].

Microscopy and imaging—All microscopy was performed utilizing a DeltaVision Elite Image Restoration System (Applied Precision) with either 40x/0.65-1.35 or 63x/1.42 oil objective. The worms were anesthetized with levamisole (5 µM, Sigma Cat. No L0380000) and mounted on 2% agarose pads for their respective imaging and quantification. Images were processed utilizing ImageJ imaging software[49].

DNA damage response assay and germ cells imaging—The methods previously described were used[28,30]. Briefly, for scoring of apoptotic corpses in nematodes, L1-staged synchronized N2 wild type and DNA repair deficient mutants were exposed to different doses of drugs followed by germ cells apoptosis assay. Between 18 to 24 hours past L4-staged nematodes, adult staged worms were assayed with differential interference contrast

(DIC) microscopy (Nomarski) optics and the vital DNA dye acridine orange (Sigma Cat. No A6024). Nematodes were incubated in the dark for 2 hours at 20°C on NGM plates containing 1 ml of 50 μg/ml of acridine orange DNA dye dissolved in M9 buffer. Stained worms were transferred to fresh OP50-seeded NGM plates to incubate for 2 hours in order to clear off the stained bacteria. The acridine orange-stained and DIC-visible apoptotic corpses were counted with an exposure time of 1 second and 0.8 seconds, respectively. The engulfment of apoptotic corpses was scored utilizing the CED-1::GFP reporter and imaged similarly with an exposure time of 1 second utilizing the GFP channel. Images were collected as a series of 25/0.5 μm optical sections covering the complete thickness of the gonad arm.

Purification of recombinant GST-UNG-1—The plasmid pGEX-CeUNG-1 designed to express UNG-1 as a GST-UNG-1 fusion protein was kindly provided by Dr. Qiu-Mei Zhang-Akiyama (Japan). The plasmid was introduced into the *E. coli* strain BL21(DE3) and ampicillin resistant colonies were used for preparing whole cell extracts derived from 50 ml of cells (OD 600 of 0.6 treated with 0.1 mM IPTG for 12 hours to induce the expression level of GST-UNG-1) for the purification of the protein as previously described, except using GST-magnetic beads [14]. The GST-magnetic beads (50 μl) were washed three times with washing buffer (PBS plus 125 mM Tris-HCl pH 7.5 and 150 mM NaCl), incubated with 500 μl of whole cell extract for 2 hours at 4oC, following three washes with 200 μl of washing buffer and elution with three 100 μl of elution buffer (washing buffer containing 50 mM glutathione).

Preparation of oligonucleotide substrates and assay conditions—The preparation of the substrates and assay conditions were as previously described [36], except GST-UNG-1 was pre-incubated with the substrate in the BER reaction buffer 25 mM HEPES pH 8.0, 150 mM KCl, 0.5 mM EDTA pH 8.0, 1 % glycerol and 1 mM DTT (prepared fresh) for 30 mins at 25°C, prior to the addition of the reaction buffer (50 mM HEPES pH 7.5, 50 mM KCl and 10 mM $MgCl_2$) and a further incubation with purified GST-APN-1 for 30 mins at 37°C. The reactions were carried out, where indicated, with 20 ng of purified GST-UNG-1 and 20 ng of purified GST-APN-1 and the released product was monitored by a fluorometer (Thermo Fisher Scientific, Thermo Scientific^{TM}, model: Fluoroskan Ascent^{TM}).

Relative RNA quantification to monitor gene expression—Total RNA (RNeasy mini kit Qiagen Cat. N° 74104) was prepared from ~1000 young adult synchronized nematodes and used for cDNA synthesis (Applied Biological Materials Inc. Cat. N° G490) followed by quantitative real-time PCR (qRT-PCR). qRT-PCR was performed with the BrightGreen 2X q-PCR Mastermix (Applied Biological Materials Inc. Cat. N° MasterMix-LR) starting at 95 °C for 2 min, followed by 40 cycles at 95 °C for 5 sec, 60 °C for 30 sec and 72 °C for 30 sec. Transcript levels were normalized to the internal control *act-1* encoding the actin protein. The forward and reverse primer sequences utilized in this study were: *apn-1*: 5'-GCACATCCAGAAGACGCTGC-3' and 5'-TCTACGGTAGTTCCAGGGCT-3'; *exo-3*: 5'-AGGAGCCTGACCTCGTTTTT-3' and 5'-GTAGCCACCGTTCTTCTCTG-3'; *nth-1*: 5'-TTTCCAGTCAAACCAGAGAT-3' and 5'-AAATCCAACAGGACACAAAA-3'; *ung-1*: 5'-TTCCGGACATGTTCCTCAAA-3' and 5'-TTCATTGCCCGCGGGAACTT-3; *act-1*: 5'-TGCTGATCGTATGCAGAAGG-3' and 5'-TAGATCCTCCGATCCAGACG-3'.

RNA interference analysis—*Escherichia coli* HT115DE3 strain harboring specific RNAi constructs against *apn-1* (T05H10.2 AAB39924 10018 G6), *exo-3* (R09B3.1 AAC82328 10018 F7), *nth-1* (R10E4.5 R10E4.5 11002 D5) and *ung-1* (Y56A3A.29 Y56A3A.29 10056 D12) was grown on lysogeny broth (LB) agar plates containing ampicillin and tetracycline. Overnight cultures were grown in LB media containing ampicillin. For *apn-1*, *exo-3*, *nth-1* and *ung-1* RNAi-driven knockdown experiments, nematodes were maintained until first generation (F1) on NGM agar plates containing 1 mM IPTG (isopropyl-β-D-1-thiogalactopyranoside) enriched with a lawn of *E. coli* HT115DE3 expressing RNAi constructs in the pL4440-feeding vector at standard temperature 20 °C. For *apn-1*, *exo-3*, *nth-1* and *ung-1* RNAi-driven knockdown efficiency, mRNA expression levels were measured in synchronized young adults collected from the F1 generation of nematodes fed with *E. coli* expressing RNAi targeted to the indicated genes. The RNAi clones were obtained from the Ahringer laboratory library[50] and verified by sequencing. The depletion efficiency of *apn-1*, *exo-3*, *nth-1* and *ung-1* genes was validated by qRT-PCR. In all experiments synchronized L4-staged animals were fed RNAi expressing bacteria and the resulting F1 animals were analyzed for phenotypes.

Statistical analyses—For the Brood size analysis, statistical differences were calculated by the unpaired two-tail t-test (*P<0.03; **P<0.01; ***P< 0.0005) and represented as ± S.D. Lifespan analyses were performed utilizing the Kaplan-Meier estimator calculating the Log-rank test for statistical significance utilizing OASIS software (Online Application for the Survival Analysis of Lifespan Assays Performed in Aging Research) [45]. Germ cells death statistical significance was assessed with the Mann-Whitney U-test calculator Mean values ± s.e.m were calculated for each condition. *P<0.05; **P<0.01; ***P<0.001; ****P<0.0001 were considered to be statistically significant. N.S. = Non-Significant. Statistical differences were calculated by using the GraphPad Prism Statistical Software Mac Version 6.

3.6. Figure legends

Figure 1. *C. elegans* mutants deficient in both APN-1 and EXO-3 are hypersensitive to DOX-, MMS- and CDDP-induced DNA lesions. A, Scheme of the experimental design. B, C and D, Brood size analyses of the indicated genotypes. The data are the mean±S.D. of three independent experiments (*n*=10 monitored for 3 days). Control; Wild type: 305±17; *apn-1(tm6691)*: 181±47; *exo-3(tm4374)*: 201±29; *exo-3(tm4374); apn-1(RNAi)*: 134±61. Exposed to drugs; **B,** DOX 100 μM: Wild type: 199±37; *apn-1(tm6691)*: 108±50; *exo-3(tm4374)*: 128±29; *exo-3(tm4374); apn1(RNAi)*: 57±18. **C,** MMS 0.25 μM: Wild type: 168±15; *apn-1(tm6691)*: 93±20; *exo-3(tm4374)*: 97±15; *exo-3(tm4374); apn1(RNAi)*: 46±21. **D,** CDDP 100 μM: Wild type: 210±33; *apn-1(tm6691)*: 82±31; *exo-3(tm4374)*: 98±41; *exo-3(tm4374); apn1(RNAi)*: 63±38. Error bars represent the S.D. Unpaired two-tail t-test ***P<0.01; ****P<0.0005 were considered to be statistically significant. N.S. = Non-Significant. DOX, doxorubicin; MMS, methyl methanesulfonate; and CDDP, cisplatin.

Figure 2. *C. elegans apn-1*, but not *exo-3*, mutants are sensitive to the nucleoside 5-hmU. A, Brood size analysis of animals exposed to 5-hmU. Wild type: 269.8±46; *apn-1(tm6691)*: 102±21; *exo-3(tm4374)*: 171±43; *exo-3(tm4374); apn1(RNAi)*: 68±55. Control; Wild type: 305±17; *apn-1(tm6691)*: 181±47; *exo-3(tm4374)*: 201±29; *exo-3(tm4374); apn1(RNAi)*: 134±61. Error bars represent the S.D. Unpaired two-tail t-test ***P<0.01; ****P<0.0005 were considered to be statistically significant. N.S. = Non-Significant. **B,** Mean lifespan of the indicated animals exposed to 5-hmU. **C,** Kaplan-Meier survival plot showing the percentage of alive animals when the indicated genotypes were exposed to 5-hmU. L1-staged animals (*n* = 100) were exposed to 5-hmU (1 μM) and lifespan was blindly analyzed starting from young adult worms. The mean lifespan of two independent experiments is shown.

Figure 3. The *apn-1(tm6691)* mutant animals display increase spontaneous and 5-hmU-induced germ cell apoptosis. A, Scheme showing the region of germ cells analyzed for apoptotic corpses in the posterior side of the gonad arm. **B,** Representative images of acridine orange-stained and DIC (lower left) of control and drug-treated apoptotic corpses from the indicated genotypes. Apoptotic cell corpses were identified as bright spots correlating with raised-bottom-like refractive corpses shown on DIC images. Posterior is right and dorsal is top. Scale bar = 15 μm. **C-F,** Box and whisker plots showing quantification of apoptotic corpses from control and drug-treated animal and displaying the maximum, minimum, upper & lower quartiles, and sample median. L4-stage animals were treated with D, 5-hmU (1 μM), E, DOX 100 μM and F, MMS 0.25 μM, and apoptotic corpses were quantified the following day in the gonad arms of young adult staged worms. Statistical significance bars represent results of Mann-Whitney U-test of mean difference (*P<0.05; **P<0.01; ***P<0.001 and ****P<0.0001) computed from three independent experiments (*n* = 30).

Figure 4. 5-hmU induces CED-1 engulfment of apoptotic germ cells. A, Representative images of control and 5-hmU-treated *bcls39* [CED-1::GFP] worms. The ring around the

apoptotic corpses indicates the engulfment of apoptotic bodies shown by white arrows. Scale bar = 10 μm. **B,** Box and whisker plots showing quantification of the engulfment of apoptotic bodies.

Figure 5. *ung-1*, but not *nth-1*, mutants are sensitive to the genotoxic effects of 5-hmU. A, B and **C,** Control and 5-hmU-treated animals for analysis of brood size as described in Figure 1B-D. The data are the mean±S.D. of three independent experiments (*n*=10 monitored for 3 days). Error bars represent the S.D. Unpaired two-tail t-test ***P<0.01; ****P<0.0005 were considered to be statistically significant. N.S. = Non-Significant. A, Control; Wild type: 319±38; *nth-1(ok724)*: 260±48; *nth-1(ok724); apn1(RNAi)*: 232±30, and exposure to 5-hmU; Wild type: 269±46; *nth-1(ok724)*: 244±42; *nth-1(ok724); apn1(RNAi)*: 195±33. **B,** Control; Wild type: 319±38; *ung-1(tm2862)*: 244±39; *ung-1(tm2862); apn1(RNAi)*: 146±45 and exposure to 5-hmU; Wild type: 269±46; *ung-1(tm2862)*: 157±32; *ung-1(tm2862); apn1(RNAi)*: 65±35. **C,** Control; Wild type: 319±38; *exo-3(tm4374)*: 241±19; *exo-3(tm4374); nth-1(RNAi)*: 247±45 and exposure to 5-hmU; Wild type: 269±46; *exo-3(tm4374)*: 219±30; *exo-3(tm4374); nth-1(RNAi)*: 215±12. **D,** Representative images of acridine orange-stained and DIC (lower left) of 5-hmU treated *nth-1(ok724)* and *ung-1(tm2862)* mutant animals as described in Figure 2B. **E** and **F,** Box and whisker plots showing quantification of apoptotic corpses from control and 5-hmU-treated of E, *nth-1(ok724)* and F, *ung-1(tm2862)* mutant animals and scored as in Figure 2C.

Figure 6. Recombinant GST-UNG-1 acts on 5-hmU lesion to produce APN-1 cleavable AP site. GST-UNG-1 and GST-APN-1 were purified from *E. coli* and *S. cerevisiae* expression system, respectively [14,20]. The enzymes were incubated with the indicated stem-loop deoxyoligonucleotide substrates bearing either uracil, 5-hmU or the AP site tetrahydrofuran (THF) opposite adenine (U:A, 5-hmU:A and THF:A) at the six position from the 5′-end bearing 6-Carboxyfluorescein [36]. UNG-1 was incubated with the substrates for 30 mins at 26°C followed by the addition of APN-1 and then a further incubation for 30 mins at

37°C. The enzymatic incision of the substrate released a fluorescently labeled 5-mer product that can be detected by a fluorometer (Fluoroskan Ascent).

Figure 7. Mutants defective in the MMR, NER or HR pathway do not show significant increase in germ cell death upon exposure to 5-hmU. A, Acridine orange stained and DIC images as described in Figure 2. The images represent a component from each of the three additional main DNA repair pathways, [i] *msh-2(ok2410)* Mismatch Repair pathway, [ii] *xpa-1(ok698)* Nucleotide Excision Repair pathway and [iii] *rad-51(ok2218)* Homologous Recombination pathway, respectively. B-D, Box and whisker plots depicting quantification of apoptotic corpses observed by the DNA repair defective mutants in the absence and presence of 5-hmU treatment.

Figure 8. A model illustrating the repair of 5-hmU opposite adenine (5-hmUA) *via* the BER pathway. Under physiological conditions thymine in the genome is oxidized to 5-hmU creating the mispair 5-hmUA. In this model, UNG-1 is proposed to recognize and remove 5-hmU creating an AP site that can be processed by either APN-1 or EXO-3. In the absence of UNG-1, NTH-1 removes the 5-hmU lesion and simultaneously cleaves the resulting AP site to create a secondary 3′-blocked genotoxic lesion, 3′-α, β unsaturated aldehyde, which requires processing by the 3′-diesterase or 3′- to 5′-exonuclease activity of APN-1. The 5-hydroxymethyluracil (5-hmU) structure was obtained from PubChem (ID: 78168) and rendered with Chemaxom.

3.7. References

1 Madugundu, G. S., Cadet, J. & Wagner, J. R. Hydroxyl-radical-induced oxidation of 5-methylcytosine in isolated and cellular DNA. *Nucleic Acids Res* **42**, 7450-7460, doi:10.1093/nar/gku334 (2014).

2 Olinski, R., Starczak, M. & Gackowski, D. Enigmatic 5-hydroxymethyluracil: Oxidatively modified base, epigenetic mark or both? *Mutat Res Rev Mutat Res* **767**, 59-66, doi:10.1016/j.mrrev.2016.02.001 (2016).

3 Reynolds, D. *et al*. Regulation of transcription termination by glucosylated hydroxymethyluracil, base J, in Leishmania major and Trypanosoma brucei. *Nucleic Acids Res* **42**, 9717-9729, doi:10.1093/nar/gku714 (2014).

4 Daley, J. M., Zakaria, C. & Ramotar, D. The endonuclease IV family of apurinic/apyrimidinic endonucleases. *Mutat Res* **705**, 217-227, doi:S1383-5742(10)00086-4 [pii]10.1016/j.mrrev.2010.07.003 (2010).

5 David, S. S., O'Shea, V. L. & Kundu, S. Base-excision repair of oxidative DNA damage. *Nature* **447**, 941-950, doi:10.1038/nature05978 (2007).

6 Boorstein, R. J. *et al*. Definitive identification of mammalian 5-hydroxymethyluracil DNA N-glycosylase activity as SMUG1. *J Biol Chem* **276**, 41991-41997, doi:10.1074/jbc.M106953200 (2001).

7 Zhang, Q. M. *et al*. DNA glycosylase activities for thymine residues oxidized in the methyl group are functions of the hNEIL1 and hNTH1 enzymes in human cells. *DNA Repair (Amst)* **4**, 71-79, doi:10.1016/j.dnarep.2004.08.002 (2005).

8 Hashimoto, H., Hong, S., Bhagwat, A. S., Zhang, X. & Cheng, X. Excision of 5-hydroxymethyluracil and 5-carboxylcytosine by the thymine DNA glycosylase domain: its structural basis and implications for active DNA demethylation. *Nucleic Acids Res* **40**, 10203-10214, doi:10.1093/nar/gks845 (2012).

9 Morera, S. *et al*. Biochemical and structural characterization of the glycosylase domain of MBD4 bound to thymine and 5-hydroxymethyuracil-containing DNA. *Nucleic Acids Res* **40**, 9917-9926, doi:10.1093/nar/gks714 (2012).

10 Krokan, H. E. & Bjoras, M. Base excision repair. *Cold Spring Harb Perspect Biol* **5**, a012583, doi:10.1101/cshperspect.a012583 (2013).

11 Demple, B. & Harrison, L. Repair of oxidative damage to DNA: enzymology and biology. *Annu Rev Biochem* **63**, 915-948 (1994).

12 Friedberg, E. C. *et al.* (ASM Press, Washington, D.C., 2006).

13 Morinaga, H. *et al*. Purification and characterization of Caenorhabditis elegans NTH, a homolog of human endonuclease III: essential role of N-terminal region. *DNA Repair (Amst)* **8**, 844-851, doi:10.1016/j.dnarep.2009.04.020 (2009).

14 Nakamura, N. *et al*. Cloning and characterization of uracil-DNA glycosylase and the biological consequences of the loss of its function in the nematode Caenorhabditis elegans. *Mutagenesis* **23**, 407-413, doi:10.1093/mutage/gen030 (2008).

15 Skjeldam, H. K. *et al*. Loss of Caenorhabditis elegans UNG-1 uracil-DNA glycosylase affects apoptosis in response to DNA damaging agents. *DNA Repair (Amst)* **9**, 861-870, doi:10.1016/j.dnarep.2010.04.009 (2010).

16 Wenzel, D., Palladino, F. & Jedrusik-Bode, M. Epigenetics in C. elegans: facts and challenges. *Genesis* **49**, 647-661, doi:10.1002/dvg.20762 (2011).

17 Greer, E. L. *et al*. DNA Methylation on N6-Adenine in C. elegans. *Cell* **161**, 868-878, doi:10.1016/j.cell.2015.04.005 (2015).

18 Shatilla, A., Leduc, A., Yang, X. & Ramotar, D. Identification of two apurinic/apyrimidinic endonucleases from Caenorhabditis elegans by cross-species complementation. *DNA Repair (Amst)* **4**, 655-670 (2005).

19 Shatilla, A., Ishchenko, A. A., Saparbaev, M. & Ramotar, D. Characterization of Caenorhabditis elegans Exonuclease-3 and Evidence That a Mg(2+)-Dependent Variant Exhibits a Distinct Mode of Action on Damaged DNA. *Biochemistry* **44**, 12835-12848 (2005).

20 Yang, X. *et al*. Functional characterization of the Caenorhabditis elegans DNA repair enzyme APN-1. *DNA Repair (Amst)* **11**, 811-822, doi:S1568-7864(12)00141-3 [pii] 10.1016/j.dnarep.2012.06.009 (2012).

21 Yang, Z., Price, N. E., Johnson, K. M., Wang, Y. & Gates, K. S. Interstrand cross-links arising from strand breaks at true abasic sites in duplex DNA. *Nucleic Acids Res* **45**, 6275-6283, doi:10.1093/nar/gkx394 (2017).

22 Zakaria, C. *et al*. Caenorhabditis elegans APN-1 plays a vital role in maintaining genome stability. *DNA Repair (Amst)* **9**, 169-176, doi:S1568-7864(09)00308-5 [pii] 10.1016/j.dnarep.2009.11.007 (2010).

23 Kato, Y., Moriwaki, T., Funakoshi, M. & Zhang-Akiyama, Q. M. Caenorhabditis elegans EXO-3 contributes to longevity and reproduction: differential roles in somatic cells and germ cells. *Mutat Res* **772**, 46-54, doi:10.1016/j.mrfmmm.2015.01.001 (2015).

24 Forrest, R. A. *et al*. Activation of DNA damage response pathways as a consequence of anthracycline-DNA adduct formation. *Biochem Pharmacol* **83**, 1602-1612, doi:10.1016/j.bcp.2012.02.026 (2012).

25 Sawant, A. *et al*. Differential role of base excision repair proteins in mediating cisplatin cytotoxicity. *DNA Repair (Amst)* **51**, 46-59, doi:10.1016/j.dnarep.2017.01.002 (2017).

26 Gartner, A., Boag, P. R. & Blackwell, T. K. Germline survival and apoptosis. *WormBook*, 1-20, doi:10.1895/wormbook.1.145.1 (2008).

27 Horvitz, H. R. Genetic control of programmed cell death in the nematode Caenorhabditis elegans. *Cancer Res* **59**, 1701s-1706s (1999).

28 Papaluca, A. & Ramotar, D. A novel approach using C. elegans DNA damage-induced apoptosis to characterize the dynamics of uptake transporters for therapeutic drug discoveries. *Sci Rep* **6**, 36026, doi:10.1038/srep36026 (2016).

29 Lans, H. & Vermeulen, W. Tissue specific response to DNA damage: C. elegans as role model. *DNA Repair (Amst)* **32**, 141-148, doi:10.1016/j.dnarep.2015.04.025 (2015).

30 Craig, A. L., Moser, S. C., Bailly, A. P. & Gartner, A. Methods for studying the DNA damage response in the Caenorhabdatis elegans germ line. *Methods Cell Biol* **107**, 321-352, doi:10.1016/B978-0-12-394620-1.00011-4 (2012).

31 Gumienny, T. L., Lambie, E., Hartwieg, E., Horvitz, H. R. & Hengartner, M. O. Genetic control of programmed cell death in the Caenorhabditis elegans hermaphrodite germline. *Development* **126**, 1011-1022 (1999).

32 Mi, L. J., Chaung, W., Horowitz, R., Teebor, G. W. & Boorstein, R. J. Excessive base excision repair of 5-hydroxymethyluracil from DNA induces apoptosis in Chinese hamster V79 cells containing mutant p53. *Carcinogenesis* **22**, 179-186 (2001).

33 Zauri, M. *et al*. CDA directs metabolism of epigenetic nucleosides revealing a therapeutic window in cancer. *Nature* **524**, 114-118, doi:10.1038/nature14948 (2015).

34 Zhou, Z., Hartwieg, E. & Horvitz, H. R. CED-1 is a transmembrane receptor that mediates cell corpse engulfment in C. elegans. *Cell* **104**, 43-56 (2001).

35 Li, Z., Lu, N., He, X. & Zhou, Z. Monitoring the clearance of apoptotic and necrotic cells in the nematode Caenorhabditis elegans. *Methods Mol Biol* **1004**, 183-202, doi:10.1007/978-1-62703-383-1_14 (2013).

36 Svilar, D., Vens, C. & Sobol, R. W. Quantitative, real-time analysis of base excision repair activity in cell lysates utilizing lesion-specific molecular beacons. *J Vis Exp*, e4168, doi:10.3791/4168 (2012).

37 Lindahl, T. & Wood, R. D. Quality control by DNA repair. *Science* **286**, 1897-1905 (1999).

38 Asagoshi, K. *et al*. Single-nucleotide base excision repair DNA polymerase activity in C. elegans in the absence of DNA polymerase beta. *Nucleic Acids Res* **40**, 670-681, doi:10.1093/nar/gkr727 (2012).

39 Muzzini, D. M., Plevani, P., Boulton, S. J., Cassata, G. & Marini, F. Caenorhabditis elegans POLQ-1 and HEL-308 function in two distinct DNA interstrand cross-link repair pathways. *DNA Repair (Amst)* **7**, 941-950, doi:10.1016/j.dnarep.2008.03.021 (2008).

40 Wyatt, D. W. *et al*. Essential Roles for Polymerase theta-Mediated End Joining in the Repair of Chromosome Breaks. *Mol Cell* **63**, 662-673, doi:10.1016/j.molcel.2016.06.020 (2016).

41 Degtyareva, N. P. *et al*. Caenorhabditis elegans DNA mismatch repair gene msh-2 is required for microsatellite stability and maintenance of genome integrity. *Proceedings of the National Academy of Sciences of the United States of America* **99**, 2158-2163, doi:10.1073/pnas.032671599 (2002).

42 SenGupta, T. *et al*. Base excision repair AP endonucleases and mismatch repair act together to induce checkpoint-mediated autophagy. *Nat Commun* **4**, 2674, doi:10.1038/ncomms3674 (2013).

43 Shatilla, A. & Ramotar, D. Embryonic extracts derived from the nematode Caenorhabditis elegans remove uracil from DNA by the sequential action of uracil-DNA glycosylase and AP (apurinic/apyrimidinic) endonuclease. *Biochem J* **365**, 547-553. (2002).

44 Vidal, A. E., Boiteux, S., Hickson, I. D. & Radicella, J. P. XRCC1 coordinates the initial and late stages of DNA abasic site repair through protein-protein interactions. *Embo J* **20**, 6530-6539. (2001).

45 Fitzgerald, M. E. & Drohat, A. C. Coordinating the initial steps of base excision repair. Apurinic/apyrimidinic endonuclease 1 actively stimulates thymine DNA glycosylase by disrupting the product complex. *J Biol Chem* **283**, 32680-32690, doi:10.1074/jbc.M805504200 (2008).

46 Rinaldo, C., Bazzicalupo, P., Ederle, S., Hilliard, M. & La Volpe, A. Roles for Caenorhabditis elegans rad-51 in meiosis and in resistance to ionizing radiation during development. *Genetics* **160**, 471-479 (2002).

47 Sendoel, A. *et al*. DEPDC1/LET-99 participates in an evolutionarily conserved pathway for anti-tubulin drug-induced apoptosis. *Nature cell biology* **16**, 812-820, doi:10.1038/ncb3010 (2014).

48 Lionaki, E. & Tavernarakis, N. Assessing aging and senescent decline in Caenorhabditis elegans: cohort survival analysis. *Methods in molecular biology* **965**, 473-484, doi:10.1007/978-1-62703-239-1_31 (2013).

49 Schneider, C. A., Rasband, W. S. & Eliceiri, K. W. NIH Image to ImageJ: 25 years of image analysis. *Nat Methods* **9**, 671-675 (2012).

50 Kamath, R. S. & Ahringer, J. Genome-wide RNAi screening in Caenorhabditis elegans. *Methods* **30**, 313-321 (2003).

51 Yang, J. S. *et al*. OASIS: online application for the survival analysis of lifespan assays performed in aging research. *PLoS One* **6**, e23525, doi:10.1371/journal.pone.0023525 (2011).

3.8. Figures

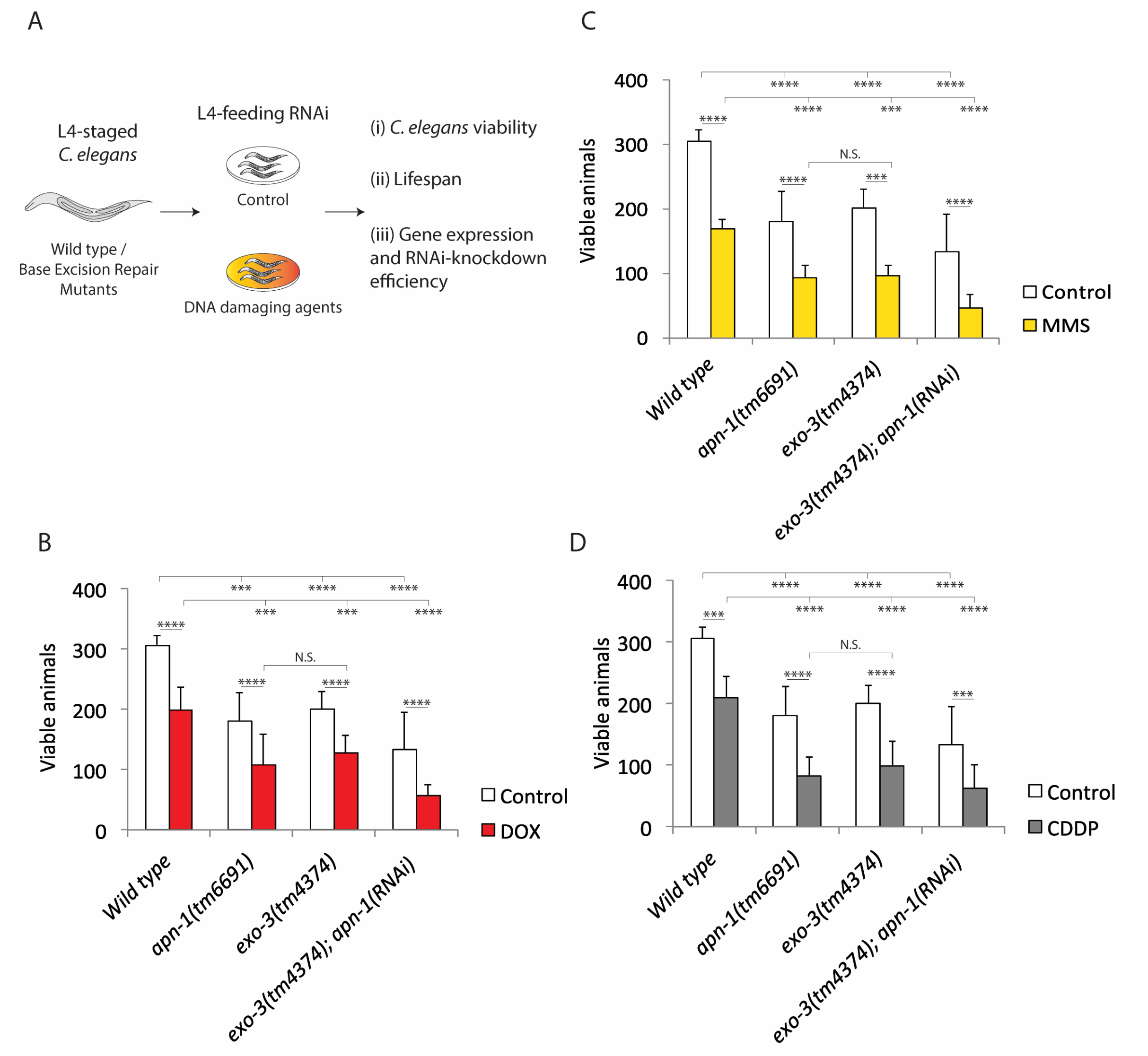

Figure 1. *C. elegans* mutants deficient in both APN-1 and EXO-3 are hypersensitive to DOX-, MMS- and CDDP-induced DNA lesions.

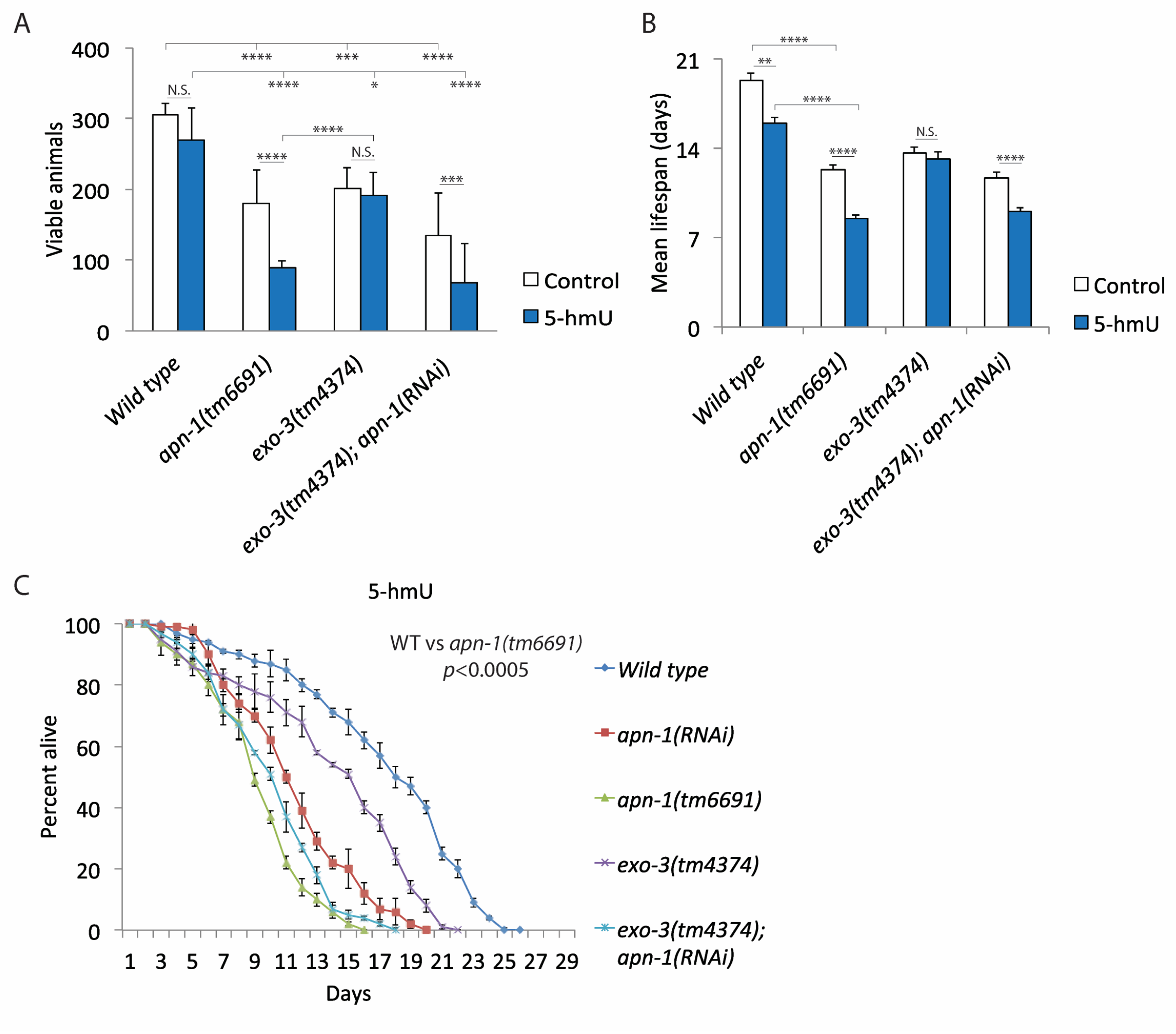

Figure 2. *C. elegans apn-1*, but not *exo-3*, mutants are sensitive to the nucleoside 5-hmU.

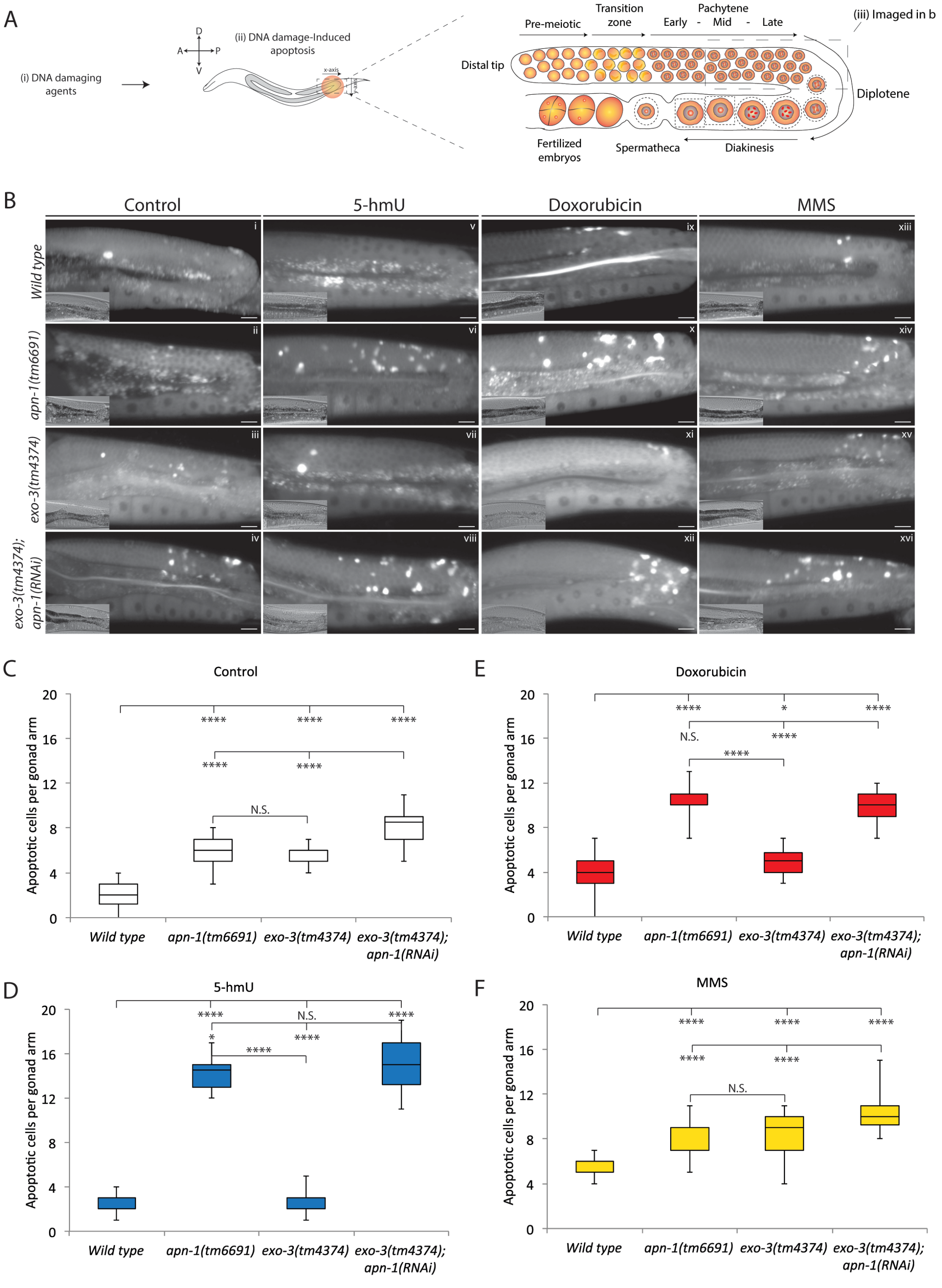

Figure 3. The *apn-1(tm6691)* mutant animals display increase spontaneous and 5-hmU-induced germ cell apoptosis.

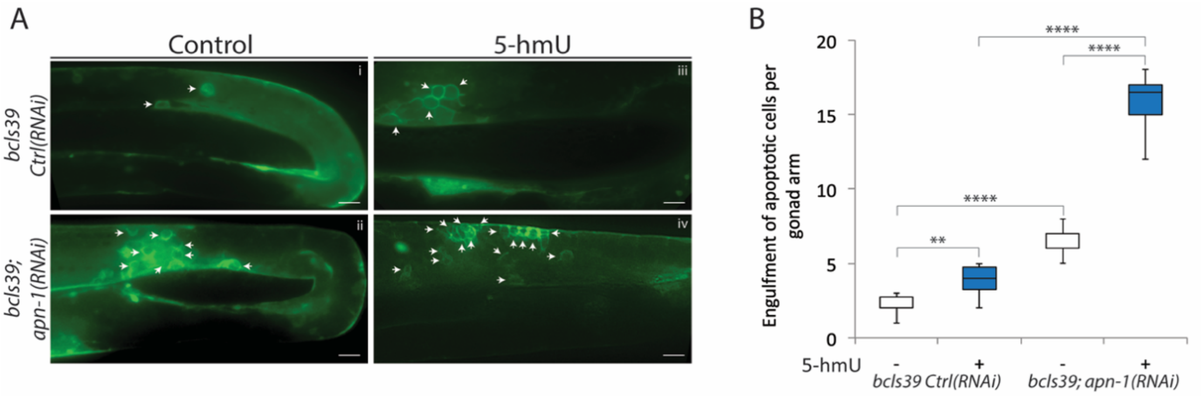

Figure 4. 5-hmU induces CED-1 engulfment of apoptotic germ cells.

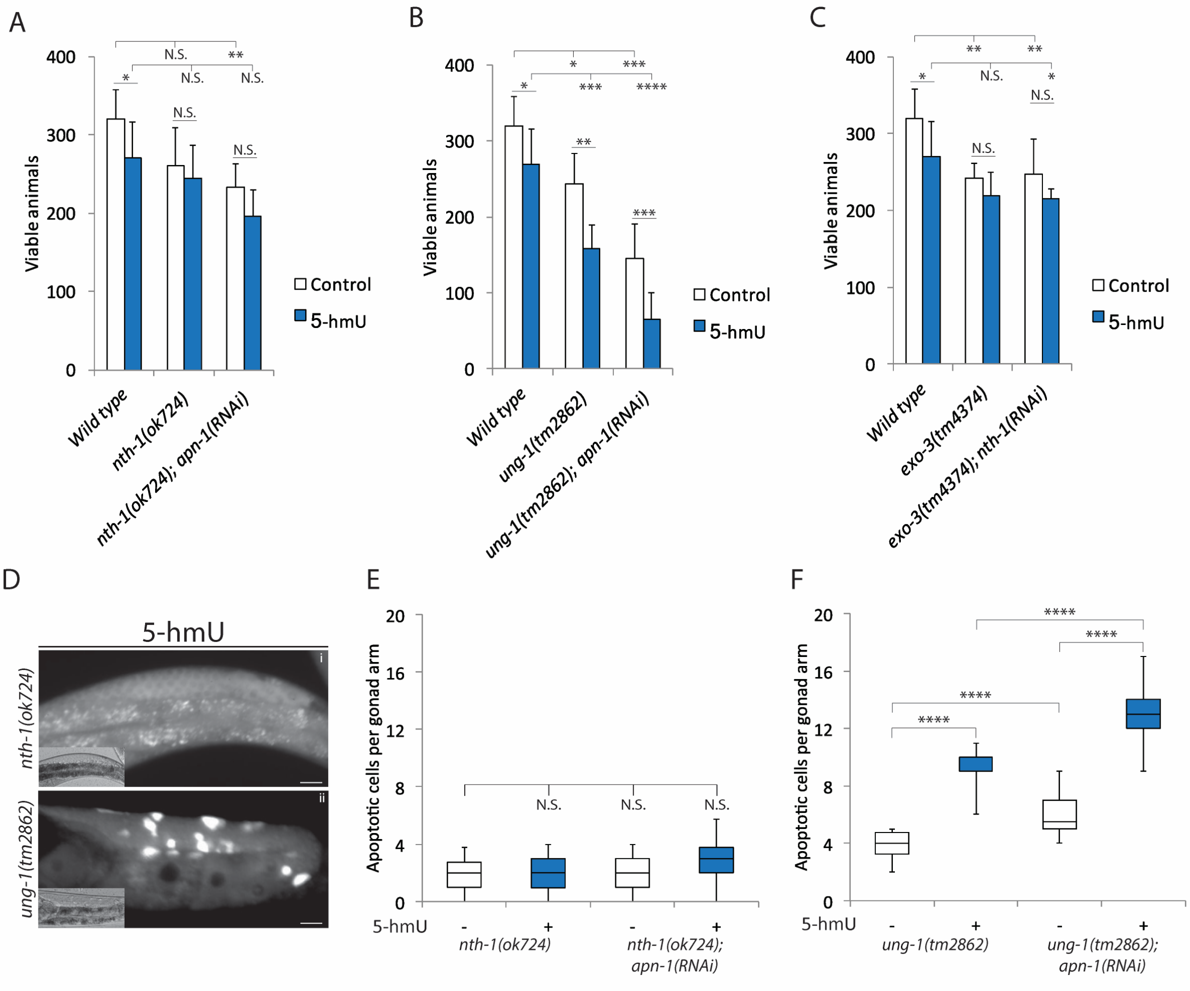

Figure 5. UNG-1 and not NTH-1 mediates the genotoxic effects of 5-hmU.

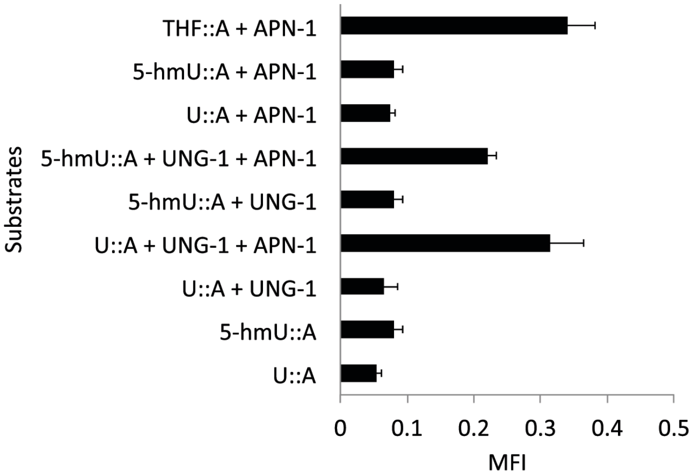

Figure 6. Recombinant GST-UNG-1 acts on 5-hmU lesion to produce APN-1 cleavable AP site.

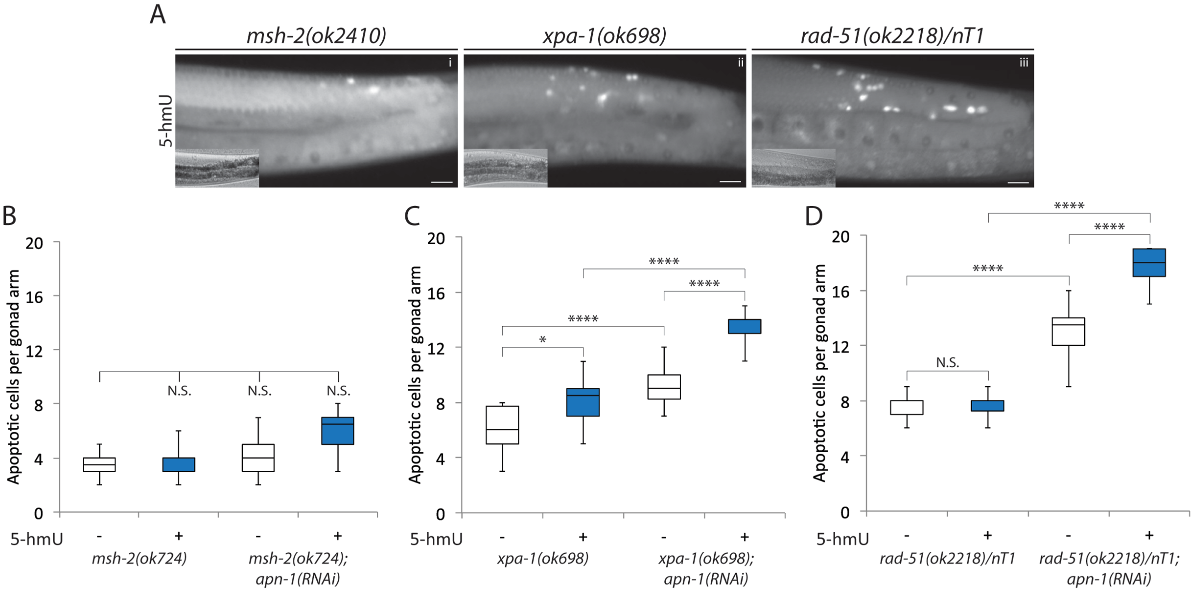

Figure 7. Mutants defective in the MMR, NER or HR pathway do not show significant increase in germ cell death upon exposure to 5-hmU.

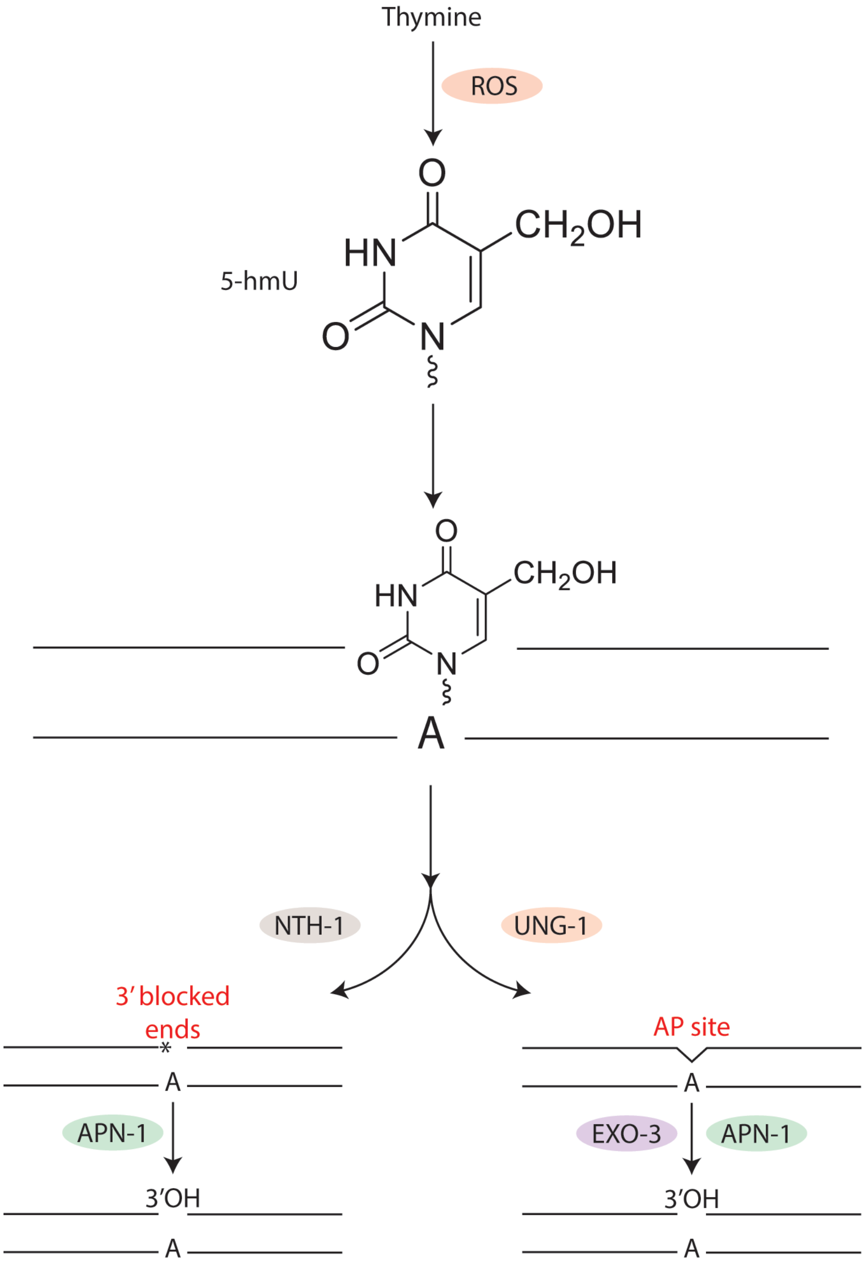

Figure 8. A model illustrating the repair of 5-hmU opposite adenine (5-hmU•A) *via* the BER pathway.

3.9. Supplemental figures

A

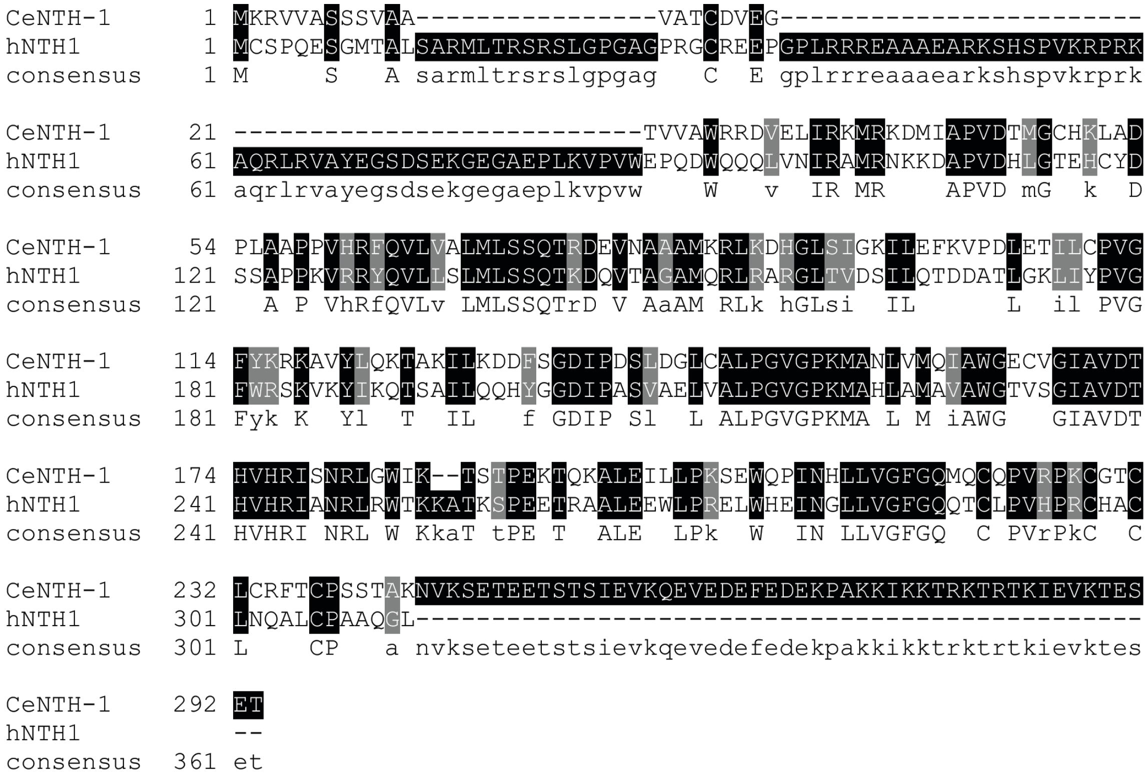

```
CeNTH-1      1 MKRVVASSSVAA----------------VATCDVEG------------------------
hNTH1        1 MCSPQESGMTALSARMLTRSRSLGPGAGPRGCREEPGPLRRREAAAEARKSHSPVKRPRK
consensus    1 M     S   A sarmltrsrslgpgag   C  E gplrrreaaaearkshspvkrprk

CeNTH-1     21 ---------------------------TVVAWRRDVELIRKMRKDMIAPVDTMGCHKLAD
hNTH1       61 AQRLRVAYEGSDSEKGEGAEPLKVPVWEPQDWQQQLVNIRAMRNKKDAPVDHLGTEHCYD
consensus   61 aqrlrvayegsdsekgegaeplkvpvw    W   v  IR MR    APVD mG  k  D

CeNTH-1     54 PLAAPPVHRFQVLVALMLSSQTRDEVNAAAMKRLKDHGLSIGKILEFKVPDLETILCPVG
hNTH1      121 SSAPPKVRRYQVLLSLMLSSQTKDQVTAGAMQRLRARGLTVDSILQTDDATLGKLIYPVG
consensus  121   A P VhRfQVLv LMLSSQTrD V AaAM RLk hGLsi  IL      L  il PVG

CeNTH-1    114 FYKRKAVYLQKTAKILKDDFSGDIPDSLDGLCALPGVGPKMANLVMQIAWGECVGIAVDT
hNTH1      181 FWRSKVKYIKQTSAILQQHYGGDIPASVAELVALPGVGPKMAHLAMAVAWGTVSGIAVDT
consensus  181 Fyk K  Yl  T  IL   f GDIP Sl  L ALPGVGPKMA L M iAWG   GIAVDT

CeNTH-1    174 HVHRISNRLGWIK--TSTPEKTQKALEILLPKSEWQPINHLLVGFGQMQCQPVRPKCGTC
hNTH1      241 HVHRIANRLRWTKKATKSPEETRAALEEWLPRELWHEINGLLVGFGQQTCLPVHPRCHAC
consensus  241 HVHRI NRL W KkaT tPE T  ALE  LPk  W  IN LLVGFGQ  C PVrPkC  C

CeNTH-1    232 LCRFTCPSSTAKNVKSETEETSTSIEVKQEVEDEFEDEKPAKKIKKTRKTRTKIEVKTES
hNTH1      301 LNQALCPAAQGL------------------------------------------------
consensus  301 L    CP   a nvkseteetstsievkqevedefedekpakkikktrktrtkievktes

CeNTH-1    292 ET
hNTH1          --
consensus  361 et
```

B

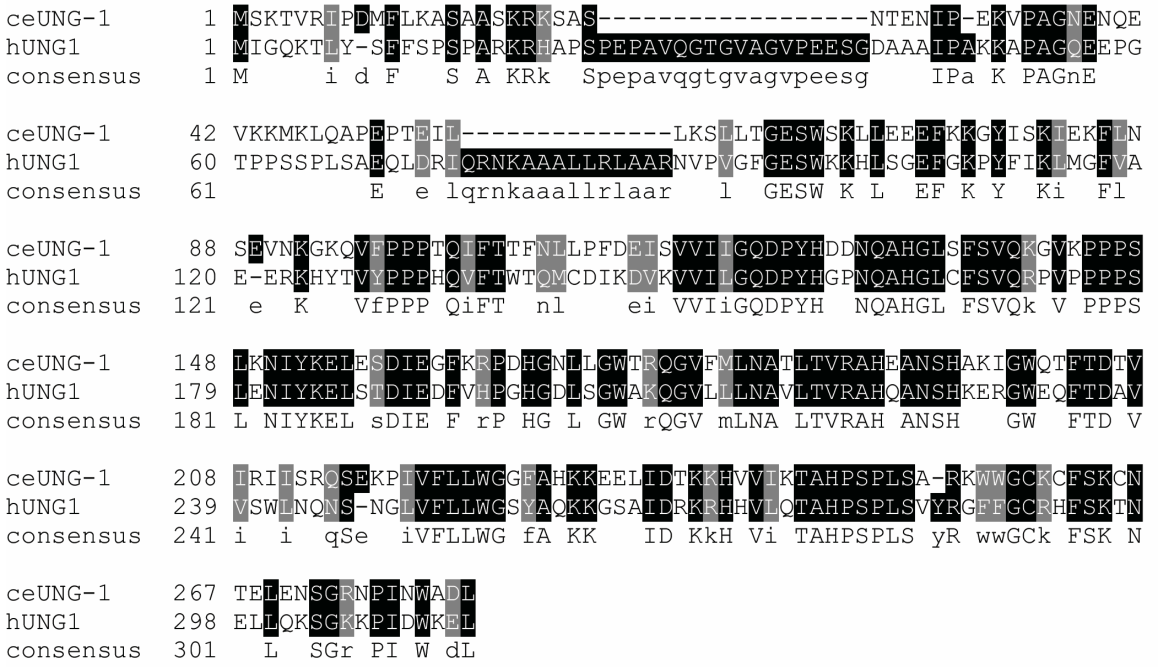

```
ceUNG-1      1 MSKTVRIPDMFLKASAASKRKSAS------------------NTENIP-EKVPAGNENQE
hUNG1        1 MIGQKTLY-SFFSPSPARKRHAPSPEPAVQGTGVAGVPEESGDAAAIPAKKAPAGQEEPG
consensus    1 M     i d F   S A KRk  Spepavqgtgvagvpeesg    IPa K PAGnE

ceUNG-1     42 VKKMKLQAPEPTEIL--------------LKSLLTGESWSKLLEEEFKKGYISKIEKFLN
hUNG1       60 TPPSSPLSAEQLDRIQRNKAAALLRLAARNVPVGFGESWKKHLSGEFGKPYFIKLMGFVA
consensus   61          E  e lqrnkaaallrlaar   l  GESW K L  EF K Y  Ki  Fl

ceUNG-1     88 SEVNKGKQVFPPPTQIFTTFNLLPFDEISVVIIGQDPYHDDNQAHGLSFSVQKGVKPPPS
hUNG1      120 E-ERKHYTVYPPPHQVFTWTQMCDIKDVKVVILGQDPYHGPNQAHGLCFSVQRPVPPPPS
consensus  121  e  K   VfPPP QiFT  nl    ei VVIiGQDPYH  NQAHGL FSVQk V PPPS

ceUNG-1    148 LKNIYKELESDIEGFKRPDHGNLLGWTRQGVFMLNATLTVRAHEANSHAKIGWQTFTDTV
hUNG1      179 LENIYKELSTDIEDFVHPGHGDLSGWAKQGVLLLNAVLTVRAHQANSHKERGWEQFTDAV
consensus  181 L NIYKEL sDIE F rP HG L GW rQGV mLNA LTVRAH ANSH   GW  FTD V

ceUNG-1    208 IRIISRQSEKPIVFLLWGGFAHKKEELIDTKKHVVIKTAHPSPLSA-RKWWGCKCFSKCN
hUNG1      239 VSWLNQNS-NGLVFLLWGSYAQKKGSAIDRKRHHVLQTAHPSPLSVYRGFFGCRHFSKTN
consensus  241 i  i  qSe  iVFLLWG fA KK   ID KkH Vi TAHPSPLS yR wwGCk FSK N

ceUNG-1    267 TELENSGRNPINWADL
hUNG1      298 ELLQKSGKKPIDWKEL
consensus  301   L  SGr PI W dL
```

Figure S1. Sequence alignment of DNA glycosylases **(A)** CeNTH-1 and hNTH1 and **(B)** CeUNG-1 and hUNG1 belonging to *C. elegans* and *H. sapiens* respectively. Numbers indicate amino acid positions. Identical or similar amino acid residues amongst the sequences are shaded in black or gray, respectively. Dashes indicate gaps. Sequence similarity: **(A)** 67.4 % and **(B)** 58.2 %.

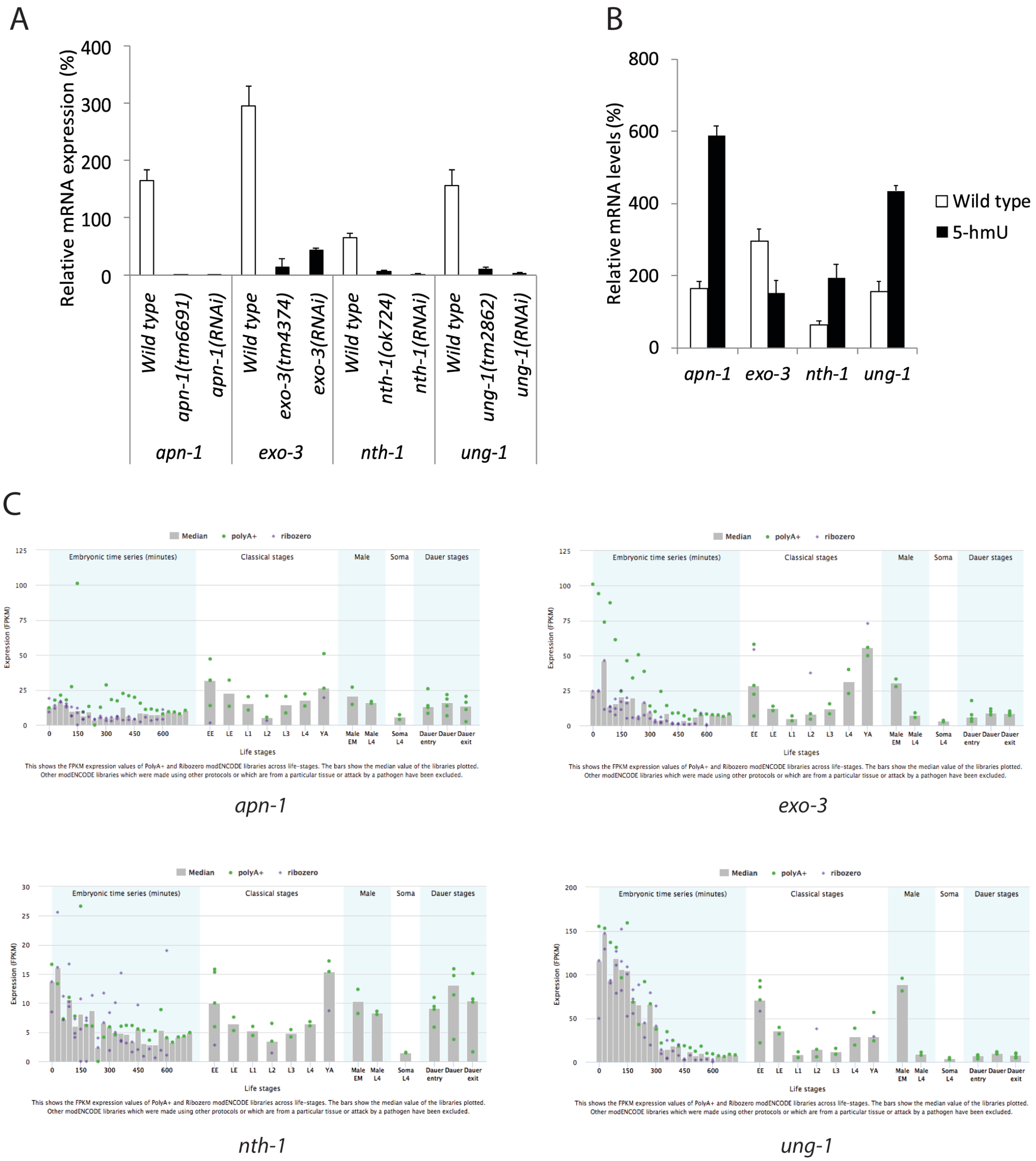

apn-1

exo-3

nth-1

ung-1

Figure S2. A, The relative gene expression of the *apn-1*, *exo-3*, *nth-1* and *ung-1* transcripts in the wild type and the respective deletion mutant animals *apn-1(tm6691)*, *exo-3(tm4374)*, *nth-1(ok724)* and *ung-1(tm2862).* RNAi-driven depletion was measured and corrected on actin as an internal control. Synchronized young adult animals were collected and mRNA levels were assessed by qRT-PCR. Data shown represent the average ± s.d. from a 60 × 15 mm petri dish of animals (n ~ 1000) pooled from three independent experiments. **B**, 5-hmU induces the expression of the *apn-1*, *nth-1* and *ung-1* genes, but not the *exo-3* gene. The animals were treated for 5 hours with 5-hmU (1 μM) and *apn-1* mRNA assessed by qRT-PCR. **C**, The expression pattern of the indicated genes during various developmental stages of *C. elegans*. The data were obtained from the Wormbase.

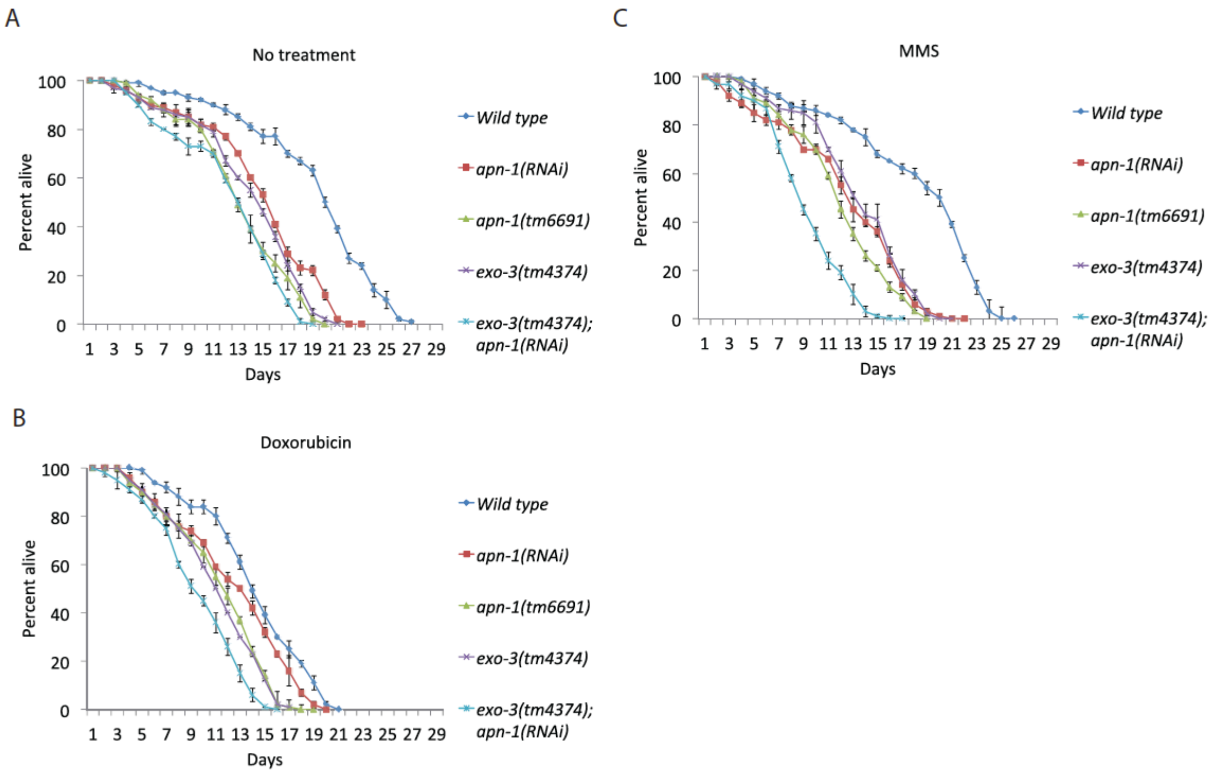

Figure S3. Kaplan-Meier survival plot of BER components exposed to DNA damaging agents. **(A, B and C)** Kaplan-Meier survival plot showing alive percentage of the indicated genotypes. L1-staged animals (n=100) were exposed to **(A)** No treatment, **(B)** DOX and **(C)** MMS. Lifespan was blindly assessed starting from young adult animals. The mean lifespan of two independent experiments is shown.

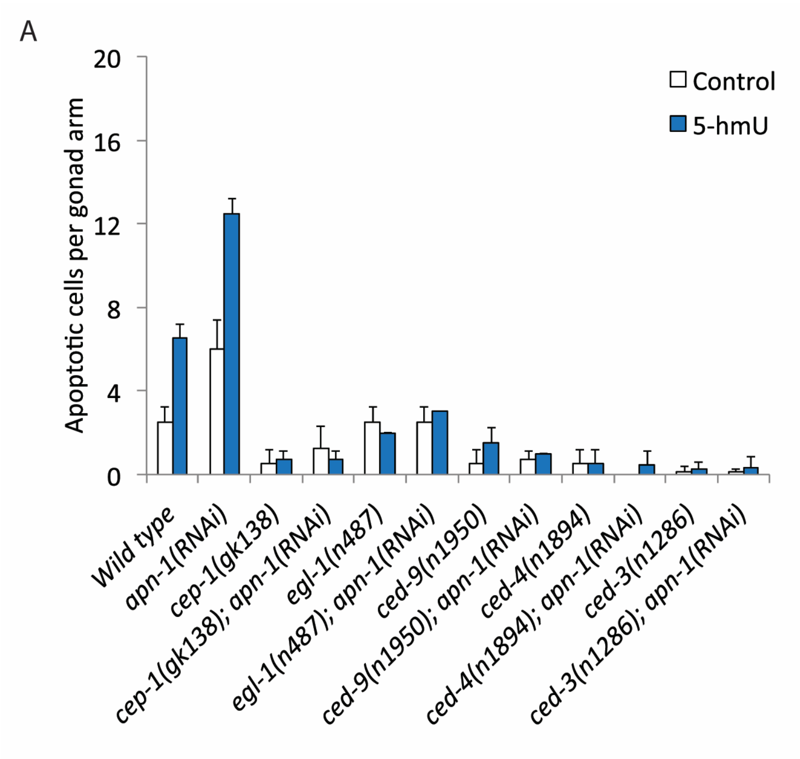

Figure S4. Genetic analysis of control and 5-hmU-induced apoptotic germ cell death. **A,** Representative chart showing the average quantification of germ cell death in three independent experiments (n=30) corresponding to the wild type and the apoptotic defective mutants *cep-1, egl-1, ced-9, ced-4* and *ced-3* without and with RNAi-driven downregulation of *apn-1* in the absence and presence of 5-hmU (1 μM). Apoptotic cell corpses were observed and scored as described in the experimental procedures.

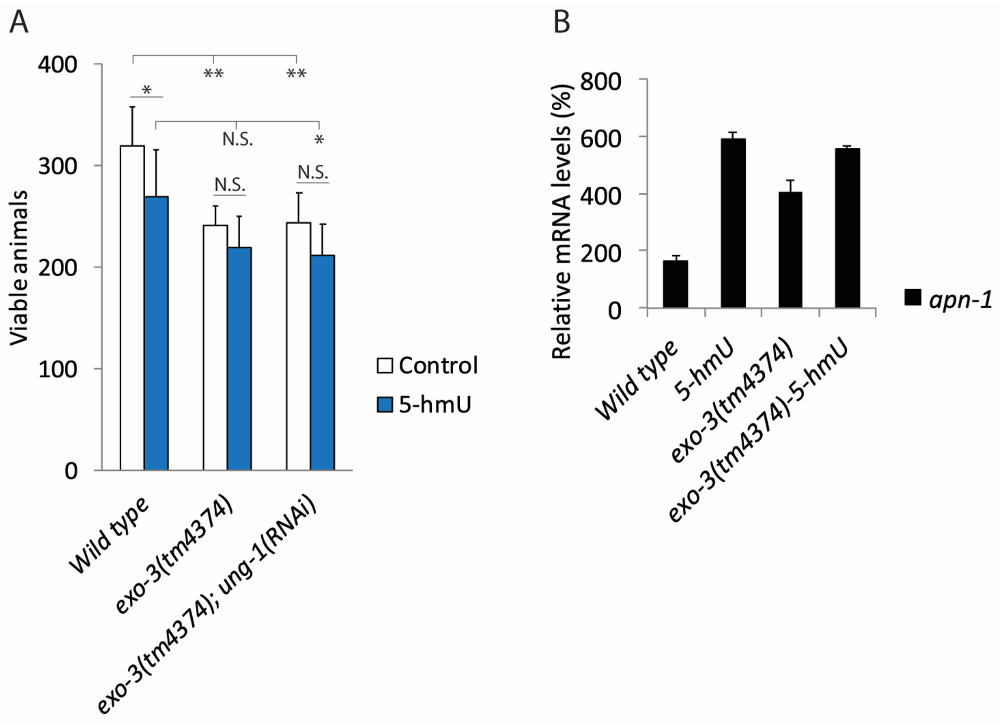

Figure S5. **A,** *exo-3(tm4374)* mutants are not sensitized to 5-hmU upon *ung-1* downregulation by RNAi. Brood size analyses of the indicated genotypes. The data are the mean±S.D. of three independent experiments (*n*=10 monitored for 3 days). Control, Wild type; *exo-3(tm4374)*; and *exo-3(tm4374); ung-1(RNAi)*. **B,** *apn-1* expression level in the wild type and *exo-3(tm4374)* mutant without and with 5-hmU exposure. The animals were untreated or treated for 5 hours with 5-hmU (1 µM) and *apn-1* mRNA assessed by qRT-PCR.

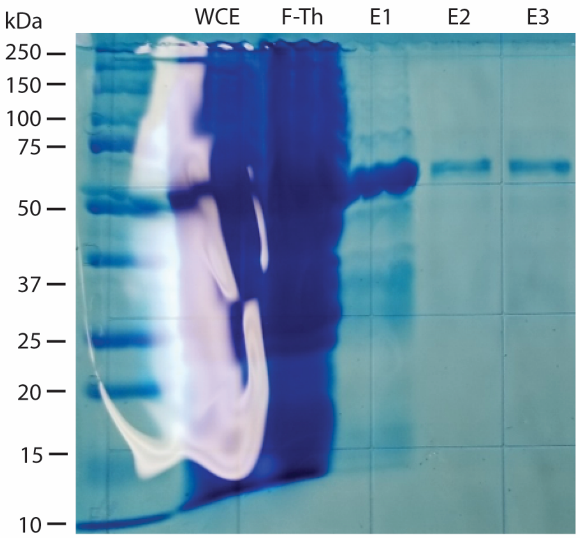

Figure S6. Recombinant GST-UNG-1 purified from an *E. coli* expression system. BL21(DE3) expressing *C. elegans* UNG-1 as a GST-UNG-1 fusion protein was purified according to Nakamura et al., 2008, but using GST-magnetic beads. WCE, whole cell extract, F-Th, flow through from the GST-magnetic beads, E1, E2 and E3 are the elution fractions.

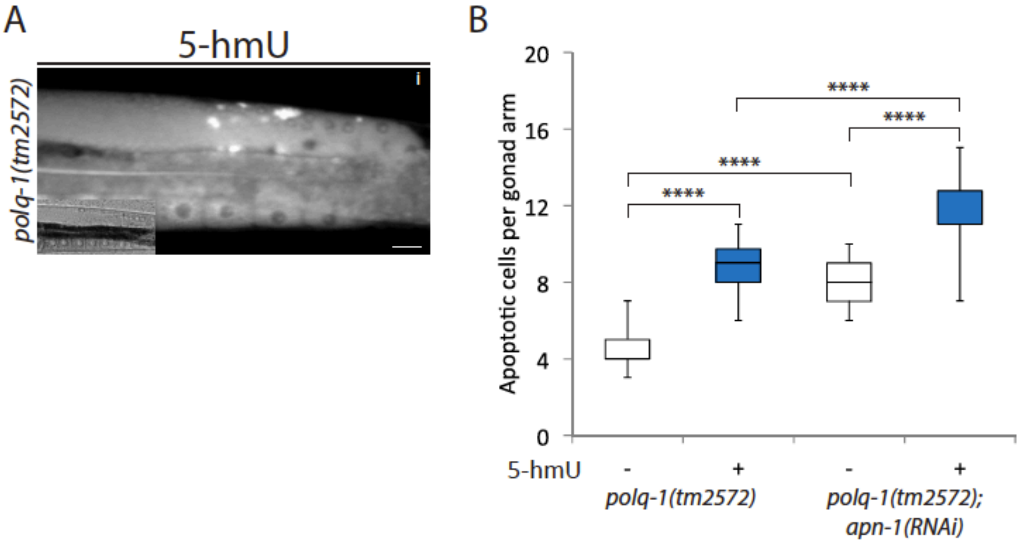

Figure S7. POLQ-1 is required for DNA synthesis after removal of 5-hmU lesions. **A,** Representative images of the posterior gonad arms of the *polq-1* mutant stained with acridine orange upon treatment with 5-hmU as described in Figure 2. **B,** Box and whisker plots showing quantification of germ cell apoptosis in *polq-1(tm2572)* and *polq-1(tm2572); apn-1(RNAi)* in the absence and presence of 5-hmU.

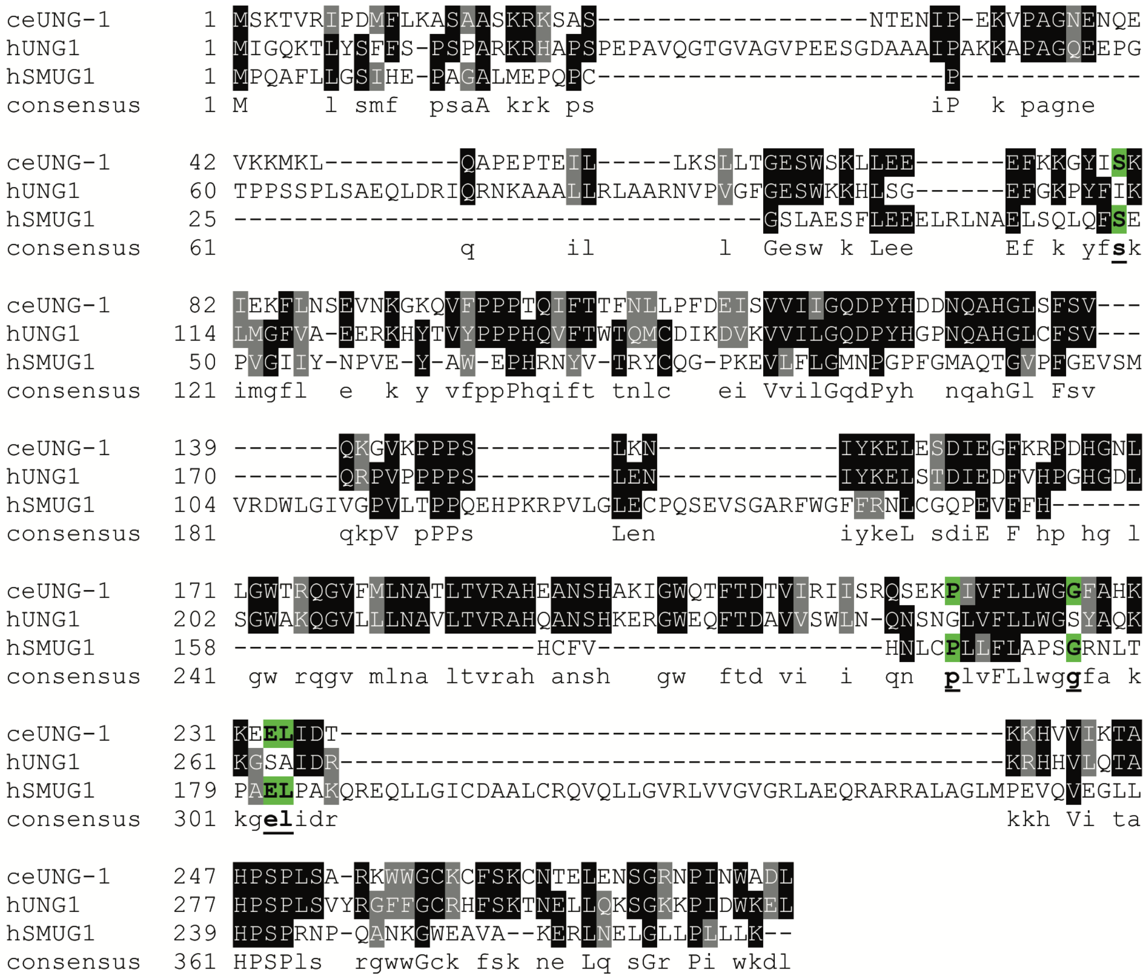

```
ceUNG-1      1 MSKTVRIPDMFLKASAASKRKSAS------------------NTENIP-EKVPAGNENQE
hUNG1        1 MIGQKTLYSFFS-PSPARKRHAPSPEPAVQGTGVAGVPEESGDAAAIPAKKAPAGQEEPG
hSMUG1       1 MPQAFLLGSIHE-PAGALMEPQPC-----------------------P------------
consensus    1 M     l smf  psaA krk ps                      iP  k pagne

ceUNG-1     42 VKKMKL---------QAPEPTEIL-----LKSLLTGESWSKLLEE------EFKKGYISK
hUNG1       60 TPPSSPLSAEQLDRIQRNKAAALLRLAARNVPVGFGESWKKHLSG------EFGKPYFIK
hSMUG1      25 -----------------------------------GSLAESFLEEELRLNAELSQLQFSE
consensus   61                q      il        l  Gesw k Lee      Ef k yfsk

ceUNG-1     82 IEKFLNSEVNKGKQVFPPPTQIFTTFNLLPFDEISVVIIGQDPYHDDNQAHGLSFSV---
hUNG1      114 LMGFVA-EERKHYTVYPPPHQVFTWTQMCDIKDVKVVILGQDPYHGPNQAHGLCFSV---
hSMUG1      50 PVGIIY-NPVE-Y-AW-EPHRNYV-TRYCQG-PKEVLFLGMNPGPFGMAQTGVPFGEVSM
consensus  121 imgfl  e  k y vfppPhqift tnlc   ei VvilGqdPyh  nqahGl Fsv

ceUNG-1    139 -------QKGVKPPPS---------LKN------------IYKELESDIEGFKRPDHGNL
hUNG1      170 -------QRPVPPPPS---------LEN------------IYKELSTDIEDFVHPGHGDL
hSMUG1     104 VRDWLGIVGPVLTPPQEHPKRPVLGLECPQSEVSGARFWGFFRNLCGQPEVFFH------
consensus  181        qkpV pPPs         Len            iykeL sdiE F hp hg l

ceUNG-1    171 LGWTRQGVFMLNATLTVRAHEANSHAKIGWQTFTDTVIRIISRQSEKPIVFLLWGGFAHK
hUNG1      202 SGWAKQGVLLLNAVLTVRAHQANSHKERGWEQFTDAVVSWLN-QNSNGLVFLLWGSYAQK
hSMUG1     158 --------------------HCFV-------------------HNLCPLLFLAPSGRNLT
consensus  241  gw rqgv mlna ltvrah ansh   gw  ftd vi  i  qn  plvFLlwggfa k

ceUNG-1    231 KEELIDT--------------------------------------------KKHVVIKTA
hUNG1      261 KGSAIDR--------------------------------------------KRHHVLQTA
hSMUG1     179 PAELPAKQREQLLGICDAALCRQVQLLGVRLVVGVGRLAEQRARRALAGLMPEVQVEGLL
consensus  301 kgelidr                                            kkh Vi ta

ceUNG-1    247 HPSPLSA-RKWWGCKCFSKCNTELENSGRNPINWADL
hUNG1      277 HPSPLSVYRGFFGCRHFSKTNELLQKSGKKPIDWKEL
hSMUG1     239 HPSPRNP-QANKGWEAVA--KERLNELGLLPLLLK--
consensus  361 HPSPls  rgwwGck fsk ne Lq sGr Pi wkdl
```

Figure S8. Sequence alignment of the DNA glycosylases CeUNG-1, hUNG1 and hSMUG1 belonging to *C. elegans* and *H. sapiens*, respectively. Numbers indicate amino acid positions. Identical or similar amino acid residues amongst the sequences are shaded in black or gray, respectively. Dashes indicate gaps. The residues in green are unique to CeUNG-1 and hSMUG1, but not hUNG1.

Chapter 4 : Imaging the pharynx to measure the uptake of doxorubicin in *C. elegans*

Sivathevy Amirthagunabalasingam[1], **Arturo Papaluca[2]**, Taramatti Harihar[1] and
Dindial Ramotar[1, *]

[1]Maisonneuve-Rosemont Hospital Research Center, and the Université de Montréal, Faculty of Medicine, Department of Medicine, Montréal, Canada; [2]Lady Davis Institute, McGill University, Montréal, Canada. *For correspondence: dindial.ramotar@umontreal.ca

Abstract

Caenorhabditis elegans offers an array of advantages to investigate the roles of uptake transporters. Herein, an epifluorescent microscopy approach was developed to monitor the uptake of the autofluorescent anticancer drug, doxorubicin, into the pharynx of *C. elegans* by organic cation transporters.

Keywords: *C. elegans*, organic cation uptake transporters, drug uptake, doxorubicin, autofluorescent drug, epifluorescent microscopy, RNAi feeding bacteria.

Citation: Amirthagunabalasingam, S., **Papaluca, A.**, Harihar, T. and Ramotar, D. (2017). Imaging the Pharynx to Measure the Uptake of Doxorubicin in Caenorhabditis elegans. Bio-protocol 7(10): e2291. DOI: 10.21769/BioProtoc.2291.

4.1. Background

Human cells have over 450 solute carrier transporters that are believed to facilitate the uptake of several ions, nutrients, as well as both therapeutic and anticancer drugs [1]. However, the roles and substrates of a large number of these uptake transporters are not known. *C. elegans* is an inexpensive model organism that offers a multitude of advantages over mammalian cells to rapidly study many biological processes that are highly conserved in nature. During the last decade, this organism has been instrumental in several drug discovery programs to identify novel small molecules, e.g., those that act as antimicrobials and inhibit oxidative stress, although the yield of bioactive compounds has been less striking [2,3]. We reason that the recovery rate could be higher if there is greater and selective influx of the molecules by uptake transporters into the animal cells. To date, only three studies have been performed to understand the roles of uptake transporters in *C. elegans* [4-6]. Thus, characterization of the function and substrate specificities of uptake transporters in this organism will be advantageous towards improving the strategies employed to identify novel bioactive molecules. Herein, we outline a method to monitor uptake of the anticancer drug doxorubicin into the pharynx of *C. elegans* [6]. Doxorubicin autofluoresces and can be readily monitored by several widely available detection systems such as the epifluorescent microscope. We note that several benefits can be derived from this approach including a hunt for novel therapeutic substrates of the transporter by competing for doxorubicin uptake.

4.2. Materials and reagents

1. Platinum wire (Thomas Scientific cat no 1233S71)
2. Pasteur Pipet (Fisher Scientific cat no 13-678-20F)
3. Frosted microscope slides (size: 1” x 3”; thickness: 1-2 mm) (UltiDent Scientific, catalog number: 170-7107A)
4. Microscope cover glass (size: 22 x 22 #1.5) (Fisher Scientific, Fisherbrand, catalog number: 12-541B)
5. Petri dish 60 x 15 mm (SARSTEDT, catalog number: 82.1194)

6. 15 ml conical tube
7. *E. coli* bacteria HT115^{DE3} with the plasmid pL4440-empty vector
8. *E. coli* bacteria HT115^{DE3} with the plasmid pL4440-oct-1 (Ahringer's collection). Sequence verified
9. *E. coli* bacteria HT115^{DE3} with the plasmid pL4440-oct-2 (Ahringer's collection). Sequence verified.
10. Bristol N2 (wild type) and RB1084 [*oct-1(ok1051*) I] from *Caenorhabditis* Genetic Center
11. Ampicillin (Sigma-Aldrich, catalog number: A9518)
12. Bacteriological agar (Wisent, catalog number: 800-010-CG)
13. Tryptone (BioBasic cat no G211)
14. Yeast extract (Wisent Cat no 800-150-LG)
15. Peptone (Wisent cat no 800 157-LG)
16. Yeast extract (for Luria Broth (LB) and NGM media purchased. *Note: For Luria Broth (LB) and NGM media purchased.*
17. Sodium chloride (NaCl) (Wisent) cat no 600-082
18. Potassium phosphate monobasic (KH_2PO_4) (Biobasic PB0445)
19. Magnesium sulfate ($MgSO_4$) (Biobasic, catalog number: MRB 0329)
20. Calcium chloride ($CaCl_2$) (Fisher Scientific, catalog: C-79-500)
21. Cholesterol (Sigma-Aldrich, catalog number: C-8503)
22. Agarose (Wisent, catalog: 800-015-CG)
23. Doxorubicin (for Research from Hôpital Maisonneuve-Rosemont, Montreal, Canada). Stock concentration at 2 mg/ml
24. Levamisol Hydrochloride (MP Biomedical, catalog: 155228)
25. Ethanol 100% (from Hôpital Maisonneuve-Rosemont cat no PO 16EAAN)
26. Bleach Lavo Pro6 (Maisonneuve Rosemont Hosptial cat no 4500000026)
27. Sodium hydroxide (NaOH) (Biobasic) Cat no SB0617
28. Sodium phosphate dibasic (Na_2HPO_4) cat no S0404
29. IPTG (Biobasic) cat no PRB0447
30. Clear nail polish from Wild Shine from Dollarama
31. LB solution (see Recipes)

32. Nematode Growth Media (NGM) (see Recipes)
33. Agar pad (see Recipes)
34. Alkaline Hypochlorite Solution for bleaching the worms (see Recipes)
35. M9 buffer (see Recipes)

4.3. Equipment

1. Incubator at 20 °C, but with range for 15 to 37 °C (Shellab model no 2020)
2. 37 °C incubator (Sanyo Mir 262)
3. 37 °C shaker (Inforst HT Multitron Standard)
4. 500 ml glass bottle (Wheaton graduated glass media bottles with lined caps)
5. Microwave Panasonic (inverter model)
6. 55 °C water bath (Precision Scientific cat 66 800)
7. Metal Spatula (VWR)
8. Flame
9. Neutrex culture tubes 16X15 mm
10. Pyrex Erlenmeyer Flask different sizes for bacteria culturing
11. Autoclave
12. Stereomicroscope Leica MZ 8 (Leica 10445538 Plan Microscope Objective Lens 1.0x) (Leica, model: MZ 8)
13. DeltaVision Elite Restoration System (GE Healthcare)
14. Fisher Vortex Genie 2 (Fisher Scientific, catalog number: 12-812)
15. Eppendorf 5810 R centrifuge (Eppendorf, model: 5810 R)
16. VWR rocking platform shakers basic (VWR)
17. Ptc-100 Programmable Thermal Controller 96 Well

4.4. Software

1. ImageJ imaging software
2. SoftWorx software

4.5. Procedure

A. Preparation of bacteria and media for worm growth

1. Bacteria preparation (*C. elegans* food)
    a. In 10 ml LB media, add 10 µl ampicillin (stock 100 mg/ml).
    b. Add few colonies of *E. coli* HT115^{DE3} empty vector bacteria.
    Alternative bacteria: *E. coli* OP50.
    c. Incubate for 6 h at 37 °C in an orbital shaker at 200 rpm.
2. *C. elegans* growth media preparation
    a. Melt the solid NGM contained in a glass bottle (500 ml) using a microwave (power level 2 for 25 min).
    b. Keep the melted media at 55 °C in a water bath about 15-20 min.
    c. Before usage, add:
    12.5 ml of 1 M KH_2PO_4 pH 6
    500 µl of 1 M $MgSO_4$
    500 µl of 1 M $CaCl_2$
    500 µl cholesterol (stock 5 mg/ml in 95% ethanol)
    500 µl of ampicillin (stock 100 mg/ml), if using knockdown bacteria strain HT115^{DE3} carrying the L4440 vector or the target gene
    d. Pour the media in 60 x 15 mm Petri dish.
    e. Let it dry at room temperature for around 1 h.
    f. Once dried, spread 70 µl of bacteria prepared in step A1 above to form a lawn.
    g. Incubate the plate overnight at 37 °C.
3. Worm growth
    a. From a grown worm plate, cut 4 pieces of approximately 1 x 1 cm agar with a pointy spatula sterilized with 100% ethanol and flame.
    b. Transfer each agar piece by turning them over onto each of 4 plates prepared in step A2.
    c. Incubate these worm plates for 2 days at 20 °C.

B. Worm synchronisation

1. The 4 plates are expected to be fill with adult worms, visualized through the stereomicroscope, and at which point the synchronization can be done.
2. Add 2 ml of Alkaline Hypochlorite solution (bleaching solution) to each plate and rapidly collect the worms in a sterile 15 ml conical tube. Date and labeled the tube with the name of the worm strain.
3. Quickly start to vortex the worms for 7 min at setting 8 on the vortex and check under the stereomicroscope if the adult worms are lysed and only the eggs are present.

   Steps B2 and B3 must be carried with care as they are critical in order for the eggs to hatch.
4. Without any delay, centrifuge in the Eppendorf 5810 R centrifuge, using swing bucket rotor (A-4-81) with adapters for 15 ml conical tubes at 1,740 x g for 2 min at 4 °C.
5. Aspirate the supernatant but leave approximately 1 ml of the solution.
6. Adding 5 ml of M9 buffer and repeat the centrifugation and aspiration as in steps B4 and B5.
7. Repeat 4 more times step B6, in order to remove any trace of the bleaching solution.
8. Incubate the eggs in the final 1 ml of M9 buffer overnight at 20 °C. During this time the eggs will hatch and produce L1 stage worms.

C. Worm under treatment

1. Bacteria preparation
   a. In 3 different tubes, add 10 ml LB media and 10 µl ampicillin (100 mg/ml).
   b. In the 1st tube, add few colonies of *E. coli* HT115^{DE3}/empty vector L4440.
   c. In the 2nd tube, add few colonies of *E. coli* HT115^{DE3}/pL4440-oct-1.
   d. In the 3rd tube, add few colonies of *E. coli* HT115^{DE3}/pL4440-oct-2.
   e. Incubate all the tubes for 5 h in a 37 °C orbital shaker.
2. Drug plate preparation
   a. Melt a bottle of 500 ml of solid NGM as above (see *C. elegans* growth media preparation above).
   b. For normal drug plates-no knockdown

        i. Transfer 30 ml of melted NGM media kept at 55 °C into a small sterile bottle. This will make 5 Petri dishes (60 x 15 mm) each containing 6 ml of NGM media.
        ii. Add the doxorubicin (stock 2 mg/ml) to the desire final concentrations for each 6 ml of NGM media and pour onto the 60 x 15 mm Petri dish. For doxorubicin use between 0.1 to 100 μM depending on the strains. Uptake was observed with as low as 0.5 μM of doxorubicin.
        iii. Important, do not forget to prepare a plate without drug.
        iv. Leave plates for at least 15 min at room temperature for the media to solidify.
        v. Add 70 μl *E. coli* HT115^{DE3}/pL4440-empty vector bacteria.
        vi. Incubate overnight the plates at 37 °C.
    c. For knockdown drug plates
        i. Transfer 30 ml of melted NMG media kept at 55 °C into a small sterile bottle.
        ii. Add 30 μl of 1 M IPTG, needed to induce the production of dsRNA from the L4440 vector carrying a fragment of the target gene.
        iii. Add to 6 ml of this media the desire concentrations of doxorubicin as above. *IMPORTANT: Do not forget to prepare a plate without drug.*
        iv. Pour the 6 ml of media with IPTG and without and with doxorubicin onto the 60 x 15 mm Petri dishes.
        v. Dry the plates, as above.
        vi. Add 70 μl *E. coli* HT115^{DE3}/ pL4440- oct-1 bacteria for 1st set of 5 plates.
        vii. Add 70 μl *E. coli* HT115^{DE3}/ pL4440- oct-2 bacteria for 2nd set of 5 plates.
        viii. Incubate the plates overnight at 37 °C.
3. Now all the plates are ready to add 50 μl of the L1 synchronized worms
4. Verify if there are nearly 50 L1-staged worms on the plates under the stereomicroscope
5. Incubate the plates at 20 °C for 3 days.

D. Microscope visualisation

1. Preparation of slides
    a. On a frosted microscope slide add one drop (~50 µl) of 3% agarose and squeeze it with another slide to form a sandwich. After 10 sec, remove one of the slide to expose the agarose.
    b. Dry the slide with the agarose at 65 °C around 15-30 min using a Programmable Thermal Controller 96 Well.
2. Mounting the worms
    a. Add 7 µl of 1 M levamisol onto the surface of the dried agar on the slide
    b. To each slide, add 10-15 young adult worms from a single treatment condition by using a platinum wire to transfer the worms.
    c. Sterilize the platinum wire using a flame before transferring the next 10-15 worms from a different treatment condition onto a new slide.
    d. Add the coverslip and seal around the slide and coverslip with clear nail polish.
3. Microscopy visualisation
    a. Add a small drop of DeltaVision Immersion oil 1.534 onto the slide in order to use objective 40x.
    b. Place the mounted slide on the microscope by inverting it.
    c. Adjust the eyepiece filter roll to POL filter.
    d. Open the SoftWorx software . See GE Healthcare manual (GE Healthcare, 2014).
    e. Press on the microscope. 3 windows will be opened (Figure 1).

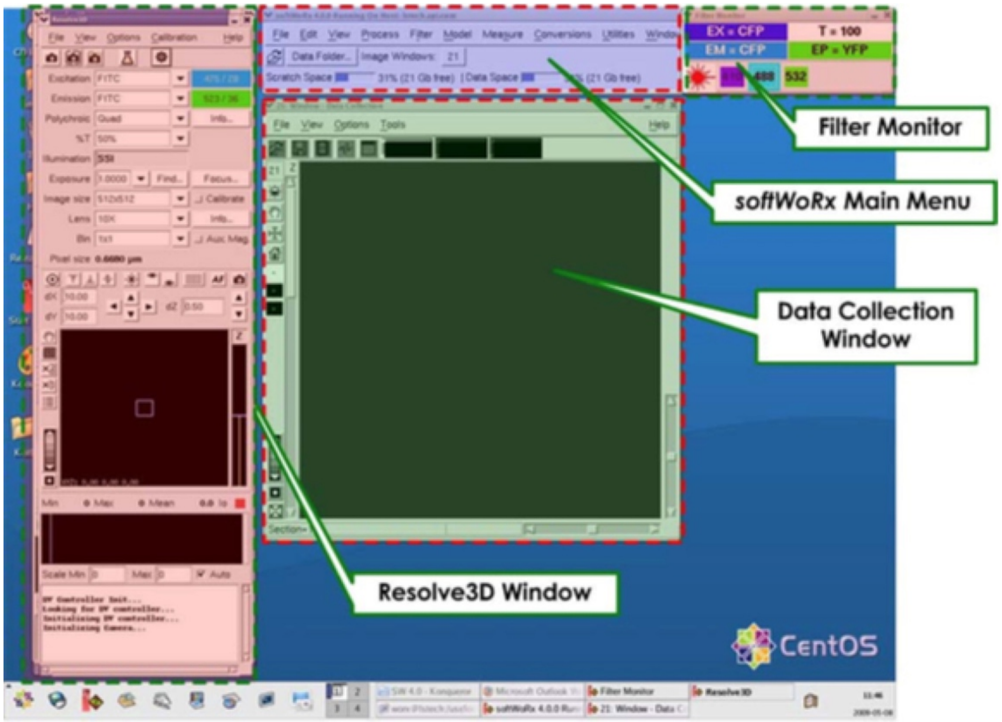

Figure 1. SoftWorx desktop display. The Resolve3D window includes acquisition parameters and controls for moving the stage, the Data Collection window displays images as they are acquired, and the Filter Monitor displays the filters currently selected.

f. On the window called Resolve3D.

g. Press on the gear wheel (setting) ⚙ to open Resolve3D setting window (Figure 2).

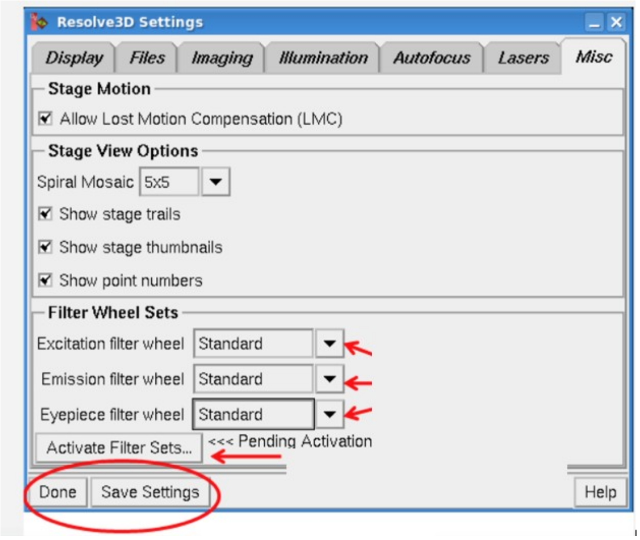

Stage Motion

☑ Allow Lost Motion Compensation (LMC)

Stage View Options

Spiral Mosaic 5x5

☑ Show stage trails

☑ Show stage thumbnails

☑ Show point numbers

Filter Wheel Sets

Excitation filter wheel Standard

Emission filter wheel Standard

Eyepiece filter wheel Standard

Activate Filter Sets... <<< Pending Activation

Figure 2. Resolve3D window setting.

i. Under MISC.
ii. Select the filters.
iii. Save settings.
iv. Under FILES (Figure 3).

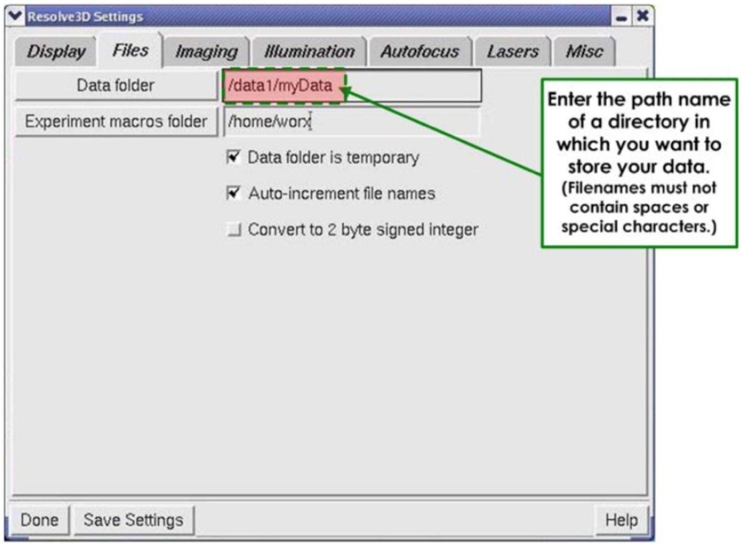

Data folder /data1/myData

Experiment macros folder /home/work

☑ Data folder is temporary

☑ Auto-increment file names

☐ Convert to 2 byte signed integer

Enter the path name of a directory in which you want to store your data. (Filenames must not contain spaces or special characters.)

Figure 3. Display of the Files tab.

i. In the Data folder field (Figure 3), enter the directory in which to save the image.
ii. In the Experiment macros folder field (Figure 3), enter the same directory.
iii. Save settings.
iv. Done.

h. In the Resolve3D window (Figure 1), set the following parameters in Figure 4.

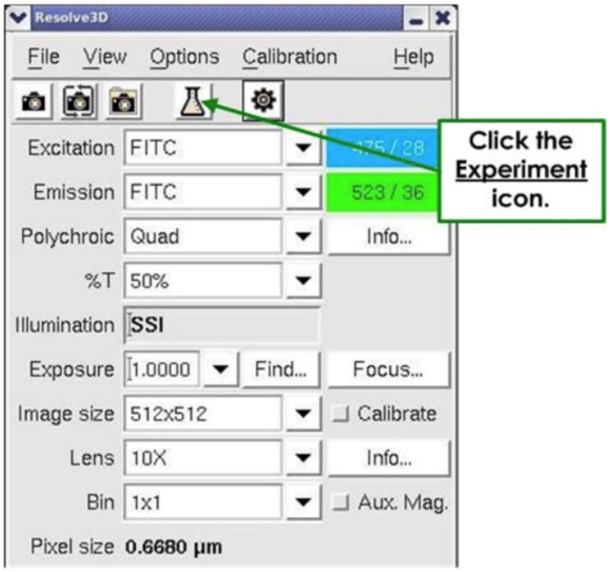

Excitation: FITC 475 / 28
Emission: FITC 523 / 36
Polychroic: Quad
%T: 50%
Illumination: SSI
Exposure: 1.0000
Image size: 512x512
Lens: 10X
Bin: 1x1
Pixel size: 0.6680 µm

Click the Experiment icon.

Figure 4. Setting the parameters.

i. Excitation: POL.
ii. Emission: POL.
iii. % T: 32%.
iv. Exposure: 0.025.
v. Lens: 40x.

i. Press on the Erlenmeyer.

j. A window called Design/Run Experiment window will be opened.

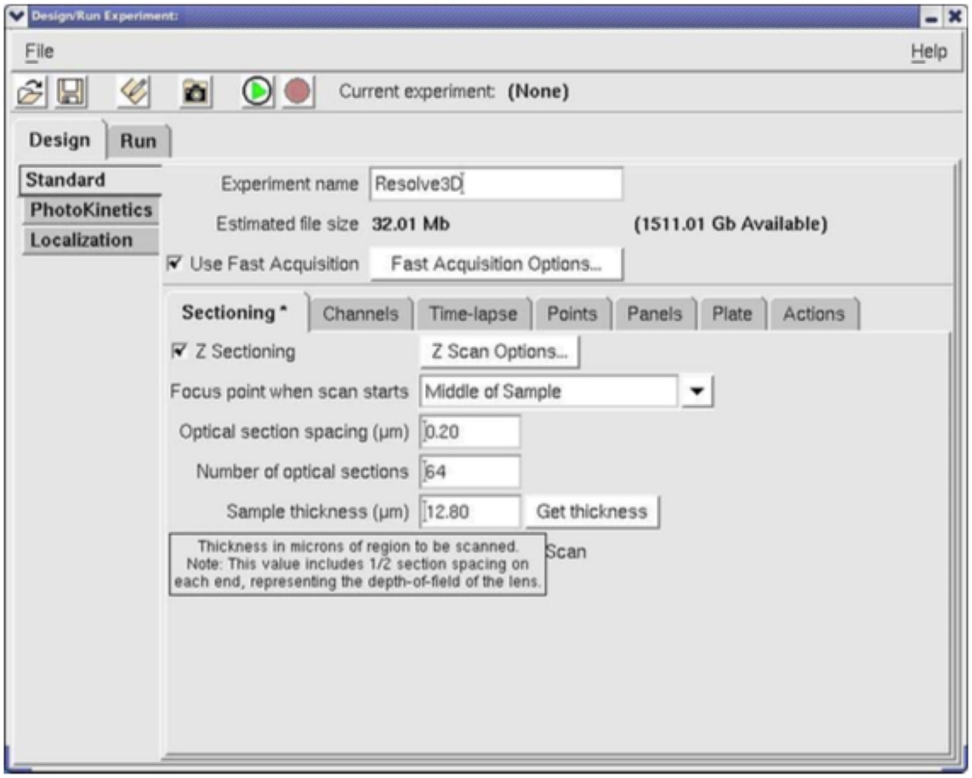

Experiment name: Resolve3D

Estimated file size: 32.01 Mb (1511.01 Gb Available)

☑ Use Fast Acquisition

☑ Z Sectioning

Focus point when scan starts: Middle of Sample

Optical section spacing (µm): 0.20

Number of optical sections: 64

Sample thickness (µm): 12.80

Thickness in microns of region to be scanned. Note: This value includes 1/2 section spacing on each end, representing the depth-of-field of the lens.

Figure 5. Design and Run experiment window.

i. Under design
   1) Experimental name field: write your file name (Figure 5).
   2) Under Sectioning

      Remove the check beside Z sectioning.
   3) Under channels (Figure 5).

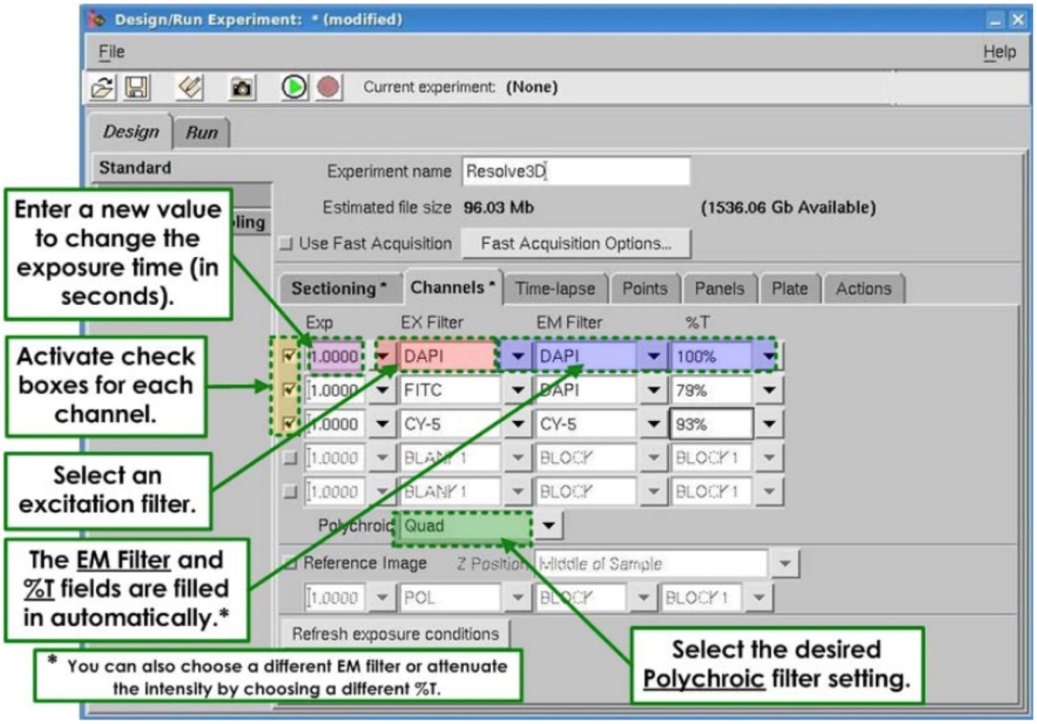

Current experiment: (None)

Experiment name: Resolve3D

Estimated file size: 96.03 Mb (1536.06 Gb Available)

☐ Use Fast Acquisition

	Exp	EX Filter	EM Filter	%T
☑	1.0000	DAPI	DAPI	100%
☑	1.0000	FITC	DAPI	79%
☑	1.0000	CY-5	CY-5	93%
☐	1.0000	BLANK 1	BLOCK	BLOCK 1
☐	1.0000	BLANK 1	BLOCK	BLOCK 1

Polychroic: Quad

☐ Reference Image Z Position: Middle of Sample

1.0000 POL BLOCK BLOCK 1

Enter a new value to change the exposure time (in seconds).

Activate check boxes for each channel.

Select an excitation filter.

The EM Filter and %T fields are filled in automatically.*

* You can also choose a different EM filter or attenuate the intensity by choosing a different %T.

Select the desired Polychroic filter setting.

Figure 6. The Channels in the Design and Run experiment window.

Check 1st box

Under EX filter: POL

Automatically EM filter will be modifying

Under% T: choose 32%

Check 2nd box

Under EX filter: FITC

Automatically EM filter will be modified

Under% T: choose100%

Check 3rd box

Under EX filter: mCherry

Automatically EM filter will be modified

Under% T: choose 100%

ii. Under Run before starting to acquire image

Image file name field, write the same name you wrote under the design/Experimental name (Figure 5).

iii. Now you are ready to acquire image by pressing on the start button ▶ as shown in Figure 7, You can adjust the image by looking on the Resolve3D window which contains the stage trails in the stage View window. This way you can focus at the pharynx level.

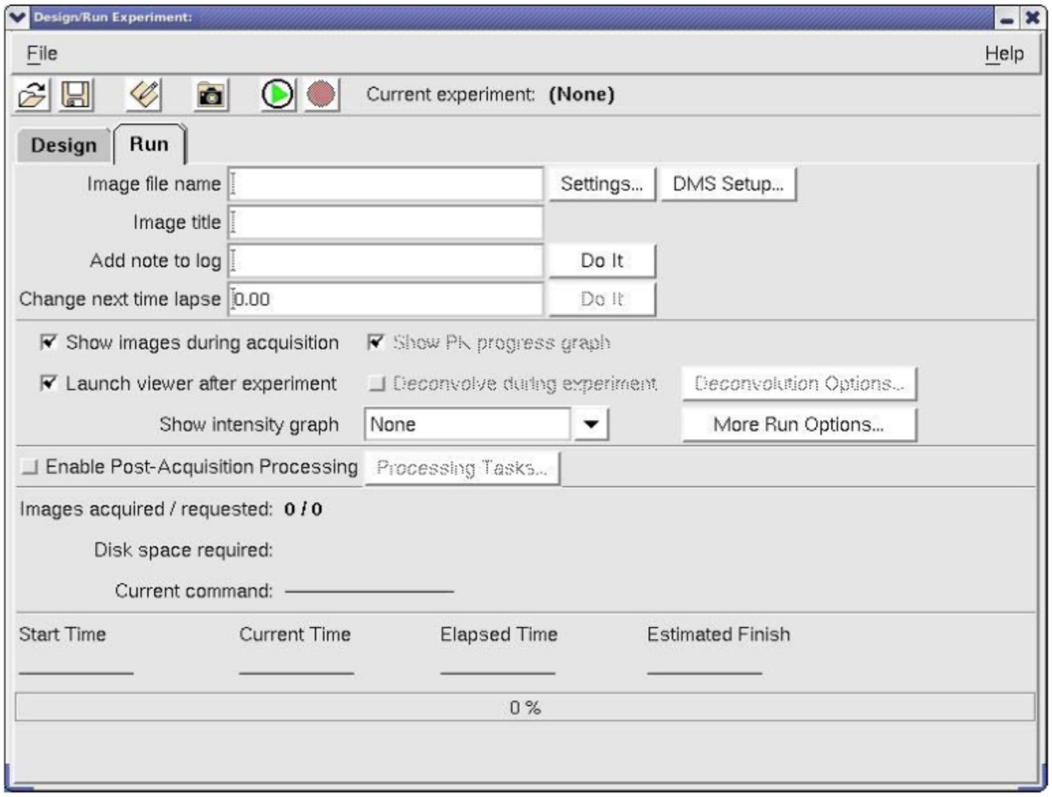

Design/Run Experiment:

Current experiment: **(None)**

Image file name

Image title

Add note to log

Change next time lapse 0.00

☑ Show images during acquisition

☑ Show PK progress graph

☑ Launch viewer after experiment

☐ Deconvolve during experiment

Show intensity graph None

☐ Enable Post-Acquisition Processing

Images acquired / requested: **0 / 0**

Disk space required:

Current command:

Start Time

Current Time

Elapsed Time

Estimated Finish

0 %

Figure 7. The start button in the Design and Run experiment window.

4. Result analysis

   a. Software used: ImageJ

      i. Drag the file to imageJ window.

      ii. Under image → Transform → rotate the image to get an image of the worm placed anterior to posterior.

      iii. Under image → Stacks → Stack to images.

iv. Under image → Color → merge channels.

Select the image which is appropriate to the desired color.

v. Create montage: under image → Stacks → make montage.

vi. Create the 3D picture based on the intensity.

vii. Take the merged image.

viii. Under Plugins → 3D → Interactive 3D surface plot.

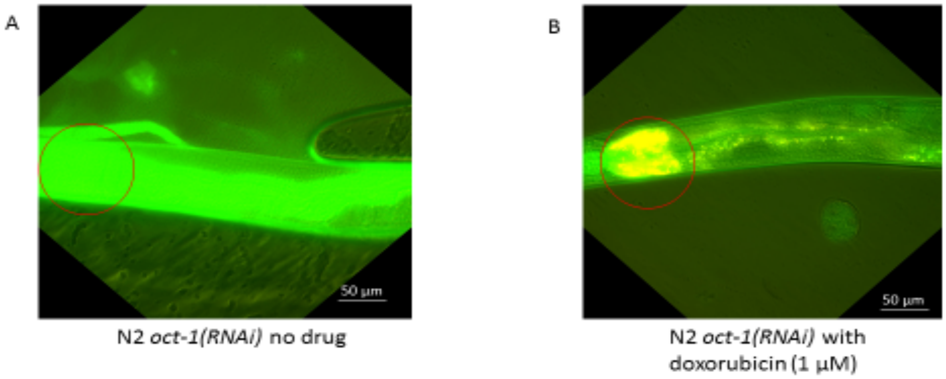

N2 *oct-1(RNAi)* no drug

N2 *oct-1(RNAi)* with doxorubicin (1 µM)

Figure 8. Uptake of doxorubicin in the N2 wild type animals downregulated for *oct-1* that causes upregulation of OCT-2. Previously, we showed that downregulation stimulated expression of *oct-2*, which drives uptake of drugs into *C. elegans* (Papaluca and Ramotar, 2016). **A.** Untreated; the absence of doxorubicin is illustrated by the lack of yellow fluorescence and the green background is autofluorescence from ingestion of food by the animal. **B.** Treated with doxorubicin (1 µM). Doxorubicin uptake is visible as yellow due to the merge of the green autofluorescence and red fluorescence from the drug. Circles show the location of the pharynx. Scale bars = 50 µm. See Data analysis for additional details.

4.6. Data analysis

The result is representative of a single worm from an experiment where 10 worms were placed onto the slide (Figure 8). The experiment was repeated three times with identical data. Fluorescence posterior to the pharynx is autofluorescence detected from the intestine

(Figure 8). The data were quantified using ImageJ according to Papaluca and Ramotar (2016)[6].

Notes:

1. Instead of using frozen bacteria as worm food, we typically use fresh culture of the bacteria.
2. Always work under sterile conditions. Be on the watch for fungus (white to black like spider net) and rarely mushroom (brownish spots). If this is the case, the best solution will be to bleach the worms and collect the eggs for new larvae.

4.7. Recipes

1. LB solution
   5 g tryptone
   2.5 g yeast extract
   5 g NaCl
   ddH_2O up to 500 ml
   Add 7.5 g of agar, if making solid media plates
2. NGM
   1.25 g peptone
   1.5 g NaCl
   8.75 g agar
   ddH_2O up to 500 ml
   Autoclave
   When the media is between 50 to 55 °C, add the following constituents before pouring the plates:
   12.5 ml of 1 M KH_2PO_4 pH 6
   500 µl of 1 M $MgSO_4$
   500 µl of 1 M $CaCl_2$
   500 µl cholesterol (stock 5 mg/ml in 95% ethanol)

500 µl of ampicillin (stock 100 mg/ml), if using the plasmid containing bacteria HT115^{DE3}

3. Agar pad

   3% agarose in water

   Melt when needed

4. Alkaline Hypochlorite solution (bleaching solution) (make fresh monthly)

   8.25 ml ddH_2O

   3.75 ml 1 N NaOH

   3.00 ml Bleach (Javel)

   5. M9 buffer

   6 g Na_2HPO_4

   3 g KH_2PO_4

   5 g NaCl

   0.25 g $MgSO_4 \cdot 7H_2O$

   per liter and sterilized by autoclaving

4.8. Acknowledgements

This work was funded by the research grant (RGPIN/202432-2012) to D.R. from the Natural Science and Engineering Research Council of Canada. A brief version of this protocol was previously described (Papaluca and Ramotar, 2016)[6].

4.9. References

1 Cesar-Razquin, A. *et al.* A Call for Systematic Research on Solute Carriers. *Cell* **162**, 478-487, doi:10.1016/j.cell.2015.07.022 (2015).

2 Burns, A. R. *et al.* A predictive model for drug bioaccumulation and bioactivity in Caenorhabditis elegans. *Nat Chem Biol* **6**, 549-557, doi:nchembio.380 (2010).

3 O'Reilly, L. P., Luke, C. J., Perlmutter, D. H., Silverman, G. A. & Pak, S. C. C. elegans in high-throughput drug discovery. *Adv Drug Deliv Rev* **69-70**, 247-253, doi:S0169-409X(13)00287-1 (2014).

4 Cheah, I. K. *et al.* Knockout of a putative ergothioneine transporter in Caenorhabditis elegans decreases lifespan and increases susceptibility to oxidative damage. *Free Radic Res* **47**, 1036-1045, doi:10.3109/10715762.2013.848354 (2013).

5 Wu, X. *et al.* Identity of the F52F12.1 gene product in Caenorhabditis elegans as an organic cation transporter. *Biochim Biophys Acta* **1418**, 239-244, doi:S0005-2736(99)00020-6 (1999).

6 Papaluca, A. & Ramotar, D. A novel approach using C. elegans DNA damage-induced apoptosis to characterize the dynamics of uptake transporters for therapeutic drug discoveries. *Sci Rep* **6**, 36026, doi:10.1038/srep36026 (2016).

Conclusion

Chapter 5 : General discussion

5.1. Chapter 2

A major challenge in achieving therapeutic concentrations of drugs into the body and subsequently targeting diseases involves crossing the epithelial and blood brain barriers to achieve such action. Membrane proteins are structures that can enhance the influx and distribution of therapeutic drugs across these barriers[1]. As such, ubiquitously expressed Organic Cation Transporters hold promise for targeting these agents to distinct organs[2] (Figure 1).

In a prototypical example of the widely studied family of OCTs, we have elucidated a basic underlying mechanism that modulates the entry of compounds, thus influencing cellular responses. This work provides for the first time an accurate model in *C. elegans* where the uptake of compounds depends on the genetic expression of *oct-1* and *oct-2* resembling those of mammals[113]. We believe that the indiscriminate uptake of compounds via OCT-2 is attributed to the fact that *oct-1* exerts regulatory functions on *oct-2* leading to the loss of homeostasis. Moreover, we propose that inducing constant levels of OCT-2 expression could be extrapolated as a strategy to develop drug screening programs in which the use of minimal drug concentration is central, and to better target chemotherapies.

5.1.1. Functional characterization of OCT-1 and OCT-2 in *C. elegans*

Despite that *C. elegans* has been an increasingly popular genetic model organism for the studies of oxidative processes, DNA damage, ageing and drug discovery[61], studies targeting specifically OCTs in *C. elegans* are scarce and to some extend underappreciated. Previous work done by Cheah *et al.*[67] showed that gene deletion of the uptake transporter OCT-1 resulted in a significant decrease in lifespan and increased oxidative damage[67]. This observation directed the hypothesis of the current study where genes of the same family could exert regulatory functions among each other. As such, it was plausible to think that the significant decrease in lifespan and increase in oxidative damage could be a result of OCT-1 exerting regulatory functions on OCT-2 leading the latter to high genetic expression. Thus, the deregulation of OCT-2 would lead to unmeasurable uptake of distinct compounds threatening the survival of the animal. Here, we unveiled for the first time specific roles for OCT-1 and OCT-2 in mediating membrane translocation of clinically relevant agents (Chapter 2, Table 1). We demonstrate that OCT-1 has no direct role in the transport of these agents, however, it exerts regulatory control on OCT-2 expression, and it is OCT-2 that is primarily involved in the uptake of these agents. As such, this study furthers our understanding of functional OCT-1 and OCT-2 in three fundamental ways:

(I) Depletion of *oct-1* elicited the upregulation of *oct-2* mainly in the head and gonads of the animals and extending through the body (unpublished observation), resulting in hypersensitivity to chemotherapeutic drugs, indicating that only the activity of OCT-2 leads to such phenotypes.

(II) The genotoxic effects produced by the DNA damaging agents were blocked exquisitely upon RNAi-driven depletion of *oct-2* exerting a protective effect in the animals. Moreover, *oct-1(ok1051)*; *oct-2(RNAi)* double mutant animals depicted similar resistance to chemotherapeutics as observed in the *oct-2* depletion mutant alone, indicating that it is indeed OCT-2 the main transporter in *C. elegans.* However, a role for OCT-1 in the uptake of selective DNA damaging agents could be attributed.

(III) Furthermore, our *in silico* modeling-based screening demonstrated that OCT-1 and OCT-2 have affinity for DNA damaging agents of diverse structural natures indicating the majority as exclusive ligands for OCT-2. After validating this method *in vivo*, we showed that animals with defective DNA repair pathways were higly sensitive to the OCT2-dependent uptake of the DNA damaging agents.

In general, OCT-2-dependent distribution of drugs represents a promising route towards better understanding drug-resistance or drug-sensitivity observed in patients during chemotherapy, and to develop better strategies to improve drug screening approaches and gene-based chemotherapies. The observations obtained from this work highlight the importance of OCTs as membrane-bound proteins that dynamically modulate the distribution of compounds into tissues.

5.1.2. Upregulation of OCT-2 and potential use in gene therapy

The use of gene therapy as an experimental technique to treat or prevent disease has been a strong field in cancer research[114]. Researchers are trying several methods including inactivating or knocking out a gene that is poorly functional[114] in order to prevent the progression of diseases. Thus, the unexpected observation that downregulation of *oct-1* leads to upregulation of *oct-2* provides an entirely new avenue to target cancer treatment. As gene therapy is currently being developed for cancer treatment, how might the upregulation of OCT-2 would benefit such treatments? And which role(s) might OCT-1 exert in this regard? Based on our results, we speculate that inactivation of *oct-1* leads to upregulation of OCT-2 and this eventually leads to higher uptake of chemotherapeutics during drug administration thus killing efficiently tumor cells. However, we are far from reaching such approach while testing a drug in clinical trials.

Following the line of thought that deletion of *oct-1* would stimulate OCT-2 to compensate for cellular functions, our investigations indicate that OCT-1 – apart from its transport abilities - might possess the functional characteristic of a transceptor[64,99]. Evidence suggests that certain transporters also act as receptors, indicating that these membrane proteins might partially execute signaling functions in addition to control of transport across membranes[115]. In this context, one could speculate that when cells are starved of substrate, OCT-1 might behave as a transceptor to promote the upregulation of OCT-2 in search for nutrients. Oppositely, when nutrients are abundant OCT-1 might keep the basal expression of OCT-2.

Similarly, this mode of regulation has been observed in *S. cerevisiae*, *Drosophila melanogaster* and *Homo sapiens*[116]. For example, in *S. cerevisiae*, the amino acid permease Gap1, combines a transporter function with a PKA signaling receptor function where the role of Gap1 in downregulating PKA signal was independent from its role in amino acid transport[115]. Similarly, a mechanism by which OCT-1 exerts regulatory control on OCT-2 also occurs in mammals, where downregulation of *OCT1* causes significant upregulation of *OCT2* and *OCT3* influencing metformin uptake[113]. Therefore, in view of OCT-1 acting as a transceptor modulating OCT-2 activity, it is plausible to think that a method in which the inactivation of OCT-1 and consequent upregulation of OCT-2 could be translated into combined gene and drug therapies.

Alternatively, other means to modulate OCTs expression have been reported[12] as upregulation of mammalian OCT2 is stimulated via PKA upon treatment with calmodulin (CaM), resulting in significant uptake of ASP^{+}[117]. Similarly, a recent report by Wu *et al.*[118] demonstrated that the sulfated polysaccharide fucoidan induced OCT2 expression via upregulation of PKA leading to an increase uptake of compounds[118] correlating with our findings (Chapter 2, Table 1). These evidences highlight yet another mechanism by which the expression of OCTs can be modulated as a strategy to enhance the efficacy of drug therapy.

5.1.3. OCT-2-dependent uptake of prooxidants

The maintenance of homeostasis in an organism could be regulated by various mechanisms, especially by controlling the uptake of nutrients and compounds available in the environment. While demonstrating that the uptake of a number of clinically relevant drugs is dependent exclusively upon OCT-2 activity, we noticed that *oct-2* downregulation sharply decreased spontaneous apoptosis and rescued shortened lifespan produced in *oct-1* deletion mutants. Based on our results, it is reasonable to speculate that prooxidants – defined as endobiotic or xenobiotic products that induce oxidative stress either by producing ROS or by hindering antioxidant pathways[119]- could be ingested by the animal and transported indiscriminately via an upregulated OCT-2.

Although we do not know how these prooxidants are originated, we observed that these molecules are capable of inducing DNA damage, which are exlusively repaired by the BER pathway. This is supported by the observation that only the BER defective *apn-1* deletion mutant - and not the MMR, NER and HR deletion mutants - exhibited higher levels of spontaneous apoptosis when *oct-2* expression is upregulated. Moreover, in a parallel study presented in Chapter 3, we propose that these prooxidants are capable of inducing oxidation of thymine originating the nucleoside 5-hmU creating DNA lesions.

Previous report demonstrates that *oct-1* deletion *C. elegans* depict a decline in lifespan as a result of a reduced uptake of the antioxidant ergothioneine[67]. Based on our observations, we could speculate that the sulphur atom on the imidazole ring of ergothioneine serves to detoxify the OCT-2-dependent uptake of prooxidants. Nonetheless, our findings raise a very important concern regarding genetic variations leading to hyperactivation of uptake transporters as previously reported[120]. This hyperactivation is likely to cause accumulation of abnormally high concentrations of genotoxic compounds and metabolites. Consequently, such toxic agents could induce substantial DNA damage over the lifetime of an individual causing genomic instability and eventually cancer.

5.1.4. OCT-2 as an *in silico* and *in vivo* drug screening method

C. elegans features powerful forward and reverse genetic tools which makes them an ideal model for the development of drug screening platforms. Identifying drug targets and understanding the mechanism of action of novel and widely used compounds is critical in drug discovery programs. To date, many popular drug-screening platforms are costly and with a low yield of bioactive compounds[111]. *Per se*, it is possible that the recovery rate of bioactive compounds could be higher if there is greater uptake of the compounds.

More recently, it has been described that a limitation when using *C. elegans* as a model for high-throughput screening (HTS) is that the use of high concentrations of living bacteria normally added to the culture media present a threat to screening as drug concentrations might differ significantly when compared to mammalian cell culture-based HTS[121]. Thus, from a pharmacological point of view, the ideal method would be to apply axenic liquid medium or medium containing dead bacteria in order to reduce potential variabilities in drug concentration[121]. We argue against these methods as *C. elegans*, in its natural environment, feeds from living bacteria which play an essential role for normal development[61]. Thus, we believe that restricting the animals from its natural habitat could impact the phenotypic outcomes e.g. by yielding false positives. In our studies, the level of living bacteria used was of standard concentration reaching an optical density of up to 0.5, without saturation. This provided an optimal environment that mimicked the natural habitat of these animals.

Herein, we efficiently integrated *C. elegans* and OCTs as a proof of concept in order to develop a cost-efficient drug discovery platform. Our study is the first to demonstrate that *C. elegans* OCT-2 is in charge of the uptake of a number of ligands. We tested doxorubicin and cisplatin as the initial cationic ligands since they are widely used chemotherapeutics transported by OCTs in human cells[22,30]. Following the notion that OCT-2 may recognize distinct chemotherapeutic drugs, in this study, we took an integrated computational and experimental approach to characterize previously unknown OCT-2 ligands using *C. elegans*.

We executed the OCT-based ligand-protein docking method to explore a list of handpicked cationic compounds and deduced that OCT-2 was promiscuous compared to OCT-1, interacting robustly with several cationic ligands. Importantly, the analysis produced a refined list of genotoxic compounds that display high protein-ligand docking scores all of which show an OCT-2 dependent *in vivo* effect of triggering germ cells apoptosis. We believe that exploiting OCT-2 in *C. elegans* could have far reaching applications and supersede other whole model systems in drug discovery programs with respect to cost and time.

Therefore, the strategy of maintaining the expression of OCT-2 transporter at optimal levels by deleting *oct-1* should represent a useful step for incorporation into any HTS platform to more efficiently identify bioactive molecules from chemical libraries. We believe that our results will help overcome the low uptake of compounds often observed in most HTS platforms and the high concentrations of bacteria used in most *C. elegans*–based HTS. Furthermore, a key aspect of this strategy is that overexpressed OCT-2 is expected to operate with significantly lower chemical concentrations as observed with cisplatin where a fixed lower concentration of the drug had no effect on the wild type, but significantly induced apoptosis in the *oct-1* deletion mutant. Thus, the previous barriers attributed to *C. elegans*-based HTS could be explained by the lack of an active mechanism to efficiently take up the compounds at lower concentrations.

In conclusion, we now provide a comprehensive readout of OCT-2 functional selectivity towards cationic molecules that have a deleterious effect on *C. elegans.* It also provides a foundation to understand the regulatory control of drug uptake to circumvent genotoxicities. In addition, we propose that OCT-2 could be exploited either through the *oct-1* gene deletion mutant or *oct-2* overexpression transgenic animals to generate a hypersensitive screening method based on *C. elegans* to facilitate HTS platforms.

5.2. Chapter 3

5.2.1. The oxidation product 5-hmU is processed by the BER pathway

Protecting DNA integrity from oxidative stress byproducts is a constant challenge for living organisms. Endogenous and exogenous factors including reactive oxygen species (ROS), such as hydrogen peroxide (H_2O_2), superoxide anion ($O_2^{\bullet -}$) and hydroxyl radical (OH) threaten genomic integrity and result in various types of DNA damage, including the formation of single altered DNA bases. Undoubtedly, oxidative stress causes cellular injury and may trigger several pathologies[122]. One of the most enigmatic ROS derivative is 5-hydroxymethyluracil (5-hmU), initially regarded as an oxidatively modified product of thymine[123]. 5-hmU is a uracil analog produced from two different oxidative sources: oxidation and/or hydroxylation of thymine produced by ROS resulting in mispair of 5-hmU with adenine (5-hmU:A); or ROS reacting with 5-methylcytosine (5-mC) resulting in 5-hydroxymethylcytosine (5-hmC), of which deamination produces 5-hmU mispaired with guanine (5-hmU:G)[123]. These mispaired single DNA bases produced by 5-hmU are often recognized as genotoxic lesions[123] which must be removed to preserve DNA integrity.

The BER pathway is crucial in eliminating specific types of oxidative DNA lesions – such as uracil analogs - that would otherwise compromise important cellular components[73,124]. In *C. elegans*, the BER is initiated upon excision of modified bases recognized by the DNA glycosylases UNG-1 and NTH-1. For instance, excision of uracil analogs from the DNA is mediated by UNG-1, which catalyzes the cut of the N-glycosylic bond from between the base to the sugar resulting in a secondary DNA lesion, named AP site[71,74,75]. The enzymes APN-1 and EXO-3 respectively, incise the AP site resulting in a single strand break[73], and further processing leads to synthesis of new nucleotides catalyzed by the DNA polymerase[125]. To date, studies investigating the interplay between BER enzymes that recognize and excise the nucleoside 5-hmU in *C. elegans* are scarce.

In our second study, we uncovered a new mechanism in which the enzymes UNG-1 and APN-1 interplay to remove 5-hmU and process the resulting AP sites in *C. elegans*. Previous reports show that *C. elegans* UNG-1 is capable of removing uracil[76], while NTH-1 has a wide substrate specificity and removes thymine glycol, 5-formyluracil and 5-hmU from lesions containing DNA substrates using purified enzymes[76,77,126]. Based on previous reports showing that APN-1 has additional enzymatic activities[73] - as opposed to EXO-3 which has limited functionalities - it would be reasonable to assume that *C. elegans* devoid of NTH-1 and APN-1 would have the most severe phenotypes when challenged with DNA damaging agents. However, when challenged with the nucleoside form of 5-hmU, we demonstrated that *C. elegans* BER mutants depicted notable phenotypes which prompted a reconsideration of the *in vivo* roles of UNG-1 and NTH-1 in this organism.

5.2.2. Detrimental effects of 5-hmU

We observed that exposure of *C. elegans* to 5-hmU resulted in a decrease in brood size and lifespan, as well as an increase in germ cell apoptosis. These results indicated that 5-hmU must be incorporated into the genome of the animal leading to detrimental effects on survival. In fact, mass spectrometry analysis revealed that mammalian cells exposed to 5-hmU displayed incorporation of this oxidized nucleoside into the genome[127,128]. We attempted to monitor the levels of 5-hmU lesions in *C. elegans* genome via mass spectrometry, but we were unable to observe an increase over background using the wild type, as well as the *ung-1* and the *apn-1* deficient mutants. We did, however, observe an increased sensitivity of *ung-1* mutants to 5-hmU, whereas *nth-1* mutants displayed no sensitivity to this nucleoside, contradicting previous reports[74,75,114].

We propose that *C. elegans* UNG-1 may have evolved to acquire a wide substrate specificity and thus could act *in vivo* to process several uracil derivatives including 5-hmU lesions. Recent observations showed that SMUG1 is the glycosylase responsible for excision of 5-hmU in mice[129,130]. Notably, *C. elegans* lacks the homologue SMUG1 glycosylase, however, *C. elegans* UNG-1 conserves key amino acid residues present in mammalian UNG1 and SMUG1, and the latter is capable of excising 5-hmU from the DNA[128].

Nevertheless, whether these conserved residues provide to *C. elegans* UNG-1 the ability to recognize and process 5-hmU mimmicking mammalian SMUG1 needs further investigation.

After excision of 5-hmU by UNG-1, the creation of an AP site leads to the recruitment of either APN-1 or EXO-3 to the site of lesion. If APN-1 and EXO-3 played redundant roles as AP endonucleases in *C. elegans*, one would expect that the absence of either enzyme would not contribute to increased sensitivity to 5-hmU. Nonetheless, our results contradict this idea as animals deficient in EXO-3 did not display sensitivity to the effects of 5-hmU, whereas animals devoid of APN-1 were highly sensitive. This suggests that APN-1 – and not EXO-3 – is the main endonuclease responsible for processing 5-hmU lesions in *C. elegans*.

Indeed, these results correlate with previous reports demonstrating that the enzymatic activity of EXO-3 depends on the DNA damaging agent[131]. For instance, expression of EXO-3 provided full resistance to the antineoplastic drug bleomycin indicating active repair of the damaged DNA, whereas expression of APN-1 provided only partial resistance to bleomycin in *C. elegans*[131]. Similarly, it has been demonstrated that EXO-3 processes the uracil analog 5-fluorouracil (5-FU)[132] as accumulation of RPA-1 foci in response to DNA damage depends mainly on EXO-3 to excise 5-FU from the DNA in order to initiate the MMR pathway[132,133].

Furthermore, both 5-hmU and 5-FU possess distinct mechanism of action driven by the only difference of an halogen and an hydroxymethyl group respectively[123,134]. This subtle structural variation could explain the specificity of EXO-3 towards 5-FU and not 5-hmU, which is processed solely by APN-1. As well, exposure of *apn-1* mutants to 5-FU did not induce significant levels of germ cell apoptosis neither reduction in brood size (unpublished observations), corroborating the hypothesis that substrate specificity differs between APN-1 and EXO-3. Certainly, these studies[131,132], linked with our results, prove that substrate specificity of both enzymes differs in many aspects and depending on the substrate, it will trigger the respective DNA repair response.

Based on our findings, it is plausible to speculate that, aside from its main function as an ExoIII AP endonuclease, EXO-3 might also play a minor role in regulating the apoptotic pathway. For instance, human APEX1/REF1 - which shares 45% DNA sequence homology with *C. elegans* EXO-3 - is a key regulator of the pro-apoptotic protein p53[135]. As such, it is likely that EXO-3 might act as an auxiliary protein in the apoptotic pathway when the base excision repair response is overburdened. Thus, EXO-3 might feature dual functions: processing the damaged DNA and eliminating cells with defective genome via apoptosis, mimicking the enzymatic role of the human APEX1/REF1. However, more research is needed for this assertion.

5.2.3. UNG-1 interacts with APN-1 to repair 5-hmU lesions

Our data allowed us to build a model where animals lacking simultaneously UNG-1 and APN-1 would be highly sensitive to 5-hmU which burdens the organism with excessive single DNA strand breaks with blocked 3′-ends (Chapter 3, Figure 7). Upon excision of 5-hmU by UNG-1, the enzymes APN-1 or EXO-3 process the AP sites[136,137]; whereas the absence of UNG-1 promotes the activation of an alternative pathway, in which NTH-1 removes the lesion instead. However, NTH-1 activity also creates a genotoxic single strand break with a blocked 3′-end, α,β unsaturated aldehyde that blocks DNA synthesis[138]. It is possible that the resulting blocked 3′-end is not rapidly removed by APN-1, in particular, if EXO-3 stimulates NTH-1, as seen for the DNA glycosylases OGG1 and TDG by APE1 in human cells[139,140], to create an abundance of blocked 3′-ends that overwhelms the 3′-diesterase and/or 3′- to 5′-exonuclease repair capacity of APN-1.

Our results show that RNAi downregulation of *nth-1* can suppress the genotoxicity of 5-hmU in *apn-1* mutants. This is consistent with the idea that if the hypersensitivity to 5-hmU observed in the *apn-1* mutants is indeed a consequence of single strand breaks with blocked 3′-ends originated by the β-lyase activity of NTH-1, then the removal of NTH-1 should rescue the lethality of these mutants. Theoretically, in the absence of NTH-1 and APN-1, UNG-1 would take over the function of removing the 5-hmU lesion and would leave an AP site to be processed by the AP endonuclease activity of EXO-3[136,137]. We disproved the idea that EXO-3 would act to remove the 3′- α,β unsaturated aldehyde generated by NTH-1, as animals devoid of both EXO-3 and APN-1 are no more sensitive to 5-hmU than animals devoid of APN-1 only. This is consistent with previous reports showing that, unlike APN-1, EXO-3 lacks a 3′- to 5′-exonuclease activity, which is possibly required to remove the 3′-blocked ends[133,141-143]. Similarly, it has been previously reported that downregulation of UNG-1 activity rescues the decreased lifespan on *exo-3* mutants by preventing the production of AP sites[137]. This phenotype was not observed when NTH-1 was defective in *exo-3* mutants, indicating that NTH-1 does not elicit intermediate lesions to be processed by EXO-3[137].

In summary, we have determined that the oxidized product of thymine, 5-hmU, is processed by the BER pathway in *C. elegans* and UNG-1 is the main DNA glycosylase required for the removal of 5-hmU lesions. Moreover, we believe that UNG-1 and APN-1 act in cooperation to remove this type of nucleoside.

5.3. Conclusion

To conclude, if similar mechanisms to those we have found in *C. elegans* do occur in humans, they could prove to be important targets for therapeutic intervention towards restoring the normal state of diseased cell phenotypes. Understanding the trafficking of potentially toxic molecules into the cells, as well as the variety of dynamic repair mechanisms that cells evolved to resist environmental insults would therefore allow us to explain the diverse and complex phenotypes observed in living organisms and take advantage of these properties towards personalized medicine. Given the progress made thus far, we predict that using *C. elegans* in combination with Organic Cation Transporters or Solute Carriers in general, will become an essential tool in the development of drug discovery.

Bibliography

1 Cournia, Z. *et al.* Membrane Protein Structure, Function, and Dynamics: a Perspective from Experiments and Theory. *J Membr Biol* **248**, 611-640, doi:10.1007/s00232-015-9802-0 (2015).

2 Lin, L., Yee, S. W., Kim, R. B. & Giacomini, K. M. SLC transporters as therapeutic targets: emerging opportunities. *Nat Rev Drug Discov* **14**, 543-560, doi:10.1038/nrd4626 (2015).

3 Cesar-Razquin, A. *et al.* A Call for Systematic Research on Solute Carriers. *Cell* **162**, 478-487, doi:10.1016/j.cell.2015.07.022 (2015).

4 Nigam, S. K. What do drug transporters really do? *Nat Rev Drug Discov* **14**, 29-44, doi:10.1038/nrd4461 (2015).

5 Schrum, J. P., Zhu, T. F. & Szostak, J. W. The origins of cellular life. *Cold Spring Harb Perspect Biol* **2**, a002212, doi:10.1101/cshperspect.a002212 (2010).

6 Li, Q. & Shu, Y. Role of solute carriers in response to anticancer drugs. *Mol Cell Ther* **2**, 15, doi:10.1186/2052-8426-2-15 (2014).

7 International Transporter, C. *et al.* Membrane transporters in drug development. *Nat Rev Drug Discov* **9**, 215-236, doi:10.1038/nrd3028 (2010).

8 Urban, T. J. & Giacomini, K. M. in *Drug Transporters* 11-33 (John Wiley & Sons, Inc., 2006).

9 Grundemann, D., Gorboulev, V., Gambaryan, S., Veyhl, M. & Koepsell, H. Drug excretion mediated by a new prototype of polyspecific transporter. *Nature* **372**, 549-552, doi:10.1038/372549a0 (1994).

10 Koepsell, H. The SLC22 family with transporters of organic cations, anions and zwitterions. *Mol Aspects Med* **34**, 413-435, doi:10.1016/j.mam.2012.10.010 (2013).

11 Schlessinger, A. *et al.* Comparison of human solute carriers. *Protein Sci* **19**, 412-428, doi:10.1002/pro.320 (2010).

12 Ciarimboli, G. & Schlatter, E. Regulation of organic cation transport. *Pflugers Arch* **449**, 423-441, doi:10.1007/s00424-004-1355-5 (2005).

13 Sprowl, J. A. *et al.* A phosphotyrosine switch regulates organic cation transporters. *Nat Commun* **7**, 10880, doi:10.1038/ncomms10880 (2016).

14 Popp, C. *et al.* Amino acids critical for substrate affinity of rat organic cation transporter 1 line the substrate binding region in a model derived from the tertiary structure of lactose permease. *Mol Pharmacol* **67**, 1600-1611, doi:10.1124/mol.104.008839 (2005).

15 Koepsell, H. Polyspecific organic cation transporters: their functions and interactions with drugs. *Trends Pharmacol Sci* **25**, 375-381, doi:10.1016/j.tips.2004.05.005 (2004).

16 Jonker, J. W. & Schinkel, A. H. Pharmacological and physiological functions of the polyspecific organic cation transporters: OCT1, 2, and 3 (SLC22A1-3). *J Pharmacol Exp Ther* **308**, 2-9, doi:10.1124/jpet.103.053298 (2004).

17 Wu, X. *et al.* Identity of the organic cation transporter OCT3 as the extraneuronal monoamine transporter (uptake2) and evidence for the expression of the transporter in the brain. *J Biol Chem* **273**, 32776-32786 (1998).

18 Kimura, H. *et al.* Human organic anion transporters and human organic cation transporters mediate renal transport of prostaglandins. *J Pharmacol Exp Ther* **301**, 293-298 (2002).

19 Dresser, M. J., Gray, A. T. & Giacomini, K. M. Kinetic and selectivity differences between rodent, rabbit, and human organic cation transporters (OCT1). *J Pharmacol Exp Ther* **292**, 1146-1152 (2000).

20 Koepsell, H., Schmitt, B. M. & Gorboulev, V. Organic cation transporters. *Rev Physiol Biochem Pharmacol* **150**, 36-90, doi:10.1007/s10254-003-0017-x (2003).

21 Mehrens, T. *et al.* The affinity of the organic cation transporter rOCT1 is increased by protein kinase C-dependent phosphorylation. *J Am Soc Nephrol* **11**, 1216-1224 (2000).

22 Andreev, E., Brosseau, N., Carmona, E., Mes-Masson, A. M. & Ramotar, D. The human organic cation transporter OCT1 mediates high affinity uptake of the anticancer drug daunorubicin. *Sci Rep* **6**, 20508, doi:10.1038/srep20508 (2016).

23 Moreno-Navarrete, J. M. *et al.* OCT1 Expression in adipocytes could contribute to increased metformin action in obese subjects. *Diabetes* **60**, 168-176, doi:10.2337/db10-0805 (2011).

24 Minematsu, T. & Giacomini, K. M. Interactions of tyrosine kinase inhibitors with organic cation transporters and multidrug and toxic compound extrusion proteins. *Mol Cancer Ther* **10**, 531-539, doi:10.1158/1535-7163.MCT-10-0731 (2011).

25 Papaluca, A. & Ramotar, D. A novel approach using C. elegans DNA damage-induced apoptosis to characterize the dynamics of uptake transporters for therapeutic drug discoveries. *Sci Rep* **6**, 36026, doi:10.1038/srep36026 (2016).

26 Schaeffeler, E. *et al.* DNA methylation is associated with downregulation of the organic cation transporter OCT1 (SLC22A1) in human hepatocellular carcinoma. *Genome Med* **3**, 82, doi:10.1186/gm298 (2011).

27 Chen, L. *et al.* Genetic polymorphisms in organic cation transporter 1 (OCT1) in Chinese and Japanese populations exhibit altered function. *J Pharmacol Exp Ther* **335**, 42-50, doi:10.1124/jpet.110.170159 (2010).

28 Zhou, Y. *et al.* Genetic variants of OCT1 influence glycemic response to metformin in Han Chinese patients with type-2 diabetes mellitus in Shanghai. *Int J Clin Exp Pathol* **8**, 9533-9542 (2015).

29 Ballestero, M. R. *et al.* Expression of transporters potentially involved in the targeting of cytostatic bile acid derivatives to colon cancer and polyps. *Biochem Pharmacol* **72**, 729-738, doi:10.1016/j.bcp.2006.06.007 (2006).

30 Zhang, S. *et al.* Organic cation transporters are determinants of oxaliplatin cytotoxicity. *Cancer Res* **66**, 8847-8857, doi:10.1158/0008-5472.CAN-06-0769 (2006).

31 More, S. S. *et al.* Organic cation transporters modulate the uptake and cytotoxicity of picoplatin, a third-generation platinum analogue. *Mol Cancer Ther* **9**, 1058-1069, doi:10.1158/1535-7163.MCT-09-1084 (2010).

32 Thomas, J., Wang, L., Clark, R. E. & Pirmohamed, M. Active transport of imatinib into and out of cells: implications for drug resistance. *Blood* **104**, 3739-3745, doi:10.1182/blood-2003-12-4276 (2004).

33 Gupta, S. *et al.* Human organic cation transporter 1 is expressed in lymphoma cells and increases susceptibility to irinotecan and paclitaxel. *J Pharmacol Exp Ther* **341**, 16-23, doi:10.1124/jpet.111.190561 (2012).

34 Okuda, M., Saito, H., Urakami, Y., Takano, M. & Inui, K. cDNA cloning and functional expression of a novel rat kidney organic cation transporter, OCT2. *Biochem Biophys Res Commun* **224**, 500-507 (1996).

35 Ciarimboli, G. *et al.* Organic cation transporter 2 mediates cisplatin-induced oto- and nephrotoxicity and is a target for protective interventions. *Am J Pathol* **176**, 1169-1180, doi:10.2353/ajpath.2010.090610 (2010).

36 Bacq, A. *et al.* Organic cation transporter 2 controls brain norepinephrine and serotonin clearance and antidepressant response. *Mol Psychiatry* **17**, 926-939, doi:10.1038/mp.2011.87 (2012).

37 Winter, T. N., Elmquist, W. F. & Fairbanks, C. A. OCT2 and MATE1 provide bidirectional agmatine transport. *Mol Pharm* **8**, 133-142, doi:10.1021/mp100180a (2011).

38 Nies, A. T., Koepsell, H., Damme, K. & Schwab, M. Organic cation transporters (OCTs, MATEs), in vitro and in vivo evidence for the importance in drug therapy. *Handb Exp Pharmacol*, 105-167, doi:10.1007/978-3-642-14541-4_3 (2011).

39 Ciarimboli, G. *et al.* New clues for nephrotoxicity induced by ifosfamide: preferential renal uptake via the human organic cation transporter 2. *Mol Pharm* **8**, 270-279, doi:10.1021/mp100329u (2011).

40 Schmitt, B. M. & Koepsell, H. Alkali cation binding and permeation in the rat organic cation transporter rOCT2. *J Biol Chem* **280**, 24481-24490, doi:10.1074/jbc.M414550200 (2005).

41 Soodvilai, S., Nantavishit, J., Muanprasat, C. & Chatsudthipong, V. Renal organic cation transporters mediated cadmium-induced nephrotoxicity. *Toxicol Lett* **204**, 38-42, doi:10.1016/j.toxlet.2011.04.005 (2011).

42 Schmitt, B. M. *et al.* Charge-to-substrate ratio during organic cation uptake by rat OCT2 is voltage dependent and altered by exchange of glutamate 448 with glutamine. *Am J Physiol Renal Physiol* **296**, F709-722, doi:10.1152/ajprenal.90323.2008 (2009).

43 Aoki, M. *et al.* Kidney-specific expression of human organic cation transporter 2 (OCT2/SLC22A2) is regulated by DNA methylation. *Am J Physiol Renal Physiol* **295**, F165-170, doi:10.1152/ajprenal.90257.2008 (2008).

44 Grabner, A. *et al.* LAPTM4A interacts with hOCT2 and regulates its endocytotic recruitment. *Cell Mol Life Sci* **68**, 4079-4090, doi:10.1007/s00018-011-0694-6 (2011).

45 Aperia, A. C. Intrarenal dopamine: a key signal in the interactive regulation of sodium metabolism. *Annu Rev Physiol* **62**, 621-647, doi:10.1146/annurev.physiol.62.1.621 (2000).

46 Filipski, K. K., Mathijssen, R. H., Mikkelsen, T. S., Schinkel, A. H. & Sparreboom, A. Contribution of organic cation transporter 2 (OCT2) to cisplatin-induced nephrotoxicity. *Clin Pharmacol Ther* **86**, 396-402, doi:10.1038/clpt.2009.139 (2009).

47 Yokoo, S. *et al.* Differential contribution of organic cation transporters, OCT2 and MATE1, in platinum agent-induced nephrotoxicity. *Biochem Pharmacol* **74**, 477-487, doi:10.1016/j.bcp.2007.03.004 (2007).

48 Jonker, J. W. *et al.* Reduced hepatic uptake and intestinal excretion of organic cations in mice with a targeted disruption of the organic cation transporter 1 (Oct1 [Slc22a1]) gene. *Mol Cell Biol* **21**, 5471-5477, doi:10.1128/MCB.21.16.5471-5477.2001 (2001).

49 Troncone, L. & Rufini, V. 131I-MIBG therapy of neural crest tumours (review). *Anticancer Res* **17**, 1823-1831 (1997).

50 Wang, D. S. *et al.* Involvement of organic cation transporter 1 in hepatic and intestinal distribution of metformin. *J Pharmacol Exp Ther* **302**, 510-515, doi:10.1124/jpet.102.034140 (2002).

51 Jonker, J. W., Wagenaar, E., Van Eijl, S. & Schinkel, A. H. Deficiency in the organic cation transporters 1 and 2 (Oct1/Oct2 [Slc22a1/Slc22a2]) in mice abolishes renal secretion of organic cations. *Mol Cell Biol* **23**, 7902-7908 (2003).

52 Ramalingam, S. S. *et al.* Phase 2 study of irinotecan and paclitaxel in patients with recurrent or refractory small cell lung cancer. *Cancer* **116**, 1344-1349, doi:10.1002/cncr.24753 (2010).

53 Gorboulev, V. *et al.* Cloning and characterization of two human polyspecific organic cation transporters. *DNA Cell Biol* **16**, 871-881, doi:10.1089/dna.1997.16.871 (1997).

54 Tatsumi, S. *et al.* Organic cation transporter 2 and tumor budding as independent prognostic factors in metastatic colorectal cancer patients treated with oxaliplatin-based chemotherapy. *Int J Clin Exp Pathol* **7**, 204-212 (2014).

55 Rabik, C. A. & Dolan, M. E. Molecular mechanisms of resistance and toxicity associated with platinating agents. *Cancer Treat Rev* **33**, 9-23, doi:10.1016/j.ctrv.2006.09.006 (2007).

56 Pabla, N. & Dong, Z. Cisplatin nephrotoxicity: mechanisms and renoprotective strategies. *Kidney Int* **73**, 994-1007, doi:10.1038/sj.ki.5002786 (2008).

57 Naka, A. *et al.* Organic cation transporter 2 for predicting cisplatin-based neoadjuvant chemotherapy response in gastric cancer. *Am J Cancer Res* **5**, 2285-2293 (2015).

58 Brenner, S. The genetics of Caenorhabditis elegans. *Genetics* **77**, 71-94 (1974).

59 in *C. elegans II* (eds D. L. Riddle, T. Blumenthal, B. J. Meyer, & J. R. Priess) (1997).

60 Consortium, C. e. S. Genome sequence of the nematode C. elegans: a platform for investigating biology. *Science* **282**, 2012-2018 (1998).

61 Kaletta, T. & Hengartner, M. O. Finding function in novel targets: C. elegans as a model organism. *Nat Rev Drug Discov* **5**, 387-398, doi:10.1038/nrd2031 (2006).

62 Bailly, A. & Gartner, A. Germ cell apoptosis and DNA damage responses. *Adv Exp Med Biol* **757**, 249-276, doi:10.1007/978-1-4614-4015-4_9 (2013).

63 Veriepe, J., Fossouo, L. & Parker, J. A. Neurodegeneration in C. elegans models of ALS requires TIR-1/Sarm1 immune pathway activation in neurons. *Nat Commun* **6**, 7319, doi:10.1038/ncomms8319 (2015).

64 Patten, S. A., Parker, J. A., Wen, X. Y. & Drapeau, P. Simple animal models for amyotrophic lateral sclerosis drug discovery. *Expert Opin Drug Discov* **11**, 797-804, doi:10.1080/17460441.2016.1196183 (2016).

65 Tada, M. *et al.* Coexistence of Huntington's disease and amyotrophic lateral sclerosis: a clinicopathologic study. *Acta Neuropathol* **124**, 749-760, doi:10.1007/s00401-012-1005-5 (2012).

66 Wu, X. *et al.* Identity of the F52F12.1 gene product in Caenorhabditis elegans as an organic cation transporter. *Biochim Biophys Acta* **1418**, 239-244 (1999).

67 Cheah, I. K. *et al.* Knockout of a putative ergothioneine transporter in Caenorhabditis elegans decreases lifespan and increases susceptibility to oxidative damage. *Free Radic Res* **47**, 1036-1045, doi:10.3109/10715762.2013.848354 (2013).

68 Brosseau, N., Andreev, E. & Ramotar, D. Complementation of the Yeast Model System Reveals that Caenorhabditis elegans OCT-1 Is a Functional Transporter of Anthracyclines. *PLoS One* **10**, e0133182, doi:10.1371/journal.pone.0133182 (2015).

69 Aouida, M., Rubio-Texeira, M., Thevelein, J. M., Poulin, R. & Ramotar, D. Agp2, a member of the yeast amino acid permease family, positively regulates polyamine transport at the transcriptional level. *PLoS One* **8**, e65717, doi:10.1371/journal.pone.0065717 (2013).

70 Iyama, T. & Wilson, D. M., 3rd. DNA repair mechanisms in dividing and non-dividing cells. *DNA Repair (Amst)* **12**, 620-636, doi:10.1016/j.dnarep.2013.04.015 (2013).

71 Hoeijmakers, J. H. Genome maintenance mechanisms for preventing cancer. *Nature* **411**, 366-374, doi:10.1038/35077232 (2001).

72 O'Neil, N. & Rose, A. DNA repair. *WormBook*, 1-12, doi:10.1895/wormbook.1.54.1 (2006).

73 Daley, J. M., Zakaria, C. & Ramotar, D. The endonuclease IV family of apurinic/apyrimidinic endonucleases. *Mutat Res* **705**, 217-227, doi:10.1016/j.mrrev.2010.07.003 (2010).

74 Prasad, R. *et al.* A review of recent experiments on step-to-step "hand-off" of the DNA intermediates in mammalian base excision repair pathways. *Mol Biol (Mosk)* **45**, 586-600 (2011).

75 Swain, U. & Rao, K. S. Age-dependent decline of DNA base excision repair activity in rat cortical neurons. *Mech Ageing Dev* **133**, 186-194, doi:10.1016/j.mad.2012.01.001 (2012).

76 Skjeldam, H. K. *et al.* Loss of Caenorhabditis elegans UNG-1 uracil-DNA glycosylase affects apoptosis in response to DNA damaging agents. *DNA Repair (Amst)* **9**, 861-870, doi:10.1016/j.dnarep.2010.04.009 (2010).

77 Morinaga, H. *et al.* Purification and characterization of Caenorhabditis elegans NTH, a homolog of human endonuclease III: essential role of N-terminal region. *DNA Repair (Amst)* **8**, 844-851, doi:10.1016/j.dnarep.2009.04.020 (2009).

78 Zakaria, C. *et al.* Caenorhabditis elegans APN-1 plays a vital role in maintaining genome stability. *DNA Repair (Amst)* **9**, 169-176, doi:10.1016/j.dnarep.2009.11.007 (2010).

79 Asagoshi, K. *et al.* Single-nucleotide base excision repair DNA polymerase activity in C. elegans in the absence of DNA polymerase beta. *Nucleic Acids Res* **40**, 670-681, doi:10.1093/nar/gkr727 (2012).

80 Kelley, M. R., Logsdon, D. & Fishel, M. L. Targeting DNA repair pathways for cancer treatment: what's new? *Future Oncol* **10**, 1215-1237, doi:10.2217/fon.14.60 (2014).

81 Lans, H. & Vermeulen, W. Nucleotide Excision Repair in Caenorhabditis elegans. *Mol Biol Int* **2011**, 542795, doi:10.4061/2011/542795 (2011).

82 Neher, T. M., Bodenmiller, D., Fitch, R. W., Jalal, S. I. & Turchi, J. J. Novel irreversible small molecule inhibitors of replication protein A display single-agent activity and synergize with cisplatin. *Mol Cancer Ther* **10**, 1796-1806, doi:10.1158/1535-7163.MCT-11-0303 (2011).

83 Shuck, S. C., Short, E. A. & Turchi, J. J. Eukaryotic nucleotide excision repair: from understanding mechanisms to influencing biology. *Cell Res* **18**, 64-72, doi:10.1038/cr.2008.2 (2008).

84 Barret, J. M., Cadou, M. & Hill, B. T. Inhibition of nucleotide excision repair and sensitisation of cells to DNA cross-linking anticancer drugs by F 11782, a novel fluorinated epipodophylloid. *Biochem Pharmacol* **63**, 251-258 (2002).

85 D'Incalci, M. & Galmarini, C. M. A review of trabectedin (ET-743): a unique mechanism of action. *Mol Cancer Ther* **9**, 2157-2163, doi:10.1158/1535-7163.MCT-10-0263 (2010).

86 Barakat, K. H. *et al.* Virtual screening and biological evaluation of inhibitors targeting the XPA-ERCC1 interaction. *PLoS One* **7**, e51329, doi:10.1371/journal.pone.0051329 (2012).

87 Usanova, S. *et al.* Cisplatin sensitivity of testis tumour cells is due to deficiency in interstrand-crosslink repair and low ERCC1-XPF expression. *Mol Cancer* **9**, 248, doi:10.1186/1476-4598-9-248 (2010).

88 Li, G. M. Mechanisms and functions of DNA mismatch repair. *Cell Res* **18**, 85-98, doi:10.1038/cr.2007.115 (2008).

89 Modrich, P. Mismatch repair, genetic stability, and cancer. *Science* **266**, 1959-1960 (1994).

90 Martin, S. A., Lord, C. J. & Ashworth, A. Therapeutic targeting of the DNA mismatch repair pathway. *Clin Cancer Res* **16**, 5107-5113, doi:10.1158/1078-0432.CCR-10-0821 (2010).

91 Dianov, G., Bischoff, C., Piotrowski, J. & Bohr, V. A. Repair pathways for processing of 8-oxoguanine in DNA by mammalian cell extracts. *J Biol Chem* **273**, 33811-33816 (1998).

92 Kinsella, T. J. Coordination of DNA mismatch repair and base excision repair processing of chemotherapy and radiation damage for targeting resistant cancers. *Clin Cancer Res* **15**, 1853-1859, doi:10.1158/1078-0432.CCR-08-1307 (2009).

93 Li, Y. H. *et al.* Inhibition of non-homologous end joining repair impairs pancreatic cancer growth and enhances radiation response. *PLoS One* **7**, e39588, doi:10.1371/journal.pone.0039588 (2012).

94 Lemmens, B. B. & Tijsterman, M. DNA double-strand break repair in Caenorhabditis elegans. *Chromosoma* **120**, 1-21, doi:10.1007/s00412-010-0296-3 (2011).

95 Boulton, S. J. *et al.* Combined functional genomic maps of the C. elegans DNA damage response. *Science* **295**, 127-131, doi:10.1126/science.1065986 (2002).

96 Frank, A. O. *et al.* Discovery of a potent inhibitor of replication protein a protein-protein interactions using a fragment-linking approach. *J Med Chem* **56**, 9242-9250, doi:10.1021/jm401333u (2013).

97 Budke, B. *et al.* RI-1: a chemical inhibitor of RAD51 that disrupts homologous recombination in human cells. *Nucleic Acids Res* **40**, 7347-7357, doi:10.1093/nar/gks353 (2012).

98 Jhaveri, K., Taldone, T., Modi, S. & Chiosis, G. Advances in the clinical development of heat shock protein 90 (Hsp90) inhibitors in cancers. *Biochim Biophys Acta* **1823**, 742-755, doi:10.1016/j.bbamcr.2011.10.008 (2012).

99 Messaoudi, S., Peyrat, J. F., Brion, J. D. & Alami, M. Recent advances in Hsp90 inhibitors as antitumor agents. *Anticancer Agents Med Chem* **8**, 761-782 (2008).

100 Kim, Y. S. *et al.* Update on Hsp90 inhibitors in clinical trial. *Curr Top Med Chem* **9**, 1479-1492 (2009).

101 Levitan, D. & Greenwald, I. Facilitation of lin-12-mediated signalling by sel-12, a Caenorhabditis elegans S182 Alzheimer's disease gene. *Nature* **377**, 351-354, doi:10.1038/377351a0 (1995).

102 Braungart, E., Gerlach, M., Riederer, P., Baumeister, R. & Hoener, M. C. Caenorhabditis elegans MPP+ model of Parkinson's disease for high-throughput drug screenings. *Neurodegener Dis* **1**, 175-183, doi:10.1159/000080983 (2004).

103 Ogg, S. *et al.* The Fork head transcription factor DAF-16 transduces insulin-like metabolic and longevity signals in C. elegans. *Nature* **389**, 994-999, doi:10.1038/40194 (1997).

104 Gieseler, K., Grisoni, K. & Segalat, L. Genetic suppression of phenotypes arising from mutations in dystrophin-related genes in Caenorhabditis elegans. *Curr Biol* **10**, 1092-1097 (2000).

105 Sternberg, P. W. & Han, M. Genetics of RAS signaling in C. elegans. *Trends Genet* **14**, 466-472 (1998).

106 O'Reilly, L. P., Luke, C. J., Perlmutter, D. H., Silverman, G. A. & Pak, S. C. C. elegans in high-throughput drug discovery. *Adv Drug Deliv Rev* **69-70**, 247-253, doi:10.1016/j.addr.2013.12.001 (2014).

107 Harris, T. W. *et al.* WormBase: a multi-species resource for nematode biology and genomics. *Nucleic Acids Res* **32**, D411-417, doi:10.1093/nar/gkh066 (2004).

108 Zheng, S. Q., Ding, A. J., Li, G. P., Wu, G. S. & Luo, H. R. Drug absorption efficiency in Caenorhbditis elegans delivered by different methods. *PLoS One* **8**, e56877, doi:10.1371/journal.pone.0056877 (2013).

109 Melov, S. *et al.* Extension of life-span with superoxide dismutase/catalase mimetics. *Science* **289**, 1567-1569 (2000).

110 Keaney, M. & Gems, D. No increase in lifespan in Caenorhabditis elegans upon treatment with the superoxide dismutase mimetic EUK-8. *Free Radic Biol Med* **34**, 277-282 (2003).

111 Burns, A. R. *et al.* A predictive model for drug bioaccumulation and bioactivity in Caenorhabditis elegans. *Nat Chem Biol* **6**, 549-557, doi:10.1038/nchembio.380 (2010).

112 Kamath, R. S. & Ahringer, J. Genome-wide RNAi screening in Caenorhabditis elegans. *Methods* **30**, 313-321 (2003).

113 Chen, L. *et al.* OCT1 is a high-capacity thiamine transporter that regulates hepatic steatosis and is a target of metformin. *Proc Natl Acad Sci U S A* **111**, 9983-9988, doi:10.1073/pnas.1314939111 (2014).

114 Naldini, L. Gene therapy returns to centre stage. *Nature* **526**, 351-360, doi:10.1038/nature15818 (2015).

115 Diallinas, G. Transceptors as a functional link of transporters and receptors. *Microb Cell* **4**, 69-73, doi:10.15698/mic2017.03.560 (2017).

116 Schothorst, J. *et al.* Yeast nutrient transceptors provide novel insight in the functionality of membrane transporters. *Curr Genet* **59**, 197-206, doi:10.1007/s00294-013-0413-y (2013).

117 Wilde, S. *et al.* Calmodulin-associated post-translational regulation of rat organic cation transporter 2 in the kidney is gender dependent. *Cell Mol Life Sci* **66**, 1729-1740, doi:10.1007/s00018-009-9145-z (2009).

118 Wu, X. *et al.* Fucoidan elevates surface organic cation transporter 2 expression via upregulation of protein kinase A in uric acid nephropathy. *Exp Ther Med* **14**, 4153-4159, doi:10.3892/etm.2017.5077 (2017).

119 Carocho, M. & Ferreira, I. C. A review on antioxidants, prooxidants and related controversy: natural and synthetic compounds, screening and analysis methodologies and future perspectives. *Food Chem Toxicol* **51**, 15-25, doi:10.1016/j.fct.2012.09.021 (2013).

120 Shu, Y. *et al.* Evolutionary conservation predicts function of variants of the human organic cation transporter, OCT1. *Proc Natl Acad Sci U S A* **100**, 5902-5907, doi:10.1073/pnas.0730858100 (2003).

121 Carretero, M., Solis, G. M. & Petrascheck, M. C. elegans as Model for Drug Discovery. *Curr Top Med Chem* **17**, 2067-2076, doi:10.2174/1568026617666170131114401 (2017).

122 Madugundu, G. S., Cadet, J. & Wagner, J. R. Hydroxyl-radical-induced oxidation of 5-methylcytosine in isolated and cellular DNA. *Nucleic Acids Res* **42**, 7450-7460, doi:10.1093/nar/gku334 (2014).

123 Olinski, R., Starczak, M. & Gackowski, D. Enigmatic 5-hydroxymethyluracil: Oxidatively modified base, epigenetic mark or both? *Mutat Res Rev Mutat Res* **767**, 59-66, doi:10.1016/j.mrrev.2016.02.001 (2016).

124 David, S. S., O'Shea, V. L. & Kundu, S. Base-excision repair of oxidative DNA damage. *Nature* **447**, 941-950, doi:10.1038/nature05978 (2007).

125 Swain, U. R., K.S. in *Brain Aging and Therapeutic Interventions* (ed M. K.; Rattan Thakur, S. I. S.) Ch. 2, (Springer Science, 2012).

126 Nakamura, N. *et al.* Cloning and characterization of uracil-DNA glycosylase and the biological consequences of the loss of its function in the nematode Caenorhabditis elegans. *Mutagenesis* **23**, 407-413, doi:10.1093/mutage/gen030 (2008).

127 Mi, L. J., Chaung, W., Horowitz, R., Teebor, G. W. & Boorstein, R. J. Excessive base excision repair of 5-hydroxymethyluracil from DNA induces apoptosis in Chinese hamster V79 cells containing mutant p53. *Carcinogenesis* **22**, 179-186 (2001).

128 Zauri, M. *et al.* CDA directs metabolism of epigenetic nucleosides revealing a therapeutic window in cancer. *Nature* **524**, 114-118, doi:10.1038/nature14948 (2015).

129 Kemmerich, K., Dingler, F. A., Rada, C. & Neuberger, M. S. Germline ablation of SMUG1 DNA glycosylase causes loss of 5-hydroxymethyluracil- and UNG-backup uracil-excision activities and increases cancer predisposition of Ung-/-Msh2-/- mice. *Nucleic Acids Res* **40**, 6016-6025, doi:10.1093/nar/gks259 (2012).

130 Boorstein, R. J. *et al.* Definitive identification of mammalian 5-hydroxymethyluracil DNA N-glycosylase activity as SMUG1. *J Biol Chem* **276**, 41991-41997, doi:10.1074/jbc.M106953200 (2001).

131 Shatilla, A., Leduc, A., Yang, X. & Ramotar, D. Identification of two apurinic/apyrimidinic endonucleases from Caenorhabditis elegans by cross-species complementation. *DNA repair* **4**, 655-670, doi:10.1016/j.dnarep.2005.02.005 (2005).

132 SenGupta, T. *et al.* Base excision repair AP endonucleases and mismatch repair act together to induce checkpoint-mediated autophagy. *Nature communications* **4**, 2674, doi:10.1038/ncomms3674 (2013).

133 Shatilla, A., Leduc, A., Yang, X. & Ramotar, D. Identification of two apurinic/apyrimidinic endonucleases from Caenorhabditis elegans by cross-species complementation. *DNA Repair (Amst)* **4**, 655-670 (2005).

134 Krokan, H. E., Drablos, F. & Slupphaug, G. Uracil in DNA--occurrence, consequences and repair. *Oncogene* **21**, 8935-8948, doi:10.1038/sj.onc.1205996 (2002).

135 Gaiddon, C., Moorthy, N. C. & Prives, C. Ref-1 regulates the transactivation and pro-apoptotic functions of p53 in vivo. *EMBO J* **18**, 5609-5621, doi:10.1093/emboj/18.20.5609 (1999).

136 Shatilla, A. & Ramotar, D. Embryonic extracts derived from the nematode Caenorhabditis elegans remove uracil from DNA by the sequential action of uracil-DNA glycosylase and AP (apurinic/apyrimidinic) endonuclease. *Biochem J* **365**, 547-553. (2002).

137 Kato, Y., Moriwaki, T., Funakoshi, M. & Zhang-Akiyama, Q. M. Caenorhabditis elegans EXO-3 contributes to longevity and reproduction: differential roles in somatic cells and germ cells. *Mutat Res* **772**, 46-54, doi:10.1016/j.mrfmmm.2015.01.001 (2015).

138 Zhang, Q. M. *et al.* DNA glycosylase activities for thymine residues oxidized in the methyl group are functions of the hNEIL1 and hNTH1 enzymes in human cells. *DNA Repair (Amst)* **4**, 71-79, doi:10.1016/j.dnarep.2004.08.002 (2005).

139 Vidal, A. E., Boiteux, S., Hickson, I. D. & Radicella, J. P. XRCC1 coordinates the initial and late stages of DNA abasic site repair through protein-protein interactions. *Embo J* **20**, 6530-6539. (2001).

140 Fitzgerald, M. E. & Drohat, A. C. Coordinating the initial steps of base excision repair. Apurinic/apyrimidinic endonuclease 1 actively stimulates thymine DNA glycosylase by disrupting the product complex. *J Biol Chem* **283**, 32680-32690, doi:10.1074/jbc.M805504200 (2008).

141 Shatilla, A., Ishchenko, A. A., Saparbaev, M. & Ramotar, D. Characterization of Caenorhabditis elegans Exonuclease-3 and Evidence That a Mg(2+)-Dependent Variant Exhibits a Distinct Mode of Action on Damaged DNA. *Biochemistry* **44**, 12835-12848 (2005).

142 Yang, X. *et al.* Functional characterization of the Caenorhabditis elegans DNA repair enzyme APN-1. *DNA Repair (Amst)* **11**, 811-822, doi:S1568-7864(12)00141-3 [pii] 10.1016/j.dnarep.2012.06.009 (2012).

143 Yang, Z., Price, N. E., Johnson, K. M., Wang, Y. & Gates, K. S. Interstrand cross-links arising from strand breaks at true abasic sites in duplex DNA. *Nucleic Acids Res* **45**, 6275-6283, doi:10.1093/nar/gkx394 (2017).

Annexe I: Compounds examined in this research

5-hydroxymethyluracil:

PCID 78168

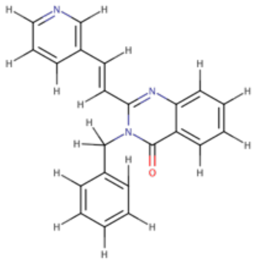

B02: PCID 5738263

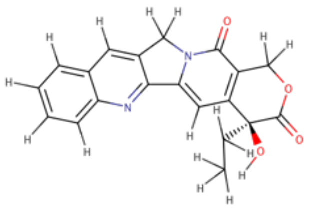

Camptothecin: PCID 24360

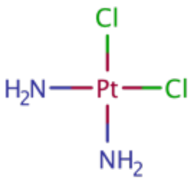

Cisplatin: PCID 441203

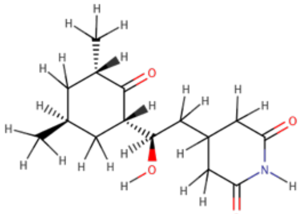

Cycloheximide: PCID 6197

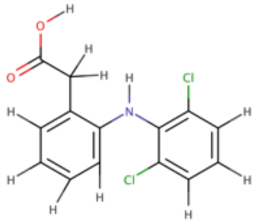

Diclofenac: PCID 3033

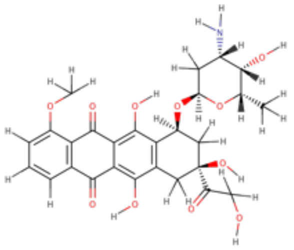

Doxorubicin: PCID 31703

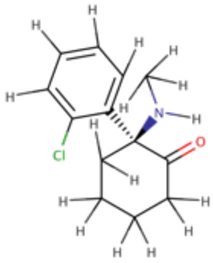

Ketamine: PCID 3821

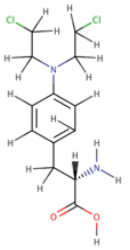

Melphalan: PCID 460612

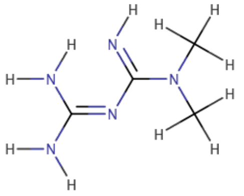

Metformin: PCID 4091

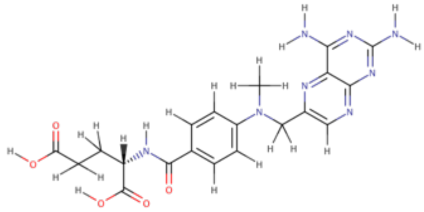

Methotrexate: PCID 126941

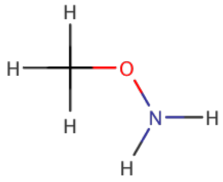

Methoxyamine: PCID 4131

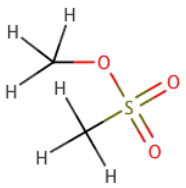

Methyl metanesulfonate:

PCID 4156

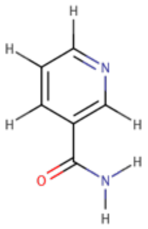

Nicotinamide: PCID 936

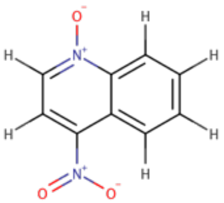

4-Nitroquinoline N-oxide: PCID 5955

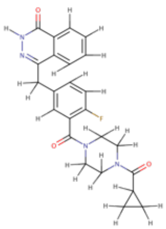

Olaparib: PCID 23725625

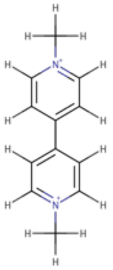

Paraquat: PCID 15939

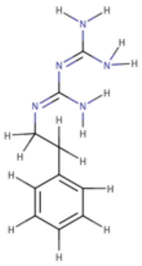

Phenformin: PCID 8249

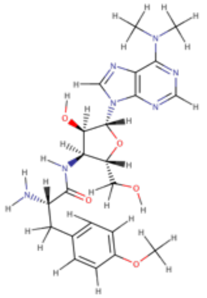

Puromycin: PCID 439530

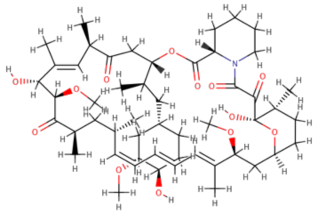

Rapamycin: PCID 5284616

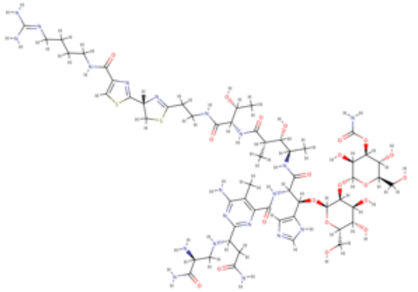

Zeocin: PCID 71668282

Annexe II: Articles in published formats

www.nature.com/scientificreports

SCIENTIFIC REPORTS

Received: 30 August 2016
Accepted: 10 October 2016
Published: 27 October 2016

A novel approach using *C. elegans* DNA damage-induced apoptosis to characterize the dynamics of uptake transporters for therapeutic drug discoveries

Arturo Papaluca & Dindial Ramotar

Organic cation transporter (OCT) function is critical for cellular homeostasis. *C. elegans* lacking OCT-1 displays a shortened lifespan and increased susceptibility to oxidative stress. We show that these phenotypes can be rescued by downregulating the OCT-1 paralogue, OCT-2. Herein, we delineate a biochemical pathway in *C. elegans* where uptake of genotoxic chemotherapeutics such as doxorubicin and cisplatin, and subsequent DNA damage-induced apoptosis of germ cells, are dependent exclusively upon OCT-2. We characterized OCT-2 as the main uptake transporter for doxorubicin, as well as a number of other therapeutic agents and chemical compounds, some identified through ligand-protein docking analyses. We provide insights into the conserved features of the structure and function and gene regulation of *oct-1* and *oct-2* in distinct tissues of *C. elegans*. Importantly, our innovative approach of exploiting *C. elegans* uptake transporters in combination with defective DNA repair pathways will have broad applications in medicinal chemistry.

The nematode *Caenorhabditis elegans* has a plethora of advantages as a useful *in vivo* model system[1]. Indeed, this organism exhibits a broad array of phenotypes that can be easily monitored for changes in various genetic/physiological pathways. For example, it can be utilized to understand the roles of Organic Cation Transporters (OCTs) in the uptake of therapeutic substrates[2]. In fact, evidence from mammalian systems dictates that OCTs mediate the uptake of chemotherapeutic drugs such as oxaliplatin and daunorubicin[3,4]. Hence, elucidating the molecular underpinnings of OCTs and consequent development of tools to modulate their transport activity *in vivo* are expected to improve chemotherapeutic outcome.

In *C. elegans*, little is known about the roles of OCTs and their affinity towards distinct substrates. OCT-1 was the first uptake transporter characterized from *C. elegans* and when expressed in mammalian cells was shown to mediate the transport of the organic cation tetraethylammonium, a prototypical substrate used for classifying OCTs[5]. *C. elegans* deleted for *oct-1* exhibits a shortened lifespan and increased susceptibility to oxidative stress, which led to the proposition that OCT-1 facilitates the import of antioxidants required to protect *oct-1* mutant animals from oxidative stress[2]. However, uptake of ergothioneine, the purported antioxidant substrate of OCT-1, was not reduced in *oct-1* mutant animals as compared to the parent[2]. Therefore, it seems plausible that an alternative explanation could account for the *oct-1* mutant animal phenotypes.

Recently, we documented that the expression of *C. elegans* OCT-1 can restore uptake of the chemotherapeutic drug doxorubicin into *Saccharomyces cerevisiae* cells lacking the regulator Agp2, an amino acid transporter that when deleted blocked the expression of several target genes including the polyamine transporters Dur3 and Sam3[6]. No further studies were done to determine whether OCT-1 substituted for the regulatory function of Agp2 or directly for the roles of Dur3 and Sam3, as both of these transporters also mediate the transport of doxorubicin[6]. Furthermore, it remained unknown whether OCT-1 might mediate the transport of doxorubicin into *C. elegans*. Besides OCT-1, *C. elegans* possesses another related member of the SLC22 organic cation

Maisonneuve-Rosemont Hospital, Research Center, Université de Montréal, Department of Medicine, 5415 Boul. de l'Assomption, Montréal, Québec H1T 2M4, Canada. Correspondence and requests for materials should be addressed to D.R. (email: dindial.ramotar@umontreal.ca)

transporter family, i.e., OCT-2. OCT-2 shares 22.56% identity with OCT-1, but differs in having an extended N-terminal of 172 amino acid residues that is unrelated to OCT-1. To date, no studies have assigned a structural and functional role to the putative *C. elegans* OCT-2 transporter.

During the last decade, *C. elegans* has become instrumental in several drug discovery programs[1,7]. However, in many high-throughput screens performed so far to identify novel small molecules, e.g., those that act as antimicrobials, extend lifespan, inhibit oxidative stress or prevent multidrug resistance, the yield of bioactive compounds is typically in the range of 0.03% to less than 1%[1,8]. It is possible that the recovery rate could be higher if there is greater influx of the molecules. High-throughput screens at higher initial concentrations of the small molecules may alleviate this issue, but could be cost prohibitive. As such, we propose that characterization of the function and substrate specificities of uptake transporters in *C. elegans* will be advantageous towards improving the strategies employed to identify novel bioactive molecules.

In this study, we report a number of novel findings regarding the OCT-1 and OCT-2 transporters of *C. elegans*. We show for the first time that (i) unlike the downregulation of *oct-1*, depletion of *oct-2* did not affect the lifespan of the animals and, instead, rescues the shortened lifespan of *oct-1* deletion animals, (ii) *oct-1* downregulation leads to *oct*-2 upregulation, which in turn mediates uptake of toxic environmental compounds and chemotherapeutic drugs, (iii) upregulation of OCT-2 increases uptake of prooxidants, as judged by the activation of the oxidative stress response reporter GST-4::GFP, leading to germ cell death, as well as to damages to other tissues that could account for the shortened lifespan of *oct-1* deletion animals, (iv) oct-2 upregulation mediates the accumulation of clinically relevant genotoxic anticancer drugs that sensitizes DNA repair deficient animals to germ cell death and diminishes their survival, and (v) ligand-protein docking analysis can be exploited to define substrates such as DNA damaging agents that tightly bind to OCT-2 and which can be validated by suitable readouts. Our findings represent a robust OCT-based strategy to screen a plethora of new therapeutic drugs useful for treating human illnesses, and provide crucial information for rapid recognition of their pharmaceutical benefits and adverse effects.

Results

oct-2 deficiency rescues the shortened lifespan of oct-1 deletion mutants. It has been postulated that *C. elegans* mutants deleted for *oct-1* are defective in uptake of antioxidants and, as a consequence, exhibit shortened lifespan and increased susceptibility to oxidative stress[2]. However, the fact that *oct-1* mutants show no defect in the uptake of the key antioxidant ergothioneine is inconsistent with this hypothesis. As such, we postulate that *oct-1* gene deletion could instead lead to increased uptake of prooxidants from the environment if the loss of OCT-1 activates expression of a related transporter. This notion is based on the fact that *OCT1* knockout mice manifest upregulation of two related transporter genes, *OCT2* and *OCT3*[9]. We therefore performed a homology search using *C. elegans* OCT-1 as a query for protein sequences in the *C. elegans* Wormbase. This analysis revealed a second *C. elegans* member of the organic cation transporter family SLC22, i.e., OCT-2, which shares 22.56% identity with OCT-1 (Figure S1). The predicted protein sequence of OCT-2 indicated that it possesses an extended N-terminal of 172 amino acid residues (Figure S1), suggesting that it is structurally distinct from OCT-1. To date, there is no previous report assigning a functional role to this putative transporter OCT-2 in *C. elegans*. We set out to characterize the molecular function of OCT-2 by first evaluating whether its RNA-interference (RNAi)-driven depletion might influence lifespan of *C. elegans*. In this experiment, L1-staged wild type animals were systematically fed bacteria harbouring the HT115 RNAi vector targeting *oct-2* to measure adult lifespan, using *oct-1* downregulation or the *oct-1* gene deletion mutant *oct-1*(*ok1051*) for comparison (Fig. 1A)[10]. As expected, *oct-1*(*RNAi*) or *oct-1* deletion mutants exhibited a shortened lifespan compared to wild type (Fig. 1B)[2]. In contrast, *oct-2*(*RNAi*) animals displayed a nearly normal lifespan (Fig. 1B). Quantitative real-time PCR (qRT-PCR) was used to ensure that *oct-1* and *oct-2* expression were indeed downregulated by the RNAi-driven approach (Figure S2A), and that this did not interfere with the expression of another transporter gene, namely *pes-23* (Figure S2B), indicating that RNAi did not have off-target effects. Surprisingly, when *oct-2* was downregulated in the *oct-1* deletion mutant *oct-1*(*ok1051*), the resulting *oct-1*(*ok1051*)*; oct-2*(*RNAi*) animals exhibited prolonged lifespan as compared to the *oct-1*(*ok1051*) mutants alone and approaching that of wild type worms (Fig. 1B). Thus, it would appear that the *oct-1* mutant phenotype is dependent on OCT-2 function. A simple interpretation is that depletion of OCT-1 may cause the upregulation of *oct-2* expression, such that OCT-2 mediates the uptake of toxic compounds that affect survival.

A gene expression analysis dataset available from the Wormbase for both *oct-1* and *oct-2*[11], revealed that *oct-2* expression is normally higher than *oct-1* across *C. elegans* developmental stages (i.e. from the first larval stage (L1) to the fourth larval stage (L4)), as well as in the hermaphrodite gonads (Figure S3). We examined whether downregulation of *oct-1* would alter *oct-2* expression levels by comparing the *oct-1* and *oct-2* gene expression in the wild type to that of the *oct-1*(*ok1051*) mutant. We found in the latter that *oct-2* gene expression was significantly augmented, while the *act-1* mRNA levels, used as a control, were unchanged (Fig. 1C). This finding further supports the notion that the effects of *oct-1* depletion on the lifespan of the worms are attributable to *oct-2* upregulation.

The SKN-1 target GST-4::GFP is upregulated by oct-1(RNAi), and blocked by oct-2(RNAi). We examined whether the elevated levels of oxidative damage reported for the *oct-1* deletion mutant is dependent on OCT-2 function[2]. To test this, we used a reporter strain *dvls19* (GST-4::GFP) in which the promoter of the *gst-4* gene (encoding glutathione *S*-transferase 4) is fused to GFP. GST-4 is a target for the conserved SKN-1/Nrf2 transcriptional activator that plays a role in the defense against oxidative stress[12,13]. The *dvls19* strain showed a basal level of GST-4::GFP expression in the intestine of a representative animal (Fig. 1D), which was upregulated following RNAi downregulation of *oct-1* (Fig. 1D). In contrast, this *dvls19* strain showed lower than basal levels of GST-4::GFP expression when *oct-2* was downregulated by RNAi (Fig. 1D) and quantified by plate assay (Fig. 1E).

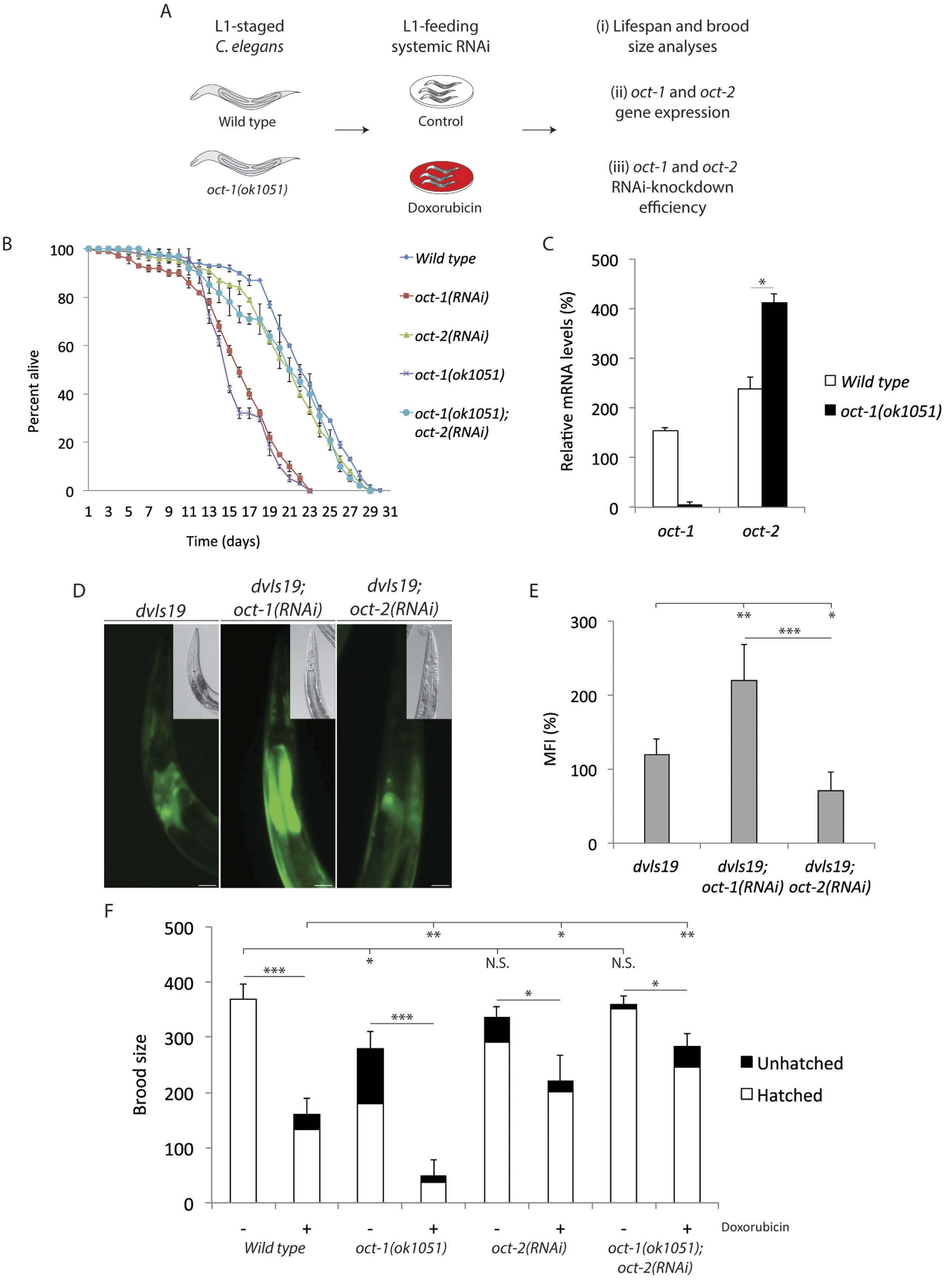

Figure 1. Upregulation of *oct-2* gene expression shortens the lifespan and increases the sensitivity of *C. elegans* towards doxorubicin. (**A**) Scheme of the experimental design and the readouts analyses under different conditions. (**B**) Lifespan analysis of the indicated genotypes. L1-staged animals ($n = 100$) were fed the control and the indicated RNAi under normal growth conditions and lifespan was blindly assessed starting from young adult animals. The mean lifespan of two independent experiments is depicted. (**C**) The relative gene expression of the *oct-1* and *oct-2* transcripts in the wild type and the *oct-1*(*ok1051*) deletion mutant animals was measured and corrected on actin as an internal control. Synchronized young adult animals were collected and mRNA levels were assessed by qRT-PCR. Data shown represent the average ± s.d. and student T-test *$P < 0.05$ from a 60 × 15 mm petri dish of animals ($n \sim 1000$) pooled from two independent experiments. (**D**) Representative images of the oxidative stress-inducible GST-4::GFP reporter and DIC (higher right) of the indicated genotypes. All images were maximum projections of the whole *dvsI19* strain, but cropped from the pharynx to the primary section of the intestine for representation. (**E**) Increased GFP intensity depicting uptake of prooxidants. The GST-4::GFP activation was measured with Fluoroskan Ascent Microplate reader set at λ^{ex}544 nm–λ^{em}590 nm. The mean fluorescence intensity (MFI) is represented as percentage corrected on wild type. (**F**) Brood size analysis of the indicated animals under standard conditions (no treatment) and upon exposure to 100 μM doxorubicin. The data are mean ± S.D. No treatment: Wild type = 369.5 ± 27 ($n = 17$), *oct-1*(*ok1051*) = 280 ± 29 ($n = 23$), *oct-2* (*RNAi*) = 335.5 ± 20.5 ($n = 20$), *oct-1*(*ok1051*); *oct-2*(*RNAi*) = 360.5 ± 14.8 ($n = 21$). Doxorubicin treatment (100 μM): Wild type = 170 ± 29.1 ($n = 24$), *oct-1*(*ok1051*) = 58 ± 29.2 ($n = 19$), *oct-2*(*RNAi*) = 220.5 ± 47 ($n = 21$), *oct-1*(*ok1051*); *oct-2*(*RNAi*) = 283 ± 23.1 ($n = 27$). Error bars represent the S.D. Unpaired two-tail t-test *$P < 0.03$; **$P < 0.01$; ***$P < 0.0005$ were considered to be statistically significant. N.S. = Non Significant.

These findings are consistent with a model whereby *oct-2* upregulation, *via oct-1* deletion, allows entry of toxic compounds such as prooxidants into *C. elegans* causing oxidative stress and leading to a shortened lifespan.

OCT-2, and not OCT-1, mediates the genotoxic effects of the anticancer drug doxorubicin. To determine whether OCT-1 regulation of OCT-2 would be involved in the differential uptake of toxic compounds, we treated worms with the chemotherapeutic drug doxorubicin at concentrations that did not lead to developmental arrest[14], and monitored the survival of the animals by scoring brood size. Doxorubicin uptake depends upon cationic transporters in *Saccharomyces cerevisiae*[6] and mammalian cells[4], and has been shown to trigger germ cell apoptosis in *C. elegans*[14]. L1stage wild type animals treated with doxorubicin showed ~55% decrease in brood size as compared to the untreated animals (Fig. 1F). In contrast, the *oct-1*(*ok1051*) mutants displayed a significant level of unhatched or dead embryos, and when treated with doxorubicin showed a sharp decrease (nearly 80%) in brood size (Fig. 1F). While these observations were unexpected as the loss of the uptake transporter should cause drug resistance, we reasoned that the enhanced doxorubicin sensitivity of the *oct-1*(*ok1051*) mutant animals can be explained by an increase uptake of the drug due to the upregulation of *oct-2*. We therefore examined the sensitivity of worms depleted for *oct-2* following exposure to doxorubicin. *oct-2*(*RNAi*) caused wild type animals to become less sensitive to doxorubicin with only 27% decrease in brood size, as compared to 55% for the control RNAi (Fig. 1F). Importantly, RNAi-driven depletion of *oct-2* in the *oct-1*(*ok1051*) mutant partially suppressed embryonic arrest and abolished the hypersensitivity of these animals towards doxorubicin showing less than a 20% reduction in brood size compared to 80% in *oct-1*(*ok1051*) mutant RNAi control (Fig. 1F). *oct-2*(*RNAi*) did not completely block doxorubicin toxicity on brood size of the *oct-1*(*ok1051*) mutant, perhaps reflecting residual *oct-2* expression. Also since this mutant was deleted for the *oct-1* gene, a direct role for OCT-1 in doxorubicin uptake is excluded (Fig. 1F). Collectively, these observations strongly support the notion that OCT-2 has a predominant role over OCT-1 in uptake of doxorubicin.

OCT-2 allows the accumulation of doxorubicin in C. elegans tissues. Based on the above findings, we examined whether OCT-2 might allow the accumulation of doxorubicin in *C. elegans* tissues. As target we chose the pharynx, a relatively large muscular organ that allow food consumption (Fig. 2A). We found that OCT-1 was localized at the anterior and posterior sides of the terminal bulb of the pharynx by imaging the *dpy-5*(*e907*)*; sEx12154* strain featuring an *oct-1::GFP* fusion (Fig. 2B), thereby validating this organ for uptake studies. Since no similar *oct-2::GFP* fusion has yet been constructed, we assessed the pharynx for *oct-2* expression by measuring RNA levels in the heads, severed just posterior to the pharynx, of 300 each of wild type and *oct-1*(*ok1051*) animals. The results reveal that *oct-2* is expressed at higher levels than *oct-1* in the pharynx of the wild type animals and that its expression was stimulated nearly 2-fold in *oct-1*(*ok1051*) animals as compared to the wild type (Fig. 2C), suggesting that *oct-2* is inducible in the pharynx.

We took advantage of the physical property of doxorubicin, which emits fluorescence at wavelengths of λ^{ex}470 nm–λ^{em}585 nm, as a convenient means to monitor its uptake through OCT-1 and OCT-2 *in situ* by imaging the pharynx. Of note, *C. elegans* tissues have low levels of autofluorescence particularly at the posterior terminal bulb of the pharynx (Fig. 2D[i]) where most substances accumulate prior to consumption[15]. However, following exposure of wild type animals to doxorubicin, the emitted fluorescence was greater than background autofluorescence confirming consumption of the drug by the animals (Fig. 2D[iv]). Strikingly, the *oct-1*(*ok1051*) mutant did not reduce the fluorescence intensity of doxorubicin in the pharynx, instead depicting a markedly stimulated intensity (Fig. 2D[v]). To test whether the stimulated uptake of doxorubicin in the *oct-1*(*ok1051*) mutant could result from upregulation of *oct-2*, we downregulated *oct-2* expression in this mutant. Under this condition, extremely low levels of doxorubicin accumulated in the *oct-1*(*ok1051*)*; oct-2*(*RNAi*) animals (Fig. 2D[vi]). It is noteworthy that the deletion mutant *eat-2*(*ad453*), i.e., with a slow pumping pharynx[16], also showed OCT-2-dependent uptake of doxorubicin, excluding the possibility that this transporter functions only when there is a surplus of nutrients (Figure S4).

Doxorubicin uptake in the pharynx of the *oct-1*(*ok1051*) strains was independently confirmed using another assay employing the Fluoroskan instrument, which measures the fluorescence intensity of the drug (Fig. 2E). Using this approach, *oct-1*(*ok1051*) animals showed a concentration-dependent uptake over a range (10–100 μM) of doxorubicin into the pharynx, which was blocked by RNAi-driven depletion of *oct-2* (Fig. 2F). We tested whether uptake of another fluorescence compound, fluorescein which is anionic in nature, would be similarly dependent upon OCT-2. While fluorescein showed a concentration dependent uptake, ranging from 1 to 100 μM, into the pharynx of the *oct-1*(*ok1051*) mutant, it was not affected by *oct-2* downregulation in *oct-1*(*ok1051*)*; oct-2*(*RNAi*) animals (Fig. 2F). These findings suggest that OCT-2 may recognize differences in charges and display specificity in the uptake of substrates into *C. elegans* tissues.

OCT-2-mediated uptake of doxorubicin is blocked by choline in the pharynx. Human OCT1 and OCT2 were shown to transport other cationic molecules such as choline[17]. Thus if choline is also a substrate of *C. elegans* OCT-2 we would expect it to compete for doxorubicin uptake into the pharynx. Choline has the physical property of emitting fluorescence, but at lower wavelengths of λ^{ex}290 nm–λ^{em}345 nm and is undetectable at the wavelength index used for monitoring doxorubicin uptake. Treatment of the *oct-1*(*ok1051*) animal with doxorubicin in the presence of equimolar amounts of choline (50 and 100 μM), impeded uptake of doxorubicin into the pharynx (Fig. 2G), clearly indicating that OCT-2 has the ability to recognize and compete for other cationic compounds. Therefore, we predict that the competition for doxorubicin uptake can be readily exploited as an assay to determine whether a putative ligand can serve as a substrate for OCT-2.

The oct-1(ok1051) mutant animals display increased spontaneous and drug-induced germ cell death that is suppressed by oct-2 downregulation. Analogous to many stem cell systems, *C. elegans*

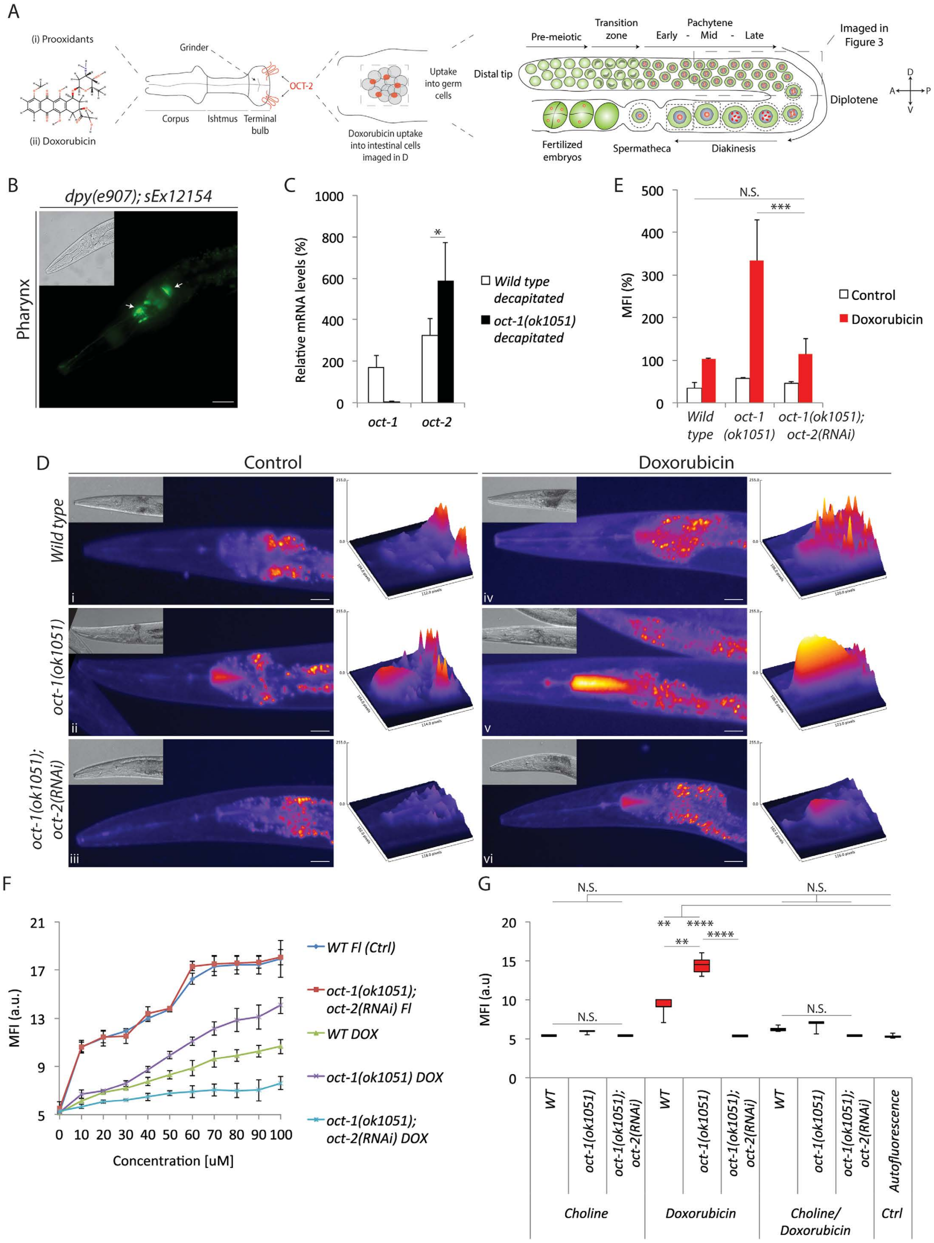

Figure 2. Doxorubicin transport into the pharynx is stimulated by *oct-2* upregulation and efficiently competed by choline. (**A**) Model suggesting OCT-2 localization at the terminal bulb of the pharynx, the fluorescence (red dots) where the drug is detected, i.e., the posterior side of the pharynx and the initial part of the intestine (as imaged in **F**), and the region of germ cells analysed for apoptotic corpses in the gonad (see below). (**B**) DIC (upper left) and fluorescence image of *dpy-5*(*e907*)*; sEx12154* [OCT-1::GFP] genotype depicting OCT-1 localization in the pharynx (arrows in **B**). Enlargement of the pharynx is represented by a scale bar = 7 µm. (**C**) Relative gene expression of *oct-1* and *oct-2* transcripts measured in severed heads ($n = 300$) collected from wild type and *oct-1*(*ok1051*) animals and corrected to actin and *pmp-3*. (**D**) Representative 'fire' look-up images of the pharynx from untreated (control) and doxorubicin treated animals. The respective DIC images are shown in the upper left corner of each panel. Images to the right of each pharynx depict a 3D representation of the doxorubicin (100 µM) treatment signal intensity for the indicated genotypes. Data is representative of experiments performed in duplicates ($n = 20$). Enlargement of the pharynx is represented by a scale bar = 10 µm. Fluorescence posterior to the pharynx is autofluorescence detected from the intestine. (**E**) Quantification of doxorubicin uptake using a Fluoroskan plate reader. The mean fluorescence intensity (MFI) is represented as percentage corrected to wild type. White bars denote untreated animals where similar autofluorescence was detected in all genotypes. (**F**) *oct-2*(*RNAi*)diminishes the concentration-dependent uptake of doxorubicin (DOX) and not fluorescein (Fl) into the pharynx of *oct-1*(*ok1051*) mutant animals. (**G**) Comparison of doxorubicin uptake in the absence and presence of equimolar amounts of choline. Box and whisker plots represent duplicates ($n = 10$) of signal intensity measured from both compounds in the pharynx. Data is represented as ± S.D Student T-test ± S.D Student T-test *$P < 0.05$; **$P < 0.01$; ***$P < 0.001$; ****$P < 0.0001$ and N.S. = Non Significant.

has a self-renewing germ cell population derived from a cellular niche located at the distal tip (see Fig. 2A)[18]. These germ cells progress through distinct stages of differentiation and must faithfully maintain the genome. They are very sensitive to genotoxic compounds and respond by using conserved DNA repair mechanisms to maintain genomic stability[19]. Germ cells with excessive DNA damage undergo apoptosis and are unable to form viable embryos[18,20]. We chose to monitor germ cell apoptosis as an experimental system to determine whether OCT-2 would be involved in the uptake of genotoxic anticancer drugs. This approach has the advantage of allowing assessment of the uptake of genotoxic anticancer drugs that do not emit fluorescence or are unavailable in radioactively labeled form. To monitor apoptotic germ cells, we first quantified *in vivo* germ cell corpses in the proximal zone of the gonad arm (see Fig. 2A) by utilizing differential interference contrast (DIC) microscopy and staining with the DNA dye acridine orange[21]. In wild type animals, one to four apoptotic cells were detected (Fig. 3A[i]), as previously reported[22]. In contrast, the *oct-1*(*RNAi*) or the *oct-1*(*ok1051*) mutants depicted an average of five to eight apoptotic cells (Fig. 3A[ii,iv]). Analysis of gene expression in the gonads from 100 each of dissected wild type and *oct-1*(*ok1051*) animals revealed that *oct-1* gene deletion greatly stimulated the expression of *oct-2* mRNA (Fig. 3B). Thus, the two-fold increase of apoptotic cells in the gonads of the *oct-1*(*ok1051*) animals may result from import of prooxidants, as assessed by activation of GST-4::GFP, that can damage the genome of the germ cells leading to embryos with hatching defects (Fig. 1F). Unlike the *oct-1*(*RNAi*), the *oct-2*(*RNAi*) animals displayed nearly the same average number of apoptotic cells as the wild type (Fig. 3A[iii vs. i]). Interestingly, RNAi-driven depletion of *oct-2* in the *oct-1*(*ok1051*) mutant sharply reduced germ cell death, which was undetectable in some animals (Fig. 3A[v]).

To confirm that the acridine orange-stained germ cells are undergoing apoptosis, as well as to avoid uptake differences of this dye, we evaluated a downstream step of the apoptotic pathway, i.e., engulfment of apoptotic cells by the CED-1 protein to signal phagocytic degradation[23,24]. We employed an imaging strategy that utilizes the *bcls39* strain which carries CED-1::GFP as a reporter of engulfed apoptotic cells[25]. The *bcls39* strain with control RNAi showed engulfment of 1 to 3 physiological apoptotic cells (Fig. 3C[i]), whereas downregulation of *oct-1* engendered increased engulfment recapitulating the enhanced germ cell apoptosis observed in the *oct-1*(*ok1051*) mutant (Fig. 3A[iv] vs. C[ii]). As expected, downregulation of *oct-2* in the *bcls39; oct-2*(*RNAi*) background displayed control levels of engulfment (Fig. 3C[iii]). Taken together, we propose that OCT-2 possesses the ability to transport toxic compounds such as prooxidants that cause germ cell death. These prooxidants are likely to cause damages to various tissues and may therefore account for reduced lifespan observed in the *oct-1*(*RNAi*) or *oct-1*(*ok1051*) animals (Fig. 1B).

We examined whether the OCT-2 dependent accumulation of doxorubicin would lead to the stimulation of germ cell death. Treatment of wild type worms with doxorubicin elevated the levels of apoptotic cell corpses as visualized by both acridine orange staining (Fig. 3A[vi]) and engulfment of the cells (Fig. 3C[iv]) (and quantified as in Fig. 3D,E, respectively). *oct-1*(*RNAi*) or the *oct-1* deletion mutants treated with doxorubicin showed substantially higher levels of acridine orange-stained apoptotic cells (Fig. 3A [vii,ix] and quantified as in Fig. 3D), which paralleled increased CED-1::GFP engulfment of the cells as compared to the wild type (Fig. 3C[v vs. iv] and quantified as in Fig. 3E). In contrast, far fewer engulfed apoptotic corpses appeared in doxorubicin exposed animals downregulated for *oct-2* (Fig. 3C[vi],E). As expected based on acridine orange staining and engulfment of apoptotic cells, mutants deleted for *cep-1*, *egl-1*, *ced-9*, *ced-4* or *ced-3*, which manifest defects in the apoptotic pathway did not show enhanced apoptotic corpses (Figure S5[ii–vi], respectively), i.e., unlike wild type animals upregulated for OCT-2 and treated with doxorubicin (Figure S5[i]). Several conclusions can be derived from these observations: (i) OCT-2 has a predominant role over OCT-1 in the uptake of doxorubicin, (ii) doxorubicin uptake leads to induced germ cell death that correlates with decrease survival, and (iii) both the drug uptake and the induced-germ cell death are OCT-2 dependent.

Cisplatin-induced germ cell death requires OCT-2 function.

We assessed whether germ cell death in our experimental model can be used to monitor the uptake of genotoxic drugs that are not readily available as either fluorescently- or radioactively-labeled form. Since human OCT1 has been shown to transport members of the platinum family of anticancer drugs that act by creating intra- and inter-strand DNA cross-links[26], we tested the role of *C. elegans* OCT-1 and OCT-2 in the uptake of cisplatin using germ cell death as a reporter. We monitored germ cell apoptosis in the absence and presence of cisplatin in the following four genotypes: wild type, *oct-1*(*ok1051*), *oct-2*(*RNAi*) and *oct-1*(*ok1051*)*; oct-2*(*RNAi*). Cisplatin induced an increased level of germ cell death in the wild type, which was further greatly stimulated in the *oct-1*(*ok1051*) mutants (Fig. 3F). Downregulation of *oct-2* in the *oct-1*(*ok1051*) mutants prevented cisplatin-induced germ cell death (Fig. 3F). These observations strongly indicate that germ cell death induced by cisplatin primarily depends upon its uptake via OCT-2. We noted that the DNA damaging agent methyl methanesulfonate (MMS), which alkylates DNA bases resulting in both DNA-single and -double strand breaks, induced germ cell death, but independently of OCT-1 and OCT-2 function (Figure S6A). Likewise, γ-rays that create multiple DNA lesions also induced germ cell death (Figure S6B) independently of these transporters (Figure S6C). Thus, the transporter function of OCT-2 is not directly involved in the process of germ cell death induced by the DNA damaging agents.

OCT-2-dependent transport of doxorubicin or cisplatin stimulates germ cell death in C. elegans mutants defective in DNA repair.

We next systematically examined whether mutants defective in major DNA repair pathways would show OCT-2 dependent sensitization of DNA damage-induced germ cell death. As shown in Figure S7B, the *rad-51* deletion mutant, *rad-51*(*ok2218*), lacking the RAD-51 protein needed for DNA strand invasion during homologous recombination (HR)-dependent double strand break repair, exhibited higher endogenous levels of apoptotic cell death due to spontaneous unrepaired meiotic breaks[27] as compared to wild type (Figure S7A). Treatment of the *rad-51*(*ok2218*) mutant with doxorubicin greatly stimulated apoptosis, which was further induced upon downregulation of *oct-1* in the *rad-51*(*ok2218*)*; oct-1*(*RNAi*) genotype (Figure S7C).

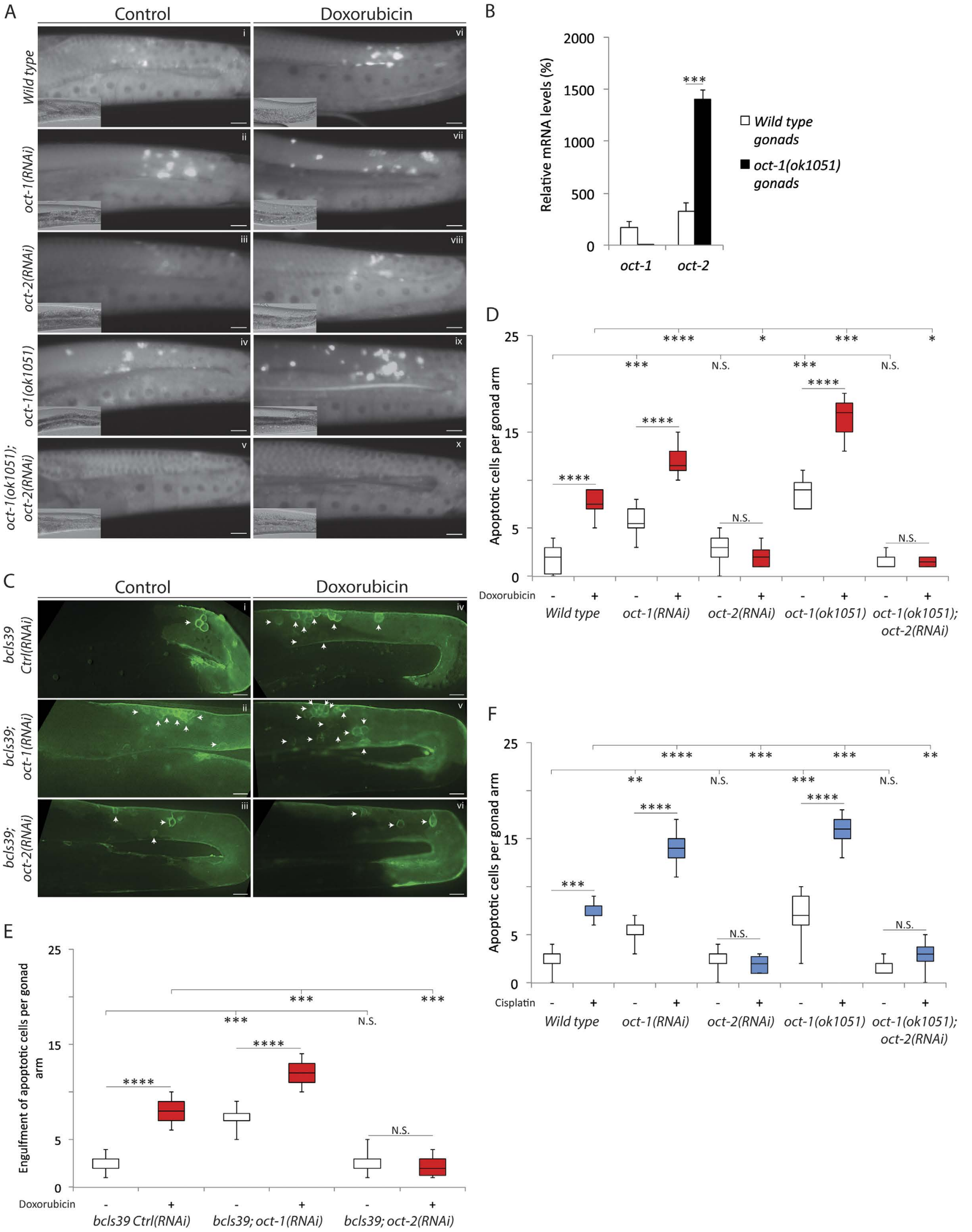

Figure 3. OCT-2-mediated transport of genotoxic compounds induce apoptotic cell death of meiotic germ cells in *C. elegans*. (**A**) Representative images of acridine orange-stained and DIC (lower left) of control and doxorubicin-induced apoptotic cell corpses from the indicated genotypes. Apoptotic cell corpses were identified as bright spots correlating with raised-bottom-like refractive corpses shown on DIC images. Posterior is right and dorsal is top. Scale bar = 15 µm. (**B**) Relative gene expression of *oct-1* and *oct-2* transcripts measured in dissected gonads ($n = 100$) collected from wild type and *oct-2*(*ok1051*) animals and corrected to actin and *pmp-3* (see experimental procedures). (**C**) Representative images of control and doxorubicin-induced *bcls39* [CED-1::GFP] clusters around apoptotic cell corpses indicated by white arrows. Data showing that OCT-2 mediated transport of compounds signal the apoptotic pathway in germ cells. Scale bar = 10 µm. (**D**) Box and whisker plots depicting quantification of apoptotic cell corpses from untreated and doxorubicin treated worms and showing maximum, minimum, upper & lower quartiles, and sample median. Statistical significance bars represent results of Mann-Whitney U-test of mean difference (*$P < 0.05$; **$P < 0.01$; ***$P < 0.001$ and ****$P < 0.0001$) computed from three independent experiments ($n = 30$). L1-stage animals were treated with doxorubicin (100 µM), and apoptotic cell corpses were analysed in young adult staged animals. Control is depicted as white and doxorubicin as red boxes. (**E**) Quantification of *bcls39* engulfment of apoptotic cell corpses in the indicated genotypes without and with doxorubicin treatment. The results are presented as shown in (**D**). (**F**) Box and whisker plots depicting quantification of apoptotic cell corpses from untreated and cisplatin treated worms and quantified as in (**D**).

Consistent with this data, *oct-2* gene expression was indeed upregulated in the *rad-51*(*ok2218*)*; oct-1*(*RNAi*) genetic background (Figure S7J). In contrast, depletion of *oct-2* by RNAi in *rad-51*(*ok2218*) animals suppressed the high level of apoptotic cells observed in this mutant upon exposure to doxorubicin (Figure S7C). These data indicate that upregulation of *oct-2* burdens the *rad-51*(*ok2218*) animals with doxorubicin-induced DNA lesions leading to enhanced germ cell death.

We also found that *apn-1*(*tm6691*) animals lacking the key enzyme APN-1, required for removing a variety of DNA lesions including oxidized bases via the base-excision DNA repair (BER) pathway[28], showed enhance germ cell death by doxorubicin when *oct-2* expression was stimulated (Figure S7E,K). This induced apoptosis was strongly attenuated following depletion of *oct-2* by RNAi (Figure S7E). These data suggest that BER in *C. elegans* is also involved in processing doxorubicin-induced oxidative DNA lesions[29] but, more importantly, OCT-2 controls the toxicity of the drug in *apn-1*(*tm6691*) mutant animals.

Unlike doxorubicin, cisplatin damages the DNA by creating DNA cross-links most of which are processed by the nucleotide excision repair (NER) and DNA mismatch repair (MMR) pathways[30]. We set out to investigate whether *oct-2* expression levels modulate cisplatin-induced germ cell death in mutants defective in either NER or MMR. Remarkably, cisplatin induced substantial levels of apoptotic cells in the *xpa-1*(*ok698*); *oct-1* (*RNAi*) (Figure S7G) and *msh-2*(*ok2410*)*; oct-1*(*RNAi*) (Figure S7I) mutants, when *oct-2* was upregulated (Figure S7L,M, respectively). These two DNA repair defective mutants were effectively protected from the onslaught of cisplatin-induced DNA lesions upon RNAi-driven depletion of *oct-2* (Figure S7G,I, respectively), consistent with the involvement of OCT-2 in the transport of cisplatin.

It is noteworthy that amongst the DNA repair deficient animals, only in the case of the *apn-1*(*tm6691*)*; oct-1*(*RNAi*) genotype was there a significant increase in spontaneous germ cell death (Figure S7D). One possible explanation for this observation is that OCT-2 mediated uptake of prooxidants may lead to oxidative lesions that must be repaired by BER[28]. Collectively, the above data suggest that by combining defects in DNA repair pathways with functional organic cation transporters such as OCT-2, it is possible to determine whether an unknown compound has genotoxic effects and the type of lesions it may create.

Ligand-protein docking analysis predicts the substrate specificity of OCT-2. To gather insights into the substrates that can be recognized by OCT-2, we first made predictions of its protein structure relative to OCT-1 by inputting the respective primary protein sequences into the I-TASSER protein structure prediction server for *in silico* analyses[31]. The I-TASSER server employed known Protein Data Bank (PDB) structures as threading templates to predict the OCT-1 and OCT-2 structures (Table S1A,B). OCT-1 and OCT-2 were both modeled based on the X-ray diffraction structure of the glucose transporter GLUT3/SLC2A3 from *Homo sapiens* (PDB ID: 5c65) and validated with the glucose transporters GLUT1–4 structures (PDB ID: 4gc0) (Table S2A,B)[32]. The analysis revealed that OCT-1 and OCT-2 have predicted structures similar to each other (Fig. 4A,B). The comparative models of OCT-1 and OCT-2 were computed by utilizing several criteria as described in the materials and methods (Table S3). The final predicted 3D structure of OCT-1 and OCT-2 featured the entire 12 transmembrane domain helices (Figure S8A,B). Overall, the analysis predicted structures for both OCT-1 and OCT-2 that belong to solute carrier transporter family (Fig. 4A,B).

We next determined whether the anticancer drugs, doxorubicin and cisplatin, would dock onto the predicted structures of OCT-1 and OCT-2. We utilized the BSP-SLIM and COACH algorithms[33,34] to predict the amino acid residues of the transporters constituting the ligand–protein docking sites (Fig. 4C and Table S4). Since the BSP-SLIM server did not recognize the cisplatin chemical structure, a related member of the platinum drug family, carboplatin, was used. The OCT-1 and OCT-2 models interacting with doxorubicin computed a C-score of 0.38 and 0.75, respectively (Fig. 4C) (see materials and methods, Table S4). The predicted key residues mediating interaction between the drugs and the transporters suggest that the binding pockets of OCT-1 and OCT-2 are structurally different (Fig. 4C), making the ligand-protein binding highly selective depending upon the chemical structure of the ligand.

The OCT-1 and OCT-2 models were also evaluated for their ability to discriminate between the interacting ligands and probable non-binder compounds. As non-binder compounds, we targeted the nonsteroidal anti-inflammatory drug diclofenac, which is classified as an organic anion. The predicted models showed that no residues of OCT-1 or OCT-2 interact with diclofenac (Fig. 4D and Table S5). Thus, it is possible to perform protein-ligand modeling studies in order to predict and uncover novel substrates for uptake by these transporters, which could be further corroborated by the above *in vivo* assays.

Predicted ligands of OCT-1 and OCT-2 and experimental validation. So far, the roles of transporters in the uptake of a vast majority of genotoxic cationic drugs have not been tested in *C. elegans*. We sought to identify which of the known cationic drugs would be taken up by OCT-1 and/or OCT-2. A number of drugs were selected based on two criteria (i) mechanism of action and (ii) biological response. We assessed the docking ability of each compound with OCT-1 and OCT-2. From 19 tested ligands, four resulted with a docking score of zero, whereas the remaining 15 revealed a docking score > 3.5 favouring avid binding with OCT-2 (Table 1 dataset, docking score columns). Amongst these 15 ligands, some possess distinct pharmacological attributes such as creating different types of DNA lesions (Table S6). We next experimentally validated the *in silico* analyses using our drug-induced apoptosis assay as readout. We found that a number of the compounds that docked onto OCT-2 were capable of triggering high level of apoptotic cell death when *oct-2* was upregulated by *oct-1*(*RNAi*), as compared to the control RNAi (Table 1 dataset; numbers in the bracket are from control RNAi). There were also ligands that act by damaging the DNA such as melphalan and methoxyamine, which did not dock onto OCT-2, but induced apoptotic corpses (Table 1 dataset). We postulate that these non-binders might use alternative transporters to enter the animal.

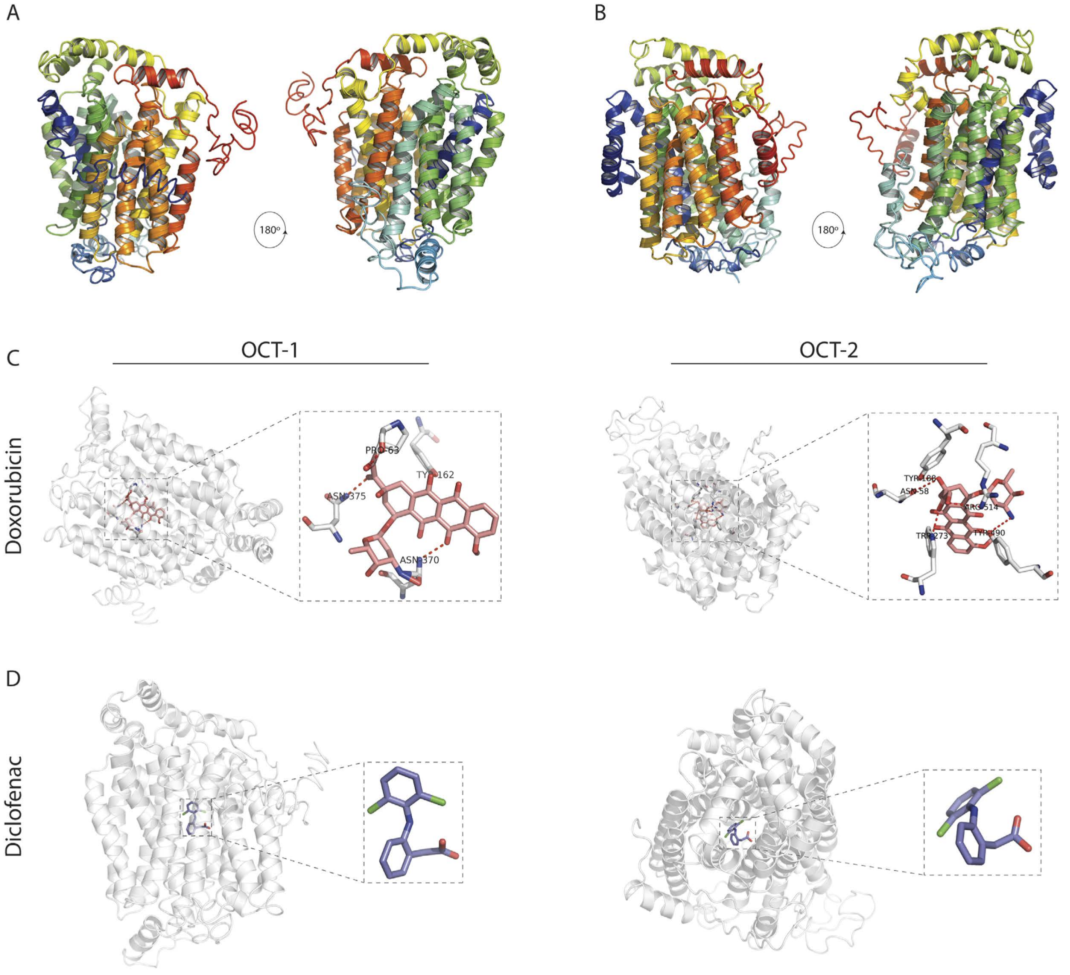

Figure 4. Structural modelling and protein-ligand docking of *C. elegans* OCT-1 and OCT-2. (**A,B**) Structural models of OCT-1 and OCT-2 were generated on the basis of GLUT3 (PDB ID: 5c65) structure and sequence conservation. N-terminal and C-terminal are coloured blue and red, respectively. (**C,D**) Predicted binding models of OCT-1 and OCT-2 with cationic and anionic ligands doxorubicin (pink) and diclofenac (purple), respectively. Residues making polar contacts with the ligands are depicted with sticks and represented with dotted red lines; oxygen atoms are coloured in red, nitrogen atoms in blue and carbon atoms in white. All representative figures were rendered with PyMol.

As a final validation, we focused on the ligand B02, which robustly docked only onto OCT-2 with a docking score of 5.4 (Table 1 dataset, Fig. 5A vs. B). B02 was shown to interfere with human RAD51 in DNA strand exchange and nuclear focus formation in response to DNA damage[35–37]. However, to our knowledge the pharmacological effect of B02 has not been tested in *C. elegans*. To confirm that B02 enters via the OCT-2 transporter, we tested the effect of the compound on wild type, *oct-1*(*ok1051*) and the *oct-1*(*ok1051*); *oct-2*(*RNAi*) backgrounds at concentrations ranging from 1 to 75 μM. Notably, extreme toxicity was observed with 75 μM B02 for all the genotypes. Therefore, we reduced the concentrations to 5 μM and observed that *oct-2* upregulation caused sterility (Fig. 5C) resulting in a decrease in viable animals (Fig. 5E) and phenocopying the *rad-51* homozygotes as previously reported[38]. As predicted from our model, the B02 ligand did not cause reduction in viable animals in the *oct-1*(*ok1051*); *oct-2*(*RNAi*) genetic background (Fig. 5D) and restored the number of broods to nearly untreated levels (Fig. 5E). These compelling data revealed for the first time that the B02 inhibitor of RAD51 is functionally active in *C. elegans* and requires exclusive uptake by OCT-2. We conclude that the docking scores of ligands and quantifiable endpoints provide valuable tools to monitor transporter-mediated drug uptake into *C. elegans*. This approach is particularly suitable for newly developed drugs that cannot be readily labeled or lack fluorescent properties for uptake studies.

Discussion

In this study, we established for the first time the function of OCT-2 in *C. elegans*, as well as the specific roles for OCT-1 and OCT-2 in mediating tissue transport of distinct compounds, such as the chemotherapeutic drugs anthracyclines and cisplatin. We show that OCT-1 has no direct role in the transport of these compounds, however, it exerts control on *oct-2* expression, and it is OCT-2 that is primarily involved in the uptake of these agents.

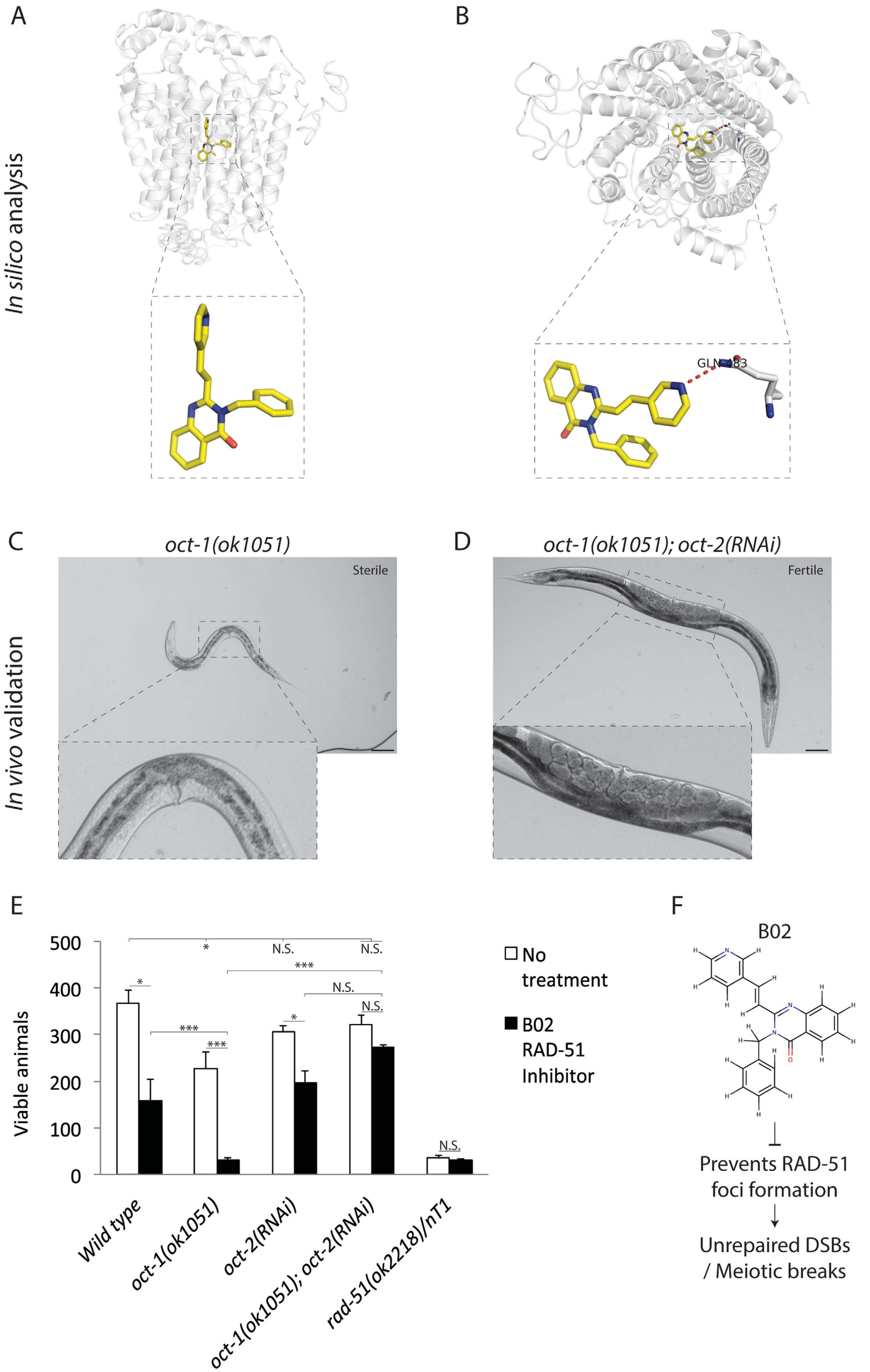

Figure 5. The B02 inhibitor of RAD-51 mimics the *rad-51/rad-51* homozygotes phenotypes when *oct-2* is upregulated. (**A,B**) Depiction of the ligand-protein docking of OCT-1 and OCT-2 modelled with B02 and showing exclusive binding of the drug to OCT-2. (**C**) DIC image showing that B02 causes embryonic lethality (diminishing number of germ cells) in the *oct-1*(*ok1051*) mutant. (**D**) DIC image showing that *oct-2* downregulation in the *oct-1*(*ok1051*) mutant animals restores fertility. In (**C,D**) Scale bar = 35 µm. (**E**) B02 diminishes the number of viable animals when *oct-2* is expressed. Brood size analysis of wild type, *oct-1*(*ok1051*) and *oct-1*(*ok1051*); *oct-2*(*RNAi*) and *rad-51*(*ok2218*)/*nT1* animals under standard conditions (no treatment) and

upon exposure to 5 μM B02. Data are mean ± S.D. No treatment: Wild type = 366 ± 26.7 ($n = 20$), *oct-1* (*ok1051*) = 296 ± 7.1 ($n = 29$), *oct-2*(*RNAi*) = 307 ± 11.3 ($n = 23$), *oct-1*(*ok1051*)*; oct-2*(*RNAi*) = 321 ± 19.7 ($n = 25$), *rad-51*(*ok2218*)*/nT1* = 35 ± 5.6 ($n = 9$). B02 treatment (5 μM): Wild type = 158 ± 29.7 ($n = 21$), *oct-1* (*ok1051*) = 32 ± 7.0 ($n = 17$), *oct-2*(*RNAi*) = 196 ± 26.8 ($n = 25$), *oct-1*(*ok1051*)*; oct-2*(*RNAi*) = 272 ± 7.1 ($n = 25$), *rad-51*(*ok2218*)/*nT1* = 30 ± 4.2 ($n = 10$). Error bars represent the S.D. Unpaired two-tail t-test $^*P < 0.03$; $^{**}P < 0.01$; $^{***}P < 0.0005$ were considered to be statistically significant. N.S. = Non Significant. (**F**) The RAD-51 inhibitor, B02, mode of action in *C. elegans* germline.

This conclusion is derived from three key findings. First, the *oct-1* deletion mutant *oct-1*(*ok1051*) or RNAi-driven knockdown of *oct-1* triggered the upregulation of *oct-2* in the whole body, the head and gonads of the animal, causing hypersensitivity to chemotherapeutic drugs. This phenotype is observed only when OCT-2 is present. Second, RNAi-driven knockdown of *oct-2* blocked uptake of chemotherapeutic drugs thus preventing their genotoxic effects. Since no additional drug resistance was observed in *oct-1*(*ok1051*); *oct-2*(*RNAi*) double mutant animals as compared to ones depleted for *oct-2* alone, a role for OCT-1 in the uptake of these chemotherapeutic drugs can be excluded; nonetheless OCT-1 could act as a transporter for selective ligands. And third, our *in silico* modeling-based screening of OCT-1 and OCT-2 selectively discriminated amongst DNA damaging agents those that are potential ligands for OCT-2. By validating this approach *in vivo*, we show that OCT2-dependent transport of the DNA damaging agents can sensitize mutant animals that are defective in DNA repair pathways. Collectively, these results underscore the importance of uptake transporters in regulating the entry of chemotherapeutic drugs into cells and raise the possibility that the drug-resistance and drug-sensitive responses observed by cancer patients could be governed at the level of drug uptake.

The downregulation of *oct-1* leading to upregulation of *oct-2* was an unexpected finding, and provides a compelling argument that the animal has evolved tight regulation of OCT-2. So how might OCT-1 depletion lead to the activation of OCT-2? One possibility is that both transporters have the ability to transport common essential nutrients and thus deletion of *oct-1* would stimulate OCT-2 to compensate for the deprivation of pivotal nutrients. However, we argue against this possibility, as depletion of both *oct-1* and *oct-2* expression did not result in animals with any dramatic phenotypes under normal growth conditions. A more likely possibility is that OCT-1 might belong to the recent characterized class of surface sensors that act as non-transporting transceptors by sensing the availability of nutrients and signal the regulation of downstream plasma membrane transporters[39,40]. In this model, when nutrients become scarce, OCT-1 might serve as a sensor to promote the upregulation of OCT-2 to scavenge limiting resources. Conversely, when nutrients are plentiful OCT-1 might function to sustain the basal expression of OCT-2. Precedence for this mode of regulation exists in *S. cerevisiae*, *Drosophila melanogaster* and *Homo sapiens*[41]. For instance, in *S. cerevisiae* the Ssy1 sensor, a plasma membrane protein belonging to the amino acid permease family, is endowed with no, or only limited, transport function[42]. Ssy1 senses amino acid availability by direct interaction with extracellular amino acids and transmitting the signal to zinc-finger transcription factors that trigger the expression of several downstream target genes encoding amino acid permeases[42–44]. Similar sensors exist in mammalian cells, e.g., the SGLT3 glucose sensor that binds, but does not transport, sugar molecules[45]. Thus, in view of the increasing number of sensors that are currently being identified, it is plausible that OCT-1 may indeed act either as a non-transporting or transporting sensor leading to regulation of OCT-2 expression. The exact role by which OCT-1 exerts control on OCT-2 will need further investigation, but it is noteworthy that a similar regulation appears to occur in mice where deletion of *OCT1* causes significant upregulation of mRNA transcripts of its homologues *OCT2* and *OCT3*[9].

Remarkably, *oct-2* downregulation rescued shortened lifespan and sharply decreased spontaneous apoptosis observed in the *oct-1*(*ok1051*) deletion mutant (Figs 1B and 3B). The most direct interpretation is that OCT-2 indiscriminately transports toxic compounds such as prooxidants. Although the source of these compound(s) is unknown, i.e., whether they originate from the feeding bacteria or re-adsorption of metabolites secreted by *C. elegans*, they are capable of inducing DNA lesions that must be removed by BER. This is supported by the observation that only the BER defective *apn-1* deletion mutant exhibited higher levels of spontaneous apoptosis when *oct-2* expression is upregulated. Thus, the previous report showing that *oct-1* deletion animal exhibit a decline in lifespan due to reduced uptake of the antioxidant ergothioneine can alternatively be explained if the sulphur atom on the imidazole ring of ergothioneine serves to detoxify the OCT-2-dependent uptake of prooxidants[2]. Nonetheless, our findings raise a very important concern regarding genetic variations leading to hyperactivation of uptake transporters as previously reported[46]. This hyperactivation likely to cause accumulation of abnormally high concentrations of genotoxic compounds and metabolites. Consequently, such toxic agents could induce substantial DNA damage over the lifetime of an individual causing genomic instability and eventually cancer.

Our study is the first to demonstrate that *C. elegans* OCT-2 plays a role in ligand uptake. We tested doxorubicin and cisplatin as the initial cationic ligands because they are first-line chemotherapeutics believed to be transported by OCTs in human cells[4,47]. Besides these anticancer drugs, we postulate that OCT-2 may recognize a vast array of other cationic compounds. *Per se*, we implemented the OCT-based ligand-protein docking approach and explore a short list of selected cationic compounds to deduce that OCT-2 was promiscuous compared to OCT-1 and that it interacts robustly with several cationic ligands. Importantly, the analysis produced a refined list of genotoxic compounds that display high protein-ligand docking scores all of which show an OCT-2 dependent *in vivo* effect of triggering germ cells apoptosis. We believe that exploiting OCT-2 in *C. elegans* could have far reaching applications and supersede other whole model systems in drug discovery programs with respect to cost and time. Thus, maintaining the OCT-2 transporter at optimal levels by deleting *oct-1* should represent a useful step for incorporation into any high-throughput screens to more efficiently identify bioactive molecules from chemical libraries. A key aspect of this strategy is that overexpressed OCT-2 is expected to operate with significantly lower chemical concentrations as observed with cisplatin where a fixed lower concentration of the drug had no effect on the wild type, but significantly induced apoptosis in the *oct-1*(*ok1051*) mutant (Figure S9). Thus, the previous barriers posed by *C. elegans* to find bioactive molecules could be explained by the lack of an activated mechanism to efficiently take up the compounds at lower concentrations. In short, we now provide a comprehensive readout of the OCT-2 functional selectivity towards cationic molecules that have a deleterious effect on *C. elegans,* and therefore provide a foundation to understand the regulatory control of drug uptake to circumvent genotoxicities. In addition, we hypothesize that OCT-2 could be exploited either through the *oct-1* gene deletion mutant or *oct-2* over-expression transgenic animals to generate a hypersensitive 'screening' *C. elegans* to facilitate high-throughput drug screening.

Materials and Methods

Nematode strains and culture conditions. The Bristol N2 (wild type), RB1084 [*oct-1*(*ok1051*) I], VC1973 [*rad-51*(*ok2218*) IV/nT1 [qIs51] (IV;V)]*, RB864 [*xpa-1*(*ok698*) I], RB1864 [*msh-2*(*ok2410*) I], MD701 [*bcIs39* [lim-7p::ced-1::GFP + lin-15(+)] and DA453 [*eat-2*(*ad453*) II], TJ1 [*cep-1*(*gk138*) I], MT1082 [*egl-1*(*n487*) V], MT4770 [*ced-9*(*n1950*) III], MT5287 [*ced-4*(*n1894*) III], MT3002 [*ced-3*(*n1286*) IV] and CL2166 [*dvIs19* [(pAF15) gst-4p::GFP::NLS] III] *Caenorhabditis elegans* strains were obtained from the CGC Stock center (*Caenorhabditis* Genetics Centre, University of Minnesota, Minneapolis, USA). The [*apn-1*(*tm6691*) II] were obtained from Shohei Mitani (Tokyo Women's Medical University School of Medicine, Japan and the National Bioresource Project for the nematode *C. elegans*). The alleles used in this study were all previously validated to be null. All *C. elegans* strains were maintained at 20 °C on nematode growth medium (NGM) agar (2.5 g/L peptone, 51.3 mM NaCl, 17 g/L agar, 1 mM $CaCl_2$, 1 mM $MgSO_4$, 25 mM KPO_4, and 12.9 μM cholesterol) enriched with a lawn of streptomycin-resistant *Escherichia coli* OP50 bacterial strain as a source of food. For all *in vivo* experiments, developmental staged-synchronized nematodes were obtained by hypochlorite treatment of gravid adult hermaphrodites. Eggs were allowed to hatch on M9 buffer (6g Na_2HPO_4, 3g KH_2PO_4, 5g NaCl, 0.25g $MgSO_4 \cdot 7H_2O$ per liter filter sterilized). In all experiments, animals were monitored from day 1 post-L1 larvae stage and from L4 to avoid experimental bias. *Homozygous *rad-51/rad-51* nematodes[27] show almost complete inviability due to high embryonic lethality in their progeny, thus we analyzed heterozygote nematodes due to the ease of RNAi-feeding for further analyses. *C. elegans* strains were backcrossed at least three times.

Lifespan assay. Lifespan assays were performed at 20 °C in standard conditions and assessed blindly as previously described[10].

Drug treatment. The anthracycline doxorubicin, water-soluble platinum complex cisplatin and alkylating agent methyl methanesulfonate (Sigma Cat. N° 129925) were added to the NGM agar medium before solidification (~55 °C) to obtain a final concentration of 100 μM for doxorubicin and cisplatin and 0.25 μM for methyl methanesulfonate, respectively. For all experiments, L1-staged from F1 synchronized nematodes were transferred to NGM control agar plates and containing doxorubicin, cisplatin and methyl methanesulfonate. Doxorubicin and cisplatin working concentrations were chosen based on previously reported assays[14]. All drug-containing plates were freshly made prior to each experiment. Our oncology pharmacy department (Maisonneuve-Rosemont Hospital (HMR) provided doxorubicin and cisplatin.

Microscopy and imaging. All microscopy was performed utilizing a DeltaVision Elite Image Restoration System (Applied Precision) with either 40x/0.65–1.35 or 63x/1.42 oil objective. The worms were anesthetized with levamisole (5 μM, Sigma Cat. N° L0380000) and mounted on 2% agarose pads for their respective imaging and quantification. Images were processed utilizing ImageJ imaging software[48].

DNA damage response assay and germ cells imaging. The methods previously described were used[21]. Briefly, to quantify the number of apoptotic corpses in nematodes, L1-staged synchronized N2 wild type, *oct-1*(*ok1051*) and DNA repair deficient mutants were exposed to different doses of drugs followed by germ cells apoptosis assay. Between 18 to 24 hours past L4-staged nematodes, adult moult staged nematodes were assayed with differential interference contrast (DIC) microscopy (Nomarski) optics and the vital DNA dye acridine orange (Sigma Cat. N° A6024). Nematodes were incubated in the dark for 2 hours at 20 °C on NGM plates containing 1 ml of 50 μg/μl of acridine orange DNA dye dissolved in M9 buffer. Stained nematodes were transferred to fresh OP50-seeded NGM plates to incubate for 2 hours in order to clear off the stained bacteria. The acridine orange-stained and DIC-visible apoptotic corpses were counted with an exposure time of 1 second and 0.8 seconds, respectively. The engulfment of apoptotic corpses was scored utilizing the CED-1::GFP reporter and imaged similarly with an exposure time of 1 second utilizing the GFP channel. Images were collected as a series of 25/0.5 μm optical sections covering the complete thickness of the gonad arm.

Imaging the oxidative stress-inducible GFP reporter GST-4::GFP. The uptake of prooxidants was detected by imaging the oxidative stress-inducible GFP reporter GST-4::GFP. L4-staged synchronized nematodes were maintained in NGM plates at 20 °C overnight and imaged the next day at the adult moult stage. The image analysis was performed by measuring the GFP fluorescence intensity of the whole animal utilizing the GFP channel exposed for 0.8 seconds and DIC exposed for 0.05 seconds.

Imaging the pharynx to measure the uptake of doxorubicin. To measure the uptake of doxorubicin, an approach focusing on the pharynx of *C. elegans* was developed. L4-staged synchronized nematodes were treated with doxorubicin 100 μM in NGM plates, incubated at 20 °C overnight and imaged the next day at the adult moult stage. The image analysis was performed by measuring the doxorubicin fluorescence intensity (λ^{ex}470 nm–λ^{em}585 nm) localized at the pharynx by utilizing the GFP channel and observed under a 40x/0.65–1.35 oil objective exposed for a period of time of 0.5 seconds. ImageJ[48] imaging software was utilized to determine the level of fluorescence in the pharynx region. The data of measured fluorescence intensity for doxorubicin uptake was depicted by implementing the custom built-in interactive 3D Surface Plot featured in ImageJ, which display the intensities of pixels from a region of interest of a given image. The uptake was corroborated by two means: (i) The area, the integrated density and the mean gray value were considered to calculate the corrected total pharynx fluorescence [CTPF = Integrated Density − (Area of selected pharynx X Mean fluorescence of background readings)][49], and (ii) Fluoroskan analysis (see below). To measure doxorubicin uptake in a dose-dependent manner, the nematodes were treated with 1 ml of varying concentrations (10 to 100 μM) of the drug in M9 buffer. Uptake of Fluorescein (Sigma Cat. N° F2456), at concentrations ranging from 1 to 100 μM, was used as a control.

Relative RNA quantification to monitor gene expression. Total RNA (RNeasy mini kit Qiagen Cat. N° 74104) was prepared from ~1000 L4 synchronized nematodes and used for cDNA synthesis (Invitrogen Cat. N° 28025-013) followed by quantitative real-time PCR (qRT-PCR). qRT-PCR was performed with the Supergreen Mastermix (Wisent Bioproducts Cat. N° 800-431-UL) starting at 95 °C for 2 min, followed by 40 cycles at 95 °C for 5 sec, 63 °C for 30 sec and 72 °C for 30 sec. Transcript levels were normalized to the internal controls *act-1* and *pmp-3* encoding actin and the peroxisomal membrane protein, respectively. Because there is a putative third organic cationic transporter PES-23, which shares 21.31% and 17.18% identity with OCT-1 and OCT-2, respectively, we monitored *pes-23* gene expression for off targets. The forward and reverse primer sequences utilized in this study were: *oct-1*: 5′-TTTGGAGCAGCTATGGCTTT-3′ and 5′-CTTAGCGTCAGCCCATTTTC-3′; *oct-2*: 5′-TTGGAGTCGTGCTCACGTTC-3′ and 5′-GAGTATGTGAGAAGAAAGCC-3′; *act-1*: 5′-TGCTGATCGTATGCAGAAGG-3′ and 5′-TAGATCCTCCGATCCAGACG-3′; *pmp-3*: 5′-GTTCCCGTGTTCATCACTCAT-3′ and 5′-ACACCGTCGAGAAGCTGTAGA-3′; *pes-23*: 5′-TTCTTGCCGGAGTACCTGCC-3′ and 5′-GCACACATGGAGATTCCGTT-3′.

Dissection of C. elegans heads and gonads for relative RNA quantification. Nematodes were first transferred to a dried 2% agarose pad in 10 μl of M9 buffer. Exactly 300 N2 wild type and 300 *oct-1*(*ok1051*) L4 ~ young adult moult staged nematodes were decapitated just posterior to the pharynx by utilizing a $26^{1/2}$ gauge syringe. Severed heads were washed and collected with M9 buffer in a micro-centrifuge tube and rapidly stored at −80 °C in Trizol (Ambion Life Technologies Cat. N° 15596-018). The same procedure was followed to dissect 100 gonads from L4 ~ young adult staged nematodes. In order to preserve optimum tissue integrity, the collection was made every 15 severed heads and every 10 gonads respectively. RNA extraction was performed from the pool of all collected severed heads and dissected gonads and stored at −80 °C for further qRT-PCR analysis.

RNA interference analysis. *Escherichia coli* HT115^{DE3} strain harboring specific RNAi constructs against *oct-1* and *oct-2* was grown on lysogeny broth (LB) agar plates containing ampicillin and tetracycline. Overnight cultures were grown in LB media containing ampicillin. For *oct-1* and *oct-2* RNAi-driven knockdown experiments, nematodes were maintained until first generation (F1) on NGM agar plates containing 1 mM IPTG (isopropyl-β-D-1-thiogalactopyranoside) enriched with a lawn of *E. coli* HT115^{DE3} expressing RNAi constructs in the pL4440-feeding vector at standard temperature 20 °C. For *oct-1* and *oct-2* RNAi-driven knockdown efficiency, mRNA expression levels were measured in synchronized L4-staged collected from the F1 generation of nematodes fed with *E. coli* expressing RNAi targeted to the indicated genes. The RNAi clones were obtained from the Ahringer laboratory library[50] and verified by sequencing. The depletion efficiency of *oct-1* and *oct-2* genes was validated by qRT-PCR. In all experiments synchronized L4 animals were fed RNAi expressing bacteria and the resulting F1 animals were analyzed for phenotypes.

Choline-based competition assay. L4-staged F1 nematodes were treated overnight with 50 μM and 100 μM concentrations of choline and doxorubicin as separate conditions and together in equimolar amounts in NGM agar plates. The differences in wavelength indexes between doxorubicin (λ^{ex}470 nm–λ^{em}585 nm) and choline (λ^{ex}290 nm–λ^{em}345 nm), allowed us to measure the competitive uptake in the pharynx utilizing the GFP wavelength index where only doxorubicin is detectable and not choline.

Statistical analyses. Lifespan analyses were performed utilizing the Kaplan-Meier estimator calculating the Log-rank test for statistical significance utilizing OASIS software (Online Application for the Survival Analysis of Lifespan Assays Performed in Aging Research)[51]. Germ cell death statistical significance was assessed with the Mann-Whitney U-test calculator Mean values ± s.e.m were calculated for each condition. $^{*}P < 0.05$; $^{**}P < 0.01$; $^{***}P < 0.001$; $^{****}P < 0.0001$ were considered to be statistically significant. For the Brood size analysis, statistical differences were calculated by the unpaired two-tail t-test ($^{*}P < 0.03$; $^{**}P < 0.01$; $^{***}P < 0.0005$) and represented as ± S.D. The Fluoroskan data and the Mean Fluorescence Intensity measurements extracted from the competition assay, Student T-test was calculated and represented as ± S.D ($^{***}P < 0.001$ significant). N.S. = Non Significant. Statistical differences were calculated by using the GraphPad Prism Statistical Software Mac Version 6.

Comparative structure and model construction. *C. elegans* OCT-1 (F52F12.1) and OCT-2 (ZK455.8) putative protein sequences were first obtained from the Wormbase. OCT-1 and OCT-2 were modeled using I-TASSER (Iterative Threading ASSEmbly Refinement)[31] which utilized the best 10 threading template structures from distinct species from the PDB database (Table S1a,b). We relied on the top 5 threading templates ranked by their identity and Z-score, where a Z-score higher than 1 signified a correct alignment. The final models of

OCT-1 and OCT-2 were assessed based on the X-ray diffraction structural analogs of the glucose transporter GLUT3 (PDB ID: 5c65) from *Homo sapiens* (Table S2a,b). The models took into account the following (i) the C-score criteria, a confidence score for estimating the quality of predicted models and TM-score criteria, a metric measurement of the structural similarity between two protein models from I-TASSER[52], (ii) the TM-score from ModRefiner[53] and (iii) the Z-DOPE from Modeller, an atomic distance-dependent statistical calculation from samples of native protein structures that does not depend on any adjustable criteria[54]. These final predicted structures were also assessed based on primary sequence alignment and evolutionary conservation profiles using the PROMALS3D multiple sequence and structure alignment server[55]. Finally, for the predictions of the transmembrane domains, the ResQ *B*-factor profile provided a consensus prediction where the secondary structure helices (SS) are depicted as red tubes[56] (Figure S8A,B), and corroborated with the Orientation of Protein in Membranes (OPM) server[57], the Dense Alignment Surface (DAS) method[58] and the Open-source tool for visualization of proteoforms (PROTTER)[59].

Ligand-protein docking. The ligand chemical structures for doxorubicin (ID: 31703) and diclofenac (ID: 3033) were obtained from the PubChem database[60]. Ligand-protein docking were performed through the BSP-SLIM (Binding Site Prediction with Shape-based Ligand Matching with binding pocket) and COACH algorithms[33,34], featured in the I-TASSER unified platform, to predict the residues constituting the ligand–protein docking sites and conformations of OCT-1 and OCT-2 with doxorubicin and diclofenac.

Structure visualization. OCT-1 and OCT-2 three-dimensional structures and protein-ligand interacting structures were visualized using the OpenGL PyMOL Molecular Graphics System, Mac Version 1.7.4 Schrödinger, LLC.

***In vivo* validation of the predicted ligand-protein docking models.** The ligand-protein docking was performed utilizing the BSP-SLIM server and validated following the same strategy as described in the drug treatment and DNA damage response assay and germ cells imaging sections. Synchronized L1-staged worms were exposed to the following compounds dissolved in DMSO; the RAD-51 inhibitor B02 (5 μM) (ID: 5738263) (EMD Millipore Cat. N° 553525), Camptothecin (75 μM) (ID: 24360) (Sigma Cat. N° C9911), Cycloheximide (50 μM) (ID: 6197) (Sigma Cat. N° C7698), Ketamine (ID: 3821) (predicted virtually), Melphalan (ID: 460612) (predicted virtually), and these additional compounds dissolved in water; Metformin (75 μM) (ID: 4091), Methotrexate (50 μM) (ID: 126941), Methoxyamine (10 μM) (ID: 4113) (Santa Cruz Biotechnology Cat. N° SC257710), Methyl methane sulfonate (0.25 μM) (ID: 5156) (Sigma Cat, N° 129925), Nicotinamide (100 μM) (ID: 936) (Sigma Cat. N° N3376), 4-Nitroquinoline N-oxide (75 μM) (ID: 5955) (ICN Biomedicals Cat. N° 15596), Olaparib (ID: 23725625) (predicted virtually), Paraquat (100 μM) (ID: 15939) (Sigma Cat. N° 856177), Phenformin (75 μM) (Sigma Cat. N° P7045), Puromycin (100 μM) (ID: 439530) (Sigma Cat. N° P9620), Zeocin (25 μM) (ID: 71668282) (Santa Cruz Biotechnology Cat. N° SC496345), and analyzed at the young adult stage. Methotrexate and Metformin were obtained from our oncology pharmacy department (Maisonneuve-Rosemont Hospital (HMR). A concentration of 0.2% DMSO was used for control plates. All drug-treated plates were made fresh and seeded with bacteria 12 hours prior to each experiment.

Brood size quantification to validate the effects of the RAD-51 inhibitor, B02. Single L1-staged worm from wild type and mutant genotypes were transferred to seeded NGM plates without and with B02 and maintained at 20 °C. Animals were transferred to fresh plates each day until they stopped laying eggs. The hatched larvae on each plate were counted and total number of viable larvae that developed to the L1 stage descended from a single hermaphrodite was counted. The average number of viable larvae from 10 to 25 animals of a strain was plotted as brood size where the progeny is allowed to reach adulthood and scored as being fertile or sterile. The brood size of doxorubicin-treated animals was performed similarly where unhatched and hatched progeny was plotted as the total brood size. Statistical differences were calculated by unpaired two-tail t-test (*$P < 0.03$; **$P < 0.01$; ***$P < 0.0005$; N.S. = Non Significant) and represented as ± S.D using GraphPad Prism Statistical Software.

Fluoroskan analysis. Synchronized L1-staged nematodes were exposed to doxorubicin (100 μM) as described above. L4 ~ young adult-staged nematodes were washed at least two times with M9 buffer prior to quantification. A total of 50 worms were placed into each well in duplicate in a 96 format black-well plate with optical bottom (Fisher Scientific). Doxorubicin uptake was measured with a microplate fluorometer (Fluoroskan Ascent, Thermo Scientific, USA) utilizing λ^{ex}544 nm–λ^{em}590 nm filters. Fluorescein 1 μM was used as an internal control for all genotypes. Student T-test was calculated and represented as ± S.D ***$P < 0.001$ statistical significance and N.S. = Non Significant.

References

1. O'Reilly, L. P., Luke, C. J., Perlmutter, D. H., Silverman, G. A. & Pak, S. C. C. elegans in high-throughput drug discovery. *Adv Drug Deliv Rev* **69–70,** 247–253 (2014).
2. Cheah, I. K. *et al.* Knockout of a putative ergothioneine transporter in Caenorhabditis elegans decreases lifespan and increases susceptibility to oxidative damage. *Free Radic Res* **47,** 1036–1045 (2013).
3. Koepsell, H. The SLC22 family with transporters of organic cations, anions and zwitterions. *Mol Aspects Med* **34,** 413–435 (2013).
4. Andreev, E., Brosseau, N., Carmona, E., Mes-Masson, A. M. & Ramotar, D. The human organic cation transporter OCT1 mediates high affinity uptake of the anticancer drug daunorubicin. *Sci Rep* **6,** 20508 (2016).
5. Wu, X. *et al.* Identity of the F52F12.1 gene product in Caenorhabditis elegans as an organic cation transporter. *Biochim Biophys Acta* **1418,** 239–244 (1999).
6. Brosseau, N., Andreev, E. & Ramotar, D. Complementation of the Yeast Model System Reveals that Caenorhabditis elegans OCT-1 Is a Functional Transporter of Anthracyclines. *PLoS One* **10,** e0133182 (2015).

7. Kaletta, T. & Hengartner, M. O. Finding function in novel targets: C. elegans as a model organism. *Nat Rev Drug Discov* **5,** 387–398 (2006).
8. Burns, A. R. *et al.* A predictive model for drug bioaccumulation and bioactivity in Caenorhabditis elegans. *Nat Chem Biol* **6,** 549–557 (2010).
9. Chen, L. *et al.* OCT1 is a high-capacity thiamine transporter that regulates hepatic steatosis and is a target of metformin. *Proc Natl Acad Sci USA* **111,** 9983–9988 (2014).
10. Lionaki, E. & Tavernarakis, N. Assessing aging and senescent decline in Caenorhabditis elegans: cohort survival analysis. *Methods Mol Biol* **965,** 473–484 (2013).
11. McKay, S. J. *et al.* Gene expression profiling of cells, tissues, and developmental stages of the nematode C. elegans. *Cold Spring Harb Symp Quant Biol* **68,** 159–169 (2003).
12. Fishel, M. L. *et al.* Apurinic/apyrimidinic endonuclease/redox factor-1 (APE1/Ref-1) redox function negatively regulates NRF2. *J Biol Chem* **290,** 3057–3068 (2015).
13. Cabreiro, F. *et al.* Metformin retards aging in C. elegans by altering microbial folate and methionine metabolism. *Cell* **153,** 228–239 (2013).
14. Sendoel, A. *et al.* DEPDC1/LET-99 participates in an evolutionarily conserved pathway for anti-tubulin drug-induced apoptosis. *Nat Cell Biol* **16,** 812–820 (2014).
15. Hall, D. & Altun, Z. *C. elegans Atlas*, (Cold Spring Harbor Laboratory Press, 2008).
16. McKay, J. P., Raizen, D. M., Gottschalk, A., Schafer, W. R. & Avery, L. eat-2 and eat-18 are required for nicotinic neurotransmission in the Caenorhabditis elegans pharynx. *Genetics* **166,** 161–169 (2004).
17. Hoffmann, K., Grafe, F., Wohlrab, W., Neubert, R. H. & Brandsch, M. Functional characterization of a high-affinity choline transport system in human keratinocytes. *J Invest Dermatol* **119,** 118–121 (2002).
18. Gartner, A., Boag, P. R. & Blackwell, T. K. Germline survival and apoptosis. *WormBook*, 1–20 (2008).
19. Lans, H. & Vermeulen, W. Tissue specific response to DNA damage: C. elegans as role model. *DNA Repair* (*Amst*) **32,** 141–148 (2015).
20. Horvitz, H. R. Genetic control of programmed cell death in the nematode Caenorhabditis elegans. *Cancer Res* **59,** 1701s–1706s (1999).
21. Craig, A. L., Moser, S. C., Bailly, A. P. & Gartner, A. Methods for studying the DNA damage response in the Caenorhabdatis elegans germ line. *Methods Cell Biol* **107,** 321–352 (2012).
22. Gumienny, T. L., Lambie, E., Hartwieg, E., Horvitz, H. R. & Hengartner, M. O. Genetic control of programmed cell death in the Caenorhabditis elegans hermaphrodite germline. *Development* **126,** 1011–1022 (1999).
23. Savill, J. & Fadok, V. Corpse clearance defines the meaning of cell death. *Nature* **407,** 784–788 (2000).
24. Zhou, Z., Hartwieg, E. & Horvitz, H. R. CED-1 is a transmembrane receptor that mediates cell corpse engulfment in C. elegans. *Cell* **104,** 43–56 (2001).
25. Li, Z., Lu, N., He, X. & Zhou, Z. Monitoring the clearance of apoptotic and necrotic cells in the nematode Caenorhabditis elegans. *Methods Mol Biol* **1004,** 183–202 (2013).
26. Lin, L., Yee, S. W., Kim, R. B. & Giacomini, K. M. SLC transporters as therapeutic targets: emerging opportunities. *Nat Rev Drug Discov* **14,** 543–560 (2015).
27. Rinaldo, C., Bazzicalupo, P., Ederle, S., Hilliard, M. & La Volpe, A. Roles for Caenorhabditis elegans rad-51 in meiosis and in resistance to ionizing radiation during development. *Genetics* **160,** 471–479 (2002).
28. Yang, X. *et al.* Functional characterization of the Caenorhabditis elegans DNA repair enzyme APN-1. *DNA Repair* (*Amst*) **11,** 811–822 (2012).
29. Minotti, G., Menna, P., Salvatorelli, E., Cairo, G. & Gianni, L. Anthracyclines: molecular advances and pharmacologic developments in antitumor activity and cardiotoxicity. *Pharmacol Rev* **56,** 185–229 (2004).
30. Wang, D. & Lippard, S. J. Cellular processing of platinum anticancer drugs. *Nat Rev Drug Discov* **4,** 307–320 (2005).
31. Roy, A., Kucukural, A. & Zhang, Y. I-TASSER: a unified platform for automated protein structure and function prediction. *Nat Protoc* **5,** 725–738 (2010).
32. Sun, L. *et al.* Crystal structure of a bacterial homologue of glucose transporters GLUT1-4. *Nature* **490,** 361–366 (2012).
33. Lee, H. S. & Zhang, Y. BSP-SLIM: a blind low-resolution ligand-protein docking approach using predicted protein structures. *Proteins* **80,** 93–110 (2012).
34. Yang, J., Roy, A. & Zhang, Y. Protein-ligand binding site recognition using complementary binding-specific substructure comparison and sequence profile alignment. *Bioinformatics* **29,** 2588–2595 (2013).
35. Huang, F. & Mazin, A. V. A small molecule inhibitor of human RAD51 potentiates breast cancer cell killing by therapeutic agents in mouse xenografts. *PLoS One* **9,** e100993 (2014).
36. Huang, F. & Mazin, A. V. Targeting the homologous recombination pathway by small molecule modulators. *Bioorg Med Chem Lett* **24,** 3006–3013 (2014).
37. Alagpulinsa, D. A., Ayyadevara, S. & Shmookler Reis, R. J. A Small-Molecule Inhibitor of RAD51 Reduces Homologous Recombination and Sensitizes Multiple Myeloma Cells to Doxorubicin. *Front Oncol* **4,** 289 (2014).
38. Alpi, A., Pasierbek, P., Gartner, A. & Loidl, J. Genetic and cytological characterization of the recombination protein RAD-51 in Caenorhabditis elegans. *Chromosoma* **112,** 6–16 (2003).
39. Aouida, M., Rubio-Texeira, M., Thevelein, J. M., Poulin, R. & Ramotar, D. Agp2, a member of the yeast amino acid permease family, positively regulates polyamine transport at the transcriptional level. *PLoS One* **8,** e65717 (2013).
40. Popova, Y., Thayumanavan, P., Lonati, E., Agrochao, M. & Thevelein, J. M. Transport and signaling through the phosphate-binding site of the yeast Pho84 phosphate transceptor. *Proc Natl Acad Sci USA* **107,** 2890–2895 (2010).
41. Schothorst, J. *et al.* Yeast nutrient transceptors provide novel insight in the functionality of membrane transporters. *Curr Genet* **59,** 197–206 (2013).
42. Gaber, R. F., Ottow, K., Andersen, H. A. & Kielland-Brandt, M. C. Constitutive and hyperresponsive signaling by mutant forms of Saccharomyces cerevisiae amino acid sensor Ssy1. *Eukaryot Cell* **2,** 922–929 (2003).
43. Didion, T., Regenberg, B., Jorgensen, M. U., Kielland-Brandt, M. C. & Andersen, H. A. The permease homologue Ssy1p controls the expression of amino acid and peptide transporter genes in Saccharomyces cerevisiae. *Mol Microbiol* **27,** 643–650 (1998).
44. Ljungdahl, P. O. Amino-acid-induced signalling via the SPS-sensing pathway in yeast. *Biochem Soc Trans* **37,** 242–247 (2009).
45. Bianchi, L. & Diez-Sampedro, A. A single amino acid change converts the sugar sensor SGLT3 into a sugar transporter. *PLoS One* **5,** e10241 (2010).
46. Shu, Y. *et al.* Evolutionary conservation predicts function of variants of the human organic cation transporter, OCT1. *Proc Natl Acad Sci USA* **100,** 5902–5907 (2003).
47. Zhang, S. *et al.* Organic cation transporters are determinants of oxaliplatin cytotoxicity. *Cancer Res* **66,** 8847–8857 (2006).
48. Schneider, C. A., Rasband, W. S. & Eliceiri, K. W. NIH Image to ImageJ: 25 years of image analysis. *Nat Methods* **9,** 671–675 (2012).
49. McCloy, R. A. *et al.* Partial inhibition of Cdk1 in G 2 phase overrides the SAC and decouples mitotic events. *Cell Cycle* **13,** 1400–1412 (2014).
50. Kamath, R. S. & Ahringer, J. Genome-wide RNAi screening in Caenorhabditis elegans. *Methods* **30,** 313–321 (2003).
51. Yang, J. S. *et al.* OASIS: online application for the survival analysis of lifespan assays performed in aging research. *PLoS One* **6,** e23525 (2011).

52. Zhang, Y. & Skolnick, J. Scoring function for automated assessment of protein structure template quality. *Proteins* **57,** 702–710 (2004).
53. Xu, D. & Zhang, Y. Improving the physical realism and structural accuracy of protein models by a two-step atomic-level energy minimization. *Biophys J* **101,** 2525–2534 (2011).
54. Colubri, A. *et al.* Minimalist representations and the importance of nearest neighbor effects in protein folding simulations. *J Mol Biol* **363,** 835–857 (2006).
55. Pei, J. & Grishin, N. V. PROMALS3D: multiple protein sequence alignment enhanced with evolutionary and three-dimensional structural information. *Methods Mol Biol* **1079,** 263–271 (2014).
56. Yang, J., Wang, Y. & Zhang, Y. ResQ: An Approach to Unified Estimation of B-Factor and Residue-Specific Error in Protein Structure Prediction. *J Mol Biol* (2015).
57. Lomize, M. A., Pogozheva, I. D., Joo, H., Mosberg, H. I. & Lomize, A. L. OPM database and PPM web server: resources for positioning of proteins in membranes. *Nucleic Acids Res* **40,** D370–D376 (2012).
58. von Heijne, G. Membrane protein structure prediction. Hydrophobicity analysis and the positive-inside rule. *J Mol Biol* **225,** 487–494 (1992).
59. Omasits, U., Ahrens, C. H., Muller, S. & Wollscheid, B. Protter: interactive protein feature visualization and integration with experimental proteomic data. *Bioinformatics* **30,** 884–886 (2014).
60. Kim, S. *et al.* PubChem Substance and Compound databases. *Nucleic Acids Res* (2015).

Acknowledgements

We acknowledge Dr. John Pascal (Département de Biochimie et Médecine Moléculaire, Université de Montréal) for guidance with the protein structure modeling analysis. We thank Drs Marie-Eve Lalonde and Florence Coteau (Centre de Recherche Hôpital Maisonneuve-Rosemont) for technical assistance with the gene expression and *C. elegans* genetic analyses, respectively. We thank Drs Ivan Topisirovic (Lady Davis Institute Jewish General Hospital, McGill University), Nigel O'Neil (Michael Smith Laboratories, Vancouver, BC) and Elliot Drobetsky (Université de Montréal) for critically reading the manuscript. We also thank the CGC and Shohei Mitani for strains. This work was funded by the research grant (RGPIN/202432–2012) to D.R. from the Natural Science and Engineering Research Council of Canada. A.P. was awarded with a Ph.D bourse d'excellence du Programme en Médecine Expérimentale, Université de Montréal.

Author Contributions

A.P. and D.R. designed the experiments. A.P. performed 100% of the experiments. A.P. and D.R. analyzed the data. A.P. wrote the manuscript. A.P. and D.R. corrected the final version of the manuscript.

Additional Information

Supplementary information accompanies this paper at http://www.nature.com/srep

Competing financial interests: The authors declare no competing financial interests.

How to cite this article: Papaluca, A. and Ramotar, D. A novel approach using *C. elegans* DNA damage-induced apoptosis to characterize the dynamics of uptake transporters for therapeutic drug discoveries. *Sci. Rep.* **6**, 36026; doi: 10.1038/srep36026 (2016).

SCIENTIFIC REPORTS

OPEN

UNG-1 and APN-1 are the major enzymes to efficiently repair 5-hydroxymethyluracil DNA lesions in *C. elegans*

Received: 11 January 2018
Accepted: 13 April 2018

Arturo Papaluca[1,3], J. Richard Wagner[2], H. Uri Saragovi[3] & Dindial Ramotar[1]

In *Caenorhabditis elegans*, two DNA glycosylases, UNG-1 and NTH-1, and two AP endonucleases, APN-1 and EXO-3, have been characterized from the base-excision repair (BER) pathway that repairs oxidatively modified DNA bases. UNG-1 removes uracil, while NTH-1 can remove 5-hydroxymethyluracil (5-hmU), an oxidation product of thymine, as well as other lesions. Both APN-1 and EXO-3 can incise AP sites and remove 3′-blocking lesions at DNA single strand breaks, and only APN-1 possesses 3′- to 5′-exonulease and nucleotide incision repair activities. We used *C. elegans* mutants to study the role of the BER pathway in processing 5-hmU. We observe that *ung-1* mutants exhibited a decrease in brood size and lifespan, and an elevated level of germ cell apoptosis when challenged with 5-hmU. These phenotypes were exacerbated by RNAi downregulation of *apn-1* in the *ung-1* mutant. The *nth-1* or *exo-3* mutants displayed wild type phenotypes towards 5-hmU. We show that partially purified UNG-1 can act on 5-hmU lesion *in vitro*. We propose that UNG-1 removes 5-hmU incorporated into the genome and the resulting AP site is cleaved by APN-1 or EXO-3. In the absence of UNG-1, the 5-hmU is removed by NTH-1 creating a genotoxic 3′-blocking lesion that requires the action of APN-1.

Endogenous and exogenous reactive oxygen species (ROS), such as superoxide radical anions and hydrogen peroxide generate hydroxyl radicals that react with DNA to induce a variety of DNA damage[1]. Hydroxymethyluracil (5-hmU) is a common oxidative DNA lesion induced by ROS and due to active DNA repair, it is usually present at relatively low levels in mammalian cells[1,2]. This modified base and its glucosylated derivative (base J) is also formed by enzymatic reactions in bacteriophage and protozoa[3]. In *Caenorhabditis elegans*, the main source of 5-hmU is likely ROS induced oxidation of thymine, which displays normal base pairing with adenine (5-hmU•A). Another potential source of 5-hmU involves the enzymatic oxidation of 5-methylcytosine (5-mC), which generates 5-hydroxymethylcytosine (5-hmC), a reaction that may lead to deamination by an activation-induced deaminase creating a mismatch with guanine (5-hmU•G). Efficient removal of 5-hmU would restore normal DNA base pairing, otherwise in the case of 5-hmU•G leads to a transition mutation from 5-methylcytosine to thymine[2,4,5]. However, this latter pathway is unlikely to occur in *C. elegans* because they lack 5-methycytosine, ten eleven translocation (TET) family enzymes, and other BER enzymes associated with DNA methylation (see below).

At least, four DNA glycosylases belonging to the base-excision DNA repair (BER) pathway have been identified that remove 5-hmU from the genome and these include (i) the single-strand specific monofunctional uracil DNA glycosylase 1, SMUG1[6], (ii) the bifunctional DNA glycosylase/AP lyase NTH1 that also removes a variety of oxidatively modified bases[7], (iii) the thymine DNA glycosylase TDG[8], and (iv) the methyl-CpG binding domain protein 4, MBD4 DNA glycosylase[9]. These DNA glycosylases cleave the *N*-glycosidic bond between the oxidatively modified base and the sugar moiety to produce a C1′ hydrolyzed abasic sugar. The abasic site created

[1]Maisonneuve-Rosemont Hospital, Research Center, Université de Montréal, Department of Medicine, 5415 Boul. de l'Assomption, Montréal, Québec, H1T2M4, Canada. [2]Département de Médecine Nucléaire et Radiobiologie, Faculté de Médecine et des Sciences de la Santé, Université de Sherbrooke, 3001 12 Avenue Nord, Sherbrooke, Québec, J1H5N4, Canada. [3]Lady Davis Institute for Medical Research, Jewish General Hospital, McGill University, Department of Pharmacology and Therapeutics, McGill University, Department of Pharmacology and Therapeutics, 3755 Chemin de la Côte Sainte-Catherine, Québec, Montréal, H3T1E2, Canada. Correspondence and requests for materials should be addressed to D.R. (email: dindial.ramotar@umontreal.ca)

by these DNA glycosylases, except for NTH1 with an associated β-lyase activity (see below), is incised by an apurinic/apyrimidinic (AP) endonuclease creating a 3′-hydroxyl group and 5′-deoxyribose phosphate. The latter is removed by the lyase activity of DNA polymerase β, which simultaneously with its DNA polymerase activity inserts the correct nucleotide leaving a nick that is sealed by a DNA ligase in a set of reactions that constitutes the BER pathway[10–12].

Of the multiple DNA glycosylases involved in removing 5-hmU in various organisms, only NTH-1 that shares 67.4% similarity with human NTH1 (see Figure S1A) has been conserved in *Caenorhabditis elegans*[13]. Besides NTH-1, *C. elegans* has retained one other DNA glycosylases, namely uracil DNA glycosylase UNG-1 that shares 58.2% similarity with human UNG1 (see Figure S1B)[14,15]. It seems enigmatic that this multicellular organism conserved only two DNA glycosylases, NTH-1 and UNG-1, while the unicellular organisms *Escherichia coli* and the budding yeast *Saccharomyces cerevisiae* conserved eight and five, respectively, and humans retained even more, eleven[12]. There might be a rationale for the evolutionary conservation of only NTH-1 and UNG-1 in *C. elegans*. This organism does not harbor homologs of the enzymes that program the methylation of cytosine, i.e., the DNA (cytosine-5-)-methyltransferases DNMT1 or DNMT3 to form 5-mC, as an epigenetic mark[16,17]. Furthermore, a search of the *C. elegans* genome database revealed that it lacks the Ten Eleven Translocation proteins TET1, 2 and 3 that are required to hydroxylate 5-mC to form 5-hmC and further oxidation products 5-formylcytosine and 5-carboxylcytosine in a pathway to regenerate the nonmethylated cytosine[16,17]. The lack of the TET1, 2 and 3 proteins would also prevent the conversion of thymine to 5-hmU to create the base pair 5-hmU•A in this organism. Moreover, *C. elegans* does not appear to harbor an AID/APOBEC deaminase to convert 5-hmC to 5-hmU. Since the MBD4 DNA glycosylase co-localizes to heterochromatin sites in a DNA methylation-dependent manner[9], it would seem less important for *C. elegans* to conserve a homolog of MBD4 because its genome has no or undetectable 5-mC.

Likewise, it would seem unnecessary for *C. elegans* to also conserve the thymine DNA glycosylase TDG, which would be required to remove T•G mispair formed by deamination of 5-mC in the 5-mC•G base pair. Indeed, *C. elegans* lacks both MBD4 and TDG, raising the possibility that 5-hmU lesions generated as a consequence of thymine oxidation would be processed by either a SMUG1-like and or the NTH-1 activity in *C. elegans*. However, *C. elegans* also lacks in its genome a gene encoding a SMUG1-like DNA glycosylase. Altogether, *C. elegans* appears to lack a system to methylate, hydroxylate and demethylate cytosine in a process that would lead to 5-hmU formation, as well as lacking three DNA glycosylases, SMUG1, TDG and MBD4, that would ordinarily remove 5-hmU. Therefore, we anticipate that the task of removing 5-hmU lesions from the genome of *C. elegans* would be a function devoted strictly to the NTH-1 DNA glycosylase.

The *C. elegans* NTH-1 has been expressed and purified from an *E. coli* expression system and shown to efficiently remove oxidatively modified bases such as thymine glycol, 5-formyluracil and 5-hmU from oligonucleotide substrates[13]. NTH-1 acts as a bifunctional DNA glycosylase/AP-lyase, and following the removal of the modified base, the resulting AP site is cleaved by its AP-lyase activity via a β-elimination reaction to produce a single strand break terminated with a bulky 3′-α, β unsaturated aldehyde[7]. This 3′-blocking lesion must be removed by one of the two conserved AP endonucleases/3′-diesterases, APN-1 and EXO-3, to produce a 3′-hydroxyl group for DNA repair synthesis[18–20]. If the 3′-blocking lesions are not efficiently removed, they can also generate DNA and protein crosslinks that become more deleterious than simple abasic sites[21].

In this study, we set out to investigate whether *C. elegans* mutants lacking enzymes of the BER pathway would be sensitive to exposure of the nucleoside form of 5-hmU. We report the surprising finding that *ung-1*, and not *nth-1*, mutants showed a number of phenotypes that are associated with a defect in DNA damage response when the animals were challenged with 5-hmU, suggesting that UNG-1 is the major DNA glycosylase involved in processing 5-hmU lesions. Consistent with this observation, partially purified UNG-1 was capable of removing 5-hmU from a deoxyoligonucleotide stem-loop substrate. We further show that APN-1-, but not EXO-3, -deficient mutant animals were sensitive to 5-hmU exposure and the effects were more dramatic in *ung-1; apn-1(RNAi)* knockdown mutants. We propose that UNG-1 has the ability to remove 5-hmU and channel the resulting AP site to be cleaved by APN-1 or EXO-3. In the absence of UNG-1, the 5-hmU lesion is processed by NTH-1, which creates the toxic 3′-bocking group that must be repaired by APN-1.

Results

C. elegans mutants deficient in both APN-1 and EXO-3 are hypersensitive to DOX-, MMS- and CDDP-induced DNA lesions.

It has been shown that *C. elegans* mutants deleted for the *apn-1* gene are defective in the repair of damaged DNA that contains oxidative base lesions and AP sites[22]. These mutants exhibit elevated frequency of spontaneous mutations, as well as a short lifespan[22]. Since AP endonucleases serve as key components of the BER pathway, animals deleted for the *exo-3* gene also exhibit short lifespan[23]. These observations indicate that both enzymes bear the responsibility of repairing damaged DNA lesions to maintain *C. elegans* longevity. To date, no previous evidence exists indicating that the simultaneous deletion of the *apn-1* and *exo-3* genes would render the animals to even greater sensitivity to genotoxic agents due to the accumulation of unrepaired lesions in the genome in comparison to the single deletion mutants. We set out to investigate this idea by monitoring the viability of the animals by scoring the brood size and the lifespan following exposure to different DNA damaging agents (Fig. 1A). In this experiment, L1-staged wild type and mutant animals were systematically fed the HT115 bacteria harbouring the RNAi plasmid targeting *apn-1* and *exo-3* to score the brood size, and using the *apn-1* and *exo-3* gene deletion mutants *apn-1(tm6691)* and *exo-3(tm4374)* for comparison, respectively. As expected, the deletion mutants *apn-1(tm6691)* and *exo-3(tm4374)* exhibited a significant decrease in brood size in comparison to the wild type control animals (Fig. 1B–D, white bars) consistent with previous observations[22,23]. RNA-interference (RNAi)-driven depletion of *apn-1* in the *exo-3* deletion mutant *exo-3(tm4374)* caused the resulting *exo-3(tm4374); apn-1(RNAi)* knockdown mutant animals to exhibit nearly 65% decrease in brood size as compared to the single mutants *apn-1(tm6691)* and *exo-3(tm4374)* showing ~40% and 30% decreased in brood

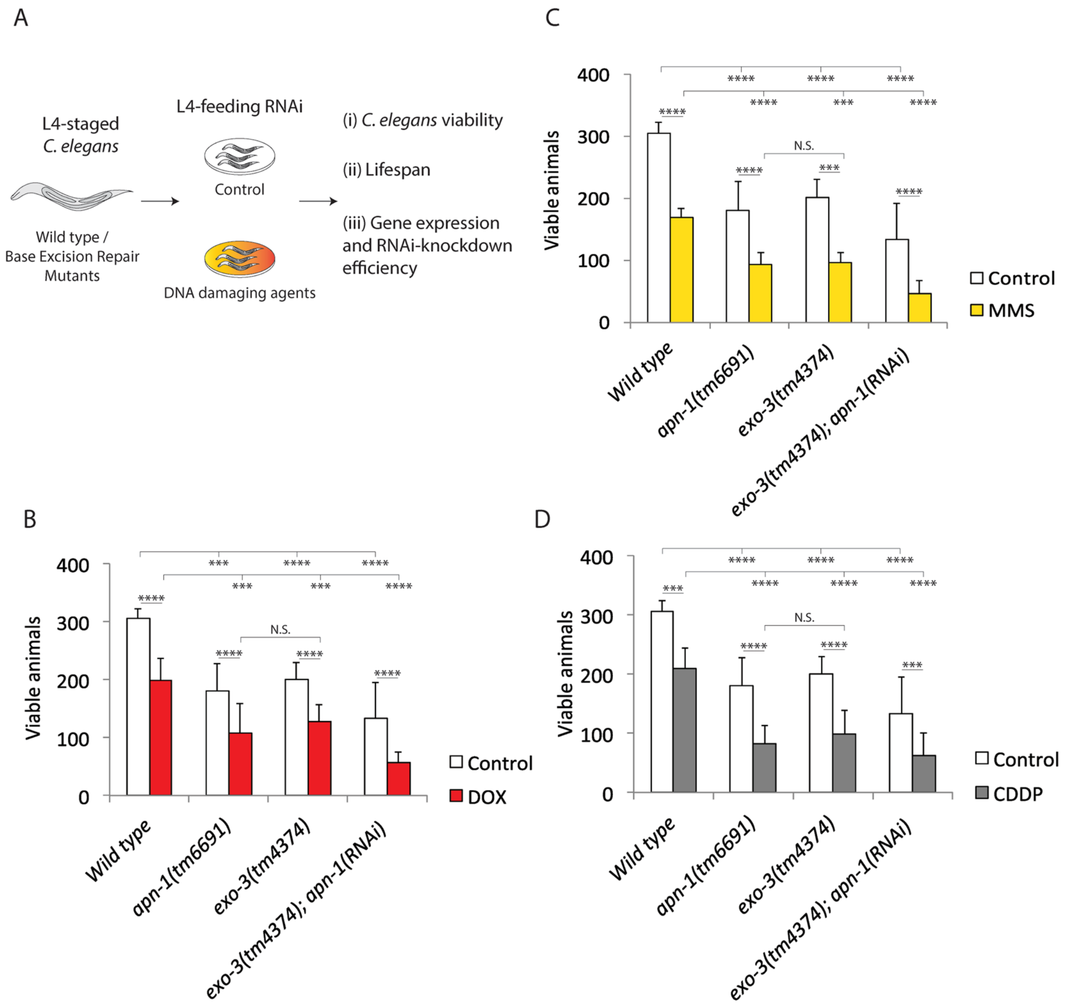

Figure 1. *C. elegans* mutants deficient in both APN-1 and EXO-3 are hypersensitive to DOX-, MMS- and CDDP-induced DNA lesions. (**A**) Scheme of the experimental design. (**B**,**C** and **D**), Brood size analyses of the indicated genotypes. The data are the mean ± S.D. of three independent experiments ($n = 10$ monitored for 3 days). Control; Wild type: 305 ± 17; *apn-1(tm6691)*: 181 ± 47; *exo-3(tm4374)*: 201 ± 29; *exo-3(tm4374); apn-1(RNAi)*: 134 ± 61. Exposed to drugs; (**B**) DOX 100 μM: Wild type: 199 ± 37; *apn-1(tm6691)*: 108 ± 50; *exo-3(tm4374)*: 128 ± 29; *exo-3(tm4374); apn1(RNAi)*: 57 ± 18. C, MMS 0.25 μM: Wild type: 168 ± 15; *apn-1(tm6691)*: 93 ± 20; *exo-3(tm4374)*: 97 ± 15; *exo-3(tm4374); apn1(RNAi)*: 46 ± 21. (**D**) CDDP 100 μM: Wild type: 210 ± 33; *apn-1(tm6691)*: 82 ± 31; *exo-3(tm4374)*: 98 ± 41; *exo-3(tm4374); apn1(RNAi)*: 63 ± 38. Error bars represent the S.D. Unpaired two-tail t-test ***$P < 0.01$; ****$P < 0.0005$ were considered to be statistically significant. N.S. = Non-Significant. DOX, doxorubicin; MMS, methyl methanesulfonate; and CDDP, cisplatin.

size, respectively (Fig. 1B–D, white bars). The effectiveness of the *apn-1(RNAi)* and *RNAi* against other genes (see below) was tested against the wild type (Figure S2A).

We investigated whether there would be a different requirement for APN-1 and EXO-3 molecular activities for processing DNA lesions produced by distinct DNA damaging agents. For this purpose, we exposed the animals to the DNA damaging agents doxorubicin (DOX), methyl methanesulfonate (MMS), and cisplatin (CDDP) that are known to create a range of DNA lesions that include oxidatively damaged bases, alkylated bases that are unstable, single and double strand breaks and interstrand crosslinks[24,25]. We used drug concentrations that allowed the animals to develop and found that DOX, MMS and CDDP induced nearly 50% decrease in brood size as observed for either the single deletion mutant *apn-1(tm6691)* or *exo-3(tm4374)* (Fig. 1B–D). The brood size decreased to 80% when the mutant *exo-3(tm4374)* knockdown for *apn-1(RNAi)* was exposed to the drugs (Fig. 1B–D). These results indicated that the repair of the lesions induced by the distinct DNA damaging agents were dependent upon the single and/or combined activity of APN-1 and EXO-3 as depletion of both enzymes resulted in an additive effect on the brood size. Thus, it would appear that these genotoxic agents are likely generating at least a common DNA lesion, such as indirect formation of AP sites from damaged base, which APN-1 and EXO-3 can compete to repair. In fact, it is known that oxidatively damaged bases are produced by doxorubicin and that the cytosine adjacent to CDDP-induced interstrand crosslinks can preferentially endure oxidative deamination to create uracil[24,25].

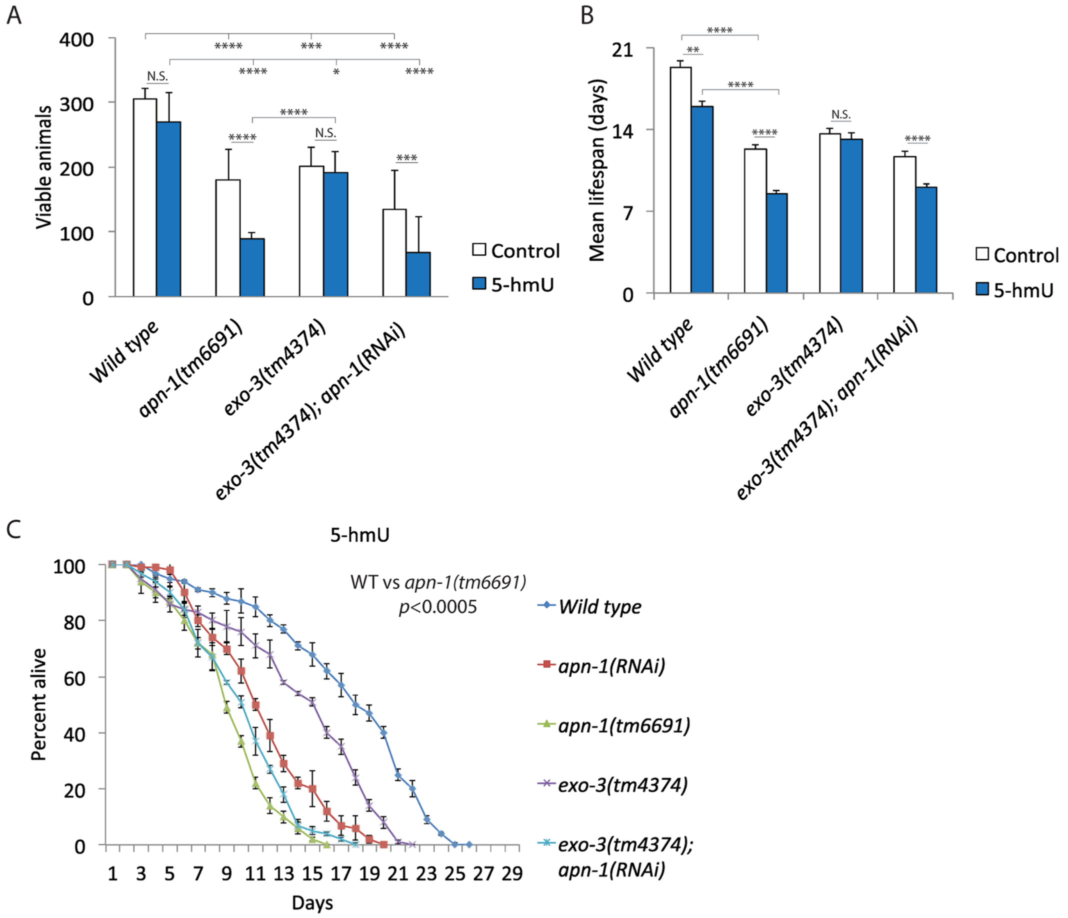

Figure 2. *C. elegans apn-1*, but not *exo-3*, mutants are sensitive to the nucleoside 5-hmU. (**A**) Brood size analysis of animals exposed to 5-hmU. Wild type: 269.8 ± 46; *apn-1(tm6691)*: 102 ± 21; *exo-3(tm4374)*: 171 ± 43; *exo-3(tm4374); apn1(RNAi)*: 68 ± 55. Control; Wild type: 305 ± 17; *apn-1(tm6691)*: 181 ± 47; *exo-3(tm4374)*: 201 ± 29; *exo-3(tm4374); apn1(RNAi)*: 134 ± 61. Error bars represent the S.D. Unpaired two-tail t-test ***$P < 0.01$; ****$P < 0.0005$ were considered to be statistically significant. N.S. = Non-Significant. (**B**) Mean lifespan of the indicated animals exposed to 5-hmU. (**C**) Kaplan-Meier survival plot showing the percentage of alive animals when the indicated genotypes were exposed to 5-hmU. L1-staged animals ($n = 100$) were exposed to 5-hmU (1 μM) and lifespan was blindly analyzed starting from young adult worms. The mean lifespan of two independent experiments is shown.

***C. elegans* apn-1, but not exo-3, mutants are sensitive to the nucleoside 5-hmU.** We have previously shown that APN-1, but not EXO-3, has the ability to process oxidized base DNA lesions, as well as exert a 3′ to 5′-exonuclease activity presumably to act on strand breaks with blocked 3′-ends[20,22]. Oxidation of thymine can lead to 5-hydroxymethyluracil (5-hmU), but as a mispair opposite adenine (5-hmU•A) [2]. We assume that feeding *C. elegans* 5-hmU would lead to its conversion into the triphosphate form and subsequent incorporation into the genome as observed for mammalian cells[1]. Since the purified *C. elegans* NTH-1 enzyme has been shown to remove 5-hmU from oligonucleotide substrate followed by a β-elimination reaction to produce the product 3′-α, β unsaturated aldehyde, instead of an AP site[13]. We predict that this latter lesion would require the function of the 3′-diesterase of either APN-1 or EXO-3 or both for its removal. Following treatment with 5-hmU, we observed that the *apn-1(tm6691)* mutants exhibited nearly 50% decrease in brood size as oppose to *exo-3(tm4374)* that showed only 5% decrease in brood size (Fig. 2A).

However, when the *exo-3(tm4374); apn-1(RNAi)* knockdown mutant was exposed to 5-hmU, we observed the same deleterious effect caused by the *apn-1(tm6691)* mutation alone: close to 50% decrease in brood size (Fig. 2A), again suggesting that EXO-3 has no major role in processing the 5-hmU lesions. To further test this possibility, we examined whether the expression level of the *apn-1* and the *exo-3* genes would be affected by 5-hmU treatment. Interestingly, we observed a nearly 3-fold induction in the expression of the *apn-1* gene when the animals were exposed to 5-hmU, while the *exo-3* gene was unaffected (Figure S2B), consistent with the notion that APN-1, and not EXO-3, is the major AP endonuclease involved in processing the 5-hmU lesion.

We next checked whether exposure to 5-hmU would affect the longevity of the animals by measuring the lifespan of the wild type and the mutant worms in the absence and presence of the nucleoside. We noticed that the lifespan of the *apn-1(tm6691)* mutants was further decreased, but not that of the *exo-3(tm4374)* mutants, when exposed to 5-hmU as compared to the untreated (Fig. 2B,C vs. Figure S3A). Downregulation of *apn-1* by RNAi in the *exo-3(tm4374)* mutants yielded the *exo-3(tm4374); apn-1(RNAi)* knockdown mutants showing a shortened lifespan towards 5-hmU that was similar to the decreased lifespan observed for the *apn-1(tm6691)* single mutant (Fig. 2B,C). We interpret this observation to suggest that APN-1, and not EXO-3, is the predominant endonuclease that is recruited to process the damaged base 5-hmU when it is incorporated into the genome of *C. elegans*. Therefore, the diminished brood size and lifespan caused by 5-hmU in the *apn-1(tm6691)* mutants are attributed to unrepaired lesions in the mitotic and post-mitotic tissues, respectively.

The apn-1(tm6691) mutant animals display increase spontaneous and 5-hmU-induced germ cell apoptosis. Like many other stem cell systems, *C. elegans* features a self-renewing germ cell population originated from a cellular lineage located at the distal tip (Fig. 3A)[26]. In these germ cells, differentiation occurs throughout distinct stages and they must maintain the integrity of the genome. When exposed to environmental insults, germ cells respond by using conserved DNA damage repair pathways that act to maintain genomic stability. Germ cells that are unable to repair damaged DNA undergo apoptosis and subsequent embryonic death[26–29]. We used this sensitive germ cell apoptosis assay to investigate whether 5-hmU would induce germ cell death in the animals and whether this effect would be enhanced in the absence of APN-1 and EXO-3. To do this, we utilized differential interference contrast (DIC) microscopy and DNA staining with acridine orange[30] to quantify the levels of apoptosis in the proximal zone of the gonad arm *in vivo* (Fig. 3A). Consistent with previous reports[31], we observed an average of 2.0 ± 1 apoptotic corpses per wild type animal (Fig. 3B[i]). In contrast, the *apn-1(tm6691)* and the *exo-3(tm4374)* mutants showed an average of 6.0 ± 1.3 and 5.5 ± 0.9 apoptotic corpses per animal, respectively (Fig. 3B[ii and iii] and C). Unlike the single mutants, the *exo-3(tm4374); apn-1(RNAi)* knockdown mutant depicted an average of 8.0 ± 1.5 apoptotic corpses per animal significantly higher than the wild type and the single mutants (Fig. 3B[iv] and C). The observation that the deficiency of both APN-1 and EXO-3 resulted in an additive effect on germ cells apoptosis, indicates that both of these enzymes function independently to promote base excision repair of spontaneous DNA damage in these germ cells.

On the basis of the above results, we challenged the wild type and mutant animals with 5-hmU, as well as the DNA damaging agents DOX and MMS that are known to induce germ cell apoptosis[22,28]. When the wild type animals were exposed to either 5-hmU, DOX and MMS they displayed an average 3.0 ± 1.0, 4.0 ± 2.0 and 5.0 ± 1.0 apoptotic cells per animal, respectively (Fig. 3B[v, ix and xiii] and D–F), suggesting that these doses are effective at causing slight genotoxicity to the germ cells of the wild type animals. In contrast, when the *apn-1(tm6691)* mutant animals were exposed to either 5-hmU, DOX and MMS they showed significantly higher levels of apoptotic cells as compared to both untreated and treated wild type animals (5-hmU: 14.3 ± 1.7; DOX: 10.4 ± 1.3; MMS: 8.5 ± 1.4) (Fig. 3B[vi, x and xiv vs. ii and i] and 3D–F). The high levels of apoptotic cells observed in the *apn-1(tm6691)* mutant exposed to 5-hmU is in agreement with previous studies showing that 5-hmU incorporates into the genome and triggers apoptosis in mammalian cells[32]. Thus, it would also appear that 5-hmU is incorporated into the genome of the germ cells and requires at least the DNA repair functions of APN-1.

Unlike the *apn-1(tm6691)* mutant, the *exo-3(tm4374)* mutants treated with either 5-hmU or DOX, respectively, showed an average of 2.7 ± 1.1 or 5.1 ± 1.2 apoptotic cells per animal, which was comparable to the wild type (Fig. 3B[vii and xi vs. v and ix] and D,E), suggesting that EXO-3 has minimal role compared to APN-1 in processing 5-hmU and DOX-induced DNA lesions. However, *exo-3(tm4374)* mutants exposed to MMS, depicted an average of 8.3 ± 1.8 apoptotic cells per animal similar to the *apn-1(tm6691)* mutants (8.5 ± 1.4) (Fig. 3B[xv vs. xiv] and F). In addition, the level of apoptotic cells was augmented when the *exo-3(tm4374); apn-1(RNAi)* knockdown mutant was exposed to MMS (10.5 ± 1.7) (Fig. 3B[xvi] and F). This observation indicates that EXO-3 can compete with APN-1 to repair MMS-induced DNA lesions, but not for the 5-hmU or the DOX-induced DNA lesions (see also for lifespan Figure S3). Collectively, our results suggest that (i) 5-hmU is incorporated into the genome of the germ cells and causes genotoxicity and (ii) APN-1 plays a key role in repairing 5-hmU lesions and not EXO-3.

5-hmU induces CED-1 engulfment of apoptotic germ cells. To ensure that the quantification of the germ cell death caused by 5-hmU is not a contribution from potential artifacts induced by the acridine orange staining method and or endogenous autofluorescence, we assessed the presence of apoptotic cells using a downstream component of the apoptotic pathway, CED-1. This protein engulfs apoptotic cells to signal phagocytic degradation[33]. As previously reported, we utilized an imaging method in which the *bcls39* strain carries the CED-1::GFP as a reporter of engulfed apoptotic cells[28,34]. This *bcls39* strain with control RNAi showed an average engulfment of 2.0 ± 1.0 apoptotic cells per animal (Fig. 4A[i]), whereas depletion of *apn-1* via RNAi in the *bcls39* reporter caused an increase average engulfment of 6.7 ± 0.9 apoptotic cells due to spontaneous DNA damage (Fig. 4A[ii]) and consistent with the acridine orange staining observed by the *apn-1(tm6691)* mutant (Fig. 3B[ii]). Furthermore, exposure of the *bcls39* reporter strain and the *bcls39; apn-1(RNAi)* to 5-hmU elevated the appearance of apoptotic cells (4.0 ± 0.8 and 16.0 ± 1.5 respectively) (Fig. 4A[iii and iv] and B), supporting the notion that indeed 5-hmU creates genotoxic lesions in the germ cells that must be processed by APN-1. To confirm that 5-hmU can promote apoptotic signaling, we tested several mutants deleted for key components of the apoptotic pathway including *cep-1*, *egl-1*, *ced-9*, *ced-4* and *ced-3*[26]. As expected, none of these mutants showed significant increase in apoptotic cells following exposure to 5-hmU (Figure S4A).

ung-1, but not nth-1, mutants are sensitive to the genotoxic effects of 5-hmU. So far only two DNA glycosylases UNG-1 and NTH-1 have been identified and partially characterized in *C. elegans*[13,15]. Both UNG-1 and NTH-1 function upstream of the APN-1 and EXO-3 AP endonucleases and catalyze the first step of the BER pathway. While purified UNG-1 removes uracil, purified NTH-1 acts on thymine glycol, 5-formyl uracil and 5-hmU[13,15]. We found that both *ung-1* and *nth-1* gene expression were elevated when wild type worms were

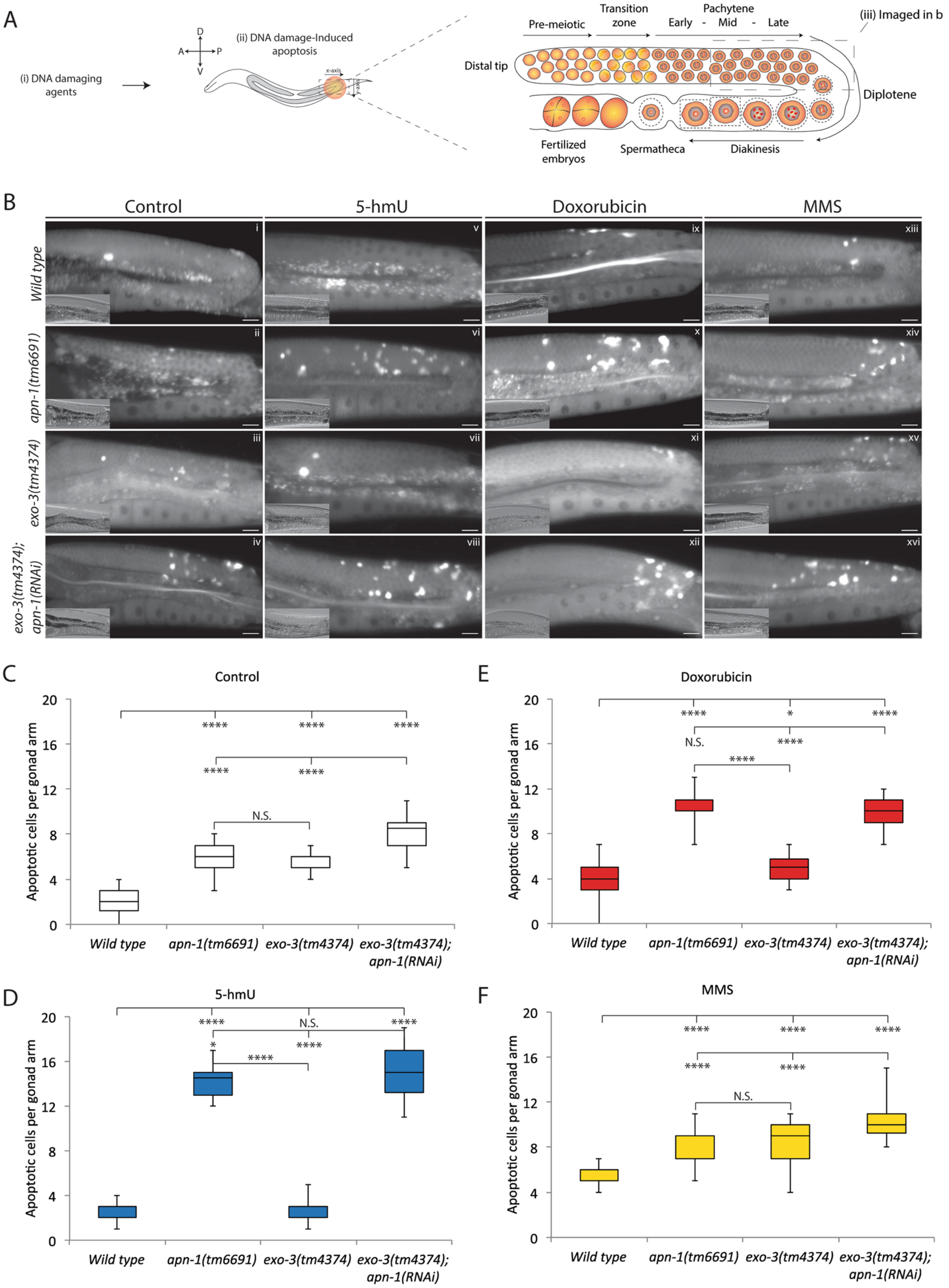

Figure 3. The *apn-1(tm6691)* mutant animals display increase spontaneous and 5-hmU-induced germ cell apoptosis. (**A**) Scheme showing the region of germ cells analyzed for apoptotic corpses in the posterior side of the gonad arm. (**B**) Representative images of acridine orange-stained and DIC (lower left) of control and drug-treated apoptotic corpses from the indicated genotypes. Apoptotic cell corpses were identified as bright spots correlating with raised-bottom-like refractive corpses shown on DIC images. Posterior is right and dorsal is top. Scale bar = 15 µm. (**C–F**) Box and whisker plots showing quantification of apoptotic corpses from control and drug-treated animal and displaying the maximum, minimum, upper & lower quartiles, and sample median. L4-stage animals were treated with (**D**) 5-hmU (1 µM), (**E**) DOX 100 µM and (**F**) MMS 0.25 µM, and apoptotic corpses were quantified the following day in the gonad arms of young adult staged worms. Statistical significance bars represent results of Mann-Whitney U-test of mean difference (*$P < 0.05$; **$P < 0.01$; ***$P < 0.001$ and ****$P < 0.0001$) computed from three independent experiments ($n = 30$).

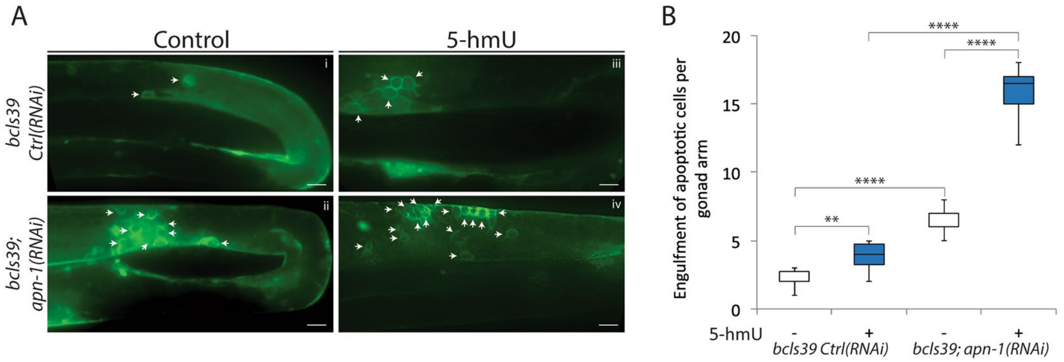

Figure 4. 5-hmU induces CED-1 engulfment of apoptotic germ cells. (**A**) Representative images of control and 5-hmU-treated *bcls39* [CED-1::GFP] worms. The ring around the apoptotic corpses indicates the engulfment of apoptotic bodies shown by white arrows. Scale bar = 10 μm. (**B**) Box and whisker plots showing quantification of the engulfment of apoptotic bodies.

treated with 5-hmU (2B). However, based on the biochemical activities, we anticipate that *nth-1* mutant would display sensitivity to 5-hmU. Survival analysis, scoring for brood size, revealed that the *nth-1(ok724)* mutant was not sensitive to 5-hmU exposure (Figure 5A) or showed increase in germ cell apoptosis under normal growth conditions or when treated with 5-hmU (2.0 ± 1.0 and 2.0 ± 1.0 respectively) (Fig 5D,E). In fact, these findings are consistent with a previous report showing that the *nth-1(ok724)* mutant do not show lifespan defects or sensitivities to oxidants such as hydrogen peroxide and paraquat[13], raising the possibility that the burden of 5-hmU lesions could be processed by another DNA glycosylase. As such, we next examined the *ung-1* mutant for responses towards 5-hmU. Unexpectedly, we found that the *ung-1(tm2862)* deletion mutants exhibited decrease viability (nearly 45%), as well as elevated levels of germ cell death upon exposure to 5-hmU (Fig. 5B,F), suggesting that UNG-1 might recognize and remove 5-hmU lesions from the genome. RNAi downregulation of *apn-1* in the *ung-1(tm2862)* mutant further decreased the viability of the animals and enhanced the number of apoptotic germ cells (nearly 80%) upon 5-hmU exposure (Fig. 5B,F), suggesting that both UNG-1 and APN-1 contribute independently to process the 5-hmU lesion. Interestingly, the diminished viability and enhanced germ cell death observed by RNAi downregulation of *apn-1* in the *ung-1(tm2862)* mutant was not seen when similar experiment was conducted in the *nth-1(ok724)* mutant (Fig. 5A,E). We interpret this finding to suggest that NTH-1 might act *in vivo* to remove some of the 5-hmU lesions and at the same time produce toxic 3′-α, β unsaturated aldehyde that requires the 3′-diesterase function of APN-1. As such, in the absence of NTH-1 these toxic 3′-α, β unsaturated aldehyde lesions are not generated.

Since *exo-3(tm4374)* mutants were not sensitive to 5-hmU, we tested whether RNAi downregulation of *ung-1* would alter its sensitivity. Interestingly, the knockdown of *ung-1* in the *exo-3(tm4374)* mutant did not sensitize the *exo-3(tm4374)* mutant to 5-hmU (Figure S5A). This unexpected finding prompted us to check whether *apn-1* gene expression level would be induced in the *exo-3(tm4374)* mutant, and as such, compensates to repair 5-hmU lesions in the absence of UNG-1. Indeed, the *apn-1* expression level was at least 2-fold higher in the *exo-3(tm4374)* mutant as compared to the wild type, and which was stimulated to 3-fold upon treatment of the animals with 5-hmU (Figure S5B). We believe that the lack of sensitivity of the *exo-3(tm4374)* mutant to 5-hmU might be explained by the induction of *apn-1* gene expression.

Recombinant UNG-1 exhibits 5-hmU activity. We next checked whether UNG-1 has the ability to remove 5-hmU from an oligonucleotide substrate. To do this, we created stem-loop deoxyoligonucleotide substrates bearing either uracil, 5-hmU or the AP site tetrahydrofuran (THF) opposite adenine (U:A, 5-hmU:A and THF:A) at the six position from the 5′-end bearing 6-Carboxyfluorescein[35]. We incubated the substrates for 30 mins at 25 °C without and with GST-UNG-1 purified from an *E. coli* expression system (Figure S6)[14] followed by the addition of *C. elegans* APN-1 purified from a *S. cerevisiae* expression system[20] and then a further incubation for 30 mins at 37 °C. The enzymatic incision of the substrate released a fluorescently labeled 5-mer product that can be detected by a fluorometer. The purified GST-UNG-1 removed uracil from the U:A substrate to create an AP site that was cleaved by the purified GST-APN-1 (Fig. 6). Interestingly, the purified GST-UNG-1 also processed the 5-hmU substrate, which was subsequently cleaved by GST-APN-1 (Fig. 6). In control experiments, GST-UNG-1 alone did not produce the cleaved product from either the U:A or the 5-hmU:A substrate, unless GST-APN-1 was added (Fig. 6), suggesting that the GST-UNG-1 preparation has no contaminating AP endonuclease or AP lyase activity. In additional controls, GST-APN-1 alone did not incise the U:A or 5-hmU:A substrate, unless the substrates were pre-incubated with GST-UNG-1 (Fig. 6). However, GST-APN-1 alone incised the THF substrate (Fig. 6) and not the GST-UNG-1 as determined in other control experiments. These data strongly suggest that UNG-1 possesses the ability to remove 5-hmU, albeit less effectively as compared to uracil (Fig. 6).

POLQ-1 is required for DNA synthesis after removal of 5-hmU lesions. Upon removal of the 5-hmU lesion and incision of the AP site by the BER pathway, a DNA polymerase would be required to fill the single nucleotide gap with a correct nucleotide[36]. A previous study identified POLQ-1 as the DNA polymerase required for the insertion of single nucleotide in the BER pathway in *C. elegans*[37]. In addition, another study

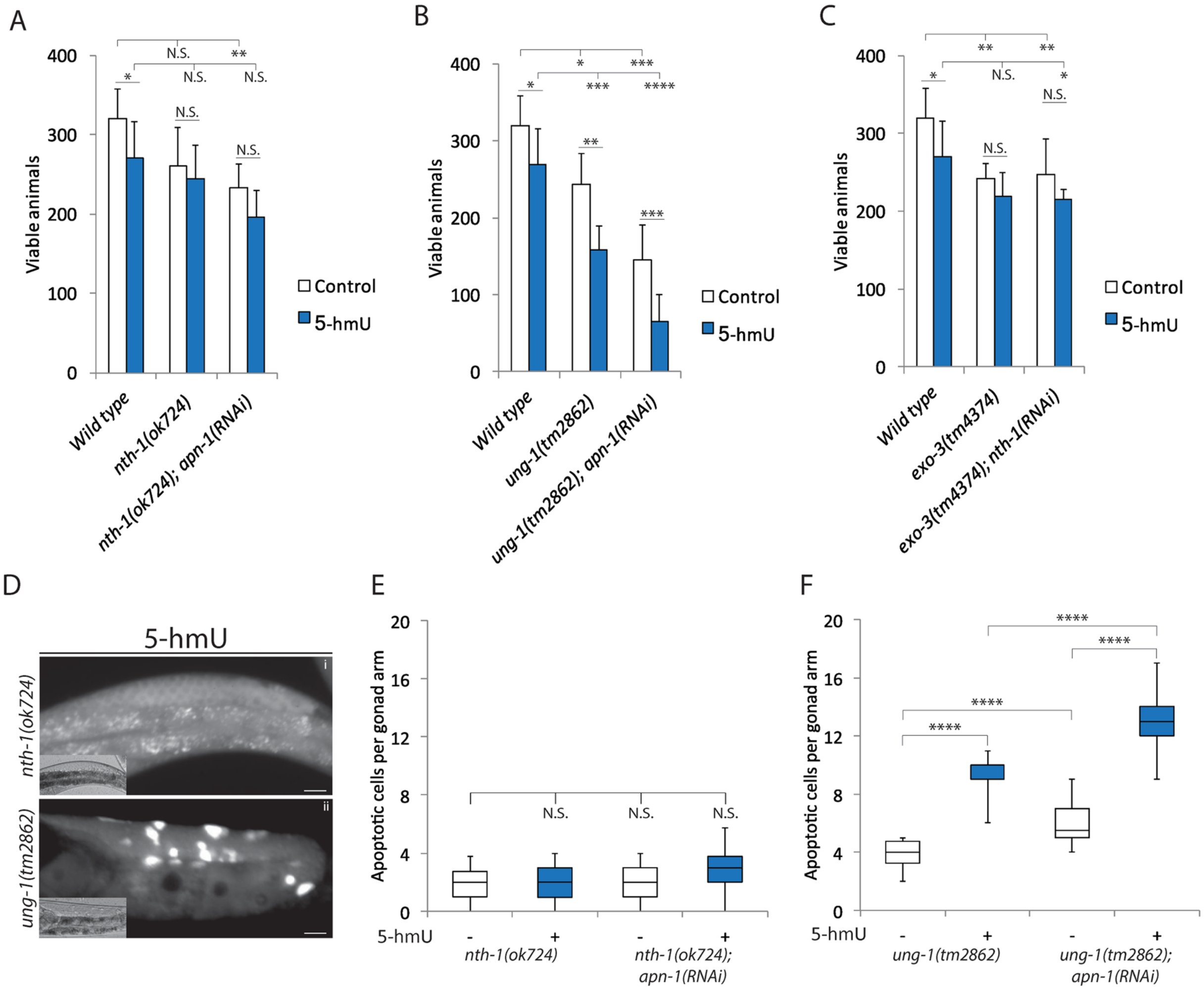

Figure 5. . *ung-1*, but not *nth-1*, mutants are sensitive to the genotoxic effects of 5-hmU. (**A**,**B** and **C**) Control and 5-hmU-treated animals for analysis of brood size as described in Fig. 1B–D. The data are the mean ± S.D. of three independent experiments ($n = 10$ monitored for 3 days). Error bars represent the S.D. Unpaired two-tail t-test ***P < 0.01; ****P < 0.0005 were considered to be statistically significant. N.S. = Non-Significant. (**A**) Control; Wild type: 319 ± 38; *nth-1(ok724)*: 260 ± 48; *nth-1(ok724); apn1(RNAi)*: 232 ± 30, and exposure to 5-hmU; Wild type: 269 ± 46; *nth-1(ok724)*: 244 ± 42; *nth-1(ok724); apn1(RNAi)*: 195 ± 33. (**B**) Control; Wild type: 319 ± 38; *ung-1(tm2862)*: 244 ± 39; *ung-1(tm2862); apn1(RNAi)*: 146 ± 45 and exposure to 5-hmU; Wild type: 269 ± 46; *ung-1(tm2862)*: 157 ± 32; *ung-1(tm2862); apn1(RNAi)*: 65 ± 35. (**C**) Control; Wild type: 319 ± 38; *exo-3(tm4374)*: 241 ± 19; *exo-3(tm4374); nth-1(RNAi)*: 247 ± 45 and exposure to 5-hmU; Wild type: 269 ± 46; *exo-3(tm4374)*: 219 ± 30; *exo-3(tm4374); nth-1(RNAi)*: 215 ± 12. (**D**), Representative images of acridine orange-stained and DIC (lower left) of 5-hmU treated *nth-1(ok724)* and *ung-1(tm2862)* mutant animals as described in Fig. 2B. (**E**,**F**) Box and whisker plots showing quantification of apoptotic corpses from control and 5-hmU-treated of (**E**) *nth-1(ok724)* and (**F**) *ung-1(tm2862)* mutant animals and scored as in Fig. 2C.

showed that POLQ-1 is involved in the repair of DNA interstrand cross-link (ICL)[38]. Furthermore, *C. elegans* disrupted for the *polq-1* gene showed hyper-activation of the DNA damage checkpoint-dependent cell-cycle arrest, as well as enhanced apoptosis in germ cells following treatment with ICL agents[38]. As such, we reasoned that POLQ-1 could be involved in processing 5-hmU and that its downregulation would leave a single nucleotide gap in the damaged strand, which in turn will trigger germ cell apoptosis. Indeed, we found that the *polq-1(tm2572)* mutants exposed to 5-hmU showed a significant increase in the average number of apoptotic cells (9.0 ± 1.0) as compared to the no treatment condition (5.0 ± 1.0) (Figure S7). Depletion of *apn-1* in the *polq-1(tm2572)* mutant resulting in the *polq-1(tm2572); apn-1(RNAi)* knockdown mutant that showed an increase in the average number of 12.0 ± 2.0 of apoptotic germ cells when treated with 5-hmU, as compared to 8.0 ± 1.0 in the untreated (Figure S7). The data suggest that POLQ-1 performs additional roles besides serving as the DNA polymerase required to fill the single nucleotide gap created following removal of 5-hmU from the genome. In fact, *C. elegans* POLQ-1 is related to the human DNA polymerase *theta* that is responsible for repairing double strand breaks in the alternative NHEJ pathway[39].

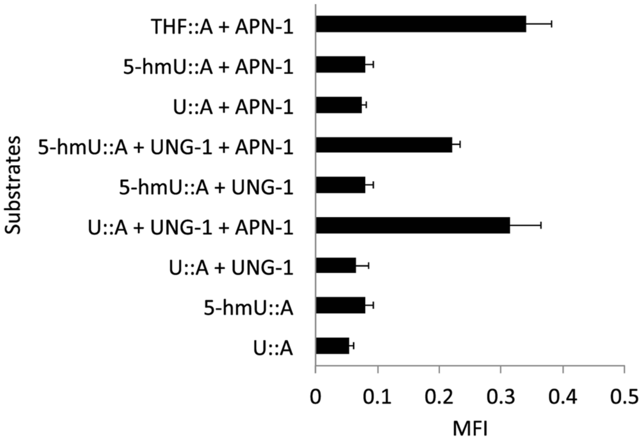

Figure 6. Recombinant GST-UNG-1 acts on 5-hmU lesion to produce APN-1 cleavable AP site. GST-UNG-1 and GST-APN-1 were purified from *E. coli* and *S. cerevisiae* expression system, respectively[14,20]. The enzymes were incubated with the indicated stem-loop deoxyoligonucleotide substrates bearing either uracil, 5-hmU or the AP site tetrahydrofuran (THF) opposite adenine (U:A, 5-hmU:A and THF:A) at the six position from the 5′-end bearing 6-Carboxyfluorescein[35]. UNG-1 was incubated with the substrates for 30 mins at 26°C followed by the addition of APN-1 and then a further incubation for 30 mins at 37°C. The enzymatic incision of the substrate released a fluorescently labeled 5-mer product that can be detected by a fluorometer (Fluoroskan Ascent).

Mutants defective in either the MMR, NER or HR pathway do not show significant increase in germ cell death upon 5-hmU exposure. We next examined whether processing of the 5-hmU lesions would be specific to the BER pathway or the lesion could be channeled to other DNA repair pathways. To do this, we selected representative mutants of the three additional DNA repair pathways, namely *msh-2* of the mismatch repair (MMR), *xpa-1* of the nucleotide excision repair (NER) and *rad-51* of the homologous recombination (HR) repair pathways and checked for the extent of germ cells apoptosis following exposure to 5-hmU.

We first assessed the levels of germ cell apoptosis in the MMR deficient mutant *msh-2(ok2410)*. These *msh-2(ok2410)* mutants did not display significant numbers of apoptotic cells either under standard growth conditions or when treated with 5-hmU (4.0 ± 1.0 and 4.0 ± 1.0, respectively) (Figs 7A[i] and 6B). Downregulation of the *apn-1* gene *via* RNAi in the *msh-2(ok2410)* mutant did not increase the average number of apoptotic cells in the *msh-2(ok2410); apn-1(RNAi)* mutant following 5-hmU exposure (4.0 ± 1.0 and 6.0 ± 2.0, respectively) (Fig. 7B), as compared to level (14.3 ± 1.7) in the treated *apn-1(tm6691)* mutant (Fig. 3B[vi vs. ii] and D). Since it was previously reported that defects in the MMR pathway reduce DNA damage-induced germ cell apoptosis following exposure to genotoxic stress[40], we interpret our finding to suggest that MSH-2 could act to recognize the 5-hmU lesion and recruits NTH-1. Thus, in the absence of MSH-2, NTH-1 would be blocked from generating the toxic 3′-α, β unsaturated aldehyde lesions in DNA and therefore protects the *apn-1* mutant from 5-hmU.We next examined whether the NER pathway mutant *xpa-1(ok698)* would undergo germ cell apoptosis when challenged with 5-hmU. These *xpa-1(ok698)* mutant animals devoid of the XPA-1 protein showed an increase in the average number of germ cell apoptosis under standard growth conditions and which was slightly elevated after exposure to 5-hmU (6.0 ± 2.0 and 8.0 ± 1.0, respectively) (Fig. 7A[ii] and C). Upon downregulation of apn-1 by RNAi, the resulting *xpa-1(ok698); apn-1 (RNAi)* knockdown mutant displayed higher levels of apoptotic cells upon exposure to 5-hmU, and depicting the same average number (14.0 ± 1.0) of apoptotic cells per animal (Fig. 7C), as the treated *apn-1(tm6691)* mutant (Figs 3B[vi vs. ii] and 2D), excluding a major role for the NER pathway in processing the 5-hmU lesion.

We finally examined the involvement of the HR pathway in processing the 5-hmU lesion using the *rad-51(ok2218)/nT1* mutant. This rad-51 mutant already showed high endogenous levels of germ cell apoptosis due to spontaneous unrepaired meiotic breaks as evidenced by an average number of apoptotic cells of 8.0 ± 1.0 under standard growth conditions (Fig. 7D). However, the number of germ cell corpse did not increase upon exposure to 5-hmU (8.0 ± 1.0) (Fig. 7A[iii] and D), suggesting that the 5-hmU lesion is this mutant is processed by other dominant DNA repair pathway. We therefore depleted *apn-1* expression via RNAi in the *rad-51(ok2218)/nT1* mutant and the resulting *rad-51(ok2218)/nT1; apn-1(RNAi)* knockdown mutant showed a substantial increase in the average number of apoptotic cells after treatment with 5-hmU (18.0 ± 1.0) (Fig. 7D). Thus, it would appear that the high level of germ cell death in the *rad-51(ok2218)/nT1; apn-1(RNAi)* mutant can be explained by an additive effect from the spontaneous germ cell death from the *rad-51* mutant and that caused by the lack of APN-1 to process the 5-hmU lesions. Taken together, we conclude that BER is the predominant pathway involved in processing the 5-hmU lesions, while the NER pathway may have a minor role and not that of the MMR and HR pathways.Discussion

In this study, we present several novel findings regarding the base-excision repair pathway in *C. elegans* that is equipped with two DNA glycosylases, UNG-1 and NTH-1, as well as two AP endonucleases/3′-diesterases, APN-1 and EXO-3, to remove damaged bases and process the resulting AP sites[4,13,15]. *C. elegans* UNG-1 has been shown to remove uracil, while NTH-1 has a broader substrate specificity and removes thymine glycol,

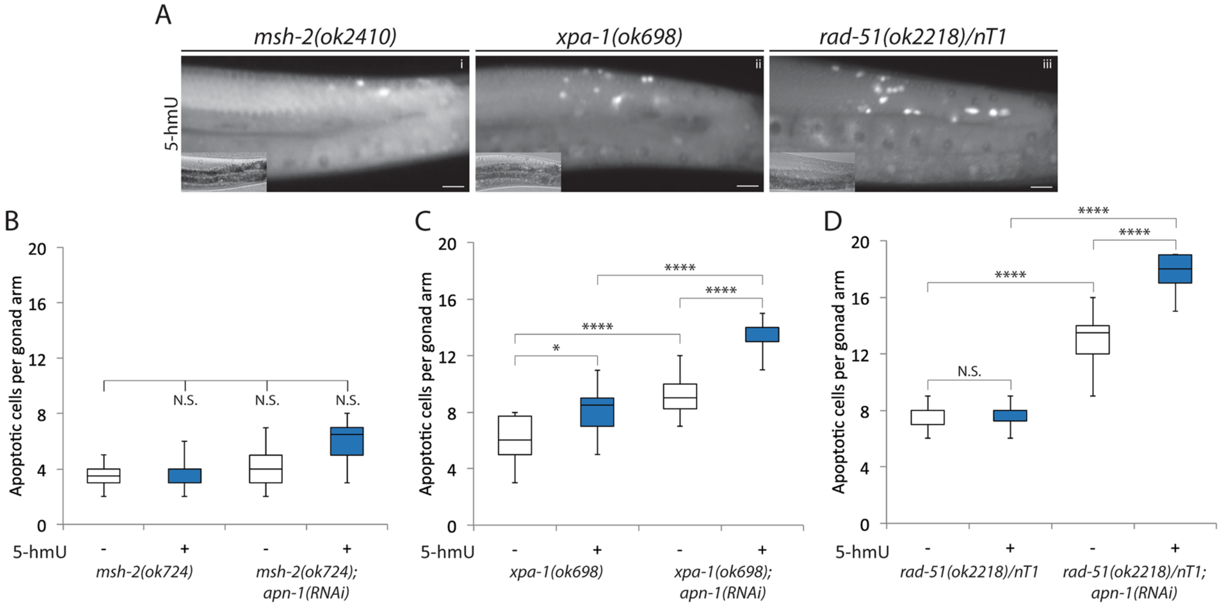

Figure 7. Mutants defective in the MMR, NER or HR pathway do not show significant increase in germ cell death upon exposure to 5-hmU. (**A**) Acridine orange stained and DIC images as described in Fig. 2. The images represent a component from each of the three additional main DNA repair pathways, [i] *msh-2(ok2410)* Mismatch Repair pathway, [ii] *xpa-1(ok698)* Nucleotide Excision Repair pathway and [iii] *rad-51(ok2218)* Homologous Recombination pathway, respectively. (**B**–**D**), Box and whisker plots depicting quantification of apoptotic corpses observed by the DNA repair defective mutants in the absence and presence of 5-hmU treatment.

5-formyluracil and 5-hmU from lesion containing DNA substrates using purified enzymes[13–15]. In the case of the two AP endonuclease/3′-diesterases, we have previously shown that APN-1 has additional enzymatic activities and can act on many types of DNA lesions *in vitro*, while this ability is restricted for EXO-3[4]. Based on the *in vitro* specificities of these enzymes one might expect that *C. elegans* devoid of both NTH-1 and APN-1 would have the most severe phenotypes when challenged with DNA damaging agents. Herein, we challenged *C. elegans* BER-deficient mutants with the nucleoside form of 5-hmU, and unexpectedly observed very striking phenotypes that prompted a reconsideration of the *in vivo* roles of UNG-1 and NTH-1 in this organism. In our approach, we exposed the animals to 5-hmU and monitored several readouts including brood size, lifespan and germ cell apoptosis. The latter analysis is a very sensitive reporter especially for agents that induce genotoxic stress and mutants defective in DNA repair exhibit elevated levels of germ cell death. The observations that 5-hmU caused a decrease in the brood size and lifespan, as well as an increase in germ cell apoptosis, prompted the conclusion that 5-hmU must be incorporated into the genome of the animals to trigger a DNA damage response. In fact, mass spectrometry analysis revealed that if mammalian cells were exposed to 5-hmU this oxidized nucleoside became incorporated into the genome[32]. We attempted to monitor the levels of 5-hmU lesion in *C. elegans* genome, but we were unable to observe a significant and consistent increase in BER deficient mutants. Further studies are in progress to examine the incoporation and repair of 5-hmU in the genomic DNA of *C. elegans.* Nonetheless, we have partially purified recombinant UNG-1 as a GST fusion protein and demonstrated that it has the ability to act on 5-hmU lesion installed on a stem-loop deoxynucleotide substrate. This finding is consistent with the *ung-1* mutants being very sensitive to 5-hmU exposure. In fact, we were surprised that the *nth-1* mutants showed very little or no sensitivity towards 5-hmU, although NTH-1 was previously shown to possess the ability to remove 5-hmU from lesion containing DNA substrates *in vitro* [13–15]. We propose that *C. elegans* UNG-1 may have evolved to acquire a broader substrate specificity and thus could act as the dominant DNA glycosylase *in vivo* to remove various modified forms of uracil such as the 5-hmU lesion. It is noteworthy that *C. elegans* lacks the related human SMUG1 DNA glycosylase, which has been shown to remove 5-hmU[6], and the *C. elegans* UNG-1 shares a modest 12.6% identity with SMUG1[32]. A closer examination of the identity revealed that *C. elegans* UNG-1 shares five amino acid residues Ser58, Pro218, Gly226, Glu233 and Leu234 that are unique to human SMUG1 residues Ser48, Pro166, Gly174, Glu181 and Leu182 and the mouse SMUG1, but which are absent in human UNG1 (Figure S8). Whether these five residues are involved in conferring upon *C. elegans* UNG-1 the human SMUG1 ability to recognize and process 5-hmU will need to be investigated.

UNG-1 action on 5-hmU would leave an AP site that can be processed by either APN-1 or EXO-3 (see model in Fig. 8). If the AP endonuclease function of APN-1 and EXO-3 is redundant in *C. elegans*, then the absence of either enzyme would not cause sensitivity to 5-hmU. Since our data revealed that (i) *C. elegans* mutants devoid of APN-1 were sensitive to 5-hmU, but not EXO-3 deficient animals, (ii) *apn-1*, and not *exo-3*, gene expression was inducible upon treatment of the animals with 5-hmU, and (iii) *apn-1* gene expression is constitutively higher in the *exo-3* mutant, we strongly suggest that APN-1 has a vital role in processing the 5-hmU lesions. In fact,

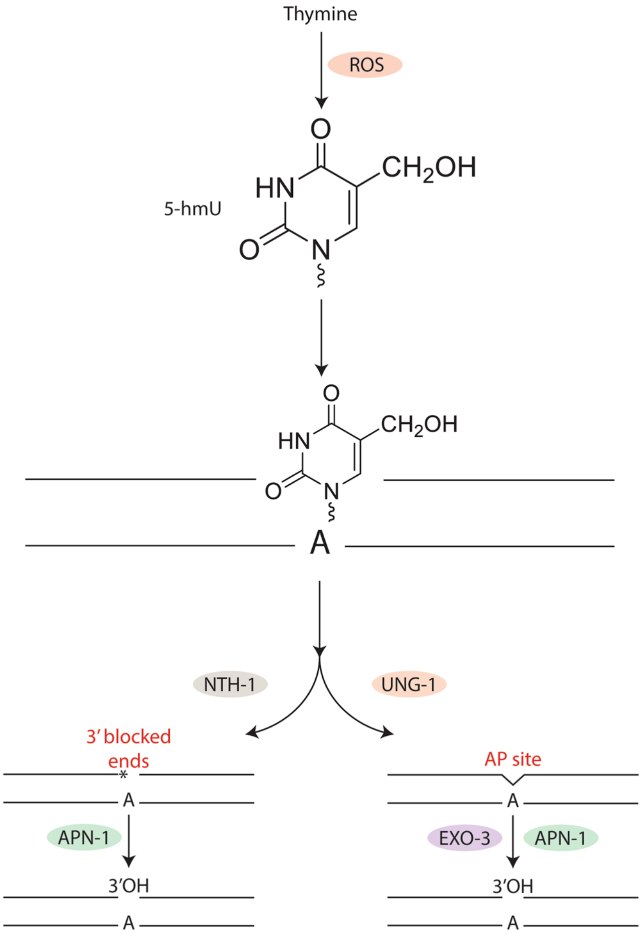

Figure 8. A model illustrating the repair of 5-hmU opposite adenine (5-hmU•A) *via* the BER pathway. Under physiological conditions thymine in the genome is oxidized to 5-hmU creating the mispair 5-hmU•A. In this model, UNG-1 is proposed to recognize and remove 5-hmU creating an AP site that can be processed by either APN-1 or EXO-3. In the absence of UNG-1, NTH-1 removes the 5-hmU lesion and simultaneously cleaves the resulting AP site to create a secondary 3′-blocked genotoxic lesion, 3′-α, β unsaturated aldehyde, which requires processing by the 3′-diesterase or 3′- to 5′-exonuclease activity of APN-1. The 5-hydroxymethyluracil (5-hmU) structure was obtained from PubChem (ID: 78168) and rendered with Chemaxom.

we have previously reported that APN-1 has distinct function(s) from EXO-3, and more recently SenGupta *et al*., 2013 showed that accumulation of the early DNA damage response foci, RPA-1, following treatment with the anticancer agent 5-fluorouracil, depends primarily on EXO-3 role to incise the DNA in order to initiate the mismatch repair pathway[18,41]. We propose a model whereby UNG-1 removes 5-hmU creating an AP site that is either processed by APN-1 or EXO-3[23,42] (Fig. 8). In the absence of UNG-1, the 5-hmU lesion is processed by the second pathway whereby NTH-1 removes the lesion, but simultaneously creates a genotoxic single strand break with a blocked 3′-end, α,β unsaturated aldehyde that blocks DNA repair synthesis[7]. It is possible that the resulting blocked 3′-end is not rapidly removed by APN-1, in particular, if EXO-3 stimulates NTH-1, as seen for the DNA glycosylases OGG1 and TDG by APE1 in human cells[43,44], to create an abundance of blocked 3′-ends that overwhelms the 3′-diesterase and or 3′- to 5′-exonuclease repair capacity of APN-1. Therefore, animals devoid of both UNG-1 and APN-1 would be extremely sensitive to 5-hmU due to excessive accumulation of single strand breaks with blocked 3′-ends. If indeed the *apn-1* mutant sensitivity to 5-hmU is a result of NTH-1 β-lyase activity generating the production of single strand breaks with blocked 3′-ends, then the removal of NTH-1 should rescue the lethality of the *apn-1* mutant. In fact, we showed herein that RNAi downregulation of *nth-1* can suppress the genotoxic effects of 5-hmU in the *apn-1* mutants. A similar suppressive effect was also observed in the *msh-2*; *apn-1(RNAi)* knockdown mutant, which may implicate MSH-2 in the same pathway as NTH-1. Thus, in the absence of NTH-1 and APN-1, as in the *nth-1(ok724)* mutant downregulated for *apn-1* by RNAi, the 5-hmU lesion would be removed by UNG-1 leaving an AP site that will be processed by the AP endonuclease activity of EXO-3[23,42]. We exclude the possibility that EXO-3 acts to remove the 3′- α, β unsaturated aldehyde generated by NTH-1, as the *exo-3(tm4374); apn-1(RNAi)* knockdown mutant is no more sensitive to 5-hmU than the *apn-1(tm6691)* single mutant. Consistent with this notion, we have previously shown that EXO-3, unlike APN-1, lacks a 3′- to 5′-exonuclease activity, which might be the activity needed to remove such bulky and toxic 3′-blocked end[18–21]. In fact, it has been reported that diminishing UNG-1 activity to prevent production of AP sites recues the lifespan defect of the *exo-3* mutants[23]. This phenomenon was not observed in *exo-3* mutants devoid of NTH-1, suggesting that this DNA glycosylase is not producing intermediate lesions to be processed by EXO-3[23].

In short, we have established that the oxidized product of thymine, 5-hmU, is genotoxic in *C. elegans* and that this lesion is predominantly processed by the BER pathway. The most striking observation from our study is the requirement of UNG-1 for the removal of 5-hmU. We believe that *C. elegans* may have conserved only UNG-1 and NTH-1, which have evolved to recognize a broad spectrum of modified bases.

Materials and Methods

Nematode strains and culture conditions. The [*apn-1(tm6691)* II], [*exo-3(tm4374)* I], [*ung-1(tm2862)* III] and [*polq-1(tm2572)* III] were obtained from Shohei Mitani (Tokyo Women's Medical University School of Medicine, Japan and the National Bioresource Project for the nematode *C. elegans*). The Bristol N2 (wild type), MD701 [*bcIs39* [lim-7p::ced-1::GFP + lin-15(+)], RB877 [*nth-1(ok724)* III], RB1864 [*msh-2(ok2410)* I], RB864 [*xpa-1(ok698)* I], VC1973 [*rad-51(ok2218) IV/nT1* [qIs51] (IV;V)] *, TJ1 [*cep-1(gk138)* I], MT1082 [*egl-1(n487)* V], MT4770 [*ced-9(n1950)* III], MT5287 [*ced-4(n1894)* III], MT3002 [*ced-3(n1286)* IV] *Caenorhabditis elegans* strains were obtained from the CGC Stock center (*Caenorhabditis* Genetics Centre, University of Minnesota, Minneapolis, USA). The alleles utilized in this work were all previously validated to be null. All *C. elegans* strains were maintained at 20 °C on nematode growth medium (NGM) agar (2.5 g/L peptone, 51.3 mM NaCl, 17 g/L agar, 1 mM $CaCl_2$, 1 mM $MgSO_4$, 25 mM KPO_4, and 12.9 μM cholesterol) enriched with a lawn of streptomycin-resistant *Escherichia coli* OP50 bacterial strain as a source of food. For all *in vivo* experiments, developmental staged-synchronized nematodes were obtained by hypochlorite treatment of gravid adult hermaphrodites. Eggs were allowed to hatch on M9 buffer (6 g Na_2HPO_4, 3 g KH_2PO_4, 5 g NaCl, 0.25 g $MgSO_4$•$7H_2O$ per liter filter sterilized). In all experiments, animals were monitored from day 1 post-L1 larvae stage and from L4 to avoid experimental bias. *Homozygous *rad-51/rad-51*[45] animals show almost complete inviability due to high embryonic lethality in their progeny, therefore we monitored heterozygote animals due to the easy RNAi-feeding for further analyses. *C. elegans* strains were backcrossed at least three times.

Drug treatment. For drug treatment we followed the same protocol as recently reported[28]. The anthracycline doxorubicin, alkylating agent methyl methanesulfonate (Sigma Cat. No 129925), the oxidative agent 5-hydroxymethyluracil and the water-soluble platinum compound cisplatin were added to the NGM agar medium (55 °C) before solidification to obtain a final concentration of 100 μM for doxorubicin and cisplatin, 0.25 μM for methyl methanesulfonate and 1 μM for 5-hydroxymethyluracil (molecular weight 258 g/mole), respectively. For all experiments, L1-staged from F1 synchronized nematodes were transferred to NGM control agar plates and containing doxorubicin, cisplatin and methyl methanesulfonate. Doxorubicin and cisplatin working concentrations were chosen based on previously reported assays[46]. All drug-containing plates were freshly made prior to each experiment. 5-hydroxy-2′-deoxyuridine (5-hmU) was prepared as previously described[47]. The oncology pharmacy department of the Maisonneuve-Rosemont Hospital (HMR), provided doxorubicin and cisplatin.

Brood size analyses. Single L1-staged worm from wild type and mutant genotypes were transferred to seeded NGM plates without and with the drugs and maintained at 20 °C. Worms were transferred to fresh plates each day until they ceased laying eggs. The hatched larvae on each plate were counted and total number of viable larvae that developed to the L1 stage descended from a single hermaphrodite was counted. The average number of viable larvae from 10 to 25 animals of a strain was plotted as brood size where the progeny is allowed to reach adulthood and scored as being fertile or sterile. The brood size quantification in this analysis follows the same method as previously reported[28].

Lifespan assay. Lifespan analyses were performed at 20°C in standard conditions and assessed blindly as previously reported[48].

Microscopy and imaging. All microscopy was performed utilizing a DeltaVision Elite Image Restoration System (Applied Precision) with either 40 × /0.65–1.35 or 63 × /1.42 oil objective. The worms were anesthetized with levamisole (5 μM, Sigma Cat. No L0380000) and mounted on 2% agarose pads for their respective imaging and quantification. Images were processed utilizing ImageJ imaging software[49].

DNA damage response assay and germ cells imaging. The methods previously described were used[28,30]. Briefly, for scoring of apoptotic corpses in nematodes, L1-staged synchronized N2 wild type and DNA repair deficient mutants were exposed to different doses of drugs followed by germ cells apoptosis assay. Between 18 to 24 hours past L4-staged nematodes, adult staged worms were assayed with differential interference contrast (DIC) microscopy (Nomarski) optics and the vital DNA dye acridine orange (Sigma Cat. No A6024). Nematodes were incubated in the dark for 2 hours at 20 °C on NGM plates containing 1 ml of 50 μg/ml of acridine orange DNA dye dissolved in M9 buffer. Stained worms were transferred to fresh OP50-seeded NGM plates to incubate for 2 hours in order to clear off the stained bacteria. The acridine orange-stained and DIC-visible apoptotic corpses were counted with an exposure time of 1 second and 0.8 seconds, respectively. The engulfment of apoptotic corpses was scored utilizing the CED-1::GFP reporter and imaged similarly with an exposure time of 1 second utilizing the GFP channel. Images were collected as a series of 25/0.5 μm optical sections covering the complete thickness of the gonad arm.

Purification of recombinant GST-UNG-1. The plasmid pGEX-CeUNG-1 designed to express UNG-1 as a GST-UNG-1 fusion protein was kindly provided by Dr. Qiu-Mei Zhang-Akiyama (Japan). The plasmid was introduced into the *E. coli* strain BL21(DE3) and ampicillin resistant colonies were used for preparing whole cell extracts derived from 50 ml of cells (OD 600 of 0.6 treated with 0.1 mM IPTG for 12 hours to induce the expression level of GST-UNG-1) for the purification of the protein as previously described, except using GST-magnetic beads[14]. The GST-magnetic beads (50 µl) were washed three times with washing buffer (PBS plus 125 mM Tris-HCl pH 7.5 and 150 mM NaCl), incubated with 500 µl of whole cell extract for 2 hours at 4oC, following three washes with 200 µl of washing buffer and elution with three 100 µl of elution buffer (washing buffer containing 50 mM glutathione).

Preparation of oligonucleotide substrates and assay conditions. The preparation of the substrates and assay conditions were as previously described[35], except GST-UNG-1 was pre- incubated with the substrate in the BER reaction buffer 25 mM HEPES pH 8.0, 150 mM KCl, 0.5 mM EDTA pH 8.0, 1% glycerol and 1 mM DTT (prepared fresh) for 30 mins at 25°C, prior to the addition of the reaction buffer (50 mM HEPES pH 7.5, 50 mM KCl and 10 mM $MgCl_2$) and a further incubation with purified GST-APN-1 for 30 mins at 37°C. The reactions were carried out, where indicated, with 20 ng of purified GST-UNG-1 and 20 ng of purified GST-APN-1 and the released product was monitored by a fluorometer (Thermo Fisher Scientific, Thermo Scientific^{TM}, model: Fluoroskan Ascent^{TM}).

Relative RNA quantification to monitor gene expression. Total RNA (RNeasy mini kit Qiagen Cat. N° 74104) was prepared from ~1000 young adult synchronized nematodes and used for cDNA synthesis (Applied Biological Materials Inc. Cat. N° G490) followed by quantitative real-time PCR (qRT-PCR). qRT-PCR was performed with the BrightGreen 2 × q-PCR Mastermix (Applied Biological Materials Inc. Cat. N° MasterMix-LR) starting at 95 °C for 2 min, followed by 40 cycles at 95 °C for 5 sec, 60 °C for 30 sec and 72 °C for 30 sec. Transcript levels were normalized to the internal control *act-1* encoding the actin protein. The forward and reverse primer sequences utilized in this study were: *apn-1*: 5′-GCACATCCAGAAGACGCTGC-3′ and 5′-TCTACGGTAGTTCCAGGGCT-3′; *exo-3*: 5′-AGGAGCCTGACCTCGTTTTT-3′ and 5′-GTAGCCACCGTTCTTCTCTG-3′; *nth-1*: 5′-TTTCCAGTCAAA CCAGAGAT-3′ and 5′-AAATCCAACAGGACACAAAA-3′; *ung-1*: 5′-TTCCGGACATGTTCCTCAAA-3′ and 5′-T TCATTGCCCGCGGGAACTT-3; *act-1*: 5′-TGCTGATCGTATGCAGAAGG-3′ and 5′-TAGATCCTCCGATC CAGACG-3′.

RNA interference analysis. *Escherichia coli* HT115DE3 strain harboring specific RNAi constructs against *apn-1* (T05H10.2 AAB39924 10018 G6), *exo-3* (R09B3.1 AAC82328 10018 F7), *nth-1* (R10E4.5 R10E4.5 11002 D5) and *ung-1* (Y56A3A.29 Y56A3A.29 10056 D12) was grown on lysogeny broth (LB) agar plates containing ampicillin and tetracycline. Overnight cultures were grown in LB media containing ampicillin. For *apn-1*, *exo-3*, *nth-1* and *ung-1* RNAi-driven knockdown experiments, nematodes were maintained until first generation (F1) on NGM agar plates containing 1 mM IPTG (isopropyl-β-D-1-thiogalactopyranoside) enriched with a lawn of *E. coli* HT115DE3 expressing RNAi constructs in the pL4440-feeding vector at standard temperature 20 °C. For *apn-1*, *exo-3*, *nth-1* and *ung-1* RNAi-driven knockdown efficiency, mRNA expression levels were measured in synchronized young adults collected from the F1 generation of nematodes fed with *E. coli* expressing RNAi targeted to the indicated genes. The RNAi clones were obtained from the Ahringer laboratory library[50] and verified by sequencing. The depletion efficiency of *apn-1*, *exo-3*, *nth-1* and *ung-1* genes was validated by qRT-PCR. In all experiments synchronized L4-staged animals were fed RNAi expressing bacteria and the resulting F1 animals were analyzed for phenotypes.

Statistical analyses. For the Brood size analysis, statistical differences were calculated by the unpaired two-tail t-test (*P < 0.03; **P < 0.01; ***P < 0.0005) and represented as ± S.D. Lifespan analyses were performed utilizing the Kaplan-Meier estimator calculating the Log-rank test for statistical significance utilizing OASIS software (Online Application for the Survival Analysis of Lifespan Assays Performed in Aging Research)[51]. Germ cells death statistical significance was assessed with the Mann-Whitney U-test calculator Mean values ± s.e.m were calculated for each condition. *P < 0.05; **P < 0.01; ***P < 0.001; ****P < 0.0001 were considered to be statistically significant. N.S. = Non-Significant. Statistical differences were calculated by using the GraphPad Prism Statistical Software Mac Version 6.

References

1. Madugundu, G. S., Cadet, J. & Wagner, J. R. Hydroxyl-radical-induced oxidation of 5-methylcytosine in isolated and cellular DNA. *Nucleic Acids Res* **42**, 7450–7460 (2014).
2. Olinski, R., Starczak, M. & Gackowski, D. Enigmatic 5-hydroxymethyluracil: Oxidatively modified base, epigenetic mark or both? *Mutat Res Rev Mutat Res* **767**, 59–66 (2016).
3. Reynolds, D. *et al*. Regulation of transcription termination by glucosylated hydroxymethyluracil, base J, in Leishmania major and Trypanosoma brucei. *Nucleic Acids Res* **42**, 9717–9729 (2014).
4. Daley, J. M., Zakaria, C. & Ramotar, D. The endonuclease IV family of apurinic/apyrimidinic endonucleases. *Mutat Res* **705**, 217–227 (2010).
5. David, S. S., O'Shea, V. L. & Kundu, S. Base-excision repair of oxidative DNA damage. *Nature* **447**, 941–950 (2007).
6. Boorstein, R. J. *et al*. Definitive identification of mammalian 5-hydroxymethyluracil DNA N-glycosylase activity as SMUG1. *J Biol Chem* **276**, 41991–41997 (2001).
7. Zhang, Q. M. *et al*. DNA glycosylase activities for thymine residues oxidized in the methyl group are functions of the hNEIL1 and hNTH1 enzymes in human cells. *DNA Repair (Amst)* **4**, 71–79 (2005).
8. Hashimoto, H., Hong, S., Bhagwat, A. S., Zhang, X. & Cheng, X. Excision of 5-hydroxymethyluracil and 5-carboxylcytosine by the thymine DNA glycosylase domain: its structural basis and implications for active DNA demethylation. *Nucleic Acids Res* **40**, 10203–10214 (2012).
9. Morera, S. *et al*. Biochemical and structural characterization of the glycosylase domain of MBD4 bound to thymine and 5-hydroxymethyuracil-containing DNA. *Nucleic Acids Res* **40**, 9917–9926 (2012).
10. Krokan, H. E. & Bjoras, M. Base excision repair. *Cold Spring Harb Perspect Biol* **5**, a012583 (2013).

11. Demple, B. & Harrison, L. Repair of oxidative damage to DNA: enzymology and biology. *Annu Rev Biochem* **63**, 915–948 (1994).
12. Friedberg, E. C. *et al*. DNA repair and mutagenesis (Second ed. Friedberg, E.C., Walker, G. C., Siede, W., Woor, R. D., Schultz, R. A., & Ellenberger, T) (ASM Press, Washington, D.C., 2006).
13. Morinaga, H. *et al*. Purification and characterization of Caenorhabditis elegans NTH, a homolog of human endonuclease III: essential role of N-terminal region. *DNA Repair (Amst)* **8**, 844–851 (2009).
14. Nakamura, N. *et al*. Cloning and characterization of uracil-DNA glycosylase and the biological consequences of the loss of its function in the nematode Caenorhabditis elegans. *Mutagenesis* **23**, 407–413 (2008).
15. Skjeldam, H. K. *et al*. Loss of Caenorhabditis elegans UNG-1 uracil-DNA glycosylase affects apoptosis in response to DNA damaging agents. *DNA Repair (Amst)* **9**, 861–870 (2010).
16. Wenzel, D., Palladino, F. & Jedrusik-Bode, M. Epigenetics in C. elegans: facts and challenges. *Genesis* **49**, 647–661 (2011).
17. Greer, E. L. *et al*. DNA Methylation on N6-Adenine in C. elegans. *Cell* **161**, 868–878 (2015).
18. Shatilla, A., Leduc, A., Yang, X. & Ramotar, D. Identification of two apurinic/apyrimidinic endonucleases from Caenorhabditis elegans by cross-species complementation. *DNA Repair (Amst)* **4**, 655–670 (2005).
19. Shatilla, A., Ishchenko, A. A., Saparbaev, M. & Ramotar, D. Characterization of Caenorhabditis elegans Exonuclease-3 and Evidence That a Mg($^{2+}$)-Dependent Variant Exhibits a Distinct Mode of Action on Damaged DNA. *Biochemistry* **44**, 12835–12848 (2005).
20. Yang, X. *et al*. Functional characterization of the Caenorhabditis elegans DNA repair enzyme APN-1. *DNA Repair (Amst)* **11**, 811–822 (2012).
21. Yang, Z., Price, N. E., Johnson, K. M., Wang, Y. & Gates, K. S. Interstrand cross-links arising from strand breaks at true abasic sites in duplex DNA. *Nucleic Acids Res* **45**, 6275–6283 (2017).
22. Zakaria, C. *et al*. Caenorhabditis elegans APN-1 plays a vital role in maintaining genome stability. *DNA Repair (Amst)* **9**, 169–176 (2010).
23. Kato, Y., Moriwaki, T., Funakoshi, M. & Zhang-Akiyama, Q. M. Caenorhabditis elegans EXO-3 contributes to longevity and reproduction: differential roles in somatic cells and germ cells. *Mutat Res* **772**, 46–54 (2015).
24. Forrest, R. A. *et al*. Activation of DNA damage response pathways as a consequence of anthracycline-DNA adduct formation. *Biochem Pharmacol* **83**, 1602–1612 (2012).
25. Sawant, A. *et al*. Differential role of base excision repair proteins in mediating cisplatin cytotoxicity. *DNA Repair (Amst)* **51**, 46–59 (2017).
26. Gartner, A., Boag, P. R. & Blackwell, T. K. Germline survival and apoptosis. *WormBook* (pp. 1–20 (2008).
27. Horvitz, H. R. Genetic control of programmed cell death in the nematode Caenorhabditis elegans. *Cancer Res* **59**, 1701–1706 (1999).
28. Papaluca, A. & Ramotar, D. A novel approach using C. elegans DNA damage-induced apoptosis to characterize the dynamics of uptake transporters for therapeutic drug discoveries. *Sci Rep* **6**, 36026 (2016).
29. Lans, H. & Vermeulen, W. Tissue specific response to DNA damage: C. elegans as role model. *DNA Repair (Amst)* **32**, 141–148 (2015).
30. Craig, A. L., Moser, S. C., Bailly, A. P. & Gartner, A. Methods for studying the DNA damage response in the Caenorhabdatis elegans germ line. *Methods Cell Biol* **107**, 321–352 (2012).
31. Gumienny, T. L., Lambie, E., Hartwieg, E., Horvitz, H. R. & Hengartner, M. O. Genetic control of programmed cell death in the Caenorhabditis elegans hermaphrodite germline. *Development* **126**, 1011–1022 (1999).
32. Zauri, M. *et al*. CDA directs metabolism of epigenetic nucleosides revealing a therapeutic window in cancer. *Nature* **524**, 114–118 (2015).
33. Zhou, Z., Hartwieg, E. & Horvitz, H. R. CED-1 is a transmembrane receptor that mediates cell corpse engulfment in C. elegans. *Cell* **104**, 43–56 (2001).
34. Li, Z., Lu, N., He, X. & Zhou, Z. Monitoring the clearance of apoptotic and necrotic cells in the nematode Caenorhabditis elegans. *Methods Mol Biol* **1004**, 183–202 (2013).
35. Svilar, D., Vens, C. & Sobol, R. W. Quantitative, real-time analysis of base excision repair activity in cell lysates utilizing lesion-specific molecular beacons. *J Vis Exp*, e4168 (2012).
36. Lindahl, T. & Wood, R. D. Quality control by DNA repair. *Science* **286**, 1897–1905 (1999).
37. Asagoshi, K. *et al*. Single-nucleotide base excision repair DNA polymerase activity in C. elegans in the absence of DNA polymerase beta. *Nucleic Acids Res* **40**, 670–681 (2012).
38. Muzzini, D. M., Plevani, P., Boulton, S. J., Cassata, G. & Marini, F. Caenorhabditis elegans POLQ-1 and HEL-308 function in two distinct DNA interstrand cross-link repair pathways. *DNA Repair (Amst)* **7**, 941–950 (2008).
39. Wyatt, D. W. *et al*. Essential Roles for Polymerase theta-Mediated End Joining in the Repair of Chromosome Breaks. *Mol Cell* **63**, 662–673 (2016).
40. Degtyareva, N. P. *et al*. Caenorhabditis elegans DNA mismatch repair gene msh-2 is required for microsatellite stability and maintenance of genome integrity. *Proceedings of the National Academy of Sciences of the United States of America* **99**, 2158–2163 (2002).
41. SenGupta, T. *et al*. Base excision repair AP endonucleases and mismatch repair act together to induce checkpoint-mediated autophagy. *Nat Commun* **4**, 2674 (2013).
42. Shatilla, A. & Ramotar, D. Embryonic extracts derived from the nematode Caenorhabditis elegans remove uracil from DNA by the sequential action of uracil-DNA glycosylase and AP (apurinic/apyrimidinic) endonuclease. *Biochem J* **365**, 547–553 (2002).
43. Vidal, A. E., Boiteux, S., Hickson, I. D. & Radicella, J. P. XRCC1 coordinates the initial and late stages of DNA abasic site repair through protein-protein interactions. *Embo J* **20**, 6530–6539 (2001).
44. Fitzgerald, M. E. & Drohat, A. C. Coordinating the initial steps of base excision repair. Apurinic/apyrimidinic endonuclease 1 actively stimulates thymine DNA glycosylase by disrupting the product complex. *J Biol Chem* **283**, 32680–32690 (2008).
45. Rinaldo, C., Bazzicalupo, P., Ederle, S., Hilliard, M. & La Volpe, A. Roles for Caenorhabditis elegans rad-51 in meiosis and in resistance to ionizing radiation during development. *Genetics* **160**, 471–479 (2002).
46. Sendoel, A. *et al*. DEPDC1/LET-99 participates in an evolutionarily conserved pathway for anti-tubulin drug-induced apoptosis. *Nature cell biology* **16**, 812–820 (2014).
47. Samson-Thibault, F., Madugundu, G. S., Gao, S., Cadet, J. & Wagner, J. R. Profiling Cytosine Oxidation in DNA by LC-MS/MS. *Chemical Research in Toxicology* **25**(9), 1902–1911 (2012).
48. Lionaki, E. & Tavernarakis, N. Assessing aging and senescent decline in Caenorhabditis elegans: cohort survival analysis. *Methods in molecular biology* **965**, 473–484 (2013).
49. Schneider, C. A., Rasband, W. S. & Eliceiri, K. W. NIH Image to ImageJ: 25 years of image analysis. *Nat Methods* **9**, 671–675 (2012).
50. Kamath, R. S. & Ahringer, J. Genome-wide RNAi screening in Caenorhabditis elegans. *Methods* **30**, 313–321 (2003).
51. Yang, J. S. *et al*. OASIS: online application for the survival analysis of lifespan assays performed in aging research. *PLoS One* **6**, e23525 (2011).

Acknowledgements

We thank Taramatti Harihar and Rana Rizk for the preparation of the recombinant GST-UNG-1 and repeating the data in Fig. 6. We also thank Dr. Alex Parker (Département de Neurosciences Université de Montréal and Centre de Recherche du CHUM) for providing the RNAi feeding bacterial strains. We are grateful to the CGC and

Shohei Mitani for providing the *C. elegans* strains. This work was supported by a grant from the Natural Science and Engineering Research Council of Canada to D.R. (RGPIN/202432–2012). A.P. holds a Fonds de Recherche du Québec – Santé (FRQS) Research Doctoral Award.

Author Contributions

A.P., J.R.W., and D.R. designed the experiments. A.P. performed most of the experiments. A.P., J.R.W., H.U.S., and D.R. analyzed the data. A.P. and D.R. wrote the manuscript. A.P., D.R., J.R.W., and H.U.S corrected the final version of the manuscript.

Additional Information

Supplementary information accompanies this paper at https://doi.org/10.1038/s41598-018-25124-1.

Competing Interests: The authors declare no competing interests.

Imaging the Pharynx to Measure the Uptake of Doxorubicin in *Caenorhabditis elegans*

Sivathevy Amirthagunabalasingam[1], Arturo Papaluca[2], Taramatti Harihar[1] and Dindial Ramotar[1, *]

[1]Maisonneuve-Rosemont Hospital Research Center, and the Université de Montréal, Faculty of Medicine, Department of Medicine, Montréal, Canada; [2]Lady Davis Institute, McGill University, Montréal, Canada

*For correspondence: dindial.ramotar@umontreal.ca

[Abstract] *Caenorhabditis elegans* offers an array of advantages to investigate the roles of uptake transporters. Herein, an epifluorescent microscopy approach was developed to monitor the uptake of the autofluorescent anticancer drug, doxorubicin, into the pharynx of *C. elegans* by organic cation transporters.

Keywords: *C. elegans*, Organic cation uptake transporters, Drug uptake, Doxorubicin, Autofluorescent drug, Epifluorescent microscopy, RNAi feeding bacteria

[Background] Human cells have over 450 solute carrier transporters that are believed to facilitate the uptake of several ions, nutrients, as well as both therapeutic and anticancer drugs (Cesar-Razquin *et al.*, 2015). However, the roles and substrates of a large number of these uptake transporters are not known. *C. elegans* is an inexpensive model organism that offers a multitude of advantages over mammalian cells to rapidly study many biological processes that are highly conserved in nature. During the last decade, this organism has been instrumental in several drug discovery programs to identify novel small molecules, *e.g.*, those that act as antimicrobials and inhibit oxidative stress, although the yield of bioactive compounds has been less striking (Burns *et al.*, 2010; O'Reilly *et al.*, 2014). We reason that the recovery rate could be higher if there is greater and selective influx of the molecules by uptake transporters into the animal cells. To date, only three studies have been performed to understand the roles of uptake transporters in *C. elegans* (Wu *et al.*, 1999; Cheah *et al.*, 2013; Papaluca and Ramotar, 2016). Thus, characterization of the function and substrate specificities of uptake transporters in this organism will be advantageous towards improving the strategies employed to identify novel bioactive molecules. Herein, we outline a method to monitor uptake of the anticancer drug doxorubicin into the pharynx of *C. elegans* (Papaluca and Ramotar, 2016). Doxorubicin autofluorescence can be readily monitored by several widely available detection systems such as the epifluorescent microscope. We note that several benefits can be derived from this approach including a hunt for novel therapeutic substrates of the transporter by competing for doxorubicin uptake.

Materials and Reagents

1. Petri dish 60 x 15 mm (SARSTEDT, catalog number: 82.1194.500)
2. 15 ml conical tube

3. Frosted microscope slides (size: 1 x 3” ; thickness: 1-2 mm) (UltiDent Scientific, catalog number: 170-7107A)
4. Microscope cover glass (size: 22 x 22 #1.5) (Fisher Scientific, catalog number: 12-541B)
5. Platinum wire (Thomas Scientific, catalog number: 1233S71)
6. Pasteur pipet (Fisher Scientific, catalog number: 13-678-20C)
7. *E. coli* bacteria HT115^{DE3} with the plasmid pL4440-empty vector
8. *E. coli* bacteria HT115^{DE3} with the plasmid pL4440-oct-1 (Ahringer’s collection). Sequence verified
9. *E. coli* bacteria HT115^{DE3} with the plasmid pL4440-oct-2 (Ahringer’s collection). Sequence verified
10. Bristol N2 (wild type) and RB1084 [*oct-1(ok1051*) I] from *Caenorhabditis* Genetic Center
11. Ampicillin (Sigma-Aldrich, catalog number: A9518)
12. Potassium phosphate monobasic (KH_2PO_4) (Bio Basic, catalog number: PB0445)
13. Magnesium sulfate ($MgSO_4$) (Bio Basic, catalog number: MRB0329)
14. Calcium chloride dihydrate ($CaCl_2$) (Fisher Scientific, catalog number: C79-500)
15. Cholesterol (Sigma-Aldrich, catalog number: C8503)
16. Ethanol 100% (works from any company)
17. Doxorubicin (for Research from Hôpital Maisonneuve-Rosemont, Montreal, Canada). Stock concentration at 2 mg/ml
18. IPTG (Bio Basic, catalog number: PRB0447)
19. Levamisol hydrochloride (MP Biomedical, catalog number: 155228)
20. Clear nail polish from Wild Shine from Dollarama
21. Tryptone (Bio Basic, catalog number: TG217(G211)) for Luria Broth (LB) media
22. Yeast extract (Wisent Bioproducts, catalog number: 800-150-LG) for LB media
23. Sodium chloride (NaCl) (Wisent Bioproducts, catalog number: 600-082)
24. Bacteriological agar (Wisent Bioproducts, catalog number: 800-010-CG)
25. Peptone (Wisent Bioproducts, catalog number: 800-157-LG) for nematode grown media (NGM)
26. Agarose (Wisent Bioproducts, catalog number: 800-015-CG)
27. Sodium hydroxide (NaOH) (Bio Basic, catalog number: SB0617)
28. Bleach Lavo Pro6 (Lavo Inc, Montreal, Canada)
29. Sodium phosphate dibasic (Na_2HPO_4) (Bio Basic, catalog number: S0404)
30. LB solution (see Recipes)
31. Nematode growth media (NGM) (see Recipes)
32. Agar pad (see Recipes)
33. Alkaline Hypochlorite solution for bleaching the worms (see Recipes)
34. M9 buffer (see Recipes)

Equipment

1. Incubator at 20 °C, but with a range from 15 to 37 °C (SHEL LAB, model: 2020)
2. 37 °C incubator (Panasonic Healthcare, model: Mir-262)
3. 37 °C shaker (Inforst, model: Multitron Standard)
4. 500 ml glass bottle (Wheaton graduated glass media bottles with lined caps)
5. Microwave (inverter model, Panasonic Healthcare)
6. 55 °C water bath (Precision Scientific, catalog number: 66800)
7. Metal spatula (VWR)
8. Flame
9. Neutrex culture tubes 16 x 15 mm
10. Pyrex Erlenmeyer flask different sizes for bacteria culturing
11. Autoclave
12. Stereomicroscope Leica MZ 8 (Leica 10445538 Plan Microscope Objective Lens 1.0x) (Leica, model: MZ 8)
13. DeltaVision Elite Restoration System (GE Healthcare, model: DeltaVision Elite High Resolution Microscope) and the DeltaVision imaging system user's manual
14. Fisher Vortex Genie 2 (Fisher Scientific, catalog number: 12-812)
15. Eppendorf 5810 R centrifuge (Eppendorf, model: 5810 R)
16. VWR rocking platform shakers basic (VWR)
17. Ptc-100 Programmable Thermal Controller 96 Well (Bio-Rad Laboratories, model: Ptc-100® Programmable Thermal Controller)
18. Centrifuge (Sigma Centrifuge, model: Sigma 1-14)

Software

1. ImageJ imaging software
2. SoftWorx software

Procedure

A. Preparation of bacteria and media for worm growth
   1. Bacteria preparation (*C. elegans* food)
      a. In 10 ml LB medium, add 10 µl ampicillin (stock 100 mg/ml).
      b. Inoculate a few colonies of *E. coli* HT115^{DE3} empty vector bacteria into the LB + ampicillin medium.
      Note: Alternative bacteria: E. coli OP50.
      c. Incubate for 6 h at 37 °C in an orbital shaker at 200 rpm.

2. *C. elegans* growth media preparation
   a. Melt the solid NGM contained in a glass bottle (500 ml) using a microwave (power level 2 for 25 min).
   b. Keep the melted medium at 55 °C in a water bath for 15-20 min.
   c. Before usage, add:
   12.5 ml of 1 M KH_2PO_4 pH 6
   500 µl of 1 M $MgSO_4$
   500 µl of 1 M $CaCl_2$
   500 µl cholesterol (stock 5 mg/ml in 95% ethanol)
   500 µl of ampicillin (stock 100 mg/ml), if using knockdown bacteria strain HT115^{DE3} carrying the L4440 vector or the target gene.
   d. Gently invert the bottle a few times to mix all the ingredients and then pour 6 ml of the medium into each of 60 x 15 mm Petri dish.
   e. Let it dry at room temperature for around 1 h.
   f. Once dried, using a sterilized bacterial plating rod spread 70 µl of bacteria prepared in step A1 above to form a lawn. The optical density OD_{600} of the bacteria is approximately 1.0. Alternatively, the bacteria can be added as 3 drops distributed onto the plate.
   g. Incubate the plate overnight at 37 °C.
3. Worm growth
   a. From a grown worm plate, cut 4 pieces of approximately 1 x 1 cm agar with a pointy spatula sterilized with 100% ethanol and flame.
   b. Transfer each agar piece by turning them over onto each of 4 plates prepared in step A2.
   c. Incubate these worm plates for 2 days at 20 °C.

B. Worm synchronisation
1. The 4 plates are expected to be fill with adult worms, visualized through a stereomicroscope, and at which point the synchronization can be done. An alternative method to obtain a huge amount of worms is to grow them in liquid media (NGM medium without agar).
2. Add 2 ml of alkaline hypochlorite solution (bleaching solution) to each plate and rapidly collect the worms by pipetting (about 10 sec per plate) in a sterile 15 ml conical tube. Date and label the tube with the name of the worm strain. Alternatively, harvest the worms with 1 ml of M9 buffer and collect them into 15 ml conical tubes. Centrifuge in the Eppendorf 5810 R centrifuge, using swing bucket rotor (A-4-81) with adapters for 15 ml conical tubes at 1,740 *x g* for 2 min at 4 °C. Discard the M9 buffer and add 2 ml of the bleaching solution. In this way the worms are washed once.
3. Quickly start to vortex the worms for 7 min at setting 8 on the vortex and check under the stereomicroscope if the adult worms are lysed and only the eggs are present.

Note: Steps B2 and B3 must be carried out with care as they are critical for the eggs to hatch.

4. Without any delay, centrifuge in the Eppendorf 5810 R centrifuge at 1,740 *x g* for 2 min at 4 °C.

5. Aspirate the supernatant, but leave approximately 1 ml of the solution.
6. Adding 5 ml of M9 buffer and repeat the centrifugation and aspiration as in steps B4 and B5.
7. Repeat 4 more times step B6, in order to remove any trace of the bleaching solution.
8. Incubate the eggs in the final 1 ml of M9 buffer overnight at 20 °C. During this time the eggs will hatch and produce L1 stage worms.

C. Worm under treatment
   1. Bacteria preparation
      a. In 3 different tubes, add 10 ml LB medium and 10 µl ampicillin (100 mg/ml).
      b. In the 1st tube, add a few colonies of *E. coli* HT115^{DE3}/empty vector L4440.
      c. In the 2nd tube, add a few colonies of *E. coli* HT115^{DE3}/pL4440-oct-1.
      d. In the 3rd tube, add a few colonies of *E. coli* HT115^{DE3}/pL4440-oct-2.
      e. Incubate all the tubes for 5 h in a 37 °C orbital shaker.
   2. Drug plate preparation
      a. Melt a bottle of 500 ml of solid NGM as above (see *C. elegans* growth media preparation above).
      b. For normal drug plates-no knockdown
         i. Transfer 30 ml of melted NGM media kept at 55 °C into a small sterile bottle. This will make 3 Petri dishes (60 x 15 mm) each containing ~10 ml of NGM media for triplicate assays.
         ii. Add the doxorubicin (stock 2 mg/ml) to the desire final concentrations for each 6 ml of NGM media and pour onto the 60 x 15 mm Petri dish. For doxorubicin use between 0.1 to 100 µM depending on the strains. Uptake was observed with as low as 0.5 µM of doxorubicin.
         IMPORTANT: Do not forget to prepare a plate without drug.
         iii. Leave plates for at least 15 min at room temperature for the medium to solidify.
         iv. Add 70 µl *E. coli* HT115^{DE3}/pL4440-empty vector bacteria.
         v. Incubate the plates overnight at 37 °C.
      c. For knockdown drug plates
         i. Transfer 30 ml of melted NMG medium kept at 55 °C into a small sterile bottle.
         ii. Add 30 µl of 1 M IPTG, needed to induce the production of dsRNA from the L4440 vector carrying a fragment of the target gene.
         iii. Add to 6 ml of this media the desire concentrations of doxorubicin as above.
         IMPORTANT: Do not forget to prepare a plate without drug.
         iv. Pour 6 ml of media with and without IPTG and with doxorubicin onto 60 x 15 mm Petri dishes.
         v. Dry the plates, as above.
         vi. Add 70 µl *E. coli* HT115^{DE3}/pL4440-oct-1 bacteria for 1st set of 5 plates.
         vii. Add 70 µl *E. coli* HT115^{DE3}/pL4440-oct-2 bacteria for 2nd set of 5 plates.

        viii. Incubate the plates overnight at 37 °C.
3. Now all the plates are ready to add 50 µl of the L1 synchronized worms.
4. Verify if there are nearly 50 L1-staged worms on the plates under the stereomicroscope.
5. Incubate the plates at 20 °C for 3 days.

D. Microscope visualisation
1. Preparation of slides
    a. On a frosted microscope slide add one drop (~50 µl) of 3% agarose and squeeze it with another slide to form a sandwich. After 10 sec, remove one of the slide to expose the agarose.
    b. Dry the slide with the agarose at 65 °C around 15-30 min using a Programmable Thermal Controller 96 Well.
2. Mounting the worms
    a. Add 7 µl of 1 M levamisol onto the surface of the dried agar on the slide.
    b. To each slide, add 10-15 young adult worms from a single treatment condition by using a platinum wire to transfer the worms.
    c. Sterilize the platinum wire using a flame before transferring the next 10-15 worms from a different treatment condition onto a new slide.
    d. Add the coverslip and seal around the slide and coverslip with clear nail polish.
3. Microscopy visualisation

    The slide containing the worm is ready to be visualised. Place the slide on the stage of an epifluorescence microscope.

    1st Adjust the objectives
    2nd Select the filters and adjust all the necessary parameters
    3rd Once everything is ready, start capturing the images
    4th Save the images

    Below is a detail description to visualize the worms using a DeltaVision microscope.
    a. Add a small drop of DeltaVision Immersion oil 1.534 onto the slide in order to use objective 40x.
    b. Place the mounted slide on the microscope by inverting it.
    c. Adjust the eyepiece filter roll to POL filter.
    d. Open the SoftWorx software . See GE Healthcare manual (GE Healthcare, 2014).
    e. Press on the microscope.
    3 windows will be opened (Figure 1).

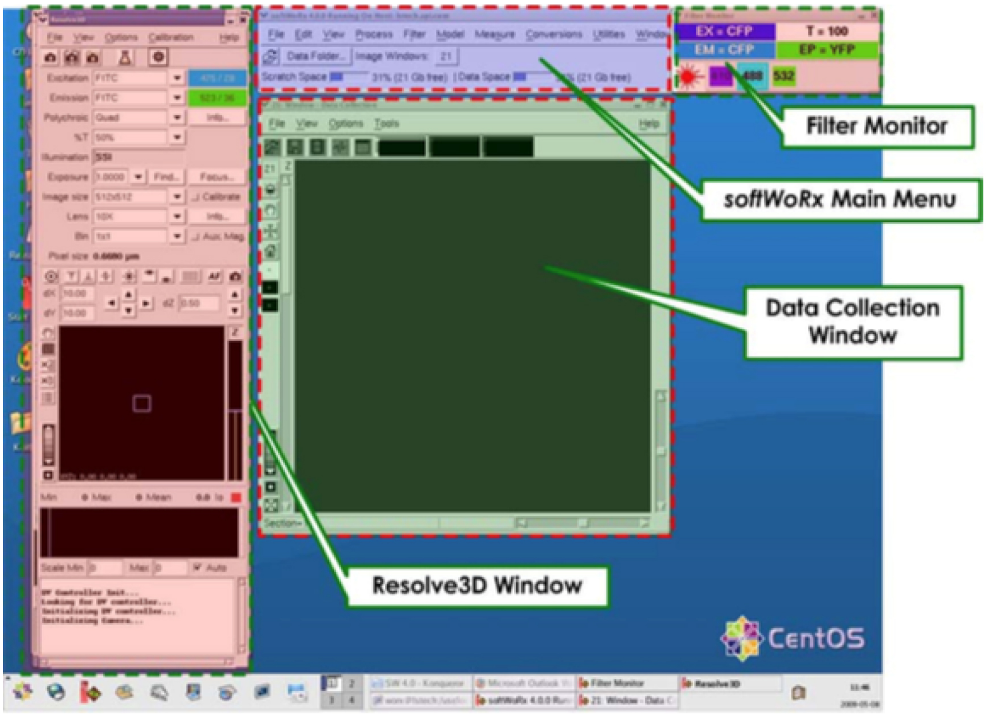

Figure 1. SoftWorx desktop display. The Resolve3D window includes acquisition parameters and controls for moving the stage, the Data Collection window displays images as they are acquired, and the Filter Monitor displays the filters currently selected.

f. On the window called Resolve3D (Figure 1).

g. Press on the gear wheel (setting) ⚙ to open Resolve3D setting window (Figure 2).

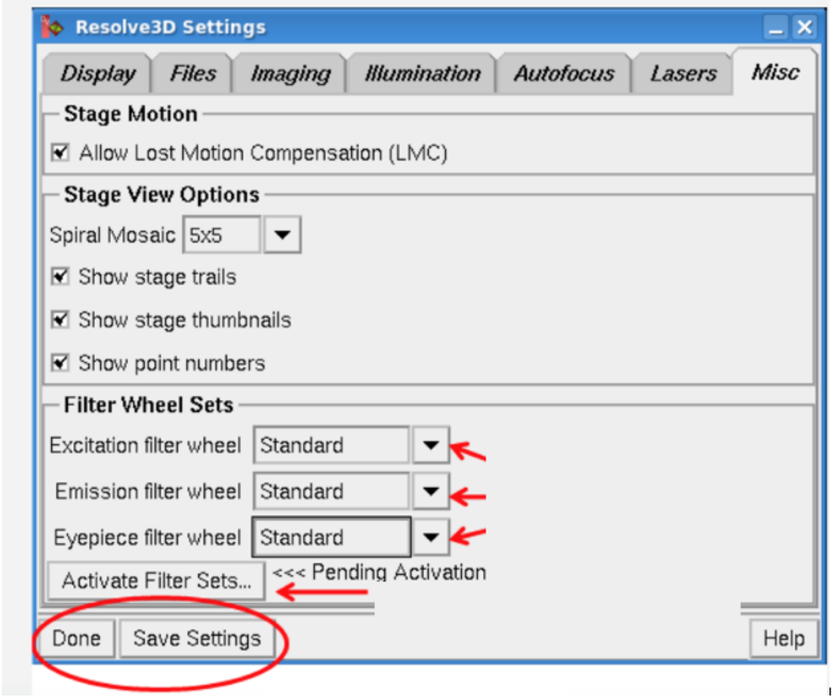

Stage Motion

☑ Allow Lost Motion Compensation (LMC)

Stage View Options

Spiral Mosaic 5x5

☑ Show stage trails

☑ Show stage thumbnails

☑ Show point numbers

Filter Wheel Sets

Excitation filter wheel Standard

Emission filter wheel Standard

Eyepiece filter wheel Standard

Activate Filter Sets... <<< Pending Activation

Figure 2. Resolve3D window setting

i. Under MISC.
ii. Select the filters.
iii. Save settings.
iv. Under FILES (Figure 3).

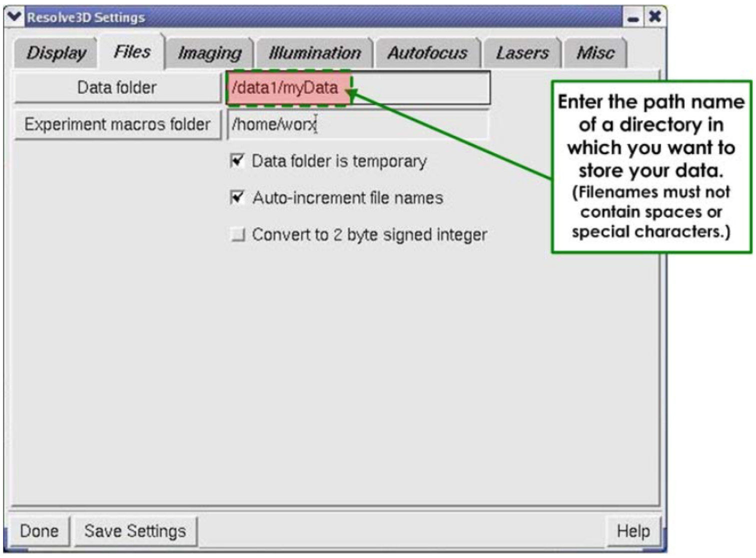

Data folder: /data1/myData
Experiment macros folder: /home/worx
☑ Data folder is temporary
☑ Auto-increment file names
☐ Convert to 2 byte signed integer

Enter the path name of a directory in which you want to store your data. (Filenames must not contain spaces or special characters.)

Figure 3. Display of the Files tab

v. In the Data folder field (Figure 3), enter the directory in which to save the image.
vi. In the Experiment macros folder field (Figure 3), enter the same directory.
vii. Save settings.
viii. Done.

h. In the Resolve3D window (Figure 1), set the following parameters in Figure 4.

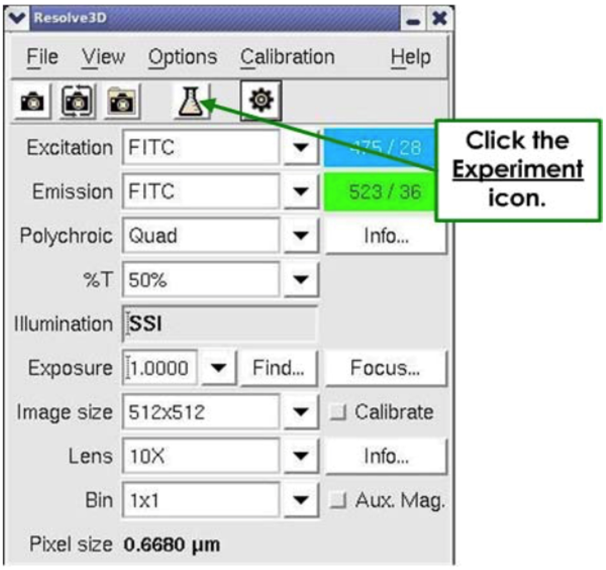

Excitation: FITC 475 / 28
Emission: FITC 523 / 36
Polychroic: Quad
%T: 50%
Illumination: SSI
Exposure: 1.0000
Image size: 512x512 ☐ Calibrate
Lens: 10X
Bin: 1x1 ☐ Aux. Mag.
Pixel size **0.6680 μm**

Click the Experiment icon.

Figure 4. Setting the parameters

    i. Excitation: POL.
    ii. Emission: POL.
    iii. % T: 32%.
    iv. Exposure: 0.025.
    v. Lens: 40x.
i. Press on the Erlenmeyer.
j. A window called Design/Run Experiment window will be opened (Figure 5).

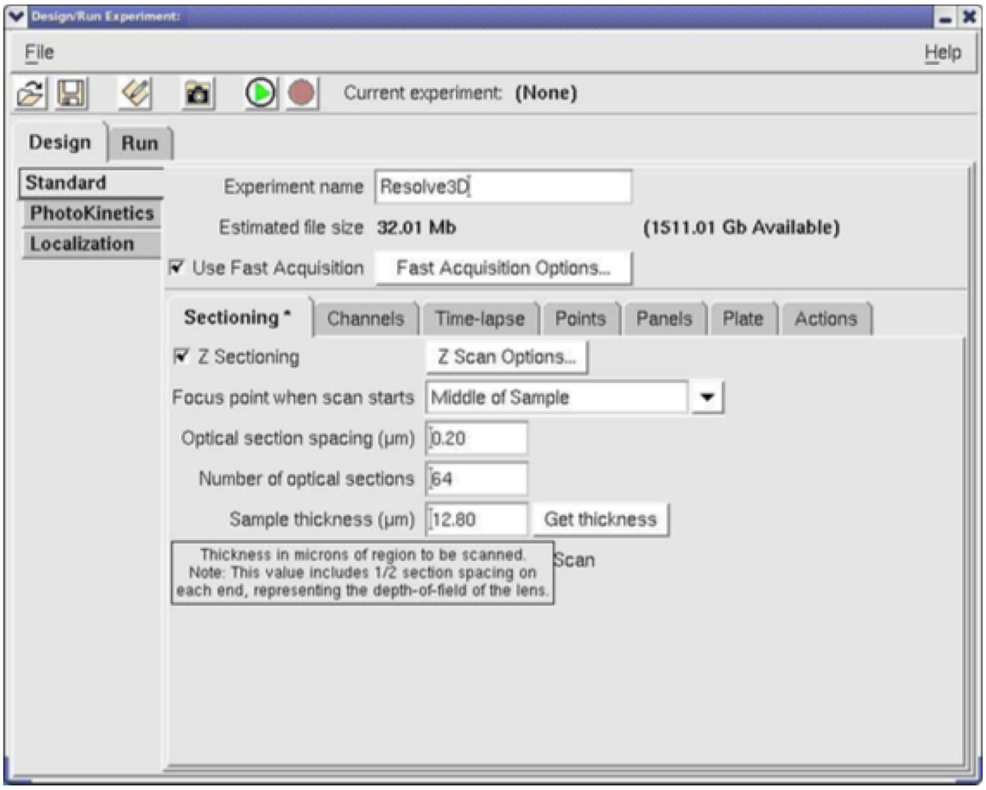

Current experiment: (None)

Experiment name: Resolve3D

Estimated file size: 32.01 Mb (1511.01 Gb Available)

☑ Use Fast Acquisition

☑ Z Sectioning

Focus point when scan starts: Middle of Sample

Optical section spacing (µm): 0.20

Number of optical sections: 64

Sample thickness (µm): 12.80

Thickness in microns of region to be scanned. Note: This value includes 1/2 section spacing on each end, representing the depth-of-field of the lens.

Figure 5. Design and Run experiment window

    i. Under design
        1) Experimental name field: write your file name (Figure 5).
        2) Under Sectioning
           Remove the check beside the Z sectioning.
        3) Under channels (Figure 5).

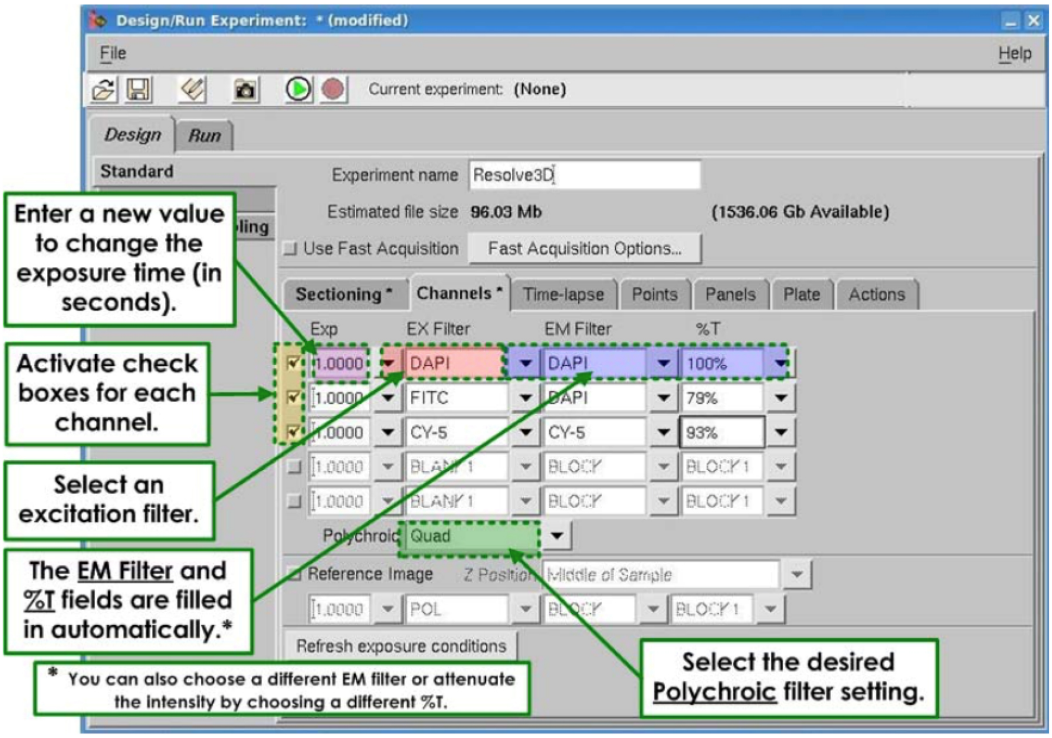

Current experiment: (None)

Experiment name: Resolve3D

Estimated file size 96.03 Mb (1536.06 Gb Available)

☐ Use Fast Acquisition

	Exp	EX Filter	EM Filter	%T
☑	1.0000	DAPI	DAPI	100%
☑	1.0000	FITC	DAPI	79%
☑	1.0000	CY-5	CY-5	93%
☐	1.0000	BLANK 1	BLOCK	BLOCK 1
☐	1.0000	BLANK 1	BLOCK	BLOCK 1

Polychroic: Quad

☐ Reference Image Z Position: Middle of Sample

1.0000 POL BLOCK BLOCK 1

Enter a new value to change the exposure time (in seconds).

Activate check boxes for each channel.

Select an excitation filter.

The EM Filter and %T fields are filled in automatically.*

* You can also choose a different EM filter or attenuate the intensity by choosing a different %T.

Select the desired Polychroic filter setting.

Figure 6. The Channels in the Design and Run experiment window

Check 1st box (Figure 6)

Under EX filter: POL

Automatically EM filter will be modifying

Under% T: choose 32%

Check 2nd box (Figure 6)

Under EX filter: FITC

Automatically EM filter will be modified

Under% T: choose100%

Check 3rd box (Figure 6)

Under EX filter: mCherry

Automatically EM filter will be modified

Under% T: choose 100%

ii. Under Run before starting to acquire image
Image file name field, write the same name you wrote under the design/Experimental name (Figure 5).

iii. Now you are ready to acquire image by pressing on the start button ▶ as shown in Figure 7. You can adjust the image by looking on the Resolve3D window which contains the stage trails in the stage View window. This way you can focus at the pharynx level.

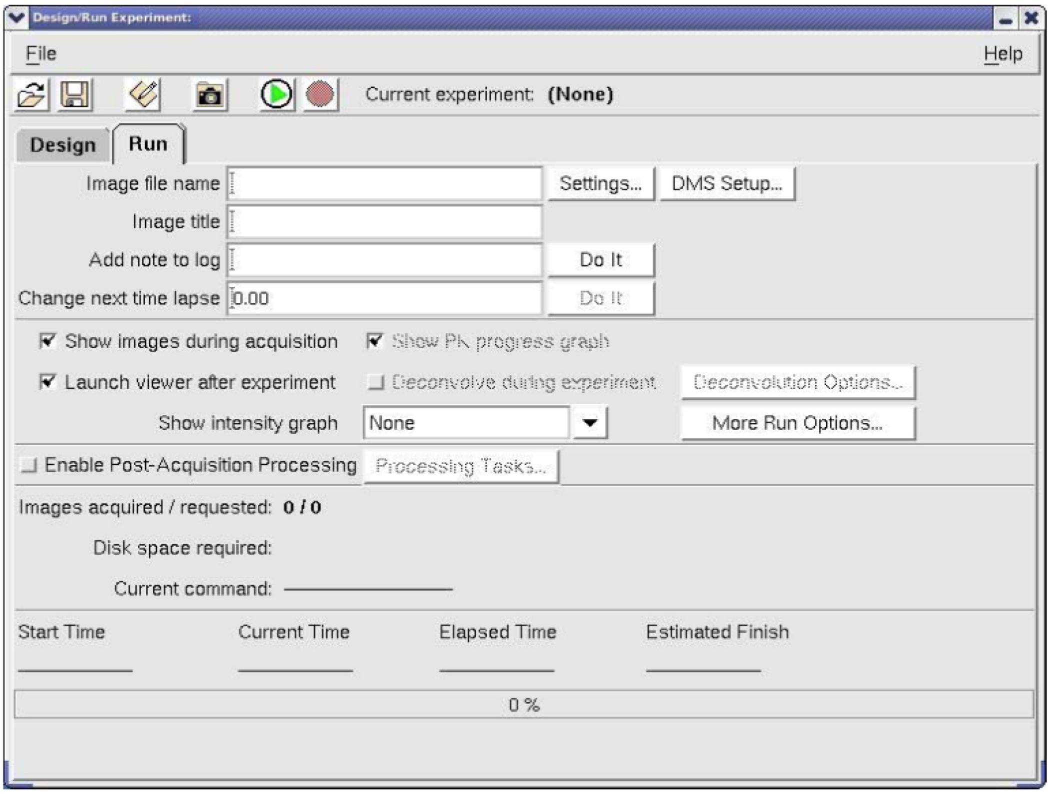

Current experiment: (None)

Image file name

Image title

Add note to log

Change next time lapse 0.00

☑ Show images during acquisition

☑ Show PK progress graph

☑ Launch viewer after experiment

☐ Deconvolve during experiment

Show intensity graph None

☐ Enable Post-Acquisition Processing

Images acquired / requested: 0 / 0

Disk space required:

Current command:

0 %

Figure 7. The start button in the Design and Run experiment window

4. Result analysis
   a. Software used: ImageJ
      i. Drag the file to imageJ window.
      ii. Under image → Transform → rotate the image to get an image of the worm placed anterior to posterior.
      iii. Under image → Stacks → Stack to images.
      iv. Under image → Color → merge channels.
      Select the image which is appropriate to the desired color.
      v. Create montage: under image → Stacks → make montage.
      vi. Create the 3D picture based on the intensity.
      Take the merged image.
      Under Plugins → 3D → Interactive 3D surface plot.

Data analysis

The result is representative of a single worm from an experiment where 10 worms were placed onto the slide (Figure 8). The experiment was repeated three times with identical data. Fluorescence posterior to the pharynx is autofluorescence detected from the intestine (Figure 8). The data were quantified using ImageJ according to Papaluca and Ramotar (2016).

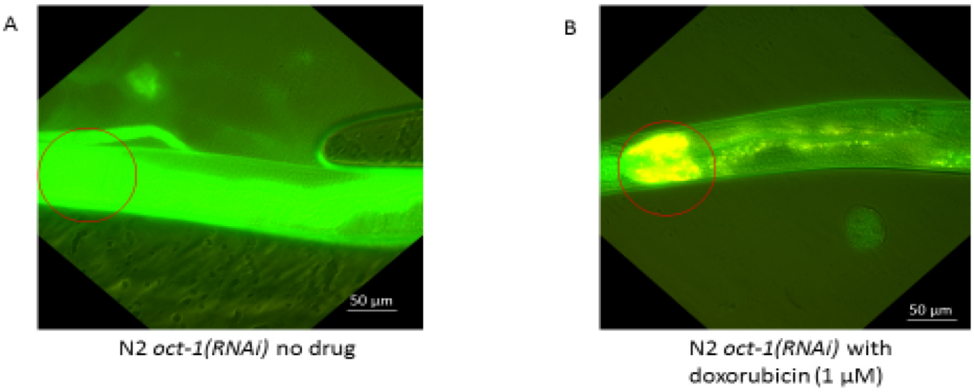

Figure 8. Uptake of doxorubicin in the N2 wild type animals downregulated for *oct-1* that causes upregulation of OCT-2. Previously, we showed that downregulation stimulated expression of *oct-2*, which drives uptake of drugs into *C. elegans* (Papaluca and Ramotar, 2016). A. Untreated; the absence of doxorubicin is illustrated by the lack of yellow fluorescence and the green background is autofluorescence from ingestion of food by the animal. B. Treated with doxorubicin (1 µM). Doxorubicin uptake is visible as yellow due to the merge of the green autofluorescence and red fluorescence from the drug. Circles show the location of the pharynx. Scale bars = 50 µm. See Data analysis for additional details.

Notes

1. Instead of using frozen bacteria as worm food, we typically use fresh culture of the bacteria.
2. Always work under sterile conditions. Be on the watch for fungus (white to black like spider net) and rarely mushroom (brownish spots). If this is the case, the best solution will be to bleach the worms and collect the eggs for new larvae.

Recipes

1. LB solution
   5 g tryptone
   2.5 g yeast extract
   5 g NaCl
   ddH$_2$O up to 500 ml
   Add 7.5 g of agar, if making solid media plates
2. Nematode growth media (NGM)
   1.25 g peptone
   1.5 g NaCl
   8.75 g agar
   ddH$_2$O up to 500 ml
   Autoclave

When the media is between 50 to 55 °C, add the following constituents before pouring the plates:
12.5 ml of 1 M KH_2PO_4 pH 6
500 µl of 1 M $MgSO_4$
500 µl of 1 M $CaCl_2$
500 µl cholesterol (stock 5 mg/ml in 95% ethanol)
500 µl of ampicillin (stock 100 mg/ml), if using the plasmid containing bacteria $HT115^{DE3}$

3. Agar pad
   3% agarose in MIlliQ water
   Melt when needed
4. Alkaline hypochlorite solution (bleaching solution) (make fresh monthly)
   8.25 ml ddH_2O
   3.75 ml 1 N NaOH
   3.00 ml Bleach (Javel)
5. M9 buffer (1 L)
   6 g Na_2HPO_4
   3 g KH_2PO_4
   5 g NaCl
   0.25 g $MgSO_4 \cdot 7H_2O$
   Sterilized by autoclaving

Acknowledgments

This work was funded by the research grant (RGPIN/202432-2012) to D.R. from the Natural Science and Engineering Research Council of Canada. A brief version of this protocol was previously described (Papaluca and Ramotar, 2016).

References

1. Burns, A. R., Wallace, I. M., Wildenhain, J., Tyers, M., Giaever, G., Bader, G. D., Nislow, C., Cutler, S. R. and Roy, P. J. (2010). A predictive model for drug bioaccumulation and bioactivity in *Caenorhabditis elegans*. *Nat Chem Biol* 6(7): 549-557.
2. Cesar-Razquin, A., Snijder, B., Frappier-Brinton, T., Isserlin, R., Gyimesi, G., Bai, X., Reithmeier, R. A., Hepworth, D., Hediger, M. A., Edwards, A. M. and Superti-Furga, G. (2015). A call for systematic research on solute carriers. *Cell* 162(3): 478-487.
3. Cheah, I. K., Ong, R. L., Gruber, J., Yew, T. S., Ng, L. F., Chen, C. B. and Halliwell, B. (2013). Knockout of a putative ergothioneine transporter in *Caenorhabditis elegans* decreases lifespan and increases susceptibility to oxidative damage. *Free Radic Res* 47(12): 1036-1045.
4. GE Healthcare (2014). DeltaVision Imaging System User's Manual. PN 29087880 AB.

5. O'Reilly, L. P., Luke, C. J., Perlmutter, D. H., Silverman, G. A. and Pak, S. C. (2014). *C. elegans* in high-throughput drug discovery. *Adv Drug Deliv Rev* 69-70: 247-253.
6. Papaluca, A. and Ramotar, D. (2016). A novel approach using *C. elegans* DNA damage-induced apoptosis to characterize the dynamics of uptake transporters for therapeutic drug discoveries. *Sci Rep* 6: 36026.
7. Wu, X., Fei, Y. J., Huang, W., Chancy, C., Leibach, F. H. and Ganapathy, V. (1999). Identity of the *F52F12.1* gene product in *Caenorhabditis elegans* as an organic cation transporter. *Biochim Biophys Acta* 1418(1): 239-244.

www.nature.com/scientificreports

SCIENTIFIC REPORTS

OPEN

Peroxiredoxin 1 interacts with and blocks the redox factor APE1 from activating interleukin-8 expression

Received: 28 October 2015
Accepted: 20 June 2016
Published: 08 July 2016

Hassan Nassour[1,*], Zhiqiang Wang[1,*,†], Amine Saad[2], Arturo Papaluca[1], Nicolas Brosseau[1], El Bachir Affar[1], Moulay A. Alaoui-Jamali[2] & Dindial Ramotar[1]

APE1 is an essential DNA repair protein that also possesses the ability to regulate transcription. It has a unique cysteine residue C65, which maintains the reduce state of several transcriptional activators such as NF-κB. How APE1 is being recruited to execute the various biological functions remains unknown. Herein, we show that APE1 interacts with a novel partner PRDX1, a peroxidase that can also prevent oxidative damage to proteins by serving as a chaperone. PRDX1 knockdown did not interfere with APE1 expression level or its DNA repair activities. However, PRDX1 knockdown greatly facilitates APE1 detection within the nucleus by indirect immunofluorescence analysis, even though APE1 level was unchanged. The loss of APE1 interaction with PRDX1 promotes APE1 redox function to activate binding of the transcription factor NF-κB onto the promoter of a target gene, the proinflammatory chemokine IL-8 involved in cancer invasion and metastasis, resulting in its upregulation. Depletion of APE1 blocked the upregulation of IL-8 in the PRDX1 knockdown cells. Our findings suggest that the interaction of PRDX1 with APE1 represents a novel anti-inflammatory function of PRDX1, whereby the association safeguards APE1 from reducing transcription factors and activating superfluous gene expression, which otherwise could trigger cancer invasion and metastasis.

Apurinic/apyrimidinic (AP) endonuclease1/redox factor-1 (APE1/Ref-1) is a multifunctional protein involved in the base excision repair (BER) of damaged DNA, as well as in transcriptional regulation[1]. These functions reside within distinct domains of the protein (Fig. 1a). APE1 hydrolyzes the 5′-phosphodiester bond at AP sites and removes a variety of blocked 3′ termini at DNA strand breaks with the aid of an AP endonuclease, 3′-diesterase and 3′- to 5′-exonuclease in order to facilitate DNA repair synthesis[1–4]. Besides its DNA repair activities, APE1 directly or indirectly regulates transcription[1]. For example, APE1 can form a complex with p300 and bind to the calcium responsive elements to suppress gene expression[5]. Furthermore, APE1 can influence the DNA binding activity of various transcription factors such as AP-1[6], NF-κB[7], Myb[8], p53[9], hypoxia inducible factor-1[10] and Pax proteins[11] via its redox cysteine residue C65 by reducing these transcription factors to ensuring their binding onto the promoter of target genes. A recent study has also shown that APE1 can negatively regulate the function of the nuclear factor erythroid-related factor 2 (NRF2), which plays a role in the defense against oxidative stress[12]. Inhibition of the redox function of APE1 potently activates NRF2 target genes, but in a manner that is independent of the production of reactive oxygen species (ROS)[12].

In order for APE1 to execute its role in DNA repair and gene regulation, there must be regulatory mechanisms that switch on/off- and fine-tune the different APE1 activities and these include (i) alteration in APE1 redox state[13], (ii) translocation of APE1 from the cytoplasm to the nucleus[14], and (iii) modulation of APE1 by post-translational modification (PTMs)[5,15,16] and proteolytic cleavage of the N-terminal 33 amino acid domain[17]. Besides these mechanisms, APE1 is known to exist in complexes with other proteins and thus modulation of its partners within the interactome could also influence APE1 function. Approximately thirty proteins have been discovered to interact with APE1 using different approaches, however, the functional implications of APE1 interaction with each individual protein partner is still not known[18,19]. So far, a single tag, such as HA fused to APE1,

[1]Maisonneuve-Rosemont Hospital, Research Center, Université de Montréal, Department of Medicine, 5415 Boul. de l'Assomption, Montréal, Québec, H1T 2M4, Canada. [2]Segal Cancer Centre and Lady Davis Institute for Medical Research, Sir Mortimer B. Davis-Jewish General Hospital, 3755 Cote Ste-Catherine Road, Montréal, Québec, H3T 1E2, Canada. *These authors contributed equally to this work. †Present address: Johns Hopkins University, Department of Pediatrics, Baltimore, USA. Correspondence and requests for materials should be addressed to D.R. (email: dindial.ramotar@umontreal.ca)

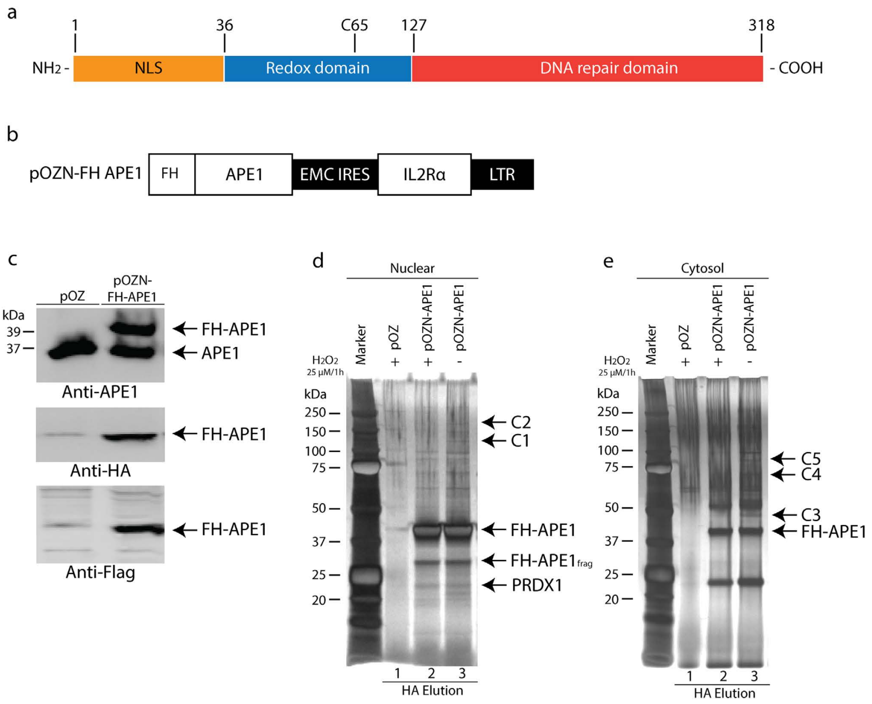

Figure 1. Structural features of APE1 and expression of the tagged form, FH-APE1, used for the complex purification from HeLaS cells. (**a**) Illustration of the structural domains of APE1. (**b**) Schematic representation of FH-APE1 construct in which IL2Rα is used for selection. (**c**) Western blot analysis validating the ectopic FH-APE1 expression. HeLaS cells were infected with retroviruses containing either the empty vector pOZ or the plasmid pOZN-FH-APE1, followed by three rounds of selection with anti-IL2Rα magnetic beads and positive cells were expanded. Total cell extracts were analyzed by Western blot probed with monoclonal anti-APE1, anti-FLAG and anti-HA respectively. (**d**,**e**) APE1 complex following purification from nuclear and cytosolic extracts, respectively. HeLaS cells expressing FH-APE1 were untreated or treated with 25 μM H_2O_2 for 1 h, while the HeLaS cells containing empty vector pOZ were only treated with 25 μM H_2O_2 for 1 h and serve as negative control for subsequent immunoprecipitation. The cells were harvested and the nuclear and cytosolic fractions were subjected to tandem immunoprecipitation with anti-FLAG followed by anti-HA resins. APE1 complex were finally eluted by HA peptides and separated on 4 to 12% gradient SDS-PAGE gels followed by silver staining. Pooled eluates were subjected to mass spectrometry to identify all the proteins forming part of the APE1 interactome. C1 and C2, and C3 to C5, indicate polypeptide bands that disappeared from the nuclear and cytosolic APE1 complex, respectively, in response to the H_2O_2 treatment. FH-APE1$_{frag}$ denotes a proteolytic form of FH-APE1. The data are representative of two independent complex purifications.

has been used to identify APE1 interacting partners[18]. The disadvantage of the single tag approach is that it brings along some non-specific proteins. Moreover, most of the studies performed to identify proteins that interact with APE1 were done under physiological conditions. In this study, we used a stringent tandem affinity approach to investigate the APE1 interactome under physiological conditions and when the cells were challenged with the oxidant hydrogen peroxide (H_2O_2). Herein, we discovered a novel APE1 interacting partner, PRDX1, which is a member of the peroxiredoxin family that acts as a peroxidase as well as serving as a chaperone to protect proteins from oxidative damage. PRDX1 interacted with APE1 under physiological conditions, both in the nucleus and cytosol. We show that shRNA knockdown of PRDX1 has no effect on APE1 expression level or its DNA repair activities. However, indirect immunofluorescence revealed that the knockdown of PRDX1 amplified the detection of APE1 in the nucleus, even though APE1 level was not altered. While this observation is consistent with APE1-PRDX1 association *in vivo*, it raises the possibility that PRDX1 might influence the transcriptional function of APE1. Indeed, we show that PRDX1 knockdown enhanced APE1 redox activity, and which acts via the transcription factor NF-κB to turn on expression of the proinflammatory chemokine interleukin-8 (IL-8) that has been shown to play a role in cancer invasion and metastasis[20,21]. In view of the regulatory role of APE1-PRDX1 interaction, we propose that PRDX1 through its association with APE1 keeps a check on APE1 redox activity from reducing and activating the transcription factor NF-κB, and thereby prevents superfluous gene expression of IL-8. To the best of our knowledge, our study is the first to demonstrate a novel role of PRDX1 as an anti-inflammatory protein that functions by blocking APE1 from activating IL-8.

Results

Expression and purification of APE1 interacting complex from HeLaS cells.

Previously, a single affinity tag was used to explore APE1 interacting partners from total cell extracts[22]. In this work, we examined the APE1 interacting partners under more stringent purification conditions by employing two affinity purification tags, FLAG and HA. In addition, we used this approach to determine whether the APE1 interactome would be influenced upon exposing cells to oxidative stress caused by the oxidant H_2O_2. We created stable HeLaS cell lines expressing a N-terminal FLAG-HA tagged APE1 from the pOZ vector (Fig. 1b) (referred herein as FH-APE1)[23]. The ectopic expression of FH-APE1 in HeLaS was validated by Western blot probed with three different antibodies, anti-APE1, anti-HA and anti-FLAG (Fig. 1c). The pOZ vector expressed FH-APE1 with the expected molecular weight of 39 kDa and to nearly the same level as the endogenous APE1 (37 kDa)(upper panel Fig. 1c).

We used this expression system to examine the proteins associated with FH-APE1 in nuclear and cytosolic extracts of the HeLaS cells. The FH-APE1 complex from nuclear extracts was purified by tandem affinity purification using anti-FLAG and -HA resins. The final HA elutions were concentrated by trichloroacetic acid (TCA) and an aliquot analyzed by SDS-PAGE that was stained with silver (Fig. 1d). Instead of isolating individual bands from the SDS-PAGE, the entire HA eluate was subjected to mass spectrometry in order to identify all the proteins. HA eluate from nuclear extract carrying the pOZ empty vector was used as a control. This stringent approach identified only five proteins (APE1, LMNA, NPM1, PRDX1 and RPS19) from the nuclear fraction and each protein was considered a hit after setting a limit for three unique peptides (Fig. 1d and Supplementary Table S2). Amongst these proteins only NPM1 was previously reported to interact with APE1 using a single affinity purification[18]. LMNA, PRDX1 and RPS19 were found for the first time to be part of the APE1 interactome. In fact, the STRING database of known and predicted protein interactions suggested a connection between NPM1 and PRDX1 on the basis that PRDX1 interacts with some of the same proteins found to interact with FH-APE1 (Supplementary Fig. S1A)[24].

The same approach was used to identify FH-APE1 complex in the cytosol (Fig. 1e). FH-APE1 was found to interact with 14 proteins (Supplementary Fig. S1b and Supplementary Table S2) and four of these PRDX1, PDIA6, PRDX2, PRDX3 are known to play a direct role in mitigating oxidative stress[25–28] (Supplementary Table S2). In fact, the STRING database suggested a connection between HSP90AB1 and APE1 on the basis that HSP90AB1 interacts with partners of FH-APE1 (Supplementary Fig. S1b)[24]. These findings suggest that APE1 forms distinct complexes in the nucleus and the cytoplasm and it appears that in the cytosol APE1 forms complexes with proteins that are involved in oxidative stress responses.

APE1 interactome changes upon treatment with H_2O_2.

We next examined whether APE1 interaction with its partners could be influenced by oxidative stress. The HeLaS cells expressing FH-APE1 were untreated and treated with H_2O_2 and the proteins associated with APE1 in the nucleus were determined by mass spectrometry. Upon treatment with a very mild dose of H_2O_2 (25 μM for 1 h), that killed less than 7% of the cells, there was no major change in the affinity purified complex, except for at least two polypeptides indicated as C1 and C2 that were diminished (Fig. 1d). However, using four fold higher concentration (100 μM for 1 h) resulted in decreased cell viability by 40%, with concomitant loss of all the nuclear APE1 interacting partners, with the exception of LMNA.

We used the same approach to examine the potential APE1 interacting partners in the cytosol upon H_2O_2 treatment. There was a decrease in the number of proteins that were associated with APE1 under the H_2O_2 treatment condition (25 μM for 1 h) and denoted as C3, C4 and C5, as compared to the untreated counterpart (Fig. 1e, lane 3 vs. 2). The oxidative stress did not interfere with some of the APE1 interactions, such as PRDX1 and PDIA6 that co-existed with APE1 under physiological conditions, but other interactions were lost and some new ones appeared (Supplementary Fig. S1b vs. S1c, Supplementary Table S2). At least nine new interactions with APE1 were detected in the cytosol following the H_2O_2 treatment (25 μM for 1 h) (Supplementary Fig. S1c). Importantly, H_2O_2 treatment preserved the interaction of APE1 with proteins involved in oxidative stress responses such as PRDX1, PDIA6, as well as gained an interaction with PRDX6 (Supplementary Fig. S1b vs. S1c). These data suggest that APE1 interaction with its partners can be regulated by oxidative stress.

Validation of interaction between APE1 and PRDX1.

Under physiological conditions, PRDX1 was the only common partner that existed with APE1 in both the nucleus and the cytosol. PRDX1 has been documented to function as an antioxidant enzyme that scavenges H_2O_2[29,30]. PRDX1 thus protects proteins, lipids, and hormone receptors from oxidation-induced inactivation and inhibits tumorigenesis[31,32]. Recent studies demonstrated that mice deficient in PRDX1 caused tissue specific loss of heterozygosity implying that PRDX1 may be involved in maintaining genomic stability perhaps through its interaction with APE1[33]. To test whether APE1 and PRDX1 indeed belong to a complex, we carried out co-immunoprecipitation experiments with anti-FLAG resin using total protein extracts derived from HeLaS cells carrying either the empty pOZ vector as control or pOZN-FH-APE1 under conditions where the cells were untreated or treated with H_2O_2 (25 μM for 1 h). The anti-FLAG antibodies pull down PRDX1 from total extracts expressing FH-APE1, but not from extracts carrying the empty vector (Fig. 2a). The co-immunoprecipitation of PRDX1 with FH-APE1 was not affected when the cells were treated with the low concentration of H_2O_2 (Fig. 2a), consistent with the mass spectrometry data.

We conducted the reciprocal experiment by using protein A magnetic beads attached with anti-PRDX1 monoclonal antibodies to immunoprecipitate PRDX1 from nuclear extract derived from HeLa cells and examined for the pull down of APE1. The nuclear extract contained the monomeric PRDX1 (22 kDa), the dimeric form (44 kDa) and perhaps a weaker high molecular weight form (~60 kDa, shown by an asterisk) (Fig. 2b, lane 3), as detected by anti-PRDX1. In addition, the nuclear extract contained the native APE1 (37 kDa), a fragment of APE1 ($APE1_{frag}$ ~32 kDa) and a higher molecular weight form (~60 kDa, shown by an asterisk) (Fig. 2b, lane 6), as detected by anti-APE1. The anti-PRDX1 magnetic beads pulled down the monomeric PRDX1, but not the dimeric form of PRDX1 or the weak 60 kDa polypeptide, as detected by the anti-PRDX1 antibodies (Fig. 2b, lane 2). The additional bands present in lane 2 were the light and heavy chains of the anti-PRDX1 antibodies, as confirmed by loading only a small amount of anti-PRDX1 on the gel (lane 1). Importantly, the anti-PRDX1 magnetic beads pulled down only the native APE1 (the 37 kDa band in lane 5), and not the $APE1_{frag}$ (~32 kDa)

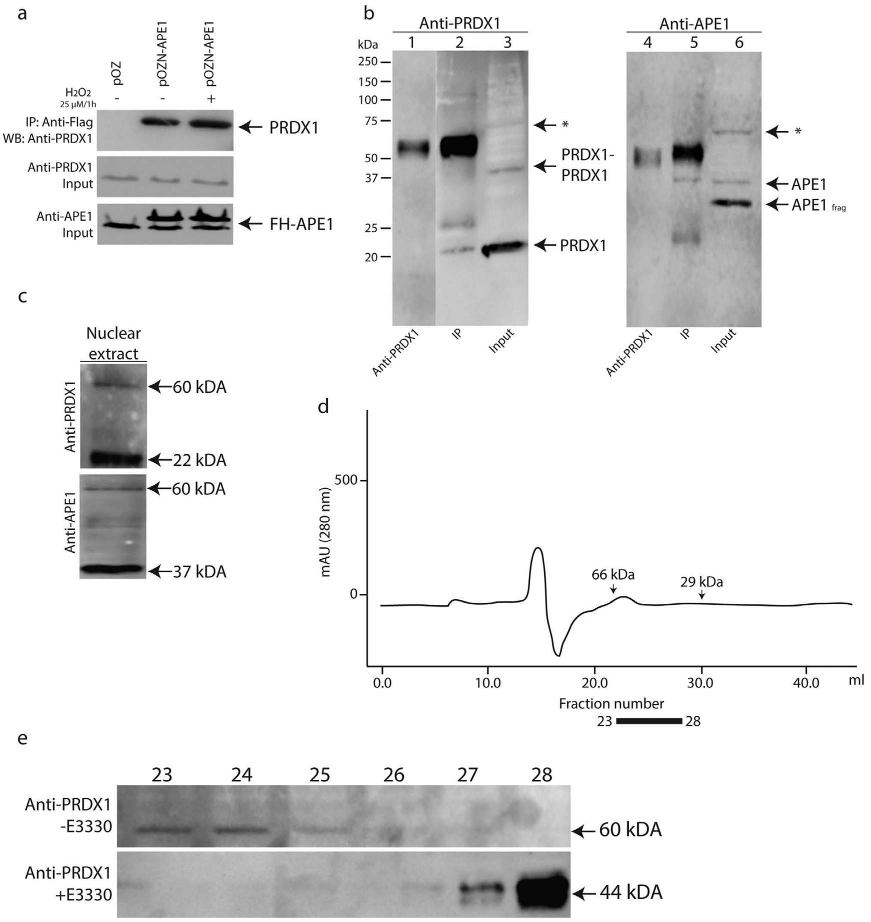

Figure 2. Validation of APE1-Prdx1 interaction. (**a**) FH-APE1 pulled down Prdx1 during immunoprecipitation. HeLaS cells expressing FH-APE1 were untreated or treated with 25 μM H_2O_2 for 1 h, while the control HeLaS cells containing empty vector pOZ were untreated, and total cell extracts were subjected to immunoprecipitation with anti-FLAG resins. Eluates were separated by 10% SDS-PAGE and probed with monoclonal anti-PRDX1. (**b**) Reciprocal immunoprecipitation showing that PRDX1 pulls down APE1 from nuclear extract. Nuclear extract prepared from HeLa was subjected to immunoprecipitation with protein A magnetic beads bearing anti-PRDX1 antibodies. Lanes 2 and 5, immunoprecipitated proteins, lanes 3 and 6, the input nuclear extract, and lanes 1 and 4, each contained 0.5 μg of anti-PRDX1 antibodies alone. Following 10% SDS-PAGE for immunoblot analysis, lanes 1 to 3 were probed with anti-PRDX1 antibodies and lanes 4 to 6 with anti-APE1 antibodies. The arrows marked by an asterisk indicate a similar size polypeptide ~60 kDa detected by either anti-PRDX1 or anti-APE1 antibodies. (**c**) Detection of a 60 kDa polypeptide by either anti-PRDX1 or anti-APE1 antibodies in nuclear extract. Nuclear extract from HeLa cells prepared in the present of the thiol blocking agent methyl methanethiosulfonate (MMTS) was subjected to Western blot analysis probed with either anti-PRDX1 or anti-APE1 antibodies. (**d**) Analysis of APEX1-PRDX1 conjugate by fast protein liquid chromatography (FPLC). HeLa cells were untreated or treated with E3330 and the nuclear extract was loaded on superose^{TM} 6 FPLC column eluted with buffer A at flow rate of 0.25 ml/min. All eluents were collected at 0.5 ml/fraction, and each eluent fraction was concentrated by Amicon Ultra followed by Western blot analysis with 10% SDS PAGE. (**e**) The APE1 specific inhibitor E3330 prevents the appearance of the 60 kDa polypeptide and causes the accumulation of the dimeric PRDX1. Eluent fractions 23 to 28 from E3330 untreated and treated cells were probed with monoclonal anti-PRDX1. Fractions 23 and 24 contained the 60 kDa polypeptide from E3330 untreated cells, while fraction 28 contained the dimeric PRDX1 (44 kDa) from E3330 treated cells. The data are representative of two or three independent experiments.

or the ~60 kDa form, as detected by anti-APE1 antibodies (Fig. 2b, lane 5), consistent with APE1 interacting with PRDX1.

To further validate the interaction between APE1 and PRDX1, we examined for formation of APE1-PRDX1 conjugates *in vivo* by preparing nuclear extract in the presence of the thiol blocking agent methyl methanethiosulfonate (MMTS) to prevent reversal of the complex and subjecting the extract to gel filtration chromatography using FPLC. Under this condition, the nuclear extract contained a prominent 60 kDa polypeptide that was detected by both anti-APE1 and anti-PRDX1 antibodies (Fig. 2c), suggesting that the polypeptide contains both APE1 and PRDX1. Upon gel filtration analysis, the 60 kDa polypeptide co-eluted with the molecular weight standard albumin (66 kDa) and eluted in fractions 23 and 24 (Fig. 2d,e). Treatment of the cells with

(E)-3-[2-(5,6-dimethoxy-3-methyl-1,4-benzoquinonyl)]-2-nonyl propenoic acid (E3330), a specific inhibitor that inhibits the redox activity of APE1 through Cys-65, Cys-93 and Cys-99 oxidation[34,35], caused the disappearance of the 60 kDa polypeptide and the appearance of a very prominent 44 kDa protein, similar in size as the dimeric PRDX1, that was detected by anti-PRDX1 in fraction 28 (Fig. 2e). Taken together, these data are consistent with the immunoprecipitation results (Fig. 2a,b) that PRDX1 interacts with APE1 to form a heterodimeric complex of nearly 60 kDa in size. Moreover, our data further suggest that in the absence of APE1 redox function, PRDX1 may exist in the oxidized (44 kDa) dimeric form.

Prdx1 knockdown did not affect APE1 protein abundance or gene expression. To explore the role of PRDX1 on APE1 function, we knocked down PRDX1 in two different cell lines, HeLa and HepG2, via a retroviral system to express shRNA against PRDX1. Briefly, the shRNA-PRDX1 (shPRDX1) or its vector control LMP transfected cells were selected for one week in the presence of puromycin (0.5 ug/ml), harvested and examined for *PRDX1* gene expression level by quantitative qPCR and the protein level by Western blot analysis using anti-PRDX1 monoclonal antibody. Four shRNA that targeted different regions of *PRDX1*, all decreased *PRDX1* gene expression level and as well as the protein level by nearly 90% in the HeLa cells, as compared to the control LMP vector and where ACTβ was used as a control (Fig. 3a,b, respectively). One of these knockdowns, shPRDX1 C1-2 was chosen for the rest of the studies, and this construct was also effective in downregulating PRDX1 in another cell line, namely HepG2 (Supplementary Fig. S2a). While PRDX1 level was decreased in the shPRDX1 knockdown cells, the protein level of APE1 remain unchanged in these cells as determined by Western blot probed with anti-APE1 antibody (Fig. 3b and Supplementary Fig. S2a). Consistent with the Western blot analysis, *APE1* gene expression was also unaltered in the different shPRDX1 knockdown clones (Fig. 3c), indicating that PRDX1 is not involved in regulating the expression level of APE1.

Prdx1 knockdown enhances APE1 detection in the nucleus. Since PRDX1 was found associated with APE1 in both the cytosol and the nucleus, we checked whether PRDX1 knockdown would alter APE1 cellular distribution. We performed indirect immunofluorescence using a polyclonal antibody against APE1 and found that APE1 detection in the nucleus was much more intense in the shPRDX1 HeLa cells, as opposed to the control cells carrying the empty LMP vector (Fig. 3d). A similar result was obtained with monoclonal antibody against APE1 (Supplementary Fig. S3). For these experiments, we could not simultaneously monitor the detection of PRDX1 in the LMP control *versus* the shPRDX1 HeLa cells as there are no commercially available anti-PRDX1 antibodies suitable for immunofluorescence analysis.

To independently check that there was indeed enhanced detection of APE1 in the shPRDX1 HeLa cells, we monitored for APE1 signal in the LMP control and shPRDX1 HeLa cells by FACS Calibur using Alexa Fluor® 594 as the secondary antibody to detect anti-APE1. In the absence of the anti-APE1 antibodies, no APE1 signal was detected from any of the three cell lines HeLa alone, HeLa with the control LMP vector or shPRDX1 (Fig. 3e). When anti-APE1 was present, the APE1 signal was detected to the same extent in both the HeLa cells and the cells carrying the LMP vector (Fig. 3e). In contrast, the APE1 signal was greatly enhanced by nearly 5-fold in the shPRDX1 HeLa cells (Fig. 3e). Clearly, the result from the FACS analysis (Fig. 3e) is consistent with that from the immunofluorescence analysis (Fig. 3d).

To exclude the possibility that the increased detection of APE1 in the PRDX1 knockdown cells could be due to mobilization of undetected forms of APE1 within the cell that translocate to the nucleus, we examined the cytosolic and nuclear levels of APE1 in the control and PRDX1 knockdown cells. There was no major change in the level of the cytosolic and nuclear levels of APE1 in the PRDX1 knockdown cells as compared to the LMP vector control (Fig. 3f). Since the total amount of APE1 in the cells did not change (Fig. 3b) and there was no significant increase in the level of APE1 in the nucleus when PRDX1 was downregulated (Fig. 3f), then mobilization of APE1 from other cellular compartments to the nucleus cannot account for the greatly enhanced detection of nuclear APE1 in the PRDX1 knockdown cells (Fig. 3d,e). On the basis of these findings, we raised the possibility that PRDX1 association with APE1 *in vivo* may prevent anti-APE1 antibodies from properly recognizing the epitopes on APE1. While this interpretation is consistent with PRDX1 forming a complex with APE1, it also raises the possibility that PRDX1 could be involved in regulating APE1 function.

PRDX1 knockdown did not affect APE1 ability to repair damaged DNA. PRDX1 exists in the nucleus, but the majority of the protein is localized to the cytosol of cells[26]. The deficiency of PRDX1 has been shown to cause elevated levels of oxidative damage to the genome[33,36], and since APE1 is a key enzyme in the repair of these lesions, we tested whether shPRDX1 knockdown would impair the AP endonuclease function of APE1. In this experiment, we used a 42-mer double stranded oligonucleotide substrate containing a single uracil at position 21 that generates a 20-mer product following the action of uracil DNA glycosylase and cleavage of the resulting AP site by APE1[37]. Nuclear extracts prepared from HeLa cells did not show any significant differences in the level of AP endonuclease activity between the LMP control or when PRDX1 level was diminished by the shRNA (Fig. 4a,b lane 6 vs. 5). In a similar manner, we checked whether downregulating PRDX1 would have an effect on the AP endonuclease activity in cells with diminished levels of APE1. To test this, we first designed a system using the pSIREN-Zs-Green vector (LUC) to knockdown APE1 in the HeLa cells and then used the resulting clone shAPE1 (Fig. 4b, lane 3 vs.1) to downregulate PRDX1 using the LMP vector (Fig. 4b, lane 8 and 4). In these cells, the shRNA against APE1 downregulated APE1 level by nearly 75% (Fig. 4b, lane 3 or 4) and in the same cells the shRNA against PRDX1 downregulated PRDX1 by 80% (Fig. 4b, lane 8), as compared to the vector control (Fig. 4b, lanes 1 and 5). The assay revealed that shPRDX1 knockdown also did not further reduce the APE1 AP endonuclease activity in cells downregulated for APE1 (Fig. 4a), indicating that the diminished levels of PRDX1 has no effect at least on APE1 AP endonuclease activity. This finding was not specific to HeLa cells as

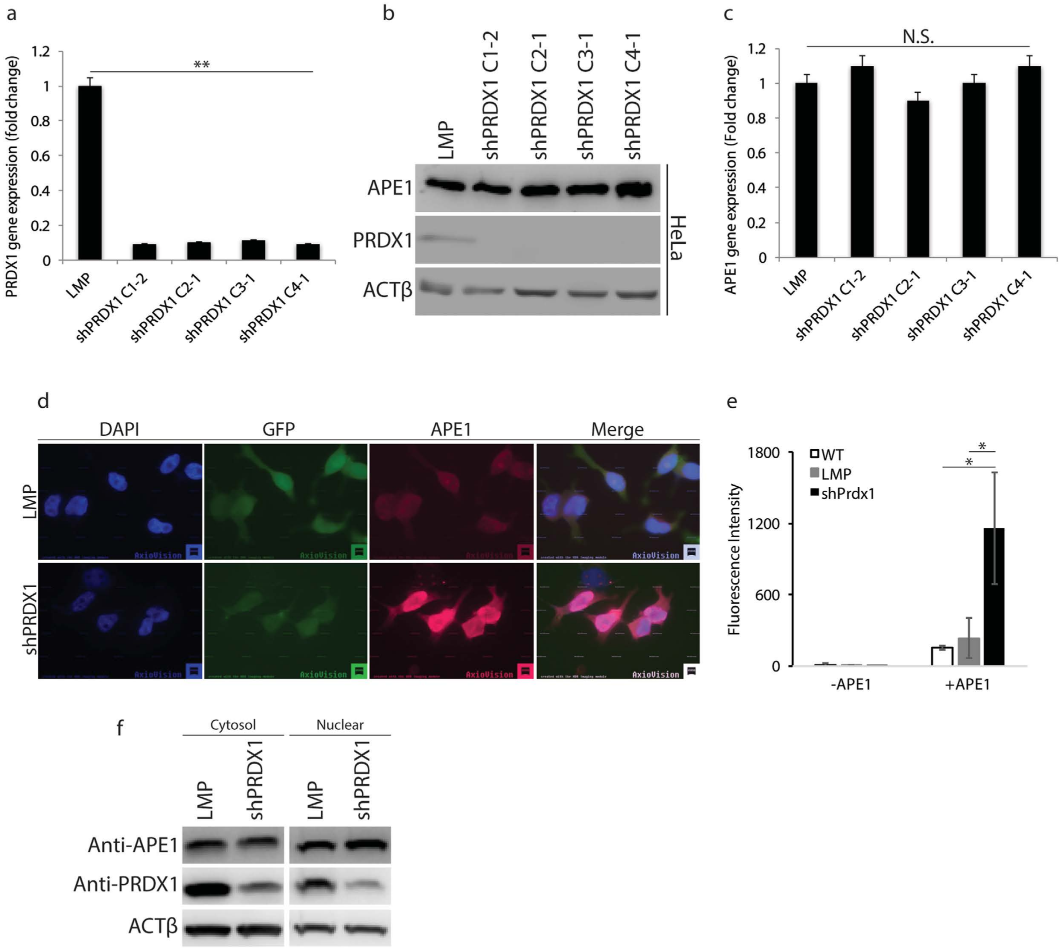

Figure 3. PRDX1 knockdown augments the detection of APE1 in the nucleus. Four different shRNA (C1-2, C2-1, C3-1, and C4-1) against PRDX1 and the LMP vector (control) packaged into retroviruses were used for infecting HeLa cells to create stable clones. After one week of selection with 0.5 µg/ml puromycin, the cells were analyzed for the expression levels of the indicated genes and proteins. (**a**) shPRDX1 downregulates *PRDX1* gene in HeLa cells. The expression of *PRDX1* was monitored by quantitative PCR analysis using total RNA isolated from HeLa cells carrying either the control LMP vector or the different shPRDX1 constructs. *PRDX1* expression was normalized to the *ACTβ* gene and the levels in the shPRDX1 knockdown cells were expressed as fold-change relative to the level in the LMP control, which was set at 1.0. (**b**) Western blot analysis showing APE1 and PRDX1 protein levels in the shPRDX1 knockdown HeLa cells. The Western blot was first probed with anti-PRDX1 antibodies and then for the levels of APE1 and *ACTβ* using anti-APE1 and anti-ACTβ antibodies, respectively. (**c**) Expression level of the *APE1* gene in the shPRDX1 knockdown cells. APE1 expression was monitored by qPCR as in panel **a**. (**d**) Indirect immunofluorescent analysis of HeLa-LMP and HeLa-shPRDX1 cells stained with polyclonal anti-APE1 antibodies. Images were captured with a Zeiss epifluorescent microscope using Cy5 and DAPI-UV filters at 67x magnification and processed with ImageJ. Merged images overlapped DAPI-stained nucleus (blue) with Cy5 staining of APE1 (red). FITC filter marks the cells expressing the GFP protein from the LMP vector. (**e**) Detection of APE1 by flow cytometry. The indicated cells were incubated without and with anti-APE1 antibodies and the APE1 signal was detected by Alexa Fluor® 594 with the FL2 (585/42) channel using FACS calibur. (**f**) APE1 subcellular distribution in the control and PRDX1 knockdown HeLa cells. APE1 and PRDX1 levels in the cytosol and nucleus of the indicated cells were determined with antibodies against APE1 and PRDX1 relative to the loading control ACTβ. The data are representative of two or three independent experiments.

similar results were obtained in HepG2 cells when PRDX1 was downregulated in the shAPE1 knockdown cells (Supplementary Fig. S2b–d).

Since PRDX1 can catalyze the detoxification of H_2O_2, we examined whether the downregulation of PRDX1 would sensitize cells to H_2O_2, and whether this would lead to increase damage to the genome requiring the 3′-repair diesterase function of APE1[4]. Interestingly, the downregulation of PRDX1 did not sensitize the HeLa cells (Fig. 4c), nor the HepG2 cells (Supplementary Fig. S2e), to increasing concentrations of H_2O_2. Likewise, the downregulation of PRDX1 did not further sensitize the shAPE1 knockdown HeLa cells when challenged with H_2O_2 (Fig. 4c). These findings exclude the possibility that PRDX1 plays a role in regulating APE1 DNA repair functions in processing H_2O_2-induced DNA lesions.

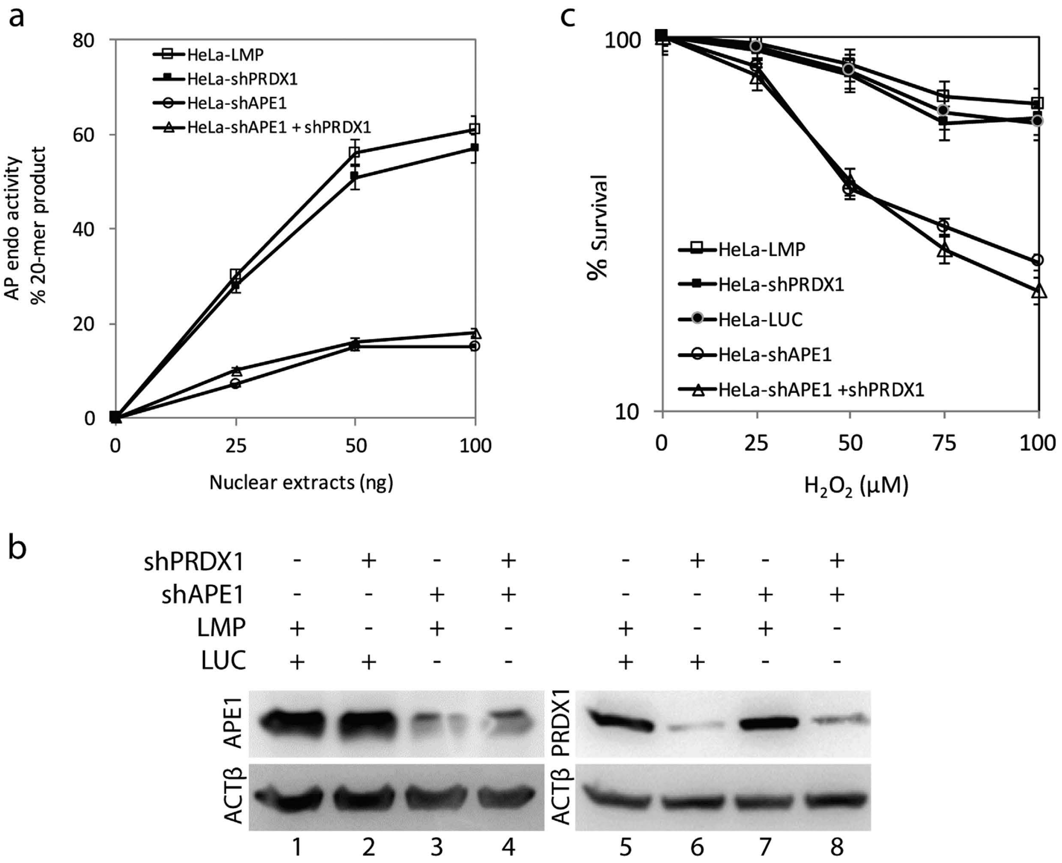

Figure 4. **PRDX1 knockdown did not interfere with APE1 ability to repair damaged DNA.** (**a**) Total nuclear extracts derived from the four indicated HeLa cell lines were assayed for APE1 AP endonuclease activity using a 42-mer double stranded oligonucleotide substrate carrying a centrally located AP site. Cleavage of the substrate produced a 20-mer product that was quantified and plotted against the concentration of the nuclear extracts. The AP endonuclease activity measurement is the average of two experiments. (**b**) Western blot showing that APE1 knockdown did not alter PRDX1 level or vice versa. Total cells extracts were prepared from the following cells HeLa carrying either the LUC or LMP control vector, shPRDX1, shAPE1, or both shPRDX1 and shAPE1 and probed by Western blot using antibodies against APE1 and PRDX1. Anti-ACTβ antibody was used to monitor equal loading of the total extracts. The data are representative of two independent experiments. (**c**) Survival of cells treated with increasing concentrations of H_2O_2. The HeLa cell lines carrying the empty vector LMP or Luc or knockdown for either PRDX1, APE1 or both were treated with H_2O_2 for 1 h and scored for survivors after 10 days using the clongenic assay. The data are the average of three independent analyses.

PRDX1 downregulation stimulates IL-8 expression that depends on APE1 level. A recent study documented that specific inhibition of the redox activity of APE1 by the inhibitor E3330 blocks TNF-α induced activation of the proinflammatory chemokine Interleukin-8 (IL-8) in HepG2 cells[38]. IL-8 can be regulated at the transcriptional level by several factors, including NF-κB, when cells encounter different stimuli such as chemical and environmental stresses[39]. Since APE1 can influence NF-κB-mediated gene expression, we examined whether disrupting PRDX1 interaction with APE1 would alter IL-8 production in the HeLa cells. Interestingly, when PRDX1 level was diminished, IL-8 secretion was stimulated by nearly 2-fold after 24 h of seeding the cells and analyzing the supernatant from the culture, as compared to the LMP control cells (Fig. 5a). This observation indicates that PRDX1 acts as a suppressor of IL-8 production in the cells.

We next tested if the stimulation of IL-8 production in the PRDX1 knockdown cells would depend on APE1 functional level. As such, we compared the level of IL-8 produced by the empty LMP vector cells, and by cells knockdown either for PRDX1, APE1 or both PRDX1 and APE1 (see Fig. 4b). Cells knockdown for APE1 displayed lower basal level of IL-8 production (Fig. 5a), consistent with the previous report that APE1 plays a role in IL-8 expression[38]. Importantly, the stimulated production of IL-8 caused by PRDX1 downregulation (Fig. 5a) was no longer observed in the cells that were also downregulated for APE1 (Fig. 5a). We interpret these data to indicate that PRDX1 association with APE1 may block APE1 redox function from turning on the transcription of IL-8.

The stimulated production of IL-8 following PRDX1 downregulation depends on NF-κB activation. Since NF-κB is reported to activate the expression of IL-8[40,41] and that APE1 can maintain this transcription factor in its active reduced state, we explored whether the mechanism by which the knockdown of PRDX1 led to

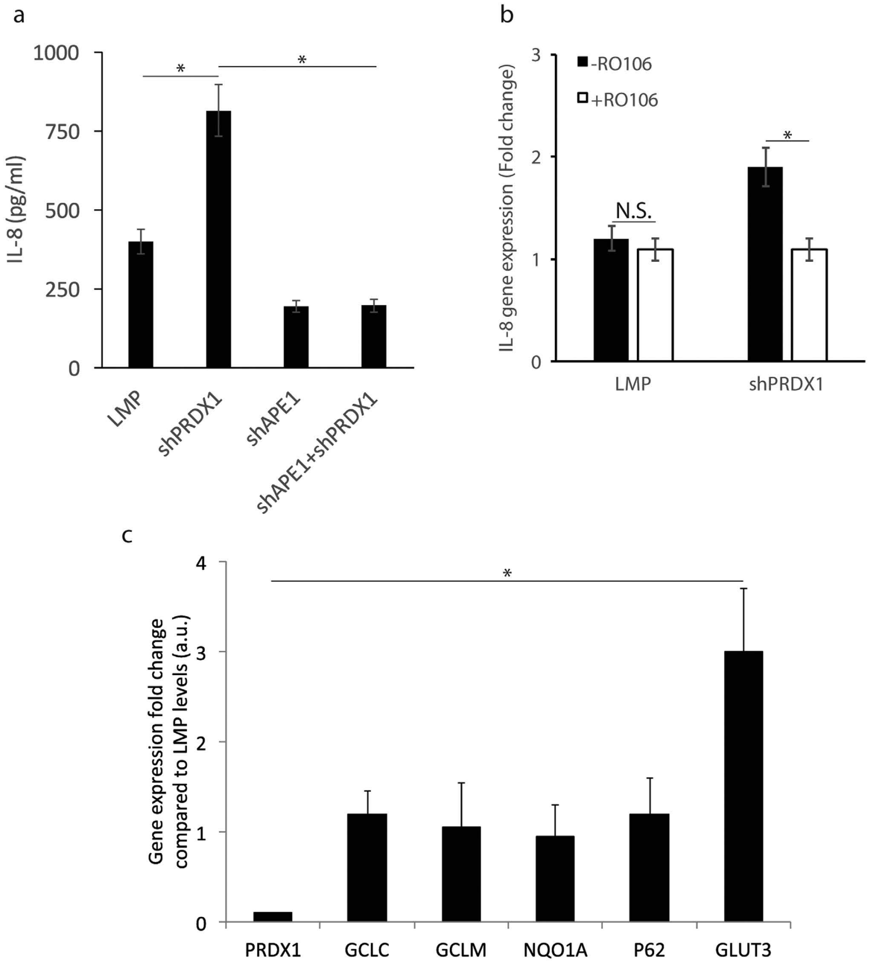

Figure 5. PRDX1 knockdown upregulates IL-8 in a manner requiring APE1 and NF-κB, but it has no effect on NRF2 targets. (**a**) PRDX1 knockdown induces IL-8 expression, but not in APE1 knockdown cells. The indicated HeLa cells were plated in 96-well plate at 15000 cells per well in duplicates in 200 μL complete DMEM with 10% FBS. The culture media was recovered and assay for IL-8 secretion using ELISA. The results are the averages of three independent experiments. (**b**) Inhibition of NF-κB activation prevents IL-8 gene induction in the PRDX1 knockdown cells. Total RNA was isolated from the HeLa cells carrying either the control LMP vector or shPRDX1 cells that were either untreated or treated with the NF-κB inhibitor RO106 (5 μM) and IL-8 gene expression was monitored by quantitative PCR analysis. The *ACTβ* gene was used for normalization. The results are the averages of two independent experiments. (**c**) NRF2 targets genes *GCLC*, *GCLM*, *NQO1A* and *P62* were unaffected in the PRDX1 knockdown cells. Total RNA was isolated from HeLa cells carrying either the control LMP vector or shPRDX1 cells and the expression of the indicated genes was monitored by quantitative PCR analysis. Gene expression was normalized to the *HPRT* gene and the levels in the shPRDX1 HeLa cells were expressed as fold-change relative to the levels in the LMP control, which was set at 1.0. The *GLUT3* gene was used as a positive control to monitor PRDX1 knockdown, as it was revealed to be highly inducible in these cells based on our microarray data. The results are the averages of two independent experiments.

the upregulation of IL-8 would involve NF-κB. To test this, we treated the LMP control and the corresponding shPRDX1 knockdown HeLa cells without and with the NF-κB inhibitor RO106 (5 μM), which inhibits IκBα ubiqutination, and thereby, prevents NF-κB translocation into the nucleus[42]. As shown in Fig. 5b, the NF-κB inhibitor blocked the activation of the *IL-8* gene in the cells knockdown for PRDX1 as quantified by the relative gene expression level using qPCR with ACTβ gene as the control. Thus, the mechanism by which PRDX1 knockdown stimulates *IL-8* gene expression requires NF-κB activation.

Besides positively regulating NF-κB, APE1 can also negatively influence the function of other transcription factors such as NRF2. The inhibition of APE1 redox activity has been shown to potently activate NRF2 target genes[12]. We checked whether PRDX1 knockdown would disrupt the redox state of APE1 and thus alter the expression levels of NRF2 targets. As shown in Fig. 5c, the shPRDX1 knockdown HeLa cells showed no significant changes in the expression levels of the established NRF2 target genes, such as *GLCC* and *GCLM*, relative to the levels from cells carrying the LMP control vector. In this analysis, the *GLUT3* gene, which we identified by microarray analysis to be negatively regulated by PRDX1, was used as a control to monitor its upregulation in the shPRDX1 knockdown cells (Fig. 5c, see discussion). Thus, even though downregulation of PRDX1 is known to

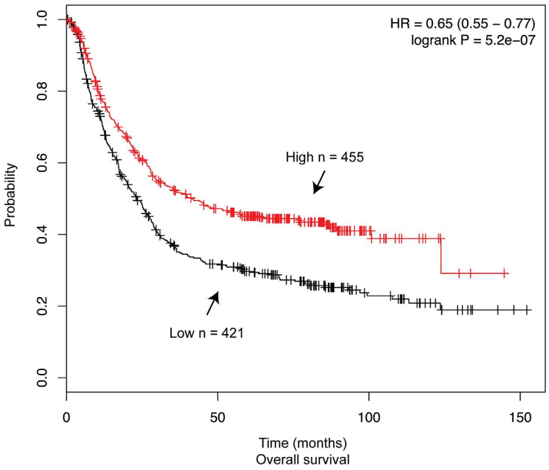

Figure 6. **Low *PRDX1* mRNA level is associated with poor overall survival of patients with gastric cancer.** Overall survival plot was generated online using the Kaplan-Meier Plotter based on signal intensity of the PRDX1 probe (208680_ at) in Affymetrix microarray gene expression data from gastric cancer patients of The Cancer Genome Atlas. Auto select best cut-off was chosen in the analysis and expression range of the probe was 2820–25698. A total of 876 patients were available and samples were split in two groups (high and low) according to the cutoff value. The hazard ratio with 95% confidence intervals and log rank *p* value was calculated.

increase the level of ROS in the cells[36], this has no consequences on the expression of the NRF2 targets. In fact, it has been shown that the inhibition of APE1 redox activity leading to the activation of the NRF2 targets does not appear to occur via accumulation of ROS[12]. We therefore interpret our findings to suggest that in the PRDX1 knockdown cells APE1 remains redox active and poised to activate NF-κB.

Low levels of PRDX1 mRNA correlate with poor survival in gastric cancer patients. We next checked whether *PRDX1* mRNA expression level would correlate with inflammation-associated cancers. Human gastric cancer is a leading cause of mortality worldwide and sporadic gastric tumors are the results of several factors, including diet and *Helicobacter pylori*-induced inflammation that elevate the production of ROS with the propensity to generate oxidatively damaged DNA[43]. To explore the potential significance of PRDX1 in preventing a proinflammatory response that would otherwise exacerbate the survival of gastric cancer patients, we used the Affymetrix gene expression to analyze 876 cases of gastric cancers from The Cancer Genome Atlas (TCGA) dataset[44]. Using the online tool Kaplan-Meier Plotter[45,46], we observed that patients with a low level of *PRDX1* mRNA have significantly decreased overall survival (logrank $P = 5.2e-07$) than those with high expression levels of this gene (Fig. 6). This difference accounts for an average of 25 months increased life expectancy for patients with higher *PRDX1* expression levels (Fig. 6). It is possible that gastric cancer patients expressing reduced levels of PRDX1 are associated with poor outcome due to the induction of a proinflammatory response.

Discussion

In this study, we used a stringent tandem affinity approach combined with mass spectrometry to compare APE1 interactome in the nucleus and the cytosol under physiological condition and when cells are treated with the oxidant H_2O_2. We uncovered a novel interaction between APE1 and PRDX1, which existed in both the nuclear and cytosolic fractions. PRDX1 did not influence APE1 DNA repair AP endonuclease activity or APE1 ability to repair damaged DNA when HeLa or HepG2 cells were exposed to H_2O_2. Consistent with this observation, it was shown that liver and kidney cell extracts derived from *prdx1*$^{-/-}$ null mice showed normal levels of three additional enzymes uracil DNA glycosylase, 8-oxoguanine DNA glycosylase, and endonuclease III homologue I of the BER pathway[36]. Interestingly, PRDX1 knockdown facilitated APE1 detection in the nucleus by the anti-APE1 monoclonal and polyclonal antibodies, although neither APE1 level nor its cellular distribution was altered. Since PRDX1 forms a conjugate with APE1 *in vivo* (Fig. 2), we suggest that PRDX1 knockdown consequently sets APE1 free such that its redox function concomitantly activate binding of the transcription factor NF-κB onto the promoter of target genes, such as *IL-8* and causing its upregulation. IL-8 is a pro-inflammatory chemokine that has been linked with cancer migration, invasion and metastasis[21]. We propose that PRDX1 interaction with APE1 represents a novel mechanism, whereby APE1 redox function is engaged in a cycle of maintaining a pool of reduced PRDX1 to detoxify endogenously accumulated H_2O_2, and in this manner APE1 is not fully available to reduce transcription factors and activate gene expression. Disrupting this balance, for example, depleting PRDX1, is expected to augment pro-inflammatory response leading to cancer invasion and metastasis. In fact, it has been shown that mice lacking PRDX1 are viable, but develop several types of diseases including a high incidence of lymphomas and hepatocellular carcinomas[47]. Tissues from *prdx1*$^{-/-}$ null mice display higher levels of ROS that correlated with significant accumulation of ROS-induced DNA base lesions as detected by liquid- and gas-chromatography/mass spectroscopy[36]. These oxidized DNA base lesions include the hydroxylated purines 8-hydroxy-2′-deoxyguanosine and 8-hydroxy-2′ deoxyadenosine and the cyclic nucleosides

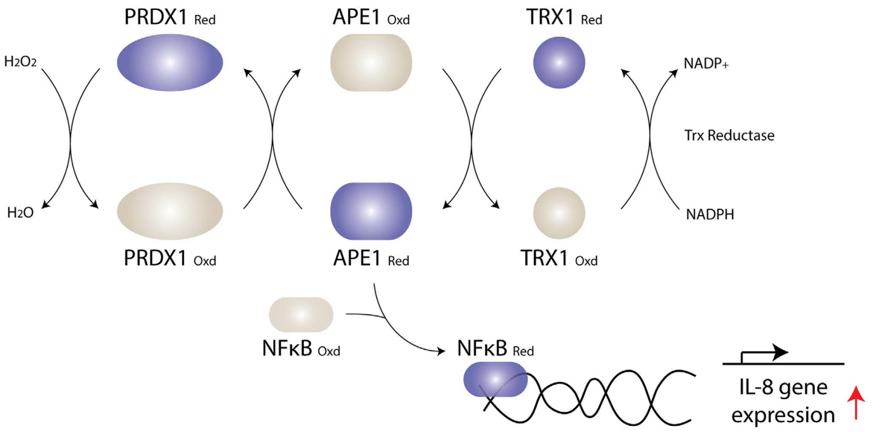

Figure 7. A model illustrating the propose role of APE1-PRDX1 interaction in regulating gene expression. Under normal metabolism, the reduced form of $PRDX1_{Red}$ decomposes the endogenously produced H_2O_2 to water and in turn becomes oxidized. The oxidized $PRDX1_{Oxd}$ is regenerated to the reduced form by the interaction with the reduced form of APE1 $_{Red}$. In this scheme, $APE1_{Oxd}$ is believed to be regenerated by thioredoxin I (TRX1). In the absence of PRDX1, there is a built up of H_2O_2 in the cells leading to the oxidation of NF-κB, which is set free from its inhibitor IKK and translocates to the nucleus. The oxidized NF-κB_{Oxd} has a redox cysteine (Cys62) that must be reduced in order for this transcription factor to bind to the promoter sequence of target genes such as IL-8. In the PRDX1 knockdown cells, APE1 is poised to reduce NF-κB resulting in the induction of IL-8 gene expression.

(5′R)-cyclo-2′-deoxyadenosine, (5′S)-cyclo-2′-deoxyadenosine, (5′R)-cyclo-2′-deoxyguanosine and (5′ S)-cyclo-2′-deoxyguanosine, which can block transcription and replication[36]. APE1 can stimulate the DNA glycosylase OGG1 to repair 8-hydroxy-2′-deoxyguanosine[48]. Moreover, APE1 has been shown to possess a nucleotide incision repair activity that can directly nick the 5′-side of a damaged nucleotide and then converts the nick into a gap by its 3′ to 5′-exonuclease activity[49,50]. Indeed, it has been shown that APE1 can remove the (5′ S)-cyclo-2′-deoxyadenosine when present at the 3′-termini of DNA[50]. Whether the loss of PRDX1 compromises APE1 ability to process these oxidized base lesions *in vivo*, for example, incising the lesions in an uncontrollable manner or unable to act on the lesions is not known. In any case, the unrepaired oxidatively produced lesions are likely to stall replication leading to DNA double strand breaks, which has the propensity to cause chromosomal rearrangements and translocations and thus also contribute to the elevated levels of age-related cancers in the *prdx1*$^{-/-}$ null mice[47].

The observation that PRDX1, APE1 and NF-κB are involved in the regulation of IL-8, strongly suggests that a similar mechanism might be operational for limiting the expression of a number of oxidative stress response genes. We identified from a microarray analysis at least 19 additional genes that are upregulated in PRDX1 knockdown and are also regulated by APE1, such as PLA2G2A and FTHL19 involved in plasma membrane lipoprotein remodeling and iron homeostasis, respectively, under oxidative stress (Supplementary Fig. S4)[51,52]. These genes have in the common, at the promoter region, a binding site for NF-κB. Thus, it seems that the elevated level of ROS produced in the absence of PRDX1 may cause the remodeling of gene expression to produce proteins to combat the consequences of oxidative damage. We propose a model (Fig. 7) suggesting that under normal growth conditions, PRDX1 acts as an anti-inflammatory protein by sequestering a pool of reduced APE in the nucleus. This limits the availability of reduced APE1 to activate the oxidized form of NF-κB and thereby suppressing the induction of the pro-inflammatory target genes such as *IL-8* (Fig. 7). In support of this model, PRDX1 has been shown to interact with the Myc Box II region of c-Myc and alters its transcriptional function[53]. In the absence of PRDX1, c-Myc fails to properly regulate some of its target genes such as *cyclin B1*, *ODC*, *GAS1* and *GADD45*[36].

A flood gate hypothesis has been proposed for the function of PRDX1 in combating oxidative stress[54]. In this simple model, it has been proposed that under the normal physiological redox state of the cell (perhaps low concentration of H_2O_2), the monomeric form of PRDX1 that possesses peroxidase activity deals with the burden of endogenously produced H_2O_2 as part of a first line defense that keeps NF-κB from being activated[55]. We provide evidence that once the level of PRDX1 is diminished the elevated level of the endogenous free radicals causes the activation of NF-κB, which is set free from its inhibitor subunit IκBα. The activated NF-κB then translocates to the nucleus leading to the induction of IL-8[36,40,41,56]. We showed that blocking the NF-κB translocation step with a known specific inhibitor RO106 prevented the induction of IL-8 in the PRDX1 knockdown cells. Binding of NF-κB to the promoter element of target genes such as *IL-8* requires that its oxidation sensitive cysteine Cys62 must be reduced. We believe that in the absence of PRDX1, APE1 is poised to maintain NF-κB in the reduced form such that it activates IL-8 expression. This is the most likely possibility as APE1 has been shown to reduce NF-κB[7]. Altogether, our data fit a model that downregulation of PRDX1 led to the activation of IL-8 in an APE1-dependent manner (see Fig. 7). Consistent with this model, APE1 knockdown blocked the high level expression of IL-8 in the PRDX1 knockdown cells.

It is noteworthy that while our studies were in progress, an independent group documented that PRDX1 depletion in the colon cancer cell line SW480 enhanced the production of ROS, and increased the expression levels of pro-inflammatory cytokines such as the tumor necrosis factor-α and interleukin (IL)-1β, as well as the chemokines IL-8 and CXCL1, and that this induction occurs by partial activation of NF-κB[57]. These independent observations reinforce the notion that PRDX1 is important to suppress the pathogenesis of inflammation-associated cancers such as colorectal and gastric and prolong the survival of the patients. Thus, the high expression of PRDX1 associated with some types of cancers, such as we show herein for gastric cancer (Fig. 6) might be to reduce inflammation.

In addition to its peroxidase activity, PRDX1 performs a role as a chaperone by protecting proteins from oxidation-induced inactivation and degradation[54,56,58]. For example, PRDX1 interacts with PTEN and prevents oxidation-induced inhibition of its phosphatase activity, which can occur as a result of a disulfide bond that forms between the two cysteines Cys71 and Cys124 in the N-terminal phosphatase domain of PTEN upon oxidation with H_2O_2[59]. The phosphatase activity of PTEN can function to dephosphorylate the lipid phosphatidylinositol triphosphates, which is required to activate the serine/threonine kinase AKT that plays a central role in suppressing H-Ras and ErbB-2 mediated oncogenic transformation[31]. Similarly, PRDX1 has been shown to maintain proper growth factors-mediated signaling pathways in different cancer models[32,60]. So far, we have no evidence that PRDX1 could serve as a chaperone to protect APE1 from inactivation or degradation, as neither APE1 endonuclease activity nor its stability was affected when PRDX1 was downregulated. We propose that oxidized PRDX1 molecules generated endogenously associate with a pool of reduced APE1, and that this interaction would serve to replenish the reduced state of PRDX1 (Fig. 7). In support of this model, inhibition of APE1 redox function with the specific inhibitor E3330 caused the accumulation of PRDX1 in its dimeric form (Fig. 2), a consequence of overoxidation of the monomeric PRDX1. Thus, under normal conditions the cycle of oxidation-reduction of PRDX1 would diminish the availability of reduced APE1 to activate the oxidized NF-κB, unless PRDX1 is depleted and according to our model leads to IL-8 expression. In the cycle of oxidation-reduction of PRDX1, the production of oxidized APE1 is expected to be reduced by thioredoxin, as oxidized APE1 has been shown previously to be in complex with reduced thioredoxin[34]. It is unlikely that thioredoxin is directly involved in the reduction of PRDX1, otherwise the inhibition of APE1 would not lead to the accumulation of the oxidized dimeric form of PRDX1. Nevertheless, further experiments are needed to examine whether inhibition of APE1 would downregulate thioredoxin or whether the depletion of thioredoxin would generate the oxidized dimeric form of PRDX1.

It has been documented that PRDX1 forms mixed disulfide intermediates with ASK1, which is required for the activation of the mitogen-activated protein kinase pathway in response to peroxide[30]. A more recent study documented that another member of the peroxiredoxin family, PRDX2 transfers oxidizing equivalents through direct protein-protein contact onto the STAT3 transcriptional activator resulting in the formation of PRDX2-STAT3 disulfide linked conjugates[61]. This relay results in the inactivation of STAT3 function in the transcriptional activation from the serum-induced promoter, but rescued upon PRDX2 depletion[61]. In a similar manner, it is possible that such relay exists between PRDX1 and APE1 and that the observed APE-PRDX1 conjugate could perform additional functions besides rendering a fraction of APE1 inactive and preventing NF-κB mediated activation of *IL-8*.

Since IL-8 plays a key role in the inflammatory response[62,63], its upregulation in the PRDX1 knockdown cells may serve to recruit neutrophils to repair damage tissues caused by ROS. Thus, IL-8 expression must be turned off, otherwise the prolong activation of the inflammatory response can lead to severe tissue damage[64]. To date, multiple pathways including MEK/ERK, ATM and NF-κB, have been shown to influence IL-8 expression[21,65]. The fact that NF-κB is involved in all aspects of the immune response as well as other biological pathways, and that its activation can be promoted by the redox function of APE1, it seems that PRDX1-APE1 mixed disulfide conjugates would constitute a mechanism to tightly regulate IL-8 expression to control the inflammatory response. Interestingly, a very recent study demonstrated that IL-8, which is upregulated by ATM action on NF-κB through the intrinsic oxidative stress that exists in metastatic cancer cells, is required to promote migration and invasion that support tumour progression[21,66,67]. Thus, the interaction of PRDX1with APE1 might serve as an auxiliary mechanism to dampen the activation of NF-κB caused by the high oxidative stress that occurs in cancer cells, thereby reducing IL-8 expression from promoting its pro-metastatic functions.

In short, the long term consequences of PRDX1 functional loss are (i) the accumulation of ROS-induced oxidized DNA base lesions that might not be efficiently repaired by APE1 leading to genomic instability, as under these conditions APE1 could be targeted for its redox role, and (ii) the induction of IL-8 that has the ability to stimulate cancer cells invasion and metastasis.

Materials and Methods

Cell lines and cell culture. HeLa, HEK293T and HepG2 cells were cultured in Dulbecco's Modified Eagle Medium (DMEM) (Wisent Inc., Cat No. 319-005-CL) supplemented with 10% of fetal bovine serum (FBS) (Wisent Inc., Cat. No. 095150) and in the presence of the antibiotics penicillin (100 U/ml) and streptomycin (0.1 mg/ml) (Wisent Inc., Cat. No. 450-201-EL). Cells were incubated at 37 °C and 5% CO_2. The HeLaS cells were cultured in MEM media supplemented with 10% FBS and the antibiotics as above.

Antibodies and reagents. The antibodies used in this study were anti-APE1 rabbit mAb (Epitomics, Cat No. 2851-1), anti-APE1 pAb antibody (Novus Biologicals, Cat No. NB100-101), anti-PRDX1 mAb antibody (Novus Biologicals, Cat No. NBP1-95676), anti-PRDX1 rabbit pAb (Cell Signalling, Cat No. 8732S), rabbit anti-FLAG pAb (Sigma, Cat No. F7425), mouse anti-HA mAb (Sigma, Cat No. H3663), goat anti-mouse IgG pAb HRP conjugate (Enzo Life Sciences, Cat No. ADI-SAB-100), goat anti-rabbit IgG pAb HRP conjugate (Enzo Life Sciences, Cat No. ADI-SAB-300-J), goat anti-rabbit IgG-CFL647 (Santa Cruz Biotechnology, sc-362292), MitoTracker Red CMXRos (Life Technologies, Cat No. M-7512). Amico Ultra (Millipore, Cat No. UFC501024). The mouse anti- ACTβ monoclonal antibodies (Santa Cruz Biotechnology, sc-69879) was used for normalizing protein content in cell extract.

Plasmid constructs. pOZ-FH-N contains a Kozak sequence, an initiation methionine, FLAG and HA tags. pOZN-APE1 were constructed by first amplifying the human APE1 from K562 cell cDNA by PCR with the primers APE1-Xho1-F1 and APE1-Not1-R1 (Supplementary Table S1), and then subcloned the fragment into pOZ-FH-N following *XhoI* and *NotI* digestion. To knockdown PRDX1, several constructs were made based on the MSCV-LTRmiR30-PIG (LMP) vector (Thermo Scientific) following the manufacturer's instructions. These knockdown constructs are named prdx1C1-2, prdx1C2-1, prdx1C3-1 and prdx1C4-1 and were all sequenced for confirmation. The hairpin shRNA templates are as following, sense and antisense sequences are underscored.

C1(HP_7670)TGCTGTTGACAGTGAGCGACCAGATGGTCAGTTTAAAGATTAGTGAAGCCACAGATGTAATCTTTAAACTGACCATCTGGCTGCCTACTGCCTCGGA C2(HP_647595)TGCTGTTGACAGTGAGCGACCAGATGGTCAGTTTAAAGATTAGTGAAGCCACAGATGTAATCTTTAAACTGACCATC TGGCTGCCTACTGCCTCGGA C3(HP_142580)TGCTGTTGACAGTGAGCGACCTGTCTGACTACAA AGGAAATAGTGAAGCCACAGATGTATTTCCTTTGTAGTCAGACAGGCTGCCTACTGCCTCGGAC4(HP_820446)TGCTGTTGACAGTGAGCGACCTGTCTGACTACAAAGGAAATAGTGAAGCCACAGATGTATTTCCTTTGTAGTCAGACAGGCTGCCTACTGCCTCGGA. To knockdown APE1, two constructs were made based on vector RNAi-Ready pSIREN-RetroQ-ZsGreen (Clontech Laboratories, Inc.) following the manufacturer's instructions: pSIREN shAPE1 1-1 and pSIREN shAPE1 2-1. Oligos APE1-shRNA-UP1 and APE1-shRNA-DWN1 were used for pSIREN shAPE1 1-1 targeting 5′-TGACAAAGAGGCAGCAGGA-3′ in APE1; oligos APE1-shRNA-UP2 and APE1-shRNA-DWN2 were used for pSIREN shAPE1 2-1 targeting 5′-GTCTGGTACGACTGGAGTACC-3′. Oligo sequences are as following:

APE1-shRNA-UP1: 5′-gatccGTGACAAAGAGGCAGCAGGATTCAAGAGATCCTGCT GCCTCTTTGTCATTTTTTg-3′; APE1-shRNA-DWN1: 5′-aattcAAAAAATGACAAAGA GGCAGCAGGATCT CTTGAATCCTGCTGCCTCTTTGTCACg-3′; APE1-shRNA-UP2: 5′-gatccGTCTGGTACGACTG GAGTACCTTCAAGAGAGGTACTCCAGTCGTACCAGACTTTTTTg-3′; and APE1-shRNA-DWN2: 5′-aattcAAAAAAGTCTGGTACGACTGGAGTACCTCTCTTGAAGGTACTCCAGTCGTACCAGACg-3′. pOZN-prdx1 was constructed by first amplifying human Prdx1from K562 cell cDNA by PCR with the primers pOZN-FH-prdx1F (5′-GCCGGAGGACTCGAGatgtcttcaggaaatgctaaaattggg-3′) and POZN-FH-prdx1R (5′-TCA GTCACGATGCGGCCGCtcacttctgcttggagaaatattcttt-3′) and then subcloned into pOZ-FH-N following *Xho*I and *Not*I digestion.

Retrovirus preparation and infection. HEK293T cells were plated in 10 cm tissue cell culture plates, 24 h prior to transfection. The following day, retroviral vectors were cotransfected with pVSV-G and pCL-Eco retrovirus packaging vector using calcium phosphate transfection method. Supernatants were collected 36 to 48 h after transfection, filtered through a 0.45 μm filter and used directly to infect target cell lines. To infect HeLaS, HeLa or HepG2 cells, the cells were plated onto 10 cm tissue cell culture plates one day prior to infection at 35% confluence. The day of transfection, the old media were removed and replaced with viral supernatants/fresh media mixture (1:1) supplemented with 0.4 μg/ml Polybrene® (Sigma-Aldrich). After 24 h infection, the viral media was removed and cells were washed at least twice with 1 x PBS and fresh media was added. Cells were subjected to selection 48 h after infection.

Cell proliferation and clonogenic assays. To determine the average rate of population doublings, HeLa-LMP, HepG2-LMP, HeLa-shPRDX1 and HepG2-shPRDX1 cells were plated into 10 cm diameter petri-dishes in duplicate with initial cell density of 1.6×10^6 cells/dish. After the indicated intervals (0 to 48 h), cells were trypsized and counted using the Countess® Automated Cell Counter (Life Technologies). The numbers were converted into population doublings according to the following formula: [log (No. of cells counted)-log (No. of cell plated)]/log(2)[68].

For the clonogenic assay, the indicated cell lines were plated in 6 cm diameter plates 24 h prior to treatment with and without the indicated concentrations of H_2O_2 for 1 hr and the colony forming unit was performed as described previously[69].

Purification of APE1 complex from HeLaS cells. A stable HeLaS cell line expressing human APE1 with N-terminal FLAG and HA tags was generated by retroviral transduction by using a previously described procedure with some modifications[23]. Nuclear extracts were prepared from 10 L of these cells as follows. The cells were washed twice with cold 1 x PBS, resuspended in hypotonic buffer (20 mM Hepes (K+), pH 7.6, 10 mM KCl, 1.5 mM $MgCl_2$, 0.2 mM PMSF, 0.5 mM benzamidine, and 1 μg/mL each of leupeptin, aprotinin, and pepstatin), and incubated on ice for 10 min. The cells were then disrupted with approximately 10 strokes of a Wheaton Dounce homogenizer (B pestle) on ice. The nuclei were pelleted for 5 min at 4 °C in a clinical centrifuge and washed once with the same volume of hypotonic buffer as the pellets, then resuspended in extraction buffer (20 mM Hepes (K+), pH 7.6, 0.42 M KCl, 1.5 mM $MgCl_2$, 0.2 mM EDTA, 25% (v/v) glycerol, 0.2 mM PMSF, 0.5 mM benzamidine, and 1 μg/mL each of leupeptin, aprotinin, and pepstatin), and sonicated (30% amplitude) for 2 min on ice. Insoluble material was pelleted for 15 min at 13,000 rpm in a Sorvall SS-34 rotor at 4 °C, and the soluble extract was dialyzed overnight against dialysis buffer (20 mM Hepes (K+), pH 7.6, 100 mM KCl, 1.5 mM $MgCl_2$, 0.2 mM EDTA, 0.2 mM PMSF, 0.5 mM benzamidine, and 1 μg/mL each of leupeptin, aprotinin, and pepstatin). The extract was subjected to centrifugation for 15 min at 13,000 rpm in a Sorvall SS-34 rotor at 4 °C to remove insoluble material, and then used for affinity purification of the APE1 complex. To prepare the cytoskeleton fraction, KCl concentration was adjusted to 100 mM KCl and insoluble material was pelleted for 15 min at 13,000 rpm in a Sorvall SS-34 rotor at 4 °C. The supernatants were used for affinity purification of the APE1 complex.

The affinity purification of APE1 was performed by sequential anti-FLAG and anti-HA resins using methods similar to those previously described with some modifications[23]. Nuclear extracts were combined with 200 μL of FLAG (M2) resin (Sigma) and incubated overnight at 4 °C. The beads were pelleted and washed twice in batch with wash buffer (20 mM Hepes (K+), pH 7.6, 100 mM KCl, 5 mM $MgCl_2$, 0.2 mM EDTA, 0.05% (v/v) NP-40, 10% (v/v) glycerol, 0.2 mM PMSF, 0.5 mM benzamidine, and 1 μg/mL each of leupeptin, aprotinin, and pepstatin). The beads were then transferred to a 1.5 mL column (Bio-Rad) and washed with 10 mL of wash buffer. Bound proteins were eluted by three successive 1 h incubations of the beads with 200 μL (for each incubation) of FLAG Elution buffer (Wash buffer plus 0.36 mg/mL FLAG peptide (Bio-basic)). The FLAG eluates were pooled, combined with 100 μL of HA resin, and incubated overnight at 4 °C. The resin was then washed in 1.5 mL column (Bio-Rad) with 10 mL of wash buffer. Bound proteins were eluted by three successive 1 h incubations of the beads with 200 μL (for each incubation) of HA elution buffer (Wash buffer plus 0.2 mg/mL HA peptide (Bio-basic)). The HA eluates were pooled and concentrated into 100 μL by 20% (w/v) trichloroacetic acid (TCA) precipitation, and an aliquot (10 μL) was analyzed by SDS-polyacrylamide gel electrophoresis and silver staining. A second aliquot (10 μL) was used for determining the identity of all the proteins in the complex by the Taplin Biological Mass Spectrometry Facility (Harvard Medical School, Boston, USA), and the remaining 80 μL kept frozen at −80 °C.

Co-immunoprecipitation of APE1 and Prdx1 from cell and nuclear extracts. For the pull down of PRDX1, HeLaS cells carrying either the empty vector pOZN or the pOZN-APE1 were grown in 10 cm plates, washed twice in 1 x PBS, resuspended in 500 μL Lysis buffer (20 mM Hepes (K+), pH 7.6, 0.3 M KCl, 1.5 mM $MgCl_2$, 0.2 mM EDTA, 0.3% (v/v) NP-40, 0.2 mM PMSF, 0.5 mM benzamidine, and 1 μg/mL each of leupeptin, aprotinin, and pepstatin), and sonicated for 2 seconds. The insoluble material was pelleted for 15 min at 13,000 rpm in a microcentrifuge, and the soluble extract was diluted with 1 mL of Lysis buffer with 10% (v/v) glycerol but lacking KCl and NP-40. Insoluble material was pelleted, and the soluble lysate was added to 30 μl of FLAG (M2) beads (Sigma) after 50 μL aliquots were taken for input, following incubation for 4 h at 4 °C. The beads were pelleted and washed with 3 × 1 mL of wash buffer (20 mM Hepes (K+), pH 7.6, 0.1 M KCl, 1.5 mM $MgCl_2$, 0.2 mM EDTA, 0.01% (v/v) NP-40, 10% (v/v) glycerol, 0.2 mM PMSF, 0.5 mM benzamidine, and 1 μg/mL each of leupeptin, aprotinin, and pepstatin). The bound proteins were eluted by elution buffer (10 mM Tris pH 7.9, 10 mM EDTA, 1% SDS), and the beads were removed by centrifugation at 2000 RPM for 1 min in a microcentrifuge. The supernatants with the eluted proteins were processed for Western blot analysis.

For the reciprocal pull down of APE1, nuclear extract was prepared from HeLa cells as previously described[70]. Briefly, the sample from the nuclear extract (900 μl in hypotonic buffer derived from 100 million cells) was precleared with 30 μl of protein A magnetic beads for 2 h to remove all non-specific interactions, then the extract was collected and mixed with another fresh 30 μl of protein A magnetic beads followed by the addition of 5 μg of anti-Prdx1 polyclonal antibodies and the mixture was allowed to rotate slowly for overnight at 4 °C. The magnetic beads were collected, washed, and the total beads with bound proteins were resuspended in loading buffer for Western blot analysis.

To detect APE1-PRDX1 conjugate. Typically 2×10^6 HeLa cells (with and without 20 μM E3330 for 4 h) were incubated for 5 mins with 80 mM methyl methanethiosulfonate (Sigma) in PBS to block free thiols from disulfide exchange reactions. Cells were then resuspended in 1 ml of fresh hypotonic buffer (10 mM Tris pH 7.3, 10 mM KCL and 1.5 mM $MgCl_2$) and transfered to a cold dounce homogenizer to be stroked 10 to 30 times to release the nuclei. Nuclei suspension was then spun down at 3900 rpm in an Eppendorf centrifuge at 4 °C for 15 mins. The nuclear pellet was resuspended in three volume of buffer II (50 mM Tris pH 7.3, 5 mM EDTA, 0.5% NP-40 and 300 mM NaCl) and incubated for 30 mins on ice. The sample was spun at 14,000 rpm in an Eppendorf centrifuge at 4 °C for 20 mins and the supernatant (nuclear extract) was transferred to a new tube. An equal volume of buffer O (50 mM Tris pH 7.3, 5 mM EDTA and 0.5% NP-40) was added to the nuclear extract. All buffers contained 10 mM beta-mercaptoethanol, 1 mM PMSF and complete protease inhibitor cocktail Tablets (Roche).

Gel filtration. Post-nuclear supernatants were loaded on Fast Protein Liquid Chromatography (FPLC) ÄKTA purifier 10/100 system was used to co-elute interacting proteins under isocratic mode. Buffer solutions were degassed prior to use. Samples were filtered and centrifuged to remove debris that may clog the column. Small amount of sample (~0.5 mL) was loaded onto the Superose^{TM} 6 column equipped with ÄKTA purifier 10/100 FPLC system. Buffer A (containing 20 mM Hepes (K +) pH 7.6, 100 mM KCl, 1.5 mM $MgCl_2$, 0.2 mM EDTA, 0.2 mM PMSF, 0.5 mM benzamidine, and with 1 μg/mL each of leupeptin, aprotinin, and pepstatin) was pumped at flow rate of 0.25 ml/min. Before loading sample onto the column, the column was first equilibrated with 1 column volume of Buffer A and then samples were eluted with 2 column volumes of same buffer. All eluents were collected at 0.5 ml/fractions. Each fraction was concentrated by Amicon Ultra prior to the Western blot analysis.

AP endonuclease assay. This assay was performed as previously described using a 42-mer substrate U21•G containing a single AP site[37]. Total cell extracts were incubated with the substrate and the reaction products were separated on 10% (w/v) polyacrylamide/7M urea gels and developed by autoradiography. The radiolabeled fragments were visualized by using a PhosphorImager (Storm 840, Molecular Dynamics), and ImageQuant LAS 400 was used for quantification. The intensity of the product was quantified using ImageJ and plotted as a percentage of increasing concentration of the total cell extracts.

Immunofluorescence assay. For immunofluorescence assay, cells were grown on sterile cover slips placed in 24 well plates one day before treatment. The following day, after treatment for the indicated time interval, cells were washed with 1X PBS twice, and fixed for 30 min with 4% PFA containing 0.1% Triton X-100. The cells were then washed three times with PBS, each for 5 min, and incubated with the anti-APE1 primary antibody (1:2000) in PBS containing 5% FBS (fetal bovine serum) for 1 hr at room temperature or overnight at 4 °C. After the unbound primary antibodies were gently washed off thrice with 1X PBS for 5 min each, the cells were incubated with appropriate goat anti-rabbit IgG-CFL647 secondary antibodies (1:500) in PBS containing 5% FBS for 1 hr at 37 °C in dark. After 1 hr incubation at room temperature, the slides were counterstained with DAPI combined with 20 μl Vecta shield mounting solution (Vector Laboratories, Inc., CA). The cover slips with the cells were mounted facing down on the glass slides. Excess liquid was wiped out with filter paper. Finally the cover slips were sealed with nail polish. The cells were then visualized under the Zeiss Microscope with an appropriate barrier and excitation filters for FITC, DAPI and Cy5 visualization. Images were captured with AxioCam MRm using a 63x objective lens.

Flow cytometry of APE1 Immunofluorescence. HeLa cells (WT, LMP, shPrdx1) were culture in 6-well plates until they reach almost full confluence. The cells were harvested with 1 ml trypsin 0.25%, centrifuged and the trypsin was removed. Cells were resuspended in 200 μl of PBS containing 4% paraformaldehyde (PFA) and incubated 15 min at room temperature (RT). Cells were centrifuged and PFA solution removed. Cells were resuspended in 50 μl of cold PBS and 450 μl of ice-cold methanol was added slowly followed by storage at −20 °C for at least 30 min. The cells were washed twice in PBS with 1% BSA, then resuspended in 150 μl of PBS with 1% BSA and incubated at RT for 20 min. Anti-APE1 antibody (1.5 μl) (Cell Signaling Technology, CAT # 4128) was added to the cells to be stained (the antibody was not added to a control set of cells). Cells were incubated 1 h RT with agitation and washed twice with 200 μl PBS with 1% BSA. The cells were resuspended in 500 μl PBS with 1% BSA and one drop of secondary Alexa Fluor® 594 antibody (Thermo Fisher Scientific, CAT # R37117) was added as well as to the set of control cells. The cells were incubated 45 min at RT, centrifuged, and resuspended in 100 μl PBS. The cells were diluted in 400 μl in FACS tubes (BD Falcon 352052) then past through FACS Calibur. Alexa Fluor® 594 was detected with FL2 (585/42). The threshold was determined using cells that were not incubated with the primary APE1 antibody and the fluorescence intensity of Alexa Fluor® 594 was multiplied by the percentage of cells that are Alexa Fluor® 594 positive.

IL-8 quantification by ELISA. Human IL-8 ELISA kit (BD Biosciences, Cat. No. 555244) was used to quantify IL-8 in culture supernatants according to the manufacturer suggested protocol. Briefly 100 μL diluted capture antibody was added to each well of 96-well plates and incubated overnight at 4 °C. The following day, the unbound capture antibody was washed thrice with 300 μL 1X wash buffer (supplied with the kit) for 5 min each. The wells were blocked with 200 μL assay diluent for 1 hr at room temperature followed by three washes each time with 300 μL 1X washing buffer for 5 min each. Next 100 μL standard or samples were added to each well and the plate was incubated for 2 hr at RT followed by 5 times wash with 300 μL 1X washing buffer. 100 μL working 1X detection solution (Detection Ab+SAv-HRP at 1:250 dil) was added to each well and the plate was incubated for 1 hr at RT followed by 7 washes with 300 μL 1X washing buffer. Finally, 100 μL substrate solution was added to each well and incubated 30 mins at RT in dark. In order to stop the reaction, 50 μl stop solution was added to each well. All samples were set as duplicates and the absorbance was measured at 450 nm using a microplate reader (BioTek, EL800 Systems).

Real-time PCR for gene expression quantification. For the isolation of total cellular RNA, the RNAeasy mini kit (Qiagen; Cat no. 74104) was used according to the manufacturer's protocol. RNA concentration was measured with NanoDrop 2000 spectrophotometer (Thermo Scientific, Wilmington, Delaware, USA). The first-strand cDNA synthesis containing 100 ng of total RNA was primed with oligo(dT) using native avian myeloblastosis virus reverse transcriptase in the presence of RNase inhibitor RNaseOUT (Thermofisher Scientific; Cat no. 10777-019). The cDNA was diluted to 10 ng/μl using RNase-free water. Quantitative real-time PCR (qRT-PCR) amplification reactions were performed with the Applied Biosystems 7500 RT PCR system (Applied Biosystems), using the PerfeCTa SYBR Green SuperMix Low Rox PCR Kit (Quanta Biosciences; Cat no. 95056). The PCR reaction contained 10.0 μl of 2X SYBR Green SuperMix, 6.00 μl RNase-free water, 500 μM forward and reverse primers (the sequences of which are listed in Supp Table S1), and 8 ng cDNA, in a total volume of 20 μl. All reactions were run in triplicate with the following program: 95 °C for 3 min, followed by 45 cycles of 95 °C for 15 sec, 58 °C for 30 sec, and 72 °C for 20 sec, finishing with a melt cycle consisting of stepwise increases in temperature from 72 °C to 99 °C. The threshold numbers (C_t values) were set within the exponential phase of the reaction and were used to calculate the relative expression for each gene normalized to either *ACTβ* (β-actin) or *HPRT* RNA in each sample. The ratio of gene expression in experimental samples compared with control *ACTβ* (β-actin) or *HPRT* samples was then calculated. The fold change for the indicated gene relative to the reference gene was calculated and plotted as bar graph with standard deviation.

Kaplan-Meier plotter analysis. The prognostic value of the *PRDX1* gene in gastric cancer was analyzed using the online tool Kaplan-Meier Plotter (http:/kmplot.com/analysis/), a database that integrates gene expression data and clinical information of breast, ovarian, lung and gastric cancers[45,46]. Kaplan-Meier Plotter uses three versions of the Affymetrix HG-U133 datasets (with 22,277 probe sets in common), and clinical data from Gene Expression Omnibus (GEO) and The Cancer Genome Atlas (TCGA) datasets. The expression of *PRDX1* in the TCGA dataset for gastric cancer was verified with the best specific probe (JetSet probes) of this gene (208680_ at). A total of 876 patients were available for analysis on overall survival. Patient samples were split into two groups according to the median value, using the query parameter of auto-select best cutoff. The signal range of the *PRDX1* probe was 2820–25698. The two patient groups (high and low expression levels) were compared using a Kaplan-Meier survival plot. The hazard ratio with 95% confidence intervals and log rank *p* value was calculated, and significance was set at $p < 0.05$.

Microarray analysis. Microarray analysis was performed on cells carrying either the empty vector or the shRNA PRDX1 knockdown construct using Illumina BeadChip® Microarray at Genome Québec Innovation Centre (McGill University, Montreal, Canada). The Illumina raw data files were imported into the FlexArray (ver 1.6.3) followed by execution of robust multi-array average (Lumi), which performs the background correction and Robust spline normalization. Principal components analysis (PCA) was used as tool to perform quality control for the data. For subsequent statistical analysis we used the SAM (Significance analysis of microarray), an algorithm implemented in Flexarray. Genes up-regulated ($\geq$2 fold change) and down-regulated ($\leq$0.5 fold change) with high statistical significance (p value < 0.01) were exported as text file for further analysis. Volcano plots of the differentially expressed genes were generated using $-\text{Log}_{10}$ (p value) and Log_2 (fold change). Venny 2.0.2 (Computational Genomic Services, CSIC) was employed for comparing gene list and drawing Venn's diagram. Functional annotation clustering of the differentially expressed genes related to biological pathways were then performed using Gene Ontology (GO) term enrichment analysis and KEGG pathway mapping through DAVID Bioinformatics Resources 6.7 (http://david.abcc.ncifcrf.gov) with ease score = 0.01 and similarity threshold = 0.50. Gene Ontology (GO) terms significantly represented among differentially expressed genes were then listed with their corresponding p value and FDR in the Supplementary Table.

Statistical analyses. Statistical differences were calculated by the unpaired two-tail t-test using the GraphPad Prism Statistical Software Mac Version 6 (*$P < 0.01$; **$P < 0.001$; N.S. non significant) and represented as ± S.D.

References

1. Tell, G., Quadrifoglio, F., Tiribelli, C. & Kelley, M. R. The many functions of APE1/Ref-1: not only a DNA repair enzyme. *Antioxid Redox Signal* **11,** 601–620, doi: 10.1089/ars.2008.2194 (2009).
2. Evans, A. R., Limp-Foster, M. & Kelley, M. R. Going APE over ref-1. *Mutat Res* **461,** 83–108 (2000).
3. Izumi, T. *et al.* Mammalian DNA base excision repair proteins: their interactions and role in repair of oxidative DNA damage. *Toxicology* **193,** 43–65, doi: S0300483X03002890 [pii] (2003).
4. Demple, B. & Harrison, L. Repair of oxidative damage to DNA: enzymology and biology. *Annu Rev Biochem* **63,** 915–948 (1994).
5. Bhakat, K. K., Izumi, T., Yang, S. H., Hazra, T. K. & Mitra, S. Role of acetylated human AP-endonuclease (APE1/Ref-1) in regulation of the parathyroid hormone gene. *Embo J* **22,** 6299–6309, doi: 10.1093/emboj/cdg595 (2003).
6. Xanthoudakis, S. & Curran, T. Identification and characterization of Ref-1, a nuclear protein that facilitates AP-1 DNA-binding activity. *The EMBO journal* **11,** 653–665 (1992).
7. Nishi, T. *et al.* Spatial redox regulation of a critical cysteine residue of NF-kappa B *in vivo*. *J Biol Chem* **277,** 44548–44556, doi: 10.1074/jbc.M202970200 (2002).
8. Xanthoudakis, S., Miao, G., Wang, F., Pan, Y. C. & Curran, T. Redox activation of Fos-Jun DNA binding activity is mediated by a DNA repair enzyme. *Embo J* **11,** 3323–3335 (1992).
9. Gaiddon, C., Moorthy, N. C. & Prives, C. Ref-1 regulates the transactivation and pro-apoptotic functions of p53 *in vivo*. *Embo J* **18,** 5609–5621 (1999).
10. Huang, L. E., Arany, Z., Livingston, D. M. & Bunn, H. F. Activation of hypoxia-inducible transcription factor depends primarily upon redox-sensitive stabilization of its alpha subunit. *J Biol Chem* **271,** 32253–32259 (1996).
11. Tell, G. *et al.* Redox effector factor-1 regulates the activity of thyroid transcription factor 1 by controlling the redox state of the N transcriptional activation domain. *J Biol Chem* **277,** 14564–14574, doi: 10.1074/jbc.M200582200 (2002).
12. Fishel, M. L. *et al.* Apurinic/apyrimidinic endonuclease/redox factor-1 (APE1/Ref-1) redox function negatively regulates NRF2. *J Biol Chem* **290,** 3057–3068, doi: 10.1074/jbc.M114.621995 (2015).
13. Kelley, M. R. & Parsons, S. H. Redox regulation of the DNA repair function of the human AP endonuclease Ape1/ref-1. *Antioxid Redox Signal* **3,** 671–683 (2001).
14. Park, M. S. *et al.* Cytoplasmic localization and redox cysteine residue of APE1/Ref-1 are associated with its anti-inflammatory activity in cultured endothelial cells. *Mol Cells* **36,** 439–445, doi: 10.1007/s10059-013-0195-6 (2013).
15. Hsieh, M. M., Hegde, V., Kelley, M. R. & Deutsch, W. A. Activation of APE/Ref-1 redox activity is mediated by reactive oxygen species and PKC phosphorylation. *Nucleic Acids Res* **29,** 3116–3122 (2001).
16. Busso, C. S., Iwakuma, T. & Izumi, T. Ubiquitination of mammalian AP endonuclease (APE1) regulated by the p53-MDM2 signaling pathway. *Oncogene* **28,** 1616–1625, doi: onc20095 (2009).
17. Fan, Z. *et al.* Cleaving the oxidative repair protein Ape1 enhances cell death mediated by granzyme A. *Nat Immunol* **4,** 145–153, doi: 10.1038/ni885 (2003).
18. Vascotto, C. *et al.* APE1/Ref-1 interacts with NPM1 within nucleoli and plays a role in the rRNA quality control process. *Mol Cell Biol* **29,** 1834–1854, doi: MCB.01337-08 (2009).
19. Tell, G., Fantini, D. & Quadrifoglio, F. Understanding different functions of mammalian AP endonuclease (APE1) as a promising tool for cancer treatment. *Cell Mol Life Sci* **67,** 3589–3608, doi: 10.1007/s00018-010-0486-4 (2010).
20. De Larco, J. E. *et al.* A potential role for interleukin-8 in the metastatic phenotype of breast carcinoma cells. *Am J Pathol* **158,** 639–646, doi: S0002-9440(10)64005-9 (2001).
21. Chen, W. T. *et al.* ATM regulation of IL-8 links oxidative stress to cancer cell migration and invasion. *Elife* **4,** doi: 10.7554/eLife.07270 (2015).
22. Vascotto, C. *et al.* Genome-wide analysis and proteomic studies reveal APE1/Ref-1 multifunctional role in mammalian cells. *Proteomics* **9,** 1058–1074, doi: 10.1002/pmic.200800638 (2009).
23. Nakatani, Y. & Ogryzko, V. Immunoaffinity purification of mammalian protein complexes. *Methods Enzymol* **370,** 430–444, doi: 10.1016/S0076-6879(03)70037-8 (2003).
24. Franceschini, A. *et al.* STRING v9.1: protein-protein interaction networks, with increased coverage and integration. *Nucleic Acids Res* **41,** D808–815, doi: gks1094 (2013).
25. Wood, Z. A., Schroder, E., Robin Harris, J. & Poole, L. B. Structure, mechanism and regulation of peroxiredoxins. *Trends Biochem Sci* **28,** 32–40, doi: S0968-0004(02)00003-8 [pii] (2003).
26. Hofmann, B., Hecht, H. J. & Flohe, L. Peroxiredoxins. *Biol Chem* **383,** 347–364, doi: 10.1515/BC.2002.040 (2002).
27. Sato, Y. *et al.* Synergistic cooperation of PDI family members in peroxiredoxin 4-driven oxidative protein folding. *Sci Rep* **3,** 2456, doi: srep02456 (2013).
28. Laboissiere, M. C., Sturley, S. L. & Raines, R. T. The essential function of protein-disulfide isomerase is to unscramble non-native disulfide bonds. *J Biol Chem* **270,** 28006–28009 (1995).
29. Rhee, S. G., Woo, H. A., Kil, I. S. & Bae, S. H. Peroxiredoxin functions as a peroxidase and a regulator and sensor of local peroxides. *J Biol Chem* **287,** 4403–4410, doi: R111.283432 (2012).

30. Jarvis, R. M., Hughes, S. M. & Ledgerwood, E. C. Peroxiredoxin 1 functions as a signal peroxidase to receive, transduce, and transmit peroxide signals in mammalian cells. *Free Radic Biol Med* **53,** 1522–1530, doi: S0891-5849(12)00490-X (2012).
31. Cao, J. *et al.* Prdx1 inhibits tumorigenesis via regulating PTEN/AKT activity. *Embo J* **28,** 1505–1517, doi: emboj2009101 (2009).
32. O'Leary, P. C. *et al.* Peroxiredoxin-1 protects estrogen receptor alpha from oxidative stress-induced suppression and is a protein biomarker of favorable prognosis in breast cancer. *Breast Cancer Res* **16,** R79, doi: bcr3691 (2014).
33. Rani, V., Neumann, C. A., Shao, C. & Tischfield, J. A. Prdx1 deficiency in mice promotes tissue specific loss of heterozygosity mediated by deficiency in DNA repair and increased oxidative stress. *Mutat Res* **735,** 39–45, doi: S0027-5107(12)00099-1 (2012).
34. Luo, M. *et al.* Characterization of the redox activity and disulfide bond formation in apurinic/apyrimidinic endonuclease. *Biochemistry* **51,** 695–705, doi: 10.1021/bi201034z (2012).
35. Vascotto, C. *et al.* Knock-in reconstitution studies reveal an unexpected role of Cys-65 in regulating APE1/Ref-1 subcellular trafficking and function. *Mol Biol Cell* **22,** 3887–3901, doi: mbc.E11-05-0391 (2011).
36. Egler, R. A. *et al.* Regulation of reactive oxygen species, DNA damage, and c-Myc function by peroxiredoxin 1. *Oncogene* **24,** 8038–8050, doi: 1208821 (2005).
37. Shatilla, A. & Ramotar, D. Embryonic extracts derived from the nematode Caenorhabditis elegans remove uracil from DNA by the sequential action of uracil-DNA glycosylase and AP (apurinic/apyrimidinic) endonuclease. *Biochem J* **365,** 547–553 (2002).
38. Cesaratto, L. *et al.* Specific inhibition of the redox activity of ape1/ref-1 by e3330 blocks tnf-alpha-induced activation of IL-8 production in liver cancer cell lines. *PLoS One* **8,** e70909, doi: 10.1371/journal.pone.0070909 (2013).
39. Hoffmann, E., Dittrich-Breiholz, O., Holtmann, H. & Kracht, M. Multiple control of interleukin-8 gene expression. *J Leukoc Biol* **72,** 847–855 (2002).
40. McCool, K. W. & Miyamoto, S. DNA damage-dependent NF-kappaB activation: NEMO turns nuclear signaling inside out. *Immunol Rev* **246,** 311–326, doi: 10.1111/j.1600-065X.2012.01101.x (2012).
41. Ishii, T., Warabi, E. & Yanagawa, T. Novel roles of peroxiredoxins in inflammation, cancer and innate immunity. *J Clin Biochem Nutr* **50,** 91–105, doi: 10.3164/jcbn.11-109 (2012).
42. Swinney, D. C. *et al.* A small molecule ubiquitination inhibitor blocks NF-kappa B-dependent cytokine expression in cells and rats. *J Biol Chem* **277,** 23573–23581, doi: 10.1074/jbc.M200842200 (2002).
43. Borrego, S. *et al.* Oxidative Stress and DNA Damage in Human Gastric Carcinoma: 8-Oxo-7′8-dihydro-2′-deoxyguanosine (8-oxo-dG) as a Possible Tumor Marker. *Int J Mol Sci* **14,** 3467–3486, doi: 10.3390/ijms14023467 (2013).
44. Integrated genomic analyses of ovarian carcinoma. *Nature* **474,** 609–615, doi: nature10166 (2011).
45. Gyorffy, B. *et al.* An online survival analysis tool to rapidly assess the effect of 22,277 genes on breast cancer prognosis using microarray data of 1,809 patients. *Breast Cancer Res Treat* **123,** 725–731, doi: 10.1007/s10549-009-0674-9 (2010).
46. Gyorffy, B., Lanczky, A. & Szallasi, Z. Implementing an online tool for genome-wide validation of survival-associated biomarkers in ovarian-cancer using microarray data from 1287 patients. *Endocr Relat Cancer* **19,** 197–208, doi: ERC-11-0329 (2012).
47. Neumann, C. A. *et al.* Essential role for the peroxiredoxin Prdx1 in erythrocyte antioxidant defence and tumour suppression. *Nature* **424,** 561–565, doi: 10.1038/nature01819 (2003).
48. Vidal, A. E., Hickson, I. D., Boiteux, S. & Radicella, J. P. Mechanism of stimulation of the DNA glycosylase activity of hOGG1 by the major human AP endonuclease: bypass of the AP lyase activity step. *Nucleic Acids Res* **29,** 1285–1292 (2001).
49. Ischenko, A. A. & Saparbaev, M. K. Alternative nucleotide incision repair pathway for oxidative DNA damage. *Nature* **415,** 183–187 (2002).
50. Mazouzi, A. *et al.* Insight into mechanisms of 3′-5′ exonuclease activity and removal of bulky 8,5′-cyclopurine adducts by apurinic/apyrimidinic endonucleases. *Proc Natl Acad Sci USA* **110,** E3071–3080, doi: 1305281110 (2013).
51. Jensen, M. D. *et al.* Involvement of oxidative pathways in cytokine-induced secretory phospholipase A2-IIA in astrocytes. *Neurochem Int* **55,** 362–368, doi: S0197-0186(09)00136-3 (2009).
52. Orino, K. *et al.* Ferritin and the response to oxidative stress. *Biochem J* **357,** 241–247 (2001).
53. Mu, Z. M., Yin, X. Y. & Prochownik, E. V. Pag, a putative tumor suppressor, interacts with the Myc Box II domain of c-Myc and selectively alters its biological function and target gene expression. *J Biol Chem* **277,** 43175–43184, doi: 10.1074/jbc.M206066200 (2002).
54. Rhee, S. G. & Woo, H. A. Multiple functions of peroxiredoxins: peroxidases, sensors and regulators of the intracellular messenger H(2)O(2), and protein chaperones. *Antioxid Redox Signal* **15,** 781–794, doi: 10.1089/ars.2010.3393 (2011).
55. Hansen, J. M., Moriarty-Craige, S. & Jones, D. P. Nuclear and cytoplasmic peroxiredoxin-1 differentially regulate NF-kappaB activities. *Free Radic Biol Med* **43,** 282–288, doi: S0891-5849(07)00296-1 (2007).
56. Chae, H. Z., Oubrahim, H., Park, J. W., Rhee, S. G. & Chock, P. B. Protein glutathionylation in the regulation of peroxiredoxins: a family of thiol-specific peroxidases that function as antioxidants, molecular chaperones, and signal modulators. *Antioxid Redox Signal* **16,** 506–523, doi: 10.1089/ars.2011.4260 (2012).
57. Chu, G. *et al.* Identification and verification of PRDX1 as aninflammation marker for colorectal cancer progression. *Am J Transl Res* **8,** 842–859 (2016).
58. Jang, H. H. *et al.* Phosphorylation and concomitant structural changes in human 2-Cys peroxiredoxin isotype I differentially regulate its peroxidase and molecular chaperone functions. *FEBS Lett* **580,** 351–355, doi: S0014-5793(05)01491-2 (2006).
59. Lee, S. R. *et al.* Reversible inactivation of the tumor suppressor PTEN by H2O2. *J Biol Chem* **277,** 20336–20342, doi: 10.1074/jbc.M111899200 (2002).
60. Chhipa, R. R., Lee, K. S., Onate, S., Wu, Y. & Ip, C. Prx1 enhances androgen receptor function in prostate cancer cells by increasing receptor affinity to dihydrotestosterone. *Mol Cancer Res* **7,** 1543–1552, doi: 1541-7786.MCR-08-0546 (2009).
61. Sobotta, M. C. *et al.* Peroxiredoxin-2 and STAT3 form a redox relay for H2O2 signaling. *Nat Chem Biol* **11,** 64–70, doi: 10.1038/nchembio.1695 (2015).
62. Shuto, T. *et al.* Activation of NF-kappa B by nontypeable Hemophilus influenzae is mediated by toll-like receptor 2-TAK1-dependent NIK-IKK alpha/beta-I kappa B alpha and MKK3/6-p38 MAP kinase signaling pathways in epithelial cells. *Proc Natl Acad Sci USA* **98,** 8774–8779, doi: 10.1073/pnas.151236098 (2001).
63. de Oliveira, S. *et al.* Cxcl8 (IL-8) mediates neutrophil recruitment and behavior in the zebrafish inflammatory response. *J Immunol* **190,** 4349–4359, doi: jimmunol.1203266 (2013).
64. Medzhitov, R. Origin and physiological roles of inflammation. *Nature* **454,** 428–435, doi: nature07201 (2008).
65. Wang, B., Cleary, P. P., Xu, H. & Li, J. D. Up-regulation of interleukin-8 by novel small cytoplasmic molecules of nontypeable Haemophilus influenzae via p38 and extracellular signal-regulated kinase pathways. *Infect Immun* **71,** 5523–5530 (2003).
66. Singh, J. K., Simoes, B. M., Howell, S. J., Farnie, G. & Clarke, R. B. Recent advances reveal IL-8 signaling as a potential key to targeting breast cancer stem cells. *Breast Cancer Res* **15,** 210, doi: bcr3436 (2013).
67. Campbell, L. M., Maxwell, P. J. & Waugh, D. J. Rationale and Means to Target Pro-Inflammatory Interleukin-8 (CXCL8) Signaling in Cancer. *Pharmaceuticals* (*Basel*) **6,** 929–959, doi: ph6080929 (2013).
68. Young, J. J., Patel, A. & Rai, P. Suppression of thioredoxin-1 induces premature senescence in normal human fibroblasts. *Biochem Biophys Res Commun* **392,** 363–368, doi: S0006-291X(10)00056-2 (2010).
69. Azam, S., Drobetsky, E. & Ramotar, D. Overexpression of the cis/trans isomerase PTPA triggers caspase 3-dependent apoptosis. *Apoptosis* **12,** 1243–1255 (2007).
70. Sui, G. *et al.* Yin Yang 1 is a negative regulator of p53. *Cell* **117,** 859–872, doi: 10.1016/j.cell.2004.06.004 (2004).

Acknowledgements

We thank Drs Helen Yu for her guidance in the APE1 complex purification, Krikor Bijian for analysis of the microarray data and T.C. Dakal for his contribution to supplemental Fig. S4 derived from the microarray data. This work was supported by research grants (MOP-93573 and RGPIN/202432-2012) to D.R. from the Canadian Institute of Health Research and the Natural Science and Engineering Research Council of Canada.

Author Contributions

H.N., Z.W., A.S. and D.R. conceived the experiments, H.N., Z.W. and A.S. conducted most of the experiments, H.N., Z.W., A.S., A.P., N.B., E.B.A., M.A.A.-J. and D.R. analyzed the results, H.N., Z.W. and D.R. wrote the paper.

Additional Information

Supplementary information accompanies this paper at http://www.nature.com/srep

Competing financial interests: The authors declare no competing financial interests.

How to cite this article: Nassour, H. *et al.* Peroxiredoxin 1 interacts with and blocks the redox factor APE1 from activating interleukin-8 expression. *Sci. Rep.* **6**, 29389; doi: 10.1038/srep29389 (2016).